Buildings, Energy and Environment Research Group
Faculty of Engineering

Novel Thermochemical Energy Storage System: From Material Development to Evaluation

By

Anti Kur, BSc, MSc

A thesis for the degree of Doctor of Philosophy in Sustainable Energy Technology

Supervisors:
Prof. Jo Darkwa
Dr. John Calautit

May, 2025

Table of Contents

Abstract

The building sector is a major contributor to global energy consumption and carbon emissions, with heating demand predominantly met by fossil fuels. As the integration of variable renewable and waste heat sources into urban heating networks expands, thermochemical energy storage (TCES) presents a promising solution, offering high energy density and the potential for long-duration storage. However, the practical deployment of TCES has been limited by material and reactor inefficiencies critical for industrial waste heat recovery.

This research aimed to develop and evaluate a novel TCES material tailored for medium-temperature waste heat applications. A new composite based on $Mg(OH)_2$ doped with 5 wt% KNO_3 and 15 wt% Al_2O_3 was synthesized and characterized. The doped material exhibited a reduced dehydration temperature from ~317 °C to 293 °C, enabling more efficient waste heat capture within the 293–400 °C range. The energy storage capacity increased from 1246 J/g to 1317 J/g. Molecular simulations predicted a thermal conductivity of 0.708 W/mK, an enhancement of 12.9% over pure $Mg(OH)_2$, which aligned well with experimental values (0.6484 W/mK).

Reactor-scale numerical modelling of 1.5 kg of the composite in an agitated fluidized bed reactor showed that dehydration began at 300 ℃ with an airflow of 28.95 kg/h, achieving a minimum fluidization velocity of 0.1850 m/s and a 99.99% reaction efficiency, releasing +5 kW of heat. Hydration initiated at 200 ℃ using a humidified air stream, with a minimum fluidization velocity of 0.01598 m/s and a 99.21% reaction efficiency, releasing −4.8 kW of heat. A water vapour to MgO molar ratio beyond 4:1 showed saturation effects, indicating water as a limiting factor in hydration.

These findings demonstrate the potential of the developed $Mg(OH)_2$-KNO_3-Al_2O_3 composite for efficient medium-temperature TCES. Future work should focus on long-term material stability, advanced reactor modelling, and full-scale validation to support real-world deployment in building energy systems.

List of Publications

Journal papers

- Kur, A., Darkwa, J., Worall, M., Calautit, J. & Boukhanauf, R. Thermal Conductivity Enhancement of Doped Magnesium Hydroxide for Medium-Temperature Heat Storage: A Molecular Dynamics Approach and Experimental Validation. *Int. J. Mol. Sci*. 2024, 25(24), 13596 https://doi.org/10.3390/ijms252011139
- Albeladi, N., Kur, A., Mokaya, R., Darkwa, J., Roger-Lund, S., Calautit, J., Worall, M. & Boukhanauf, R. Synthesis and Characterization of Doped Magnesium Hydroxide for Medium Heat Storage Application. *Materials* 2023, 16, 6296. https://doi.org/10.3390/ma16186296
- Kur, A., Darkwa, J., Calautit, J., Boukhanauf, R. & Worall, M. Solid–Gas Thermochemical Energy Storage Materials and Reactors for Low to High-Temperature Applications: A Concise Review. *Energies* 2023, 16, 756. https://doi.org/10.3390/en16020756

Conference papers

- Kur, A. Novel thermochemical reactor for variable temperature waste heat storage. *2023 East Midlands Doctoral Network Conference*; Northampton (UK); September 2023
- Kur, A., Darkwa, J., Roger-Lund, S., Calautit, J., Worall, M. & Boukhanauf, R. Synthesis and characterization of doped magnesium hydroxide for medium heat storage application. *20th International Conference on Sustainable Energy Technologies*; Nottingham (UK); August 2023
- Kur, A., Darkwa, J., Roger-Lund, S., Calautit, J., Worall, M. & Boukhanauf, R. Development and characterization of doped magnesium hydroxide for medium heat storage application. *2nd World Energy Storage Conference*; Istanbul (Turkey); December 2022

Acknowledgements

I am profoundly grateful to my supervisor, Prof. Jo Darkwa, for his exceptional guidance, mentorship, and encouragement throughout this research journey. As the saying goes, *"If I have seen further, it is by standing on the shoulders of giants"*—thank you for being that giant and for constantly challenging and inspiring me to strive for excellence.

My sincere thanks also go to Dr. John Calautit, my second supervisor, whose unwavering support and insightful suggestions, particularly regarding simulation tools and software applications, were instrumental in the success of this work. I owe immense appreciation to Dr. Rabah Boukhanouf, my internal assessor, for his detailed reviews and constructive feedback, which significantly enhanced the depth and quality of this research.

I am deeply grateful to the Tertiary Education Trust Fund (TeTFund), Nigeria, for sponsoring my PhD studies. Your generous funding made this opportunity and achievement possible.

Special thanks are due to the researchers, technicians, and fellow postgraduate colleagues who contributed in diverse ways during this project. I am especially thankful to Dr. Mark Worall for his technical support, training on the test rig, and guidance with instrumentation—your assistance was invaluable.

I deeply appreciate Dr. Rizal Sinaga, a colleague and cherished friend, and his wife, Utari, for their kindness and the memorable times we shared. Rizal's generosity in sharing his knowledge, particularly in molecular dynamics simulations, and his consistent encouragement were pivotal throughout this journey.

To my beloved wife, Doose, and our wonderful children—Senater, Kenana, and Shamimi—thank you for your unshakable love, patience, and countless sacrifices during my prolonged absence. This achievement would not have been possible without your support and understanding.

To my siblings, I remain ever grateful for your prayers, encouragement, and steadfast belief in my potential.

Finally, I dedicate this thesis to the memory of my dear parents—Wanivenge and Dio—who instilled in me the values of hard work, integrity, and perseverance. Your sacrifices and enduring love laid the foundation for everything I have achieved. I can only imagine how proud you would be today.

List of Tables

List of Figures

List of Abbreviations

Abbreviations	
LHS	Latent Heat Storage
SHS	Sensible Heat Storage
TCES	Thermochemical Energy Storage
TES	Thermal Energy Storage
DHW	Domestic Hot Water
CSTP	Concentrated Solar Thermal Power
PCM	Phase Change Material
HVAC	Heating, Ventilation, and Air Conditioning
DH	District Heating
GHG	Greenhouse Gas
HAM	Heat and Mass
HBN	Hexagonal Boron Nitride
STA	Simultaneous Thermal Analysis
YSZ	Yttria-Stabilized Zirconia
HTF	Heat Transfer Fluid
MBR	Moving Bed Reactor
FBR	Fluidized Bed Reactor
CFD	Computational Fluid Dynamics
DEM	Discrete Element Method
TCM	Thermochemical Material
BET	Brunauer-Emmett-Teller
DSC	Differential Scanning Calorimetry
EDX	Energy Dispersive X-ray
SEM	Scanning Electron Microscopy
TGA	Thermogravimetry Analysis
XPS	X-ray Photoelectron Spectroscopy
XRD	X-ray Diffractometry
LiPPS	Liquid Phase Photoelectron Spectrometer
UHV	Ultra-High Vacuum
NL-DFT	Non-Local Density Functional Theory
PSD	Pore Size Distribution/Particle Size Distribution
ICSD	Inorganic Crystal Structure Database
PDF	Powder Diffraction Form
MD	Molecular Dynamics
AMBER	Assisted Model Building with Energy Refinement
CHARMM	Chemistry at Harvard Macromolecular Mechanics
GROMACS	Groningen Machine for Chemical Simulations
NAMD	Nanoscale Molecular Dynamics
DL_POLY	Daresbury Laboratory Polymer
HOOMD	Highly Optimized Object-oriented Molecular Dynamics
LAMMPS	Large Scale Atomic/Molecular Massively Parallel Simulator
FORTRAN	Formula Translation
NPT	Number Pressure Temperature
NVE	Number Volume Energy
NVT	Number Volume Temperature
HPC	High-Performance Computer

PACKMOL	Pack Molecule
PBC	Periodic Boundary Condition
LJ	Lennard-Jones
EMD	Equilibrium Molecular Dynamics
G-K	Green-Kubo
NEMD	Non-Equilibrium Molecular Dynamics
THW	Transient Hot Wire
RDF	Radial Distribution Function
MFV	Minimum Fluidization Velocity
CSTR	Continuous Stirred Tank Reactor
EOS	Equation of State
PR	Peng-Robinson

Chapter 1: Introduction

1.1 Background

The building sector, comprising residential, commercial, and institutional buildings, is one of the largest energy consumers globally. According to the International Energy Agency (IEA), buildings account for 30% of global final energy consumption and almost 28% of direct carbon dioxide (CO_2) emissions [1]. The primary energy use in buildings is dominated by heating, ventilation, and air conditioning (HVAC) systems, which account for around 50% of total building energy consumption in many regions [2].

This energy demand for heating is largely met by the combustion of fossil fuels, which significantly contributes to the carbon footprint of the sector [3]. Given that fossil fuels account for around 74% of the heating demand in buildings, this not only contributes to climate change but also heightens concerns about energy security and affordability [4]. Hence, it is imperative to decarbonize the building sector to align with global, national, and local emission reduction targets as an urgent priority. Innovations that reduce energy consumption and emissions while simultaneously improving energy efficiency are therefore essential to achieve this.

Consequently, the transition to low or zero-carbon heating systems is crucial for decarbonizing the supply side of the built environment. Numerous viable options include geothermal and solar-thermal systems and heat pumps. However, the daily and seasonal variability of these low or zero-carbon energy sources and a mismatch between energy demand and supply pose challenges to decarbonizing individual buildings and neighbourhoods. District heating (DH) systems are well-positioned to provide the required infrastructure to meet demand from urban buildings using waste heat and zero-carbon sources, but they do need appropriate thermal energy storage facilities that can operate at different temperatures. These heat sources are commonly categorized by temperature as low-grade (ambient to 250 ℃), medium-grade (250–500 ℃), and high-grade

(>500 ℃). For instance, the UK's industrial and power generation sectors are estimated to produce approximately 391 TWh of waste heat annually across the various foregoing heat grades [5]. Additionally, substantial quantities of waste heat are generated from renewable energy sources such as solar and geothermal systems. From all the waste heat sources, medium-grade dominates, accounting for over 25% of the estimated total waste heat available in the UK [6]. Therefore, the efficient recovery and utilization of medium-grade waste heat for application in the building sector is of critical importance.

In this context, thermochemical energy storage (TCES) emerges as a promising technology to fulfil this requirement. For example, TCES materials have high energy storage densities and can be utilized for heat storage at different operating temperatures [7] from as low as 80 °C for solar-thermal applications to over 150 °C for waste heat recovery. They can retain the energy in the adsorbed state, with near-zero losses, and so potentially allowing storage inter-seasonally (i.e., storing solar energy in summer during low demand and discharging in winter during high demand), thereby offering flexibility to match the diverse thermal needs of buildings. These attributes, therefore, underscore the increased research interest in TCES in the last few decades as a promising technology for facilitating global energy transformation goals.

However, commercially available TCES materials possess relatively low thermal conductivity, which tends to affect their thermal response and thus the effectiveness of TCES reactors [8]. These materials also function at fixed and high dehydration temperatures, and are therefore unable to be used for harvesting waste heat from a wide range of heat sources [9]. There is therefore a need to gain a full understanding of the physical and chemical attributes of various potential TCES materials to enable novel materials to be developed. Accordingly, this project was focused on overcoming the scientific and technical limitations of existing medium-grade TCES materials.

1.2 Research aim and objectives

This research was aimed at developing a novel TCES material for medium-temperature waste heat storage applications. Therefore, the specific objectives of the research were to:

- Undertake comprehensive literature reviews of various thermochemical reactors and energy storage materials to establish their technical and scientific limitations.
- Screen and select core materials for the development of medium-temperature energy storage materials.
- Perform computational analysis to establish the thermophysical properties of the developed materials at molecular level.
- Undertake experimental approach to enhance the thermal performance of the developed material.
- Conduct numerical evaluation of the thermodynamic behaviour of the developed material in a model agitated fluidized bed.

1.3 Contribution to knowledge

The main contributions to knowledge from this research are summarized as follows.

Material performance improvement:

- Demonstrated that doping $Mg(OH)_2$ with 5 wt% KNO_3 significantly lowered its dehydration temperature (~24 ℃ reduction), and achieved a measurable increase in heat storage capacity, enhancing its suitability for medium-grade waste heat recovery.

Thermal conductivity enhancement strategy:

- Showed that incorporating 15 wt% Al_2O_3 nanoparticles improved thermal conductivity of doped $Mg(OH)_2$ by up to 12.9%, offering a pathway to faster heat transfer in TCES systems.

Reactor-scale modelling and system efficiency:

- Developed a novel process model for a fluidized bed reactor using 1.5 kg of material, achieving high dehydration (99.99%) and hydration (99.21%) efficiencies with approximately 5 kW energy exchange, and identified optimal operating conditions including temperature, airflow rate, and fluidization velocity.
- Identified a hydration efficiency limit related to water vapour saturation, with equilibrium reached at a 4:1 molar ratio, informing future reactor design and operation strategies.

1.4 Thesis structure

The remaining chapters of this thesis are presented as follows:

Chapter 2: Literature Review

Focuses on relevant background details in the literature related to thermochemical storage materials and reactors. It expounds on the principles governing thermochemical energy storage and its implementation, addressing technical concerns and limitations.

Chapter 3: Development of Novel TCES Materials

Covers the screening criteria for candidate materials, synthesis methods, and various characterization processes for the developed TCES materials.

Chapter 4: Thermal Enhancement Modelling of the Developed Material

Focuses on the computational approach used for analyzing the thermophysical properties of the developed materials at molecular level.

Chapter 5: Experimental Thermal Enhancement of the Developed Material

Covers the experimental approach to thermal enhancement of the developed material, leveraging the predictions from theoretical modelling.

Chapter 6: Numerical Evaluation of the Developed Material in a Model Agitated Fluidized Bed Reactor

Covers the development of multicomponent mathematical models, crucial for assessing the thermodynamic performance of the developed storage material in a model agitated fluidized bed reactor.

Chapter 7: Conclusion and Recommendations for Future Work

Provides analysis, implications, and conclusions to each theoretical and experimental aspect of the work and gives recommendations for future research.

Chapter 2: Literature Review

2.1 Introduction

This chapter gives an overview of thermal energy storage (TES), providing relevant background on the fundamental principles governing each TES technology and the practical issues related to implementation. The discussion encompasses technical concerns, current limitations, and emerging challenges in the field. Furthermore, the chapter highlights the trajectory of the state-of-the-art TCES as a promising TES option, offering insights into ongoing developments. Additionally, a forward-looking analysis is presented, outlining the anticipated future trends and advancements in this critical area of research.

2.1.1 Overview of thermal energy storage technologies

As the shift toward more sustainable energy systems becomes imperative, the significance of energy storage becomes increasingly prominent. Thermal energy storage (TES), often referred to as heat batteries, has garnered growing attention, emerging as a crucial component bridging the gap between heat demand and supply. TES serves as a valuable solution for harnessing and utilizing heat that would otherwise be wasted, playing a pivotal role in improving the energy efficiency of heat-related processes, optimizing heating systems, and increasing the utilization of renewable energy sources [10]. The three main types of TES recognized are sensible heat storage (SHS), latent heat storage (LHS), and thermochemical energy storage (TCES).

2.2 Sensible heat storage

SHS technology relies on introducing heat into a storage medium to raise its temperature while keeping its phase unchanged. The stored heat (Q) depends on factors such as the material's specific heat capacity (C_p), its quantity or mass (m), and the temperature range (ΔT) during operation [11]. This is mathematically expressed as

$$Q = mC_p\Delta T \tag{2.1}$$

Since $m = \rho V,$ where ρ and V are the medium's density and volume, the sensible storage heat capacity is also written as

$$Q = \rho V C_p \Delta T \tag{2.2}$$

So that the energy storage density of the medium is

$$\frac{Q}{V\Delta T} = \rho C_p \tag{2.3}$$

Going by the specific heat capacity, cost, and temperature range, solid and liquid materials are generally preferred as heat storage media [12]. For high-temperature thermal storage (with temperature changes exceeding 100 °C), solid materials such as sand, gravel, concrete, and metals are typically used. In contrast, for thermal storage across various temperature ranges, liquid materials like water, aquifers, some heat transfer oils, and high-temperature molten salts are commonly employed [12–14]. A comparison of some commonly used SHS materials is presented in Table 2.1.

Table 2. 1 Classification and comparison of common SHS materials [12]

Classification	**Material**	**Operation temperature (℃)**	**Density (kg/m^3)**	**Thermal conductivity (W/mK)**	**Energy density (kJ/m^3)**
Solid	Brick	0 - 1000	1500 -1800	0.9 - 1.2	1764
	Concrete	350 - 390	2307	1.36	2112
	Rock	200 - 300	2480	2 - 7	2940
	Sand	< 1500	1450	0.26	1136
	Cast iron	200 - 400	7900	29.3	6100
Liquid	Thermal oil	0 - 400	875	0.1276	1995
	Water	0 - 100	1000	0.59	4192
	Molten nitrate (KNO_3/$NaNO_3$/ $NaNO_2$)	450 - 540	1800	-	1740

The advantage of a liquid storage medium lies in the ease of being circulated (as an active system), therefore allowing for effective heat transport. Additionally, the density difference caused by heating the liquid generates buoyancy, which helps establish a desirable thermal gradient within the storage material [15]. SHS is the most established and widely used TES technique in buildings and usually employs water as a medium for storing and releasing thermal energy. The choice of water owes to its high specific heat capacity, non-toxicity, abundance, chemical stability, and high capacity rate during charge and discharge [16]. In most cases, SHS is employed in space heating and domestic hot water supply systems, where temperatures typically range between 20°C and 90 °C. For a temperature change of 70 °C within this range, water can store about 290 MJ/m^3 of thermal energy and thus remains the most used storage medium for solar-based hot water and space heating applications [17]. Water tank storage is common and cost-effective, and its efficiency can be enhanced by ensuring optimal water stratification within the tank and utilizing highly effective thermal insulation [18].

Detailed design criteria for systems with water as a heat storage material are available in the published report of Kemna et al. [19]. In the UK, where space heating is a significant energy demand, SHS systems are integrated with central heating systems to store excess heat generated by renewable sources or off-peak electricity. Water tank storage can also be used to store heated water for domestic hot water (DHW) supply. Hot water storage systems, which act as buffer storage for DHW supply, usually range in capacity from 500 litres to several cubic metres. This technology is also employed in solar thermal installations that combine DHW with building heating systems, known as Solar-Combi-Systems [18]. A typical example of a system for water tank storage consisting of a solar collector and a boiler that heats the water storage tank is shown in Figure 2.1.

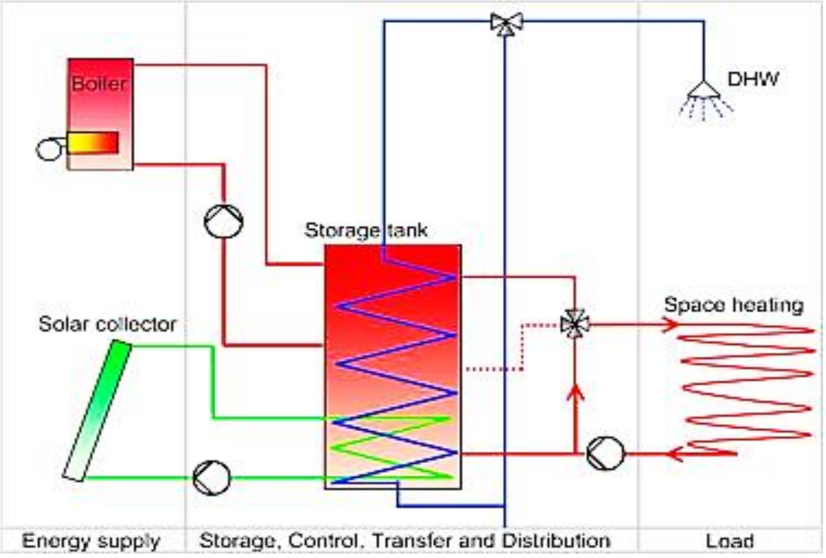

Figure 2. 1 Schematic of a combined system of solar collector and boiler for charging the storage tank [20]

Additionally, large hot water tanks are used for storing solar thermal heat over extended periods, often in conjunction with small district heating (DH) systems. They can have volumes up to several thousand cubic meters. Typically, charging temperatures are between 80-90 °C, and the usable temperature difference can be increased by using heat pumps to discharge to temperatures down to around 10 °C [18].

One of the major drawbacks to the performance of a water tank storage is its size. The large storage volume impacts system efficiency, economic viability, the ability to provide long-term storage, and the system's suitability for various applications [16]. Therefore, such systems require the development of techniques that substantially eliminate heat losses due to steam diffusion through the walls and optimize stratification within the tank to maintain good thermal performance [15]. To address these issues, modern water storage vessels are incorporated with several advanced features to improve the overall efficiency of heat storage, including [21]:

- A minimal number of thermal bridges around the storage vessel to reduce heat losses.
- Enhanced heat insulation, such as vacuum insulation.
- Siphon pipe introductions to prevent natural convection losses.
- Stratification enhancers to increase the exergy value of the stored content.
- Internal devices to reduce the speed of inlet water, preventing disturbance of stratification within the storage vessel.
- Large heat exchangers or mantle heat exchangers.

Despite these improvements, one disadvantage of using water as a SHS medium is its upper-temperature limit of around 100 °C, which restricts its applicability for high-temperature heat storage, especially in concentrated solar thermal power (CSTP) systems or industrial processes. It also has a high vapour pressure at elevated temperatures and is susceptible to corrosion [22]

2.3 Latent heat storage

In Latent heat storage (LHS), thermal energy is stored by utilizing the latent heat of phase change materials (PCMs) during phase transitions. That is, when a PCM undergoes a phase change, heat energy is either released or absorbed. LHS can be accomplished via solid-solid, solid-liquid, solid-gas, and liquid-gas phase transitions, but only two are of practical interest: solid-liquid and solid-solid [23]. Although the solid-gas and liquid-gas transitions possess a greater latent heat, their substantial volume changes during phase transition pose containment challenges, thus limiting their suitability for application in thermal storage systems [23]. For solid-liquid transition, the change of phase takes place at the melting temperature when heat is added but does not exhibit a temperature rise. Thus, the increase in heat cannot be detected and appears to be ‘hidden’ (latent). The transition from solid to liquid typically involves a slight volume change of less than 10%, and there is generally no significant pressure change [24]. These factors result in the melting or solidification of the material occurring at a constant temperature known as the phase change temperature. Therefore, the storage of heat energy within a narrow temperature range close to the phase change temperature is one of the most cherished advantages of LHS [7]. Moreover, the solid-liquid transition processes have proven to be economically competitive for application in thermal energy storage systems compared with other LHS solutions [23,25].

The amount of heat stored (ΔQ) is equivalent to the change in enthalpy (ΔH) between the solid and liquid phases [24], that is

$$\Delta Q = \Delta H = m\Delta h \tag{2.4}$$

where $m\Delta h$ is the latent heat. In a typical LHS system, the total stored heat comprises both sensible heat, observed before and after the phase change, and latent heat, observed specifically during the phase transition [25]. The phase transitions are depicted in the schematic diagram in Figure 2.2, whilst the total energy involved in each phase is expressed in Equation 2.5.

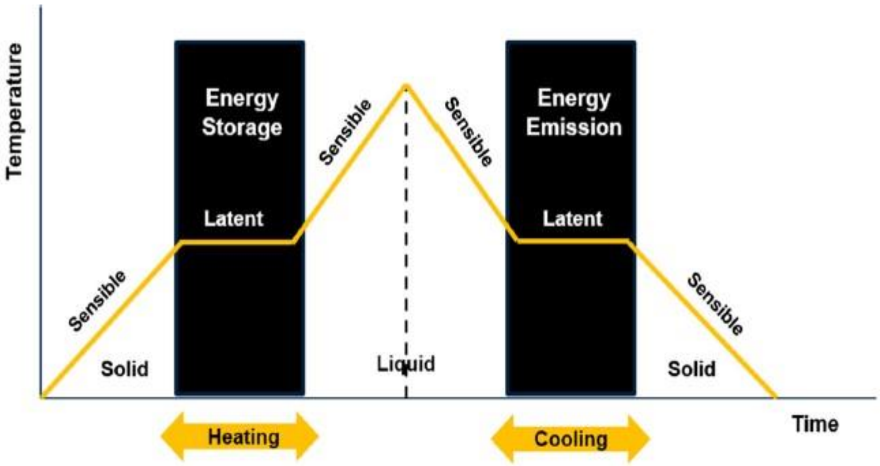

Figure 2. 2 Schematic diagram of solid-liquid and liquid-solid phase transitions of a PCM [26]

$$Q = mC_p\Delta \mathrm{T}(\mathrm{s}) + \mathrm{m}\Delta \mathrm{h} + \mathrm{m}C_p\Delta T(l) \tag{2.5}$$

where the mass (m), specific heat capacity at constant pressure (C_p), and temperature (T) are the properties of the LHS material. Generally, solid-liquid PCMs fall into different categories (Figure 2.3), each with specific properties. The properties of different PCMs are summarized in Table 2.2.

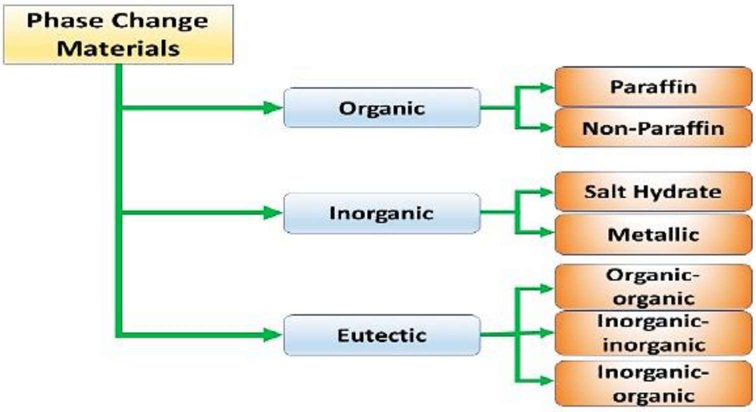

Figure 2. 3 Classification of solid-liquid PCMs [27]

Table 2. 2 Properties of different solid-liquid PCMs [28]

	Organic paraffin	**Organic non-paraffin**	**Inorganic salt hydrates**	**Inorganic metal eutectics**
Melting temperature (℃)	-12 – 187	<150	20 – 140	30 - 125
Latent heat J/m^3) x 10^6	190 – 240	140 – 430	250 – 660	300 - 800
Density (kg/m^3)	~ 810	900 – 1800	900 – 2200	~ 8000
Thermal conductivity (W/mK)	~ 0.25	0.2	0.6 – 1.2	~ 20
Toxicity	No	Some	Highly	Some
Corrosivity	Low	Some	Highly	Some
Congruent melt	Yes	Some	Most	Yes
Supercooling	No	No	Most	No

Organic PCMs offer numerous advantages. Their phase transition temperature increases with the number of carbon atoms in their chain, making them suitable for a wide range of applications. They are non-corrosive, chemically inert, and thermally stable within specified temperature ranges. Additionally, they have a congruent melting process, preventing phase segregation during repeated transitions. They also have low liquid phase undercooling, high latent heat of fusion, high nucleation rate, are recyclable, and are compatible with most construction materials [29,30]. However, organic PCMs also have several disadvantages, including low thermal conductivity, flammability, significant volume variation, and high cost [29,30]. For inorganic PCMs, salt hydrates are the most investigated. Compared to the organic PCMs, they have notable advantages, including relatively higher thermal conductivity and high LHS density. They also exhibit low volume change during phase transition and are non-flammable [29]. However, their main drawback is incongruent melting, which causes phase segregation and dwindling performance after each charge-discharge cycle. Additionally, they have poor nucleating properties, leading to supercooling before crystallization, they are corrosive and incompatible with many construction materials [31]. On the other hand, eutectics, composed of mixtures of various organic, inorganic, or hybrid phase change materials (PCMs), allow for the creation of materials with tailored thermal properties, such as specific phase change temperatures and latent heat capacities. Their key advantage lies in their customizable phase change temperatures for various applications. Organic eutectic mixtures offer additional benefits, including long-term stability, high phase change enthalpy, and ease of impregnation into porous materials due to their chemical compatibility and surface tension [32]. However, their main drawback is their high cost.

Despite these shortcomings, PCMs find applications across various sectors such as renewable energy (e.g., solar power), HVAC (Heating, Ventilation, and Air Conditioning) systems, thermal management in electronics, and building materials for energy-efficient buildings. For instance, Du et al. [26] conducted a focused review of the utilization of PCMs for both cooling and heating applications across various temperature ranges. Their findings reveal significant potential for energy savings and efficiency improvements in buildings. Specifically, PCMs have the potential to be incorporated into free cooling systems or building construction materials [26,27], to provide thermal sufficiency, enhanced indoor thermal comfort, and decreased energy consumption.

However, several grey areas and gaps still exist. While there have been advancements in expanding the operational temperature range of LHS systems, there is still a need for PCMs that can accommodate high temperatures encountered in certain applications, such as solar thermal energy storage [33]. Again, the rate of heat transfer during the phase change process can sometimes be slower than desired, requiring efficient heat exchange systems to maximize performance [31]. Ensuring the long-term stability and reliability of LHS systems remains a challenge, particularly regarding compatibility issues between PCMs and container materials as well as potential degradation mechanisms over multiple phase change cycles. Research efforts have shown that the fabrication of composite PCMs and encapsulation techniques have helped in addressing some of these issues like enhancement in thermal conductivity, cyclability, and heat transfer rate, as well as preventing the leakage of the liquid phase [30]. However, one disadvantage of PCM encapsulation is its cost, and the encapsulation can potentially impact the mechanical aspect of building materials [33].

Therefore, ongoing research and development in PCMs must address these shortcomings to facilitate the discovery and optimization of materials with desirable phase change temperatures, improved thermal conductivity, and enhanced cycling stability, thereby driving the further adoption of LHS systems.

2.4 Thermochemical energy storage

In the TCES approach, heat is stored chemically when a material (say AB) absorbs heat equal to its heat of reaction and splits into products A and B (Equation 2.6), which are stored separately. The splitting route is endothermic and is the charging process. Bringing the products together triggers a reversible reaction that releases the heat. This reversible exothermic path is the discharging process.

$$\mathrm{AB} + \Delta\mathrm{H} \leftrightarrows \mathrm{A} + \mathrm{B} \tag{2.6}$$

Therefore, reversible chemical reactions govern the storage and release of heat in TCES systems, with the amount stored determined by the enthalpy ($\Delta\mathrm{H}$) change of the reaction. The reaction typically occurs in a reactor, and the process can be run continuously using a suitable reactor design. Charging and discharging phases can be conducted in two separate reactors with storage tanks in between (Figure 2.4). Heat is introduced in Reactor 1, designated as the charging reactor, and solid component A undergoes a reaction to produce solid component B, resulting in the release of a gaseous component, in this case, water vapour. Following a storage duration, component B is transferred to

Reactor 2, where water is introduced to facilitate the release of the stored energy. The thermochemical cycle is then completed and can be initiated anew by reintroducing component A into Reactor 1.

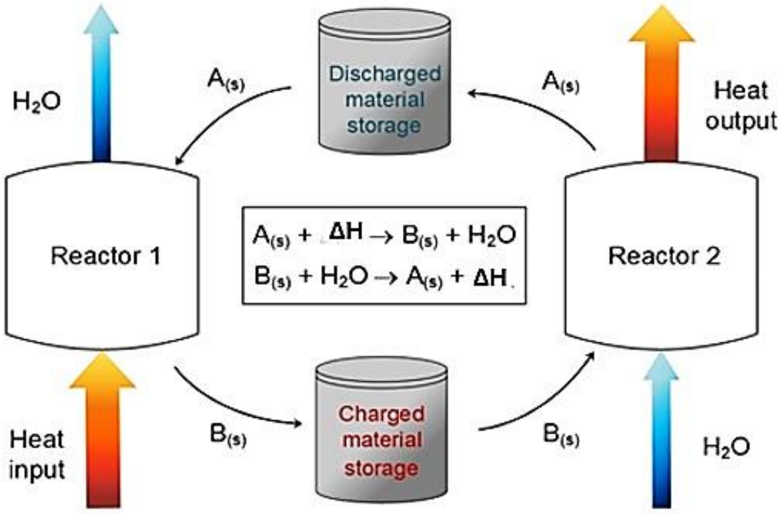

Figure 2. 4 General principle of TCES [34]

The reversibility of the chemical reactions is a key aspect of TCES. Also, of great importance to the long-term viability of the technology is the ability to repeatedly charge and discharge the storage medium without significant degradation. Therefore, identifying and using suitable materials for the storage medium is crucial, and generally, these materials should have the ability to undergo reversible reactions, have high energy density, and good thermal stability. The choice of reactions is often based on their operating temperature range. By selecting reactions that occur within a specific temperature range, TCES systems can be designed to match the thermal requirements of different applications.

The merits of TCES over the other two technologies (SHS and LHS) lie in its theoretically higher energy storage density and zero heat losses during storage [35]. Concerning energy density, it is theoretically estimated to be about 5 to 10 times higher than LHS and SHS, respectively, when compared on the same scale basis [36,37]. Thus, the theoretical higher energy storage density and zero heat loss are the salient hallmarks of the TCES principle. These features can facilitate the design of compact thermal (or heat) storage options and could be effective where space constraints are significant, especially in buildings. Additionally, TCES systems can be tuned to operate in a wide range of different temperatures and pressures [38], thus making them suitable for storing all grades of waste heat. This offers the possibility of being operated using various heat sources such as the storage of solar energy between seasons (long-term storage) and the storage and transfer of heat generated in industrial processes from one facility to another or a residential area (short-term storage). Moreover, the effective integration of TCES into district heating (DH) networks can lead to benefits such as increased energy efficiency and reliability, and reduction in energy use, costs, and greenhouse gas (GHG) emissions. Thus, TCES is potentially applicable in lowering fossil fuel consumption and related GHG emissions [39].

These attributes have attracted increasing interest in TCES research, albeit at its experimental stage, and still have some significant issues that require resolution. Some of these issues include the complexity of infrastructure as well as low levels of thermal attainment in practical systems [35]. Therefore, a robust approach to operational control and understanding of the system must have a real-time model to predict its dynamics. For this reason, numerical or modelling studies are required for deeper theoretical insights and the prediction of the system's behaviour. In addition, research still focuses on finding suitable materials with sufficient energy density, hygrothermal stability, and cyclability at conditions suitable for system operation [40]. One way is to enhance the materials' properties before integration into reactor systems [41]. Additionally, it also requires suitable reactor optimization techniques and heat exchanger frameworks [38]

The most investigated TCES candidate materials are discussed in the following Sections, starting from low-temperature through medium to high-temperature systems. The focus is only on solid-gas reactions because they are known to show better values of reaction efficiencies in reactors [42].

2.4.1 Thermochemical reactions and materials for TCES

TES based on chemical reactions is justifiably advantageous for seasonal storage [36]. These reaction systems store energy in the form of chemical potential, and the energy per mole required to break up chemical bonds is more than any other thermal storage system. These reactions are characterized by changes in the molecular composition of the reactants involved [37] and usually take place at different temperature ranges [43]. High energy storage density and reversibility, among others, are key requirements for TCES materials. It is important to emphasize that the type of reaction has immense implications for the reactor design and system integration [44].

TCES reactions are classified into three categories, namely solid-gas, liquid-gas, and gas-gas reactions, regarding the nature of the reactants and products. But for temperatures over 300 ℃, only solid-gas and, in some cases, liquid-gas reactions remain practicable [7]. Furthermore, solid-gas reactions have been widely studied as a very promising heat storage method [45]. The interest in these reactions is due to their wide range of equilibrium temperatures and self-separation of reactants. Chemical reactions (including chemical sorption processes) premised on solid-gas systems are an encouraging method for the storage and conversion of heat energy for heating or cooling purposes [46]. While the sorption processes are used to store low (<100 ℃) and medium (100–400 ℃) grade heat with enthalpies in the range of 20–70 kJ/mol [46]. Chemical reactions are utilized for the storage of medium (100–400 ℃) and high (>400 ℃) grade heat, and the enthalpies are in the range of 80–180 kJ/mol [37,43].

Different kinds of solid-gas reactions are employed for TCES. These are categorized based on the composition of the solid reactant as the most prominent [47] The reactions include those based on hydrates, hydrides, hydroxides, carbonates, and oxides. It has been suggested that whenever TCES materials are considered, their operating temperature range and enthalpy must be specified for the application. For this reason, Bauer [7] characterized the solid-gas reactions according to reaction temperatures:

- Dehydration/hydration of metal salt hydrates (40–260 °C).
- Dehydrogenation/hydrogenation of metal hydrides (80–400 °C).
- Dehydration/hydration of metal hydroxides (250–600 °C).
- Decarbonation/carbonation of metal carbonates (100–950 °C).
- Deoxygenation/oxygenation of metal oxides (600–1000 °C).

2.4.1.1 Dehydration/hydration of metal salt hydrates

TCES materials for low-temperature applications have attracted remarkable attention. Salt hydrates and composite sorbents based on salt hydrates belong to this category. They have become preferred materials for TCES in building applications [48] due to their high energy density and low turning temperatures [49]. The low turning temperatures are suitable for integration with sources like solar energy or low-grade waste heat and make them fit for residential space heating applications [49]. Much literature is available on high-potential salts, and this includes chlorides – LiCl [50], $CaCl_2$ [44–46], and $MgCl_2$ [54]; bromides–$SrBr_2$ [55,56] and LiBr [50,57]; sulfates – $MgSO_4$ [53,54,58], $Al_2(SO4)_3$ [53,59] and CuSO4 [60]. Furthermore, other promising hydrates such as Na_2S and K_2CO_3 were studied by de Jong et al. [61] and Gaeini et al. [62], respectively.

TCES materials must fulfil common conditions such as low cost, non-poisonous, and non-corrosive, in addition to having sufficient energy density and suitable turning temperatures. These requirements are fulfilled by many salt hydrates [53]. However, numerous salts proposed for low-grade thermal energy storage have failed [49]. In a typical case, for instance, van Essen et al. [53] did a theoretical study of four salt hydrates namely, $MgSO_4.7H_2O$, $Al_2(SO_4)_3.18H_2O$, $CaCl_2.2H_2O$ and $MgCl_2.6H_2O$ using a thermogravimetry and differential scanning calorimetry (TG-DSC) apparatus. Based on the measured temperature lift under practical conditions, $MgCl_2$ was considered the most promising with a high theoretical energy density of 2.8 GJ/m^3. However, both hygroscopic chlorides under investigation tended to form a gel-like material (due to melting or formation of solution) during the hydration experiments, which prohibited further water uptake. Similarly, Donkers et al.[60] studied the cyclability of $CuCl_2$, $CuSO_4$, $MgCl_2$, and $MgSO_4$ in hydration/dehydration reactions. They observed the effect of fracturing to be greater in hydrates with larger volumetric changes. In conclusion, $CuCl_2$ was adjudged the most promising heat storage material.

A systematic evaluation of 125 salt hydrates has been performed by N'Tsoukpoe et al. [59] using criteria such as safety, theoretical calculations, and thermogravimetry analysis (TGA). Out of 45 preselected salt hydrates, $SrBr_2.6H_2O$ and $LaCl_3.7H_2O$ appeared to be the most promising. However, the expected efficiency and net energy storage density (including water storage) remained low. Similarly, a review of 563 reactions has been carried out [63] to evaluate the theoretical suitability of salt hydrates as seasonal heat storage materials. Up to 25 salt hydrates were identified. By considering cost, chemical stability, reaction kinetics, and safety, K_2CO_3 was determined to be the most promising candidate, but low energy density was noticed.

Table 2. 3 Thermodynamic properties of some salt hydrates [64].

Reaction	Theoretical energy density (GJ/m^3)	Experimental energy density (GJ/m^3)	Temperature (charge/discharge) (℃)	Water vapour pressure (mbar)
$MgCl_2\cdot 6H_2O\leftrightharpoons MgCl_2\cdot H2O+5H_2O$	2.5	0.71	150/30-50	13
$MgCl_2\cdot 4H_2O\leftrightharpoons MgCl_2\cdot 2H_2O+2H_2O$	1.27	1.10	118/n.a.	13
$CaCl_2\cdot 2H_2O\leftrightharpoons CaCl_2+2H_2O$	1.1	n.a.	95	n.a.
$Al_2(SO4)_3\cdot 6H_2O\leftrightharpoons Al_2(SO4)_3+6H_2O$	1.9	n.a.	150	n.a.
$MgSO_4.6H_2O\leftrightharpoons MgSO_4.H_2O+5H_2O$	2.37	1..83	72/n.a.	13
$MgSO_4\cdot 7H_2O\leftrightharpoons MgSO_4.H_2O+6H_2O$	2.3	n.a.	150/105	n.a.
$CaSO_4\cdot 2H_2O\leftrightharpoons CaSO_4+2H_2O$	1.4	n.a.	n.a./89	n.a.
$Na_2S\cdot 5H_2O\leftrightharpoons Na2S.1/2H_2O+9/2H_2O$	2.7	n.a	80/65	13
$SrBr_2\cdot 6H_2O\leftrightharpoons SrBr_2.H_2O+5H_2O$	2.3	2.08	n.a./23.5	20
$Li_2SO_4\cdot H_2O\leftrightharpoons LiSO_4+H_2O$	0.92	0.80	103/n.a.	13
$CuSO_4\cdot 5H_2O\leftrightharpoons CuSO_4.H_2O+4H_2O$	2.07	1.85	92/n.a.	13

n.a.: not available

Table 2.2 gives the theoretical and experimental energy density, reaction temperature, and water vapour pressure of some salt hydrates [64]. It is, however, worth noting that in all these comparative investigations, the difference in behaviour is attributable to the intrinsic properties (crystal structure and thermodynamics) of the materials. Therefore, a general kinetic model of the reaction process in salt hydrates will require specific information on the material properties. So, besides the high potential shown by some salt hydrates, several associated issues are still obvious. These include poor hydrothermal stability, slow thermodynamics, high corrosivity, and toxicity [48]. Such attributes make it difficult for the monomer salt hydrates to be used for TCES without modification of their properties. For this reason, researchers have experimented with composite materials. Fopah Lele et al. [55] evaluated four salt hydrates ($CaCl_2$, $MgCl_2$, $SrBr_2$, and $MgSO_4$) and host matrices (activated carbon, expanded natural graphite, and silica gel). The results on both systems for only salts gave thermal conductivity in the range of 0.3-1.3 W/mK with a measurement uncertainty of less than 14%. Zhao et al. [65] mixed $SrBr_2$ and expanded natural graphite treated with sulfuric acid. The composite with 10 wt% of $SrBr_2$ proved satisfactory with good mass transfer performance and no degradation in water uptake.

Salt mixtures appear promising, but the general technical issue reported is mass transport within the matrix's pores due to deliquescence, overhydration (with possible leakage or pore blockage), and a low-temperature lift [48]. A proposal for pairing suitable salt hydrates according to different matrix materials, reactor analyses, and structural optimization methods for the enhancement of heat and mass (HAM) transfer has been recently published [66]. Again, selecting a suitable binary salt mixture may increase the performance of each material and avoid its unique individual shortcomings. A double salt hydrate, $Na_2Zn(SO_4)_2 \cdot 4H_2O$, has been reported as having exhibited suitable stability at the first ten hydration/dehydration cycles, with an excellent energy storage density of 4.7 GJ/m^3 and theoretical efficiency up to 77.4% [67]. It might be necessary that the influence of material characterization and reaction parameters are considered to determine the optimum mixing pair and ratio, as well as optimize system controls under different operating conditions [48]. Despite these, N'Tsoukpoe and Kuznik [9] assert that the performance achieved with salt-hydrate systems is not competitive and that the performance or advantages of the TCES materials have probably been overestimated.

2.4.1.2 Dehydrogenation/hydrogenation of metal hydrides

Metal hydrides (MHs) are compounds formed by the reversible reaction of hydrogen and metal or metal alloy, and this reversible absorption of hydrogen gas is exothermic [45]. The utilization of MHs for TCES is encouraged by high energy efficiency, high volumetric energy density, and cost [68]. It also offers flexibility in its wide range of operating temperatures. On the other hand, one of the main disadvantages of MH systems is the need for hydrogen storage [69]. This means that the MH system can be a closed system with an intermediate hydrogen storage subsystem. It is suggested that by coupling a high temperature with a low-temperature metal hydride system, a self-regulating reversible metal hydride energy storage system can be established [70].

Lithium hydride (LiH), calcium hydride (CaH_2), and magnesium hydride (MgH_2) systems have been studied for their TCES potentials. However, more attention has been paid to MgH_2 [35]. It has a working temperature between 200–500 ℃ and decomposes into Mg metal releasing hydrogen with a reaction enthalpy of 75 kJ/mol and a heat storage capacity of around 0.8 kWh/kg [45,71]. The hydrogen gas can be stored in a reservoir under the equilibrium pressure of MgH_2. For instance, the MgH_2/Mg equilibrium pressure of 10 bar at 350 °C and 20 bar at 400 °C is shown in Figure 2.5. According to Felderhoff et al. [45], if the pressure is lower than the equilibrium pressure at a given temperature (shaded area in Figure 2.5), MgH_2 decomposes until the pressure inside the system reaches the equilibrium pressure. At pressures higher than the equilibrium pressure, Mg metal can be hydrogenated (white area in Figure 2.5).

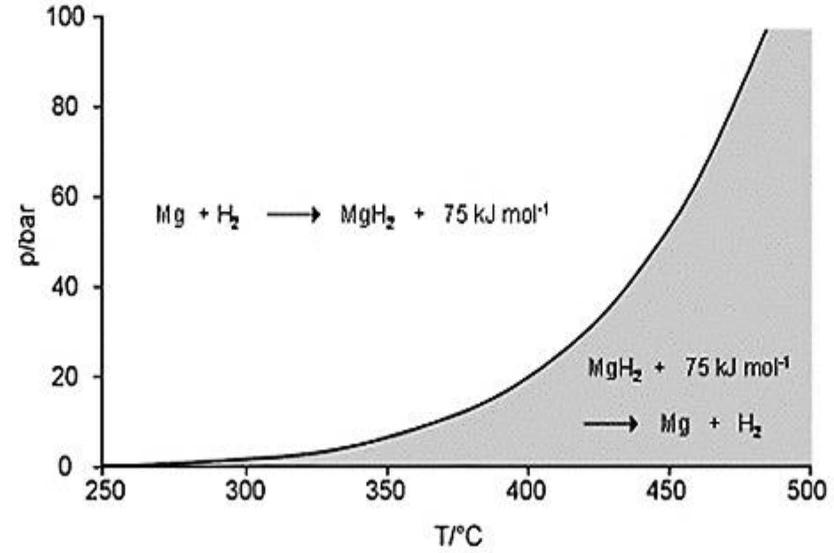

Figure 2. 5 Equilibrium pressure of MgH_2 as a function of temperature [45]

Chen et al. [35] note that the MgH_2/Mg pair suffers from poor reversibility. Its cyclic stability drops by 75% after 500 cycles [72] which is a limiting factor in the large-scale application. Additionally, its high thermodynamic stability and sluggish reaction kinetics are the major obstacles to its extensive application [73]. Table 2.3 shows the thermodynamic properties of MgH_2 [74].

Table 2. 4 Thermodynamic parameters and energy storage properties of MgH_2 [74]

Thermodynamic Parameters	Values
Formation enthalpy, kJ/(mol.H_2)	-74.5
Formation entropy, J/(mol.H_2.K)	-135
Hydrogen Storage Capacity (Theoretical)	
Gravimetric capacity, wt%	7.6
Volumetric capacity, g/(L.H_2)	110
Thermal Energy Storage Capacity (Theoretical)	
Gravimetric capacity, kJ/kg	2204
Volumetric capacity, kJ/dm^3	1763

Strategies employed to overcome these issues include the addition of nanostructures, alloying, and MgH_2-based composites. The catalytic addition of different transition metals or transition metal oxides can greatly accelerate the hydrogenation/dehydrogenation kinetics [45]. Khan et al. [75] investigated two nanostructured MgH_2 and cobalt (Co) powders. The hydrogen storage properties of the $2MgH_2$-Co powder and $2MgH_2$-Co compressed pellet were analyzed. Fast hydrogenation was observed in the de-hydride $2MgH_2$-Co compressed pellet with about 2.75 wt% absorbed in less than 1 min at 300 ℃, and a maximum hydrogen storage capacity of 4.43 wt%. The hydrogen absorption activation energy of the $2MgH_2$-Co compressed pellet was also lower than in the $2MgH_2$-Co powder. Banrejee et al. [76] prepared nanocrystalline magnesium and compared it with micro-crystalline magnesium. The developed nanocrystalline Mg exhibited improved properties with a higher hydrogen storage capacity of 6.24 wt% at 300 ℃. Prolonged ball milling led to faster hydrogenation kinetics (up to 90% of the saturation value in 15.5 minutes at 250 ℃) and a substantial decrease in the activation barrier. Nanostructuring has also been studied [77,78] with remarkable improvements in Mg-based storage properties. However, nanostructuring could result in poor thermal conductivity [35]. Also, the drawback in powder materials is usually due to their tendency towards coalescing and sintering during dehydrogenation/hydrogenation cycles.

Alloying is an effective and easy-to-handle method of improving the sorption property of MgH_2/Mg [35]. Intermetallic compounds of transition metals are among the catalytic materials that can facilitate the thermal storage processes in MgH_2 [78]. Usually, intermetallic hydrides are composites of a hydride-forming element at high temperatures and a non-hydride-forming element, such as Mg_2NiH_4 and Mg_2FeH_6. Research efforts aimed at reducing the reaction temperatures of these composite hydrides have been achieved by the addition or substitution of existing elements [79]. There seems to be a consensus that increasing the number of 3d elements would improve the kinetics by decreasing the activation energy of hydrogen desorption. For instance, the enthalpy change associated with the formation of Mg_2FeH_6 at 500 ℃ was measured to be 77.4 kJ/mol H_2, lower than the reported values of 98 kJ/mol H_2 [80]. Zhang et al. [73] also reported a decrease in the hydrogen desorption enthalpy and initial dehydrogenation temperature of MgH_2 by incorporation of either Ti or Ni. Sulaiman et al. [81] reported that 5 wt% K_2NiF_6-doped MgH_2 sample started desorbing around 260 ℃, which was a reduction of about 95 ℃ and 157 ℃ compared with the as-milled and as-received MgH_2. Additionally, the de/absorption kinetics were also improved significantly compared to the un-doped MgH_2. In another approach, Majid et al. [82] selected $TiFe_{0.8}Mn_{0.2}$, graphite, and Fe as additives. Compared to pure milled MgH_2 powder, they found that the dehydrogenation peak temperatures were decreased by 90, 160, and 165 ℃ for Mg-$TiFe_{0.8}Mn_{0.2}$-graphite, Mg-Fe-graphite, and Mg-$TiFe_{0.8}Mn_{0.2}$-Fe-graphite composites respectively. The co-addition of $TiFe_{0.8}Mn_{0.2}$, graphite, and Fe exhibited synergistic effects in improving the hydrogen desorption properties of MgH_2.

The roles of Ti-based catalysis and its consequent hydrogen storage effects on MgH_2 have been reviewed by Zhou et al. [74]. It concludes that the doping technique via Ti-based catalysts is a viable approach to enhancing the reaction of Mg-based materials. A comprehensive compilation of Ti-based catalysis of MgH_2 systems, corresponding synthesis approaches, and kinetic behaviours is presented in their review. On the other hand, Kumar et al. [83] performed calculations based on the First Principles to investigate the dehydrogenation kinetics considering doping at various layers of MgH_2 (110) surface with Ca, Al, Ga, Sc, Ni, Ti, and V. Doping at the first and second layers of MgH_2 (110) had a significant role in lowering the H_2 desorption (from surface) barrier energy. The screening approach found Al and Sc as the best possible dopants in lowering desorption temperature while preserving similar gravimetric density and bulk modulus as of pure MgH_2 system. By extending frontiers, Jain et al. [84] did an investigation of the role of alkaline metal fluoride (MgF_2) as a catalyst in the hydrogen storage behaviour of MgH_2. For a 5 mol% MgF_2 admixed into MgH_2 powder, hydrogenation measurements at 335℃ showed 92% of the absorbed theoretical capacity in less than 20 minutes (compared to 70% by pure MgH_2). Sorption studies further point to the possibility of complete absorption at low temperatures down to 145 ℃. Again, cyclic measurements made at 310 ℃ revealed an inconsequential loss in the total storage capacity. These results implied that the sensitivity of the material to atmospheric conditions is low, and it is easy to handle. Thus, it can be employed in applications where operation at relatively high temperatures is insignificant.

In the foregoing, a variety of dopants for MgH_2 have been reported, and the respective Mg-based hydride materials were enhanced. However, despite improvements in the material properties, thermodynamic tuning remains a major challenge [85]. Present approaches have been successful to some extent in addressing it, but much is still desired for practical application.

2.4.1.3 Dehydration/hydration of metal hydroxides

Thermochemical heat storage with metal hydroxides results from a reversible reaction of water (steam) and metal oxides at high temperatures (~500 ℃) and near-atmospheric pressures [72]. The alkaline earth metal hydroxides like $Mg(OH)_2$, $Ca(OH)_2$, $Sr(OH)_2$, or $Ba(OH)_2$ have been considered storage materials [45]. The initial candidate hydroxide-oxide pairs are $Mg(OH)_2/MgO$, $Ca(OH)_2/CaO$, $Sr(OH)_2/SrO$, and $Ba(OH)_2/BaO$. The theoretical turning temperatures and thermodynamic data of these hydroxides are presented in Table 2.4. The reactions are in the range of 70–1005 ℃, though most of the reactions are too low for high-temperature applications [86] thus, they usually occur at medium temperatures of $250<T<450$ ℃. The steam partial pressure and the temperature drive the hydration/dehydration reactions [36]. Figure 2.6 shows some couples that could be used for TCES application.

Table 2. 5 Equilibrium temperature and heat storage capacity of metal hydroxides [86]

Material	**Temperature (℃)**	**Reaction Enthalpy (kJ/mol)**	**Gravimetric energy density (kJ/kg)**
$Ca(OH)_2/CaO$	515	100.177	1352
$Mg(OH)_2/MgO$	265	77.745	1333
$Be(OH)_2/BeO$	70	51.276	1191
$Mn(OH)_2/MnO$	190	67.072	754
$Sr(OH)_2/SrO$	755	88.581	728.3
$Ba(OH)_2/BaO$	1005	93.462	545.47
$Ni(OH)_2/NiO$	70	47.846	516
$Zn(OH)_2/ZnO$	55	49.609	498.96
$Cd(OH)_2/CdO$	125	59.952	409.4

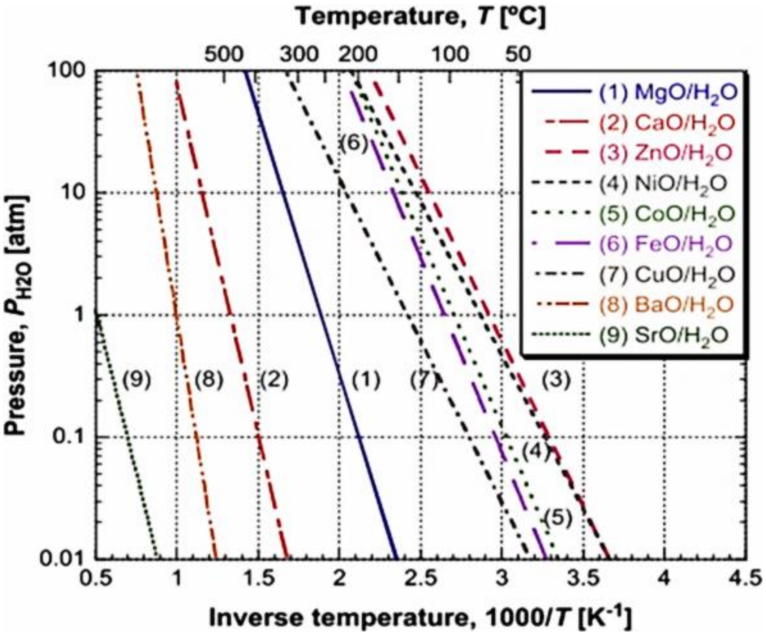

Figure 2. 6 Reaction equilibrium lines for metal oxide/water reaction systems [72]

Probably, regarding the high reaction enthalpies and energy storage densities (Table 2.4), mainly the hydroxides $Ca(OH)_2$ and $Mg(OH)_2$ have been extensively studied [35,45].

However, the $Ca(OH)_2/CaO$ system is the most explored hydroxide system for TCES, prompting tests in lab-scale reactors and thermogravimetry analysis (TGA) [38]. One reason is, the hydration of MgO is very slow in superheated steam and the rate of reaction drops with the rise in temperature [45,72]. Furthermore, the decomposition of the $Mg(OH)_2$ system takes place at a relatively lower temperature of around 330 ℃ [35] and its reaction enthalpy degenerates with temperatures up to 500 ℃, unlike that of $Ca(OH)_2$.

Given these attributes, much research has been done on the potential application of $Ca(OH)_2/CaO$ as a long-term TCES system. For instance, Schaube et al. [87] investigated a 10 mg sample of a $Ca(OH)_2/CaO$ system. Full conversion and cycling stability were reported over 100 cycles at a water partial pressure of 1 bar (even at 0.956 bar), with an equilibrium temperature of 505 ℃ and enthalpy of 104.4 kJ/mol. However, little success was achieved in the cycling stability of a 60g sample of the reaction system as degradation was reported over 25 cycles, and agglomeration was also observed [88]. Also, Criado et al.[89] investigated $Ca(OH)_2/CaO$ hydration/dehydration reaction and obtained higher rates than those reported in the literature at temperatures in the range of 400–560 ℃ and partial steam pressures between 0 and 100 kPa. However, particle attrition was observed for large particle sizes of the material. In another work, Dai et al. [90] investigated the cycling stability of the $Ca(OH)_2/CaO$ system for 20 successive dehydration/hydration cycles. Existing problems relating to agglomeration, sintering, poor thermal conductivity, and irregularity in the rate of heat release were raised. There is a consensus that major problems encountered in $Ca(OH)_2$ reactors relate to particle agglomeration and sintering, and poor heat transfer characteristics. As a result, much of the research direction has been around materials enhancement through additives (doping) or composites, as well as reactor optimization.

Huang et al. [91] tried the doping of $Ca(OH)_2$ by hexagonal boron nitride (HBN) and analysis showed improvement in both thermal conductivity and dehydration enthalpy of the material. It also revealed a 15 wt% as optimal mass content of HBN-doped composite with improved activity after 10 dehydration/rehydration cycles. In addition, a 67% rehydration conversion and energy density greater than 1000 kJ/kg were achieved. Doping of $Ca(OH)_2$ with potassium nitrate, KNO_3, has also been reported by Shkatulov et al. [92]. With 5 wt% KNO_3 addition to $Ca(OH)_2$, the dehydration temperature of the material was reduced, and the reaction rates increased but the material lost its dehydration heat by 7%. Wang et al. [93] obtained a similar result with 10 wt% KNO_3 addition and the doped $Ca(OH)_2$ further showed good cycling stability in the nitrogen atmosphere but failed in air. Gollsch et al. [94] modified $Ca(OH)_2$ powder with nanostructured flow agents to improve the powder's flowability. The additives consisted of nanostructured Si and/or Al_2O_3. Additives of weight fractions 6–12% improved the flowability of the powder. However, after cycling, the flowability of the mixtures decreased while that of the pure powder increased. Analysis showed a correlation between growth in particle size and increased flowability. Additionally, the formation of phases in the additives led to a decrease in absolute heat release of up to 50%, although some of the side products seemingly added to the measured heat release by hydrating exothermally.

To tackle the problem of low thermal conductivity and the cohesive nature of bulk powder material, Mejia et al. [95] investigated ceramic encapsulated CaO granules and $Ca(OH)_2$ granules coated with Al_2O_3 nanostructured particles. Results showed that both encapsulated materials did not change their shape after six-fold cycling. However, the Al_2O_3-coated sample exhibited volume expansion during hydration. There was a reduction in the reactivity of the ceramic sample, whereas the performance of the Al_2O_3 sample remained the same as the unmodified $Ca(OH)_2$. Afflerbach et al. [96] investigated encapsulated sample of $Ca(OH)_2$ and good mechanical stability with over ten reaction cycles was attained in a lab-scale reactor. Compared to the thermal conductivity of non-compressed powdery $Ca(OH)_2$ previously reported as 0.11 W/mK [97], the current form exhibited a lower thermal conductivity of 0.078 W/mK. Therefore, much is still required in terms of material enhancement and reactor bed optimization to enable the applicability of $Ca(OH)_2$ for TCES.

On the other hand, the reversible reaction involving magnesium hydroxide and magnesium oxide pair, $Mg(OH)_2/MgO$, is identified as suitable for heat storage in the temperature range of 300 °C to 400 °C [98]. Furthermore, it has recently been widely explored for its potential for application in the medium-temperature range of heat storage. The interest in this temperature range owes to the fact that more than a quarter of the total projected waste heat potential of 300 TWh/year in Europe is within the medium-temperature range (200–500 °C) [6]. However, earlier research by Kato et al. [99,100] indicated that the dehydration temperature for this reaction occurs above 350 ℃, which is not thermodynamically favourable for the intended application. Consequently, there arose a need to lower the dehydration temperature to cover a broader temperature range. Therefore, an investigation by Ryu et al. [101] revealed that doping $Mg(OH)_2$ with alkali metal salts could significantly reduce the dehydration temperature to achieve that purpose.

Shkatulov et al. [44] later demonstrated that nitrate salts could serve as effective dopants in hydroxides for improving dehydration outcomes. They proposed that nitrate anions could infiltrate the brucite hydroxide lattice in a way that facilitates the formation of MgO nuclei, thereby causing the structure to decompose at a lower temperature. Furthermore, they achieved a reduction of up to 50 ℃ in the dehydration temperature with sodium nitrate ($NaNO_3$) doping of $Mg(OH)_2$. However, the heat storage decreased from 1325 J/g to 1040 J/g [102]. In another study, Shkatulov and Aristov [103] used lithium nitrate ($LiNO_3$) to dope $Mg(OH)_2$, resulting in a 76 °C decrease in dehydration temperature. Similarly, Sun et al. [104] employed cerium nitrate ($Ce(NO_3)_3$) as a dopant, achieving a 29 °C reduction in dehydration temperature, however, this also reduced the heat storage capacity. Li et al. [105] incorporated 10 wt% of $LiNO_3$ into $Mg(OH)_2$, which led to a 56 °C decrease in dehydration temperature. All these studies however observed significant impacts on the heat storage capacities of the storage materials.

Therefore, there is still a need to explore other types of dopants that could protect the energy storage integrity of $Mg(OH)_2$. That is, reducing its dehydration temperature without trading off the energy stored thereby becoming applicable for storage in a wider temperature range.

2.4.1.4 Decarbonation/carbonation of metal carbonates

Decarbonation/carbonation reaction of metal carbonates has also proven to be an attractive high-temperature heat storage system. In this case, heat is used to perform the endothermic breakdown of carbonate, and the products are CO_2 and metal oxide. The interest in carbonates is due to their relatively high operating temperatures (typically over 800 ℃), high volumetric density, low operating pressure, non-toxicity, abundance, and cheapness [37,72]. The decomposition of $CaCO_3$, $SrCO_3$, $BaCO_3$, $MgCO_3$, and $PbCO_3$ has been studied [38]. However, the controversy about the high refractoriness of $MgCO_3$/MgO and the toxicity of $PbCO_3$/PbO is a drawback for further research in these materials [35]. Also, the carbonation reaction of BaO into $BaCO_3$ is hindered by the melting of the material during the decomposition step [106]. So, among the carbonates, $CaCO_3$ is considered the most promising heat storage material [35,45] and the focus will be on the $CaCO_3$/CaO system. It has been reported that after 40 high-temperature carbonation/decarbonation cycles with CaO, the carbonation (adsorptive) reaction significantly decreased because of the decrease in pore volume in the material [35]. This loss in porosity is caused by a decrease in the surface area of CaO due to the sintering of the particles [38,45], thereby inhibiting CO_2 access to the active sites within the material. Several techniques have been developed to minimize this loss in adsorption capacity. To increase the active surface area and stability of the pore structure, the use of additives, reduction of the particle size, and the synthesis of novel materials with the microporous structure were proposed [107].

To this end, Lu and Wu [108] doped nano CaO with Li_2SO_4 and showed that the Li_2SO_4-nano CaO adsorbent maintained a 51% conversion after 11 cycles compared to pure nano CaO at 27.3% under the same conditions. The superior performance of the Li_2SO_4-nano CaO adsorbent was attributed to pore enlargement due to increase in macro-pore proportion by Li_2SO_4 addition. Moreover, there were increased reaction rates and a lowering of the decomposition temperature by 15 ℃ in comparison with the pure material. In another work [109], different MgO concentrations were added to the CaO material. The additions with 5 and 10 wt% of MgO exhibited high CO_2 adsorption and retention capacity over multiple cycles. In particular, the CaO with 10 wt% MgO exhibited steady adsorption capacity over 30 cycles. Similarly, Wang [110] recently synthesized a porous MgO-stabilized nano CaO powder and realized highly effective long-term conversion because of its resistance to pore-plugging and sintering. Benitez-Guerrero [111] reported the synthesis of porous CaO/SiO_2 composites by bio-template route using calcium nitrate, $Ca(NO_3)_2$, and rice husk as support. The morphology and composition of the biomorphic material improved the CaO multicycle activity, as it served to enhance CaO and inhibited pore-plugging effects. The influence of SiO_2 on $CaO/CaCO_3$ has also been studied by Chen et al. [112]. The optimal 5 wt% SiO_2-doped $CaCO_3$ is demonstrated to enhance the reactivity, heat capacity, and 28% enhancement of the reversibility owing to the rise in grain boundary migration resistance. Table 2.5 shows the cycling stability achievements due to some dopants [112].

Table 2. 6 Comparison of cycling stability of $CaO/CaCO_3$ after doping.

Doping Materials	**Number of Cycles**	**Storage Conversion**
SiO_2	20	62.09%
Li_2SO_4	11	51.0%
MgO	20	42.03%
$Ca_3Al_2O_6$	20	51.69%

Binary metallic elements and oxides have been experimented with recently. For instance, composites of CaO doped with Mn and Fe were reported to enhance the cycling stability of the material [113]. A synergy between the small grain size and the reinforced skeletal structures prevented agglomeration of the composites, thereby enhancing their cycling stability. On the other hand, Sun et al. [114] reported that 5 wt% Al_2O_3 and 5 wt% CeO_2 co-doped on CaO showed the highest and most stable energy storage capacity under the carbonation pressure of 1.3 MPa during 30 cycles. In addition, the synthetic material possessed strong basicity and provided a large surface area and pore volume during the multicycle energy storage. Again, Raganati et al. [115] experimented with the application of an acoustic perturbation method that remarkably enhanced the carbonation performance of fine limestone particles. Indeed, it prevented agglomeration which affects carbonation from both the gaseous (CO_2) and solid ($CaCO_3$) sides of the reaction, thus enhancing the fluidization quality, reactants contact, and mass transfer coefficients. More information on in-situ data of $CaCO_3$ doping samples, measurement parameters, and results can be accessed in the work of Moller et al. [116].

Calcium carbonate has the most economic advantage of being widespread, cheap, and with high gravimetric energy density (3029 kJ/kg). The high operating temperatures make this TCES system suitable for various applications such as integration with a solar furnace and calcium looping technology. However, this system is stable only up to 20 cycles without any degradation in the absorption capacity. The cycling stability and reversibility must, however, be improved up to 1000 cycles to make this system practical [72].

2.4.1.5 Deoxygenation/oxygenation of metal oxides

Suitable transition metal oxides undergo a reduction reaction at high temperatures, and by that, thermal energy is absorbed. The reversible re-oxidation takes place below specific equilibrium temperatures, and hence, thermal energy will be delivered [117]. Thus, the reversible reduction/oxidation (redox) reactions of metal oxides show high potential as TCES materials. In comparison to the other TCES options, redox systems have the advantage of using air as both the heat transfer fluid (HTF) and the reactant. This eliminates the necessity for a different heat exchanger or gas storage needs. For this reason, TCES, based on metal oxide redox reactions, permits working with an open system [38]. In that case, it is important to investigate these systems in consistency with the control of oxygen partial pressure (pO_2)[38]. With lowering partial pressures of the reactive gas, the reduction temperature also decreases, as represented in the Van't Hoff diagram in Figure 2.7.

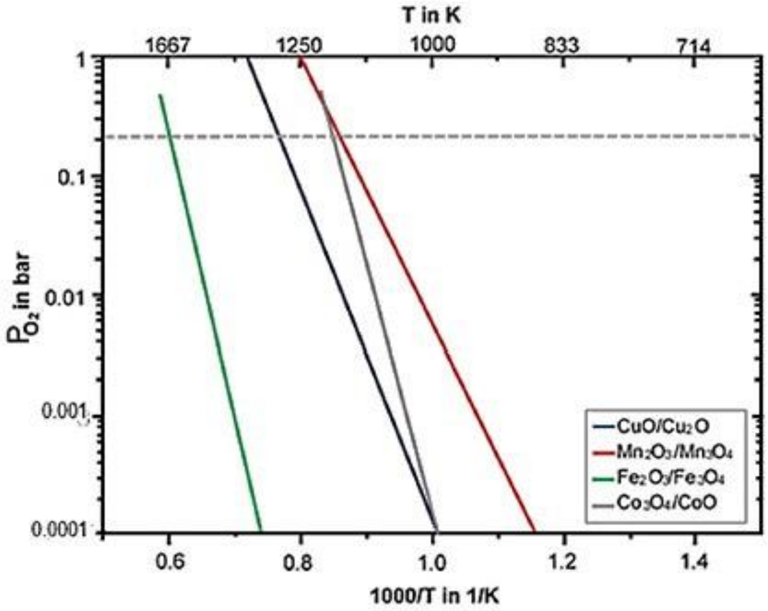

Figure 2. 7 Variation of temperature with oxygen partial pressures for Cu, Mn, Fe, and Co oxides [117]

In comparing metal oxide systems, it was revealed that only cobalt oxide (Co_3O_4), iron oxide (Fe_2O_3), copper oxide (CuO), and manganese oxide (Mn_3O_4) showed befitting reaction temperatures, enthalpies, cycling stabilities, and material costs [117]. In another work, Silakhori et al. [118] assessed redox reactions of CuO/Cu_2O, Co_3O_4/CoO, Mn_2O_3/Mn_3O_4, and Pb_3O_4/PbO using TGA. The results showed that CuO/Cu_2O and Co_3O_4/CoO were highly reversible under isothermal pressure-swing cycles, while Mn_2O_3/Mn_3O_4 exhibited slight signs of sintering, and Pb_3O_4 was unreactive up to 550℃. The free Gibbs energy ($\Delta G°$) was determined for several oxides and PbO_2/PbO, PbO_2/Pb_3O_4, Pb_3O_4/PbO, CuO/Cu_2O, and Sb_2O_5/Sb_2O_3 were confirmed to show thermal storage attributes based on negative $\Delta G°$. Among these, CuO/Cu_2O displayed a higher total enthalpy of 404.67 kJ/mol. However, the occurrence of phase transition was observed at temperatures near 1200^{o}C, and the molten state is prone to corrosiveness. Deutsch et al. [119] carried out kinetic investigations of the CuO/Cu_2O reaction cycle under isothermal and isokinetic conditions and used simultaneous thermal analysis (STA) and a lab-scale fixed-bed reactor. The outcome of the reaction resulted in substantial discrepancies between both analyses. In STA, outstanding stability of the reaction over 20 cycles was shown with a bit of sintering occurring. Heavy sintering occurred in the reactor that hampered the reaction as well as increased the reaction time thrice higher than previously reported values in literature. Alonso et al. [120] tested the suitability of CuO/Cu_2O in an argon atmosphere and the results indicated the reduction of CuO led to nearly 80% conversion. The reduction in air atmosphere was not favourable because of stronger coalescing particles that hindered the redox reactions. Synthesis of porous CuO-based granules with yttria-stabilized zirconia (YSZ) was also reported [121]. The synthesized granules exhibited high conversion over 100 consecutive cycles in air between 950 and 1050 ℃. Stable cycling performances were also obtained in the reactor for 30 consecutive isobaric and isothermal operation modes.

Cobalt and manganese oxides have also been considered promising redox systems for TCES. The CoO/Co_3O_4 system has the potential to be the most suited pure metal oxide system for TCES due to its fast reaction kinetics and complete reaction reversibility. However, cobalt oxide is also considered potentially toxic and would not be cost-effective for large-scale storage [122]. On the other hand, the Mn_2O_3/Mn_3O_4 redox couple is favoured in terms of minimal cost and toxicity in comparison to its alternatives and has been suggested as an appropriate material for TCES. However, several contentions have been singled out concerning its ability for full energy storage sustainability with the required number of cycles necessary for this application [123]. Given this, Bielsa et al. [123] studied several variables such as temperature and heating/cooling rates. A suitable choice of these variables was shown to enhance the heat storage capacity by 1.46 times in a 10-cycle test. The weight change curves during the TGA are shown in Figure 2.8. However, several levels of sintering were observed, proving the major drawback of this material.

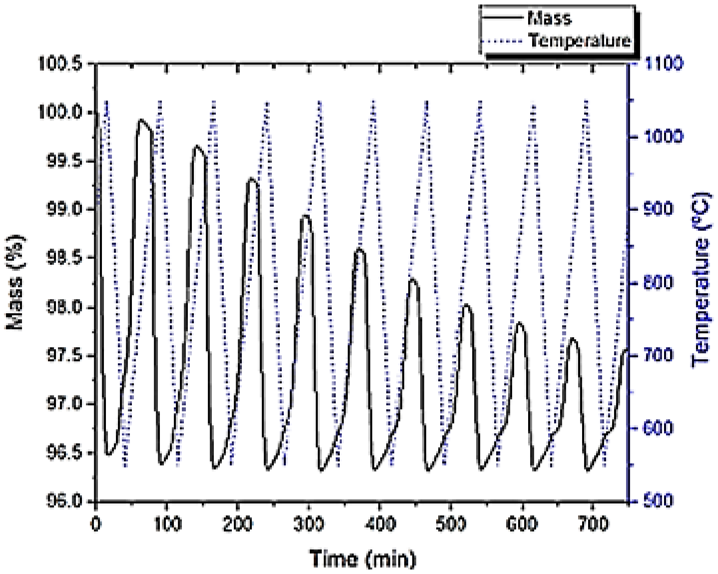

Figure 2. 8 Weight change curves during 10 Mn_2O_3/Mn_3O_4 TGA cycles between 500–1100 ℃ [123]

Andre et al. [124] studied the impact of Fe addition, which decreased the redox activity and energy storage capacity of Co_3O_4. However, the cycling stability of Mn_2O_3 was significantly improved with added Fe amounts above 20 mol%, while the energy storage capacity was unchanged. Similarly, a mixed oxide of Co-Cu-O with low amounts (<10 mol%) of Cu showed excellent cycling stability and higher reaction enthalpy among the others, Mn-Cu-O and Co-Mn-O systems [122]. Neises et al. [125] performed 30 cycles on a 5 wt% Al_2O_3-doped Co_3O_4 without any material degradation, yielding only a 50% conversion. This was attributed to the insufficient stirring and mixing of the metal oxide particle bed inside the reactor. Notwithstanding, about 400 kJ/Kg energy density was achieved per cycle. The graphical presentation of oxygen absorbed per mol of the doped Co_3O_4 during reduction is shown in Figure 2.9.

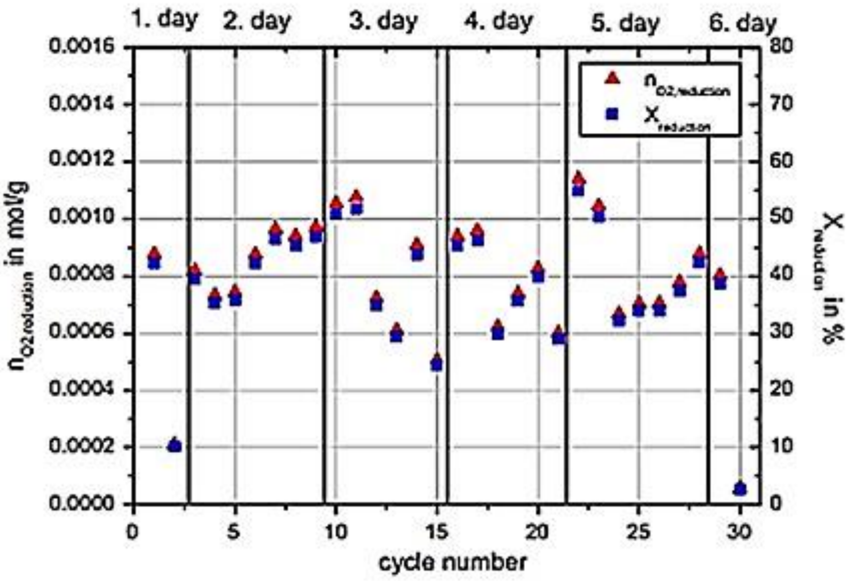

Figure 2. 9 Amount of oxygen per mol of Co_3O_4 and conversion during reduction [125]

On the contrary, Carrillo et al. [69] obtained results that indicated that operation with pure oxides (Mn_2O_3 and Co_3O_4) was more effective for TCES application compared to their mixed oxides. Although the values of heat released and absorbed for Mn_2O_3 were far from those obtained with Co_3O_4, its excellent cycling stability, low toxicity, and low cost make it an interesting candidate for heat storage applications. Relatively, the Cu_2O/CuO system has more prospects for TCES application than the CoO/Co_3O_4 system if the reaction is optimized in the reactor. In one experiment [126], isothermal runs at different oxygen partial pressures were carried out in TGA, and defined fractions of CuO samples were analyzed. Results revealed that the oxygen partial pressure affects the kinetics, and the reparameterization of the pressure term influences the kinetic analysis of the oxidation reaction. It concluded that the models described for various parameters can provide useful information for the design of redox reactors [126].

2.5 Thermochemical energy storage reactors for solid-gas reactions

Reactors provide the platform for the operation of thermochemical storage systems. To guarantee efficiency in the charging and discharging process of the TCES material, a suitable reactor concept designed for a particular operation and storage material is necessary [127]. That is, the nature of reactants or the type of reaction determines the type and design of the reactor and the system integration. Additionally, the art of designing efficient reactors is as important as materials enhancement itself. Different criteria have been used to classify reactors, such as operation mode, number of phases, reaction types, or a combination [128]. Based on the mode of operation, three major solid-gas reactors are implemented: fixed (packed) bed, moving bed, and fluidized bed reactors [72], as shown in Figure 2.10.

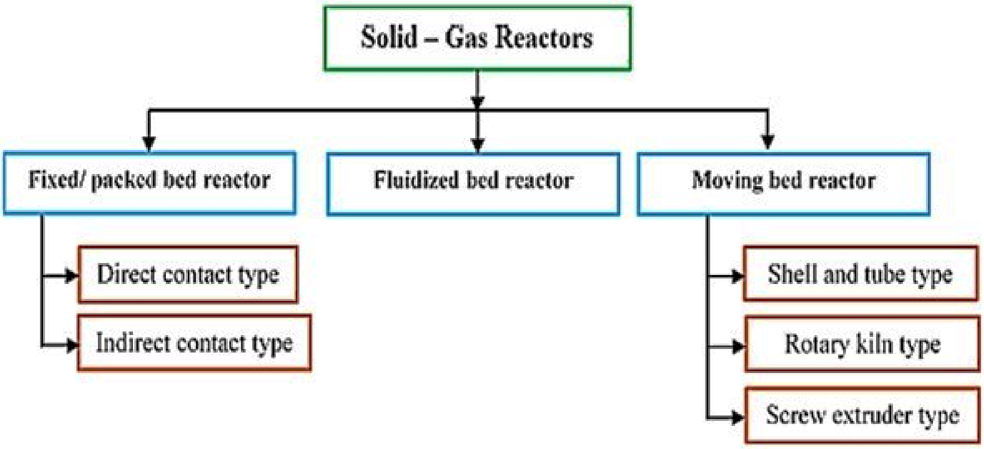

Figure 2. 10 Classification of solid-gas reactors [72]

2.5.1 Fixed-bed reactors

Fixed or packed beds are hollow tubes, pipes, or other vessels filled with packing materials for chemical processing. The packing material may contain catalyst particles or adsorbents, and the purpose of such a bed is to improve contact between two phases in a chemical process. Thus, in packed-bed reactors, the solid reactants/products are arranged in the vessel's bed during heat storage and release, with the flux of reactants passing through the stationary bed. The HTF and reactants are not in contact, resulting in heat transfer through the walls of heat exchangers.

Fixed-bed reactors are the most common lab-scale test rigs and have been investigated by Schmidt et al. [129]. In this work, several dehydration and hydration cycles were performed to study the charge and discharge characteristics of a 20 kg $Ca(OH)_2$ material. The dehydration was performed at 45 °C and the rehydration at about 55 °C. A conversion of 77% without degradation after 10 cycles was achieved. Investigation of different charging and discharging temperatures was then recommended to optimize the overall conversion of the material. Again, Ranjha et al. [130] modelled a two-dimensional rectangular bed filled with $CaO/Ca(OH)_2$ powder for different flow geometries and bed properties. They showed that increasing the porosity of the bed provided higher energy density but slowed the reaction, resulting in a lower average outlet temperature. A possible remedy for this deficiency would be to increase the bed dimensions, but this could result in a slower reaction owing to the poor thermal conductivity of the materials. This suggests that a systematic optimization process could be applied as a compromise between various parameters. However, this depends on the desired output temperature, energy requirements, and the rate of thermal energy storage and retrieval. Figure 2.11 shows the results of comparing varying bed porosities with total conversion time and the maximum outlet temperature in counter-current flow geometry.

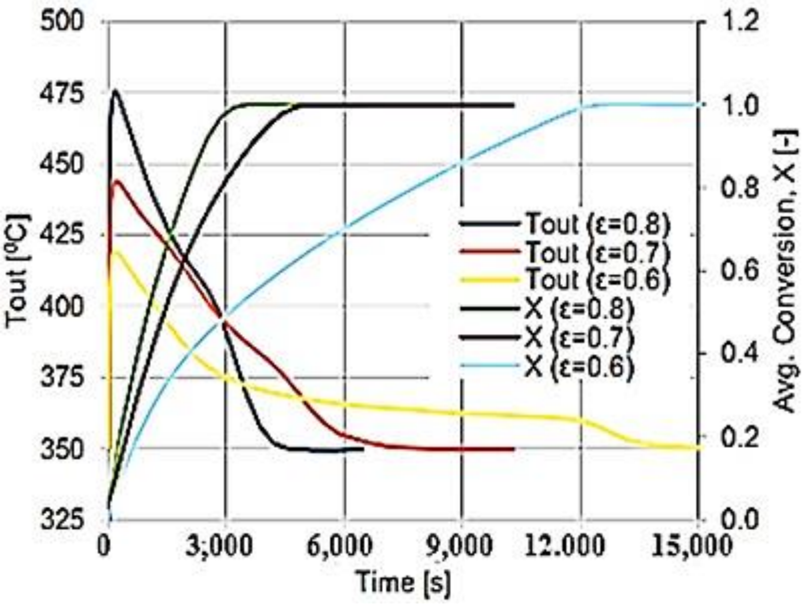

Figure 2. 11 Outlet temperature of the HTF and the conversion as a function of time during hydration for bed porosities of 0.6, 0.7, and 0.8 in counter-current flow geometry [130]

On the other hand, Funayama et al. [131] evaluated a 60 g $Ca(OH)_2$ pellet in a packed-bed reactor. The heat storage density of the bed was 1.0 MJ/L-bed, and an average heat output rate of 0.71 kW/L-bed was observed for the first 10 min under a hydration pressure of 84.6 kPa. Although the bed showed a net expansion and formation of agglomerated lumps in the middle, the effects had a small influence on the reactivity. The stability of the reaction conversion of the bed was demonstrated during 17 cycles of experiments. Figure 2.12 shows the experimental setup for the test rig.

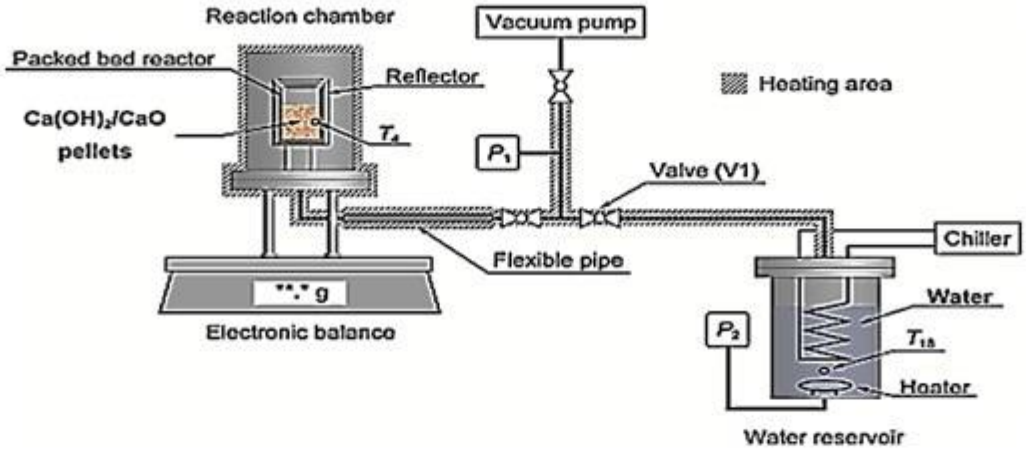

Figure 2. 12 Schematic diagram of the experimental set-up in Funayama et al. [131]

It is suggested that the heat transfer coefficients in indirectly heated fixed beds are generally limited by the low thermal conductivity of the reactants [132]. So, a fixed bed reactor in indirect operation at varying technical operating conditions was investigated by Schmidt et al. [133]. Thermal charging and discharging were experimentally demonstrated at vapour pressures between 1.4 kPa and 20 kPa. This indicated the possibility of operating the system at low vapour pressures, thus raising the total efficiency of the storage system. However, the range of operation of the $Ca(OH)_2$ system was constrained because of its efficient rate of reaction at low vapour pressure. Again, Peng et al. [134] simulated fixed bed reactors under various operating conditions, and the impact of key process parameters was evaluated. An optimized model for the design was then used to compare the performance of three TCES reactors for Mn_2O_3, $Ca(OH)_2$, and $CaCO_3$. Results showed $CaCO_3$ and $Ca(OH)_2$ with more favourable conversion efficiencies. Moreover, the HTF inlet and outlet temperature profiles also indicated that the two aforementioned reactors rapidly reached the endothermic reaction temperature. These results are shown in Figure 2.13.

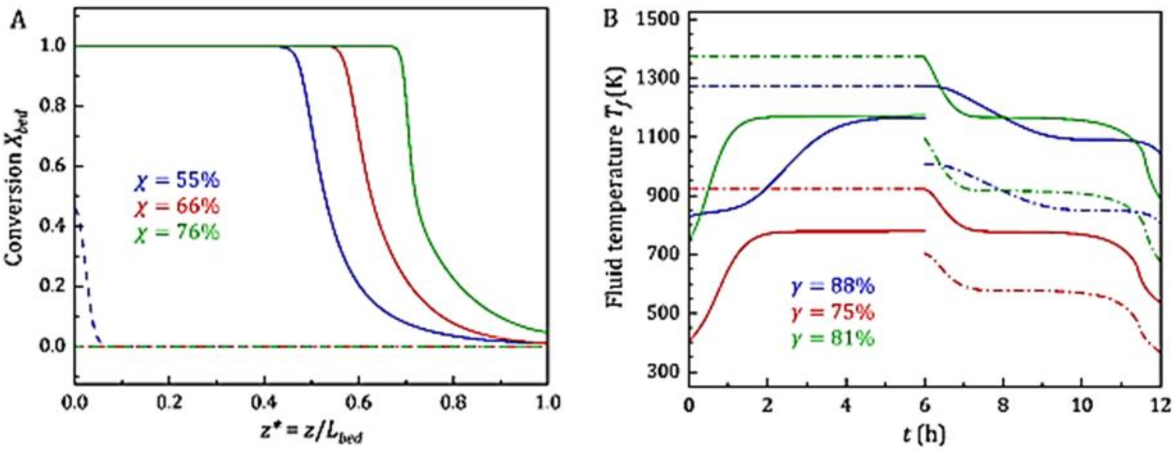

Figure 2. 13 (A) Bed conversion efficiency and (B) fluid temperature of fixed bed reactors. In A, conversions at the start of charging (t=0) are shown as dashed lines and at the end of charging (t=6 h) as solid lines. In B, fluid temperatures at the inlet are shown as dash-dotted lines and at the outlet as solid lines (blue: Mn_2O_3, red: $Ca(OH)_2$, green: $CaCO_3$) [134]

On the other hand, Schaube et al. [135] earlier investigated a reactor with direct heat transfer for the $CaO/Ca(OH)_2$ material. The simulated results of a 2D model developed showed good agreement with experiments. However, deviations were observed in temperature characteristics with an increasing flow rate of the HTF. This was due to the overestimation of the reaction rate. To forestall this in further research, they suggested the derivation of a kinetic equation adapted to real conditions, for instance, particle size, to account for diffusion limitation.

Therefore, integrating these heat storage systems into industrial processes needs additional theoretical and experimental investigations [136]. Improving the low thermal conductivity, for instance, in an indirectly heated fixed bed requires a large heat exchanger, which adds cost. To surmount this challenge, one way is to separate the heat exchanger (power) of the costly reactor from the storage material (capacity). Given this, a moving bed concept in which the material moves through the reactor could be used to accomplish this [137]

2.5.2 Moving bed reactors

In moving bed reactors (MBRs), the bed can be shuffled in continuous or regular intervals in portions, and the flow of fluid is similar to what happens in a fixed bed. Moving bed reactors were thought to have the advantage of improving thermal conductivity by enhanced solid-gas particle interaction. These solid-gas reactors can be categorized into two different regimes: (i) the axial-flow regime (concurrent and counter-current) and (ii) the crossflow pattern [138]. For instance, in the axial-flow solid-gas moving bed configuration, the advantages of the counter-current flow regime have been applied through the direct interaction of reactants. In this case, the solid flows downward while the gas goes upward as the chemical transformation occurs.

Notably, fine powders were observed to have very low flowability [139]. To improve on this, a 1D simulation of a manganese-iron oxide (Mn-Fe oxide) TCES reactor was investigated [140]. An extension of the particle flow model was simulated for a counter-current MBR, and complete conversion was attainable only for low gas as well as low rates of solid flow. So, the oxidation kinetics of the redox transition was the limiting factor. Moreover, a contrarian trend was observed in which the energy density dropped although the thermal power surged, independent of the attained conversion efficiency in the given conditions of operation (See Figure 2.14). Also, sensitivity analyses revealed the possibility of channels developing within the moving bulk material, which could slow down the heat transfer between the solid and gas. Hence, a proposal for direct and indirect heat transfer coupling was recommended as a promising operational mode.

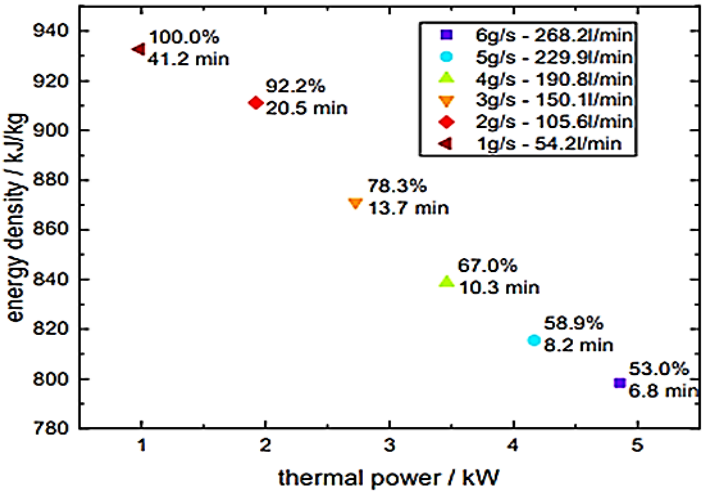

Figure 2. 14 Thermal power of the MBR for the steady state case and energy density of the material with different particle and gas flow rates [140]

Furthermore, Preisner and Linder [141] investigated the reaction behaviour of manganese-iron oxide (Mn-Fe oxide) at different temperatures and pressures. The TCES material was oxidized to an extent of 80.2% after a previous reduction of 77.1% at 20 kPa oxygen partial pressure. Moreover, a sufficiently stable oxidation/reduction reaction was established for two successive cycling tests (of 30 cycles each) in TGA. However, the flowability of the material particles was limited at high temperatures between 850 and 1050 ℃ due to mass loss, as shown in Figure 2.15.

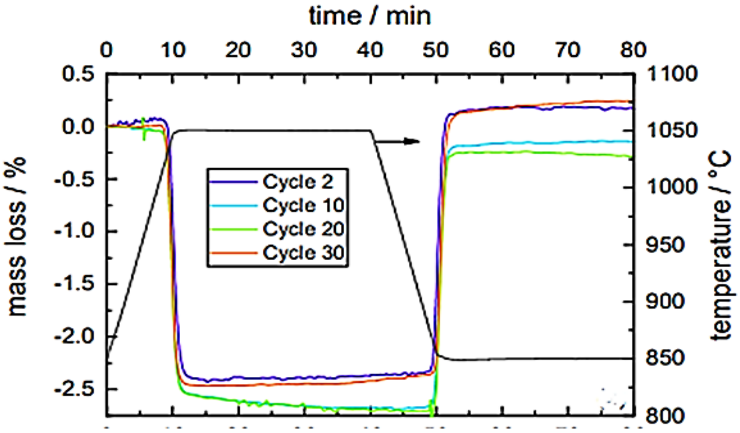

Figure 2. 15 Relative mass loss of the Mn-Fe oxide during the first 30 redox cycles [141]

Huang et al. [142] investigated the complex physical and chemical transport phenomena in MBRs. The coupled heat/mass transfer and reactions were successfully modelled based on uniform flow and plug flow. Both models showed potency for simulating the transient flow processes. Particularly, the plug flow model based on Ergun's equation successfully predicted the increased gas velocity inside the reaction zone. However, due to a lack of exact information on the heat flux input during the transient phase, the reaction zone temperature was overpredicted, and this led to an overestimated oxygen concentration at the exit. In another concept, a rotary kiln was also tested for suitability in a thermochemical storage process [106]. Rotation movement helped to improve the reactivity of the sample by mixing the particles. However, the reaction was handicapped because of strong coalescing particles. Also, the chemical conversion was significantly lower for oxidation than for reduction. For this reason, an optimization of the operation parameters such as rotational speed, particle size, gas flow, and initial mass of reactant was recommended. This would increase the conversion of both reduction and oxidation and avoid the progressive loss of the reactive fraction. So far, no successful operation of a moving bed reactor over multiple cycles has been reported [139].

2.5.3 Fluidized bed reactors

For fluidized bed reactors, the fine solid particles are sustained in suspension by the fluid's upward flow [64]. Essentially, the base of a fluidized bed is similar to that of a fixed bed. With the increase of the fluid velocity, the solid particles are suspended at the minimum fluidization velocity, hence, better heat and mass transfer can be accomplished with fluidized bed reactors (FBRs). These reactors require significantly lower gas velocities [139]. Therefore, they have been extensively suggested for more efficient TCES. However, getting the material fluidized, which, in turn, demands a huge increment in gas flow volume, has the consequence of decreasing the efficacy of the stowage mechanism. Notwithstanding, the advantages of fluidized beds over other reactors include better reaction efficiency due to enhanced fluid-particle interaction. Again, besides the limited pressure drop across the bed, fluidized beds gain from efficient HAM transfer from the continuous particulate interactions and higher transfer coefficients [143]. In addition, the uniform temperature gradient ensures the elimination of dead zones and hot spots. A comparison of the three solid-gas reactors is summarized in Table 2.6.

Table 2. 7 Comparison of fixed, moving, and fluidized bed reactors [144]

Reactor	Advantages	Disadvantages
Fixed/Packed bed	• Easier modelling	• Low heat and mass transfer • High-pressure drops
Moving bed	• Direct solid-gas heat transfer	• Complex hydrodynamics
Fluidized bed	• Minimization of hotspots and thermal instability • High heat transfer coefficients	• Complex hydrodynamics and modelling • Internal components erosion

Due to the complex hydrodynamics in FBRs, a requirement for modelling and simulation has arisen to deepen understanding of the processes. Moreover, current research efforts aim at gaining new insights into the reactants' basic molecular level, besides reactor scale-up improvements and optimization of fluidized beds [143]. Admittedly, the modelling of FBR systems can be complicated, especially when storage materials are to be included. Many researchers have done work on the modelling of physical phenomena in TCES reactors. For instance, Flegkas et al. [145] proposed a method to model FBRs based on solid-state kinetics and fluidization hydrodynamics, using the $MgO/Mg(OH)_2$ reaction couple. The reaction enthalpy dropped significantly using water, hence, the supply of steam constituted the main drawback. In another work, Angerer et al. [139] proposed a reactor concept featuring a bubbling fluidized bed with continuous, guided solid flow and immersed heat exchanger tubes. Fluidization of the $CaO/Ca(OH)_2$ powder proved herculean, but challenges were surmounted with the use of mild calcination settings and a peculiarly designed gas distributor plate. Analyses revealed that heat transfer between the reactor and the immersed heat exchangers had the largest influence on the system performance. Results of the first steady-state experiments in a new power plant implemented to investigate the idea under practical reactor conditions were reported by Rouge et al. [146]. The basic conceptual scheme of the integrated system is shown in Figure 2.16. The experimental results during dynamic and steady-state periods were fitted to a KL reactor (bubbling bed) model. The reactor performance modes were sufficiently predicted by the model, as observed during the experiments under dynamic and steady-state conditions. They suggested the model to be a relevant tool for the future expansion of the energy storage technology.

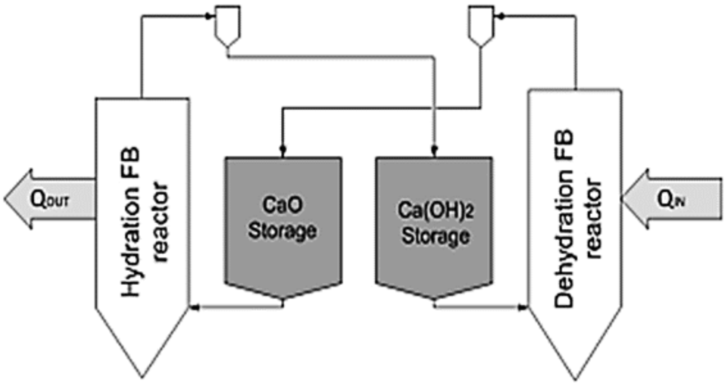

Figure 2. 16 Basic conceptual scheme of the CaO/Ca(OH)$_2$ energy storage system [146]

In addition, Mu et al. [147] carried out a numerical simulation study of thermal behaviour and hydrodynamics of FBR by using computational fluid dynamics-discrete element method (CFD-DEM). The effects of superficial gas velocity, bed height, and heat source distribution were analyzed. Results showed that both the gas superficial velocity and the bed aspect ratio had a profound influence on fluidization behaviour and temperature distributions. Figure 2.17 shows the voidage as a function of the superficial velocity and aspect ratio. This work is similar to that of Hawwash et al. [148] in which the reactor design and area ratio were shown to impact the thermal performance and energy storage during the dehydration of a TCES material.

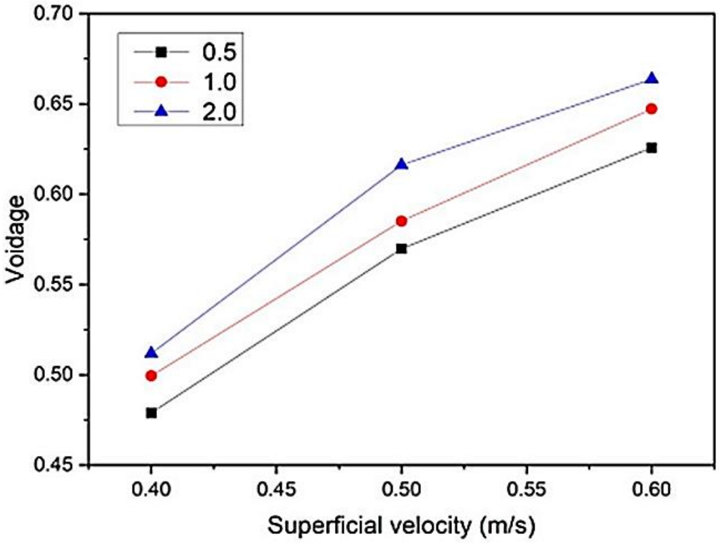

Figure 2. 17 Temporally and spatially averaged bed voidage as a function of superficial velocity and aspect ratio [147]

Despite these milestones in a bid to understand reactor dynamics, technical barriers still exist in conventional TCES systems. Efforts to enhance reactants with various additives or using different geometries of reaction beds have not abated the dynamic limitations of HAM transfers. For this reason, Darkwa et al. [149] proposed and investigated an agitated fluidized bed reactor system. The model revealed substantial improvements in adsorption capacities and enhanced heat transfer rates. However, the thermophysical variables that influence the minimal fluidization velocity in the adsorption column needed to be optimized. This would be necessary for efficient exothermic reaction and thermal exchange. Given this, the effect of agitation on the fluidization characteristics of fine materials was validated with different materials. Kim and Han [150] used fine particles (22μm) of material in a fluidized bed. The agitator was of the pitched-blade turbine type. Results showed that smoother fluidization was achieved with increasing agitation speed. Also, agglomeration and channelling were reduced by the mechanical effect of the agitation. Spectral analysis of the pressure drop fluctuation had the shape of a short-term correlation with different agitation speeds (Figure 2.18). The void fraction also increased with the increasing speed of agitation at the constant fluidizing gas velocity, as shown in Figure 2.19.

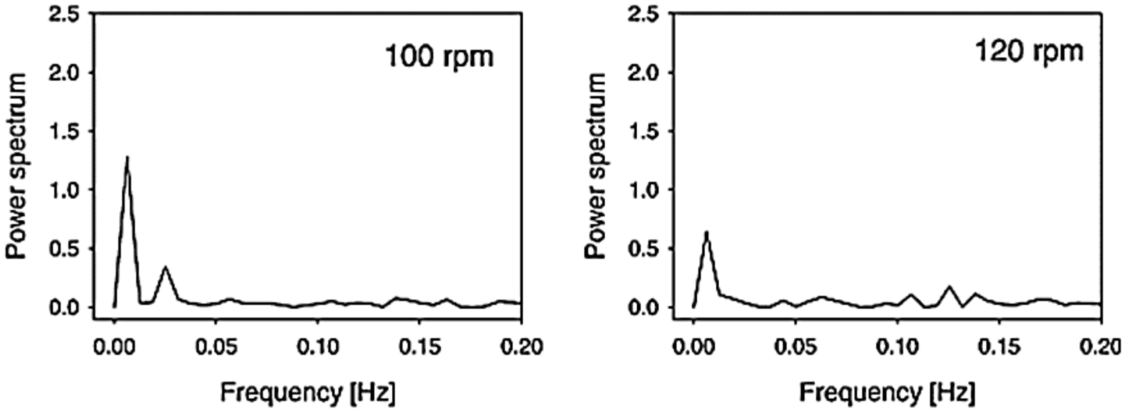

Figure 2. 18 Power spectrum of the bottom zone of the bed for different agitation speeds [150]

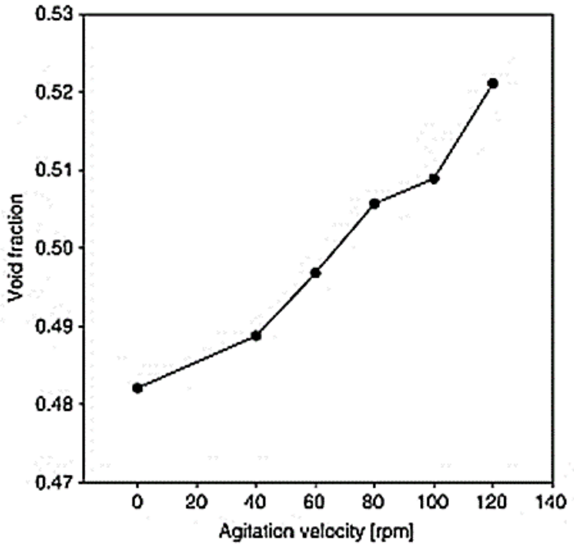

Figure 2. 19 Graph showing an increase in the void fraction of powder material with agitation speed [150]

Again, the effect of agitation on fluidization in a solid-gas fluidized bed reactor with a frame impeller was studied using a 3D unsteady CFD method [151]. The numerical method combined a two-fluid model and the kinetic theory of granular flow. Results showed that a substantially high agitation speed yielded higher performance in fluidization in addition to reduced bubble diameters and internal circulations of particles. Lv et al. [152] also reported the effective performance of a fluidized bed under mechanical agitation, where the symmetrical motion pattern of the bed particles was identified. Like others, the bubble diameter was also significantly reduced with increasing agitation speed, as presented in Figure 2.20. Furthermore, encouraging results on the reduction in entrainment rate and channel flow, and enhanced particulate interaction have been reported with an arch agitator [153]. Again, using a 3D CFD model, Shi et al. [154] established strong evidence of improved fluidization efficiency and reduction in the operation stability of a solid-gas fluidized bed.

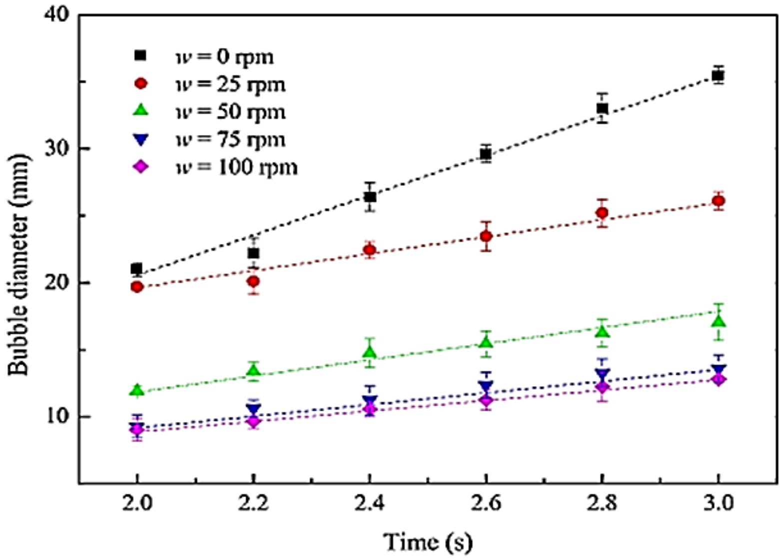

Figure 2. 20 Graph of variation of bubble diameter with agitation speed [152]

Much research effort has been devoted to the development of thermochemical reactors, but few laboratory prototypes have been tested in large-scale pilot projects. In a recent review [155], the low technology readiness level of TCES has been attributed to the cost or performance of materials and reactor design. Therefore, much effort is still required in these areas, especially in materials and reactor optimization to further the adoption of TCES technology.

2.6 Concluding remarks

This review has examined the research efforts in TCES across different temperature ranges and reactor systems. Heat storage based on inorganic hydroxide/oxide chemical transitions, particularly those based on calcium and magnesium, has been favoured for their high energy densities, good reversibility, availability, and non-toxicity.

Despite their promise, there are challenges of agglomeration, low cyclability, and low thermal conductivity that hinder their performance in reactors. Improvements in these materials' properties using additives have met with some success. Additionally, fluidized bed reactors appear to have the potential to address the issues of poor heat and mass (HAM) transfer due to their higher chances of increasing contact between solid and gas phases.

However, redesigning the bed to incorporate an efficient heat exchanger and a suitable agitator mechanism within the reactor can effectively improve particulate interactions and HAM transfer coefficients. Furthermore, using advanced simulations to describe the kinetics of TCES materials and HAM transfer components in the bed will be crucial to understanding the dynamics of the integrated system.

Chapter 3: Development of Novel TCES Materials

3.1 Materials screening

Developing a TCES system fundamentally requires sourcing a suitable storage medium (material) before application in a reactor. Therefore, finding an appropriate material is critical to creating an effective TCES system. Materials screening was the initial step in identifying potential thermochemical materials (TCMs) for suitable application. This process involved evaluating a wide range of candidate materials based on their inherent properties to determine their suitability for application via a range of criteria. Various screening techniques were employed to assess the suitability of these materials. This phase aimed to narrow the vast array of available materials to a manageable number of promising candidates for further investigation.

The general criteria for the selection of candidate materials were based on the following [64]:

- High energy density or reaction enthalpy.
- High reaction reversibility (without side products).
- Stable kinetics over multiple cycling reactions.
- Availability and low cost.
- Non-corrosivity or toxicity.

On the strength of the literature review in Chapter 2, the initial screening was done based on the concluding remarks thereof. Therefore, calcium hydroxide, $Ca(OH)_2$, and magnesium hydroxide, $Mg(OH)_2$, were selected as the core materials for further experiments and characterization.

3.2 Materials development

3.2.1 Materials selection

The core TCES materials used in this work were 99.9% purity calcium hydroxide, $Ca(OH)_2$, and 95.0% purity magnesium hydroxide, $Mg(OH)_2$, both obtained from Sigma-Aldrich, Gillingham, UK. The selection was based on the outcome of a thorough literature review, which indicated the high potential of inorganic hydroxide/oxide reversible chemical transitions for thermochemical heat storage. However, due to their reported shortcomings [45,90], composites were developed to improve their thermophysical performance. The doping materials (dopants) selected were 98.0% purity hexagonal boron nitride (BN), 99.0% purity potassium nitrate (KNO_3), and 98.0% purity lithium hydroxide monohydrate (LiOH).

Figure 3. 1 A photograph showing the core TCES materials and dopants used: (a) $Mg(OH)_2$, (b) $Ca(OH)_2$, (c) BN, (d) KNO_3, and (e) LiOH.

3.2.2 Materials preparation

The experimental materials were prepared by doping two potential candidates, $Ca(OH)_2$ and $Mg(OH)_2$. The dopants used were BN, KNO_3, and LiOH. Composites were separately made from $Mg(OH)_2$ and $Ca(OH)_2$, with variable proportions of 5, 10, 15 and 20% of the respective dopants. The dopant proportions were varied to observe the impact of dosage and determine the optimal amount that gave the desired thermophysical outcomes.

The BN-doped $Ca(OH)_2$ or $Mg(OH)_2$ were prepared following the method described by Huang et al. [91]. The 5 wt% BN mass ratio was prepared by mixing 0.05 g of BN powder, 0.95 g of $Ca(OH)_2$ or $Mg(OH)_2$ powder, and 50 ml of ethyl ethanol. This mixture was sonicated for 60 min at 48 ℃, followed by magnetic stirring for 60 min. The composite was then filtered and dried for 12 hours in the oven at 80 °C. The 10 wt%, 15 wt%, and 20 wt% ratios were prepared in a similar way using 0.1056 g, 0.1676 g, and 0.2375 g BN, respectively, at the same amount of $Ca(OH)_2$ or $Mg(OH)_2$ powder.

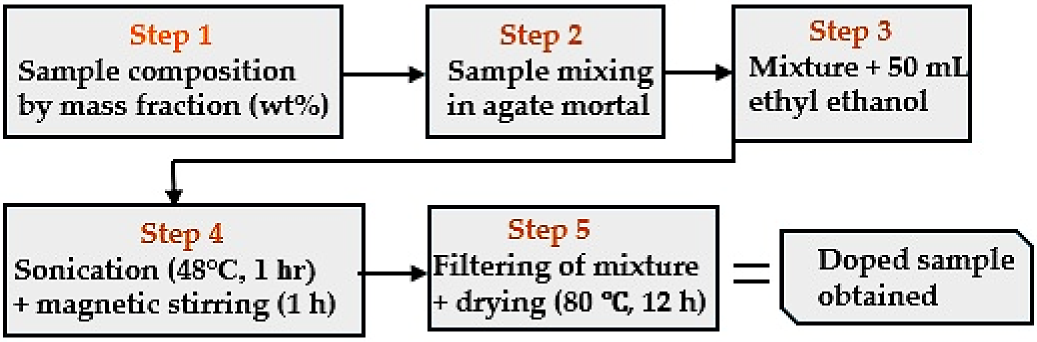

Figure 3. 2 Procedure for the development of BN-doped composites.

The KNO_3-doped $Ca(OH)_2$ or $Mg(OH)_2$ were prepared in a total controlled sample mass of 10 g. The weight of KNO_3 in each composite (5%, 10%, 15%, and 20%) was 0.5 g, 1 g, 1.5 g, and 2 g, respectively. Initial mixing of the KNO_3 and $Ca(OH)_2$ or $Mg(OH)_2$ powders was done in an agate mortar for 10 minutes to ensure a uniform blend, then transferred into a beaker for liquid mixing with 20 ml of distilled water. The mixture was stirred at 90 ℃ for 1.5 hours and oven-dried at 120 ℃ for 12 hours.

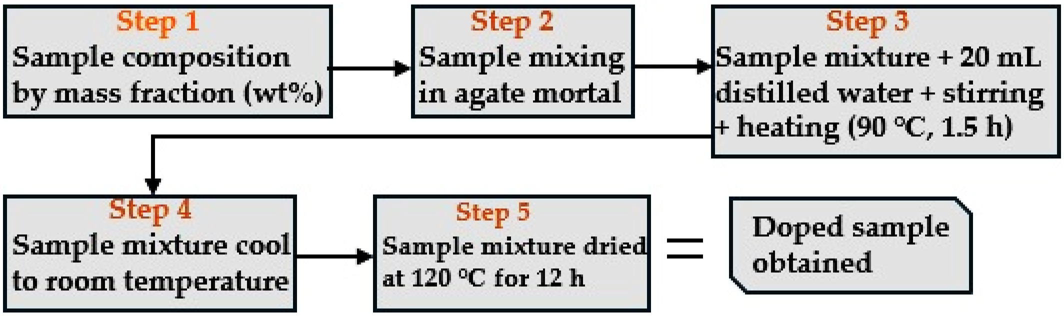

Figure 3. 3 Procedure for the development of KNO_3-doped composites.

Preparation of the LiOH-doped materials involved accurately weighing the required amounts of LiOH (monohydrate) and $Ca(OH)_2$ or $Mg(OH)_2$. The $Ca(OH)_2$/LiOH or $Mg(OH)_2$/LiOH composites were then developed by the impregnation method. First, the required amounts of $LiOH{\cdot}H_2O$ and $Ca(OH)_2$ or $Mg(OH)_2$ were weighed. An aqueous solution of LiOH was then prepared by dissolving $LiOH{\cdot}H_2O$ in ultrapure water. The $Ca(OH)_2$ or $Mg(OH)_2$ powder was impregnated with this LiOH solution by mixing and stirring continuously for 30 minutes. Following this, most of the water was evaporated using a rotary evaporator set at 40℃. Once a significant portion of the water had been removed, the remaining mixture was dried in the oven at 120 ℃ until a white solid composite powder was formed.

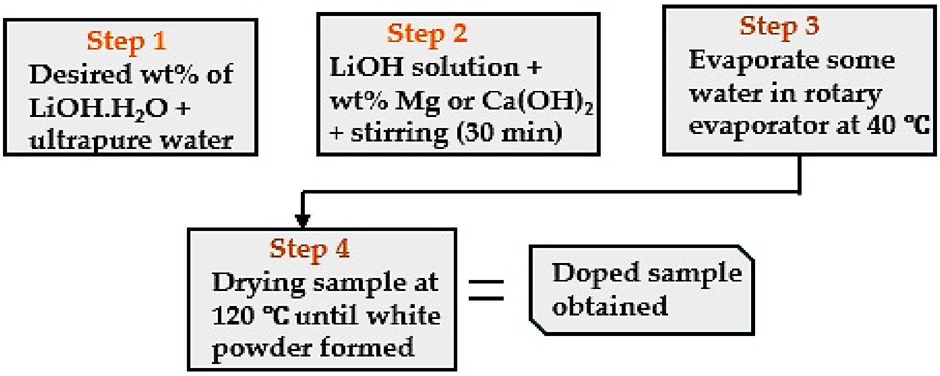

Figure 3. 4 Procedure for the development of LiOH-doped composites.

Altogether, 24 composite TCES materials were developed. For ease of reference, the labels CH, CH-BN, CH-PN, and CH-LH represent the pure $Ca(OH)_2$, BN-doped, KNO_3-doped, and LiOH-doped composites, respectively. Similarly, the labels MH, MH-BN, MH-PN, and MH-LH represent the pure $Mg(OH)_2$, BN-doped, KNO_3-doped, and LiOH-doped composites, respectively. The additive ratios are shown in Table 3.1, and Figure 3.5 shows a photo of all the doped samples.

Table 3. 1 Composites and additive ratios of the dopants.

Sample	**BN content (%)**	**Sample**	**KNO_3 content (%)**	**Sample**	**LiOH content (%)**
CH-BN5	5	CH-PN5	5	CH-LH5	5
CH-BN10	10	CH-PN10	10	CH-LH10	10
CH-BN15	15	CH-PN15	15	CH-LH15	15
CH-BN20	20	CH-PN20	20	CH-LH20	20
MH-BN5	5	MH-PN5	5	MH-LH5	5
MH-BN10	10	MH-PN10	10	MH-LH10	10
MH-BN15	15	MH-PN15	15	MH-LH15	15
MH-BN20	20	MH-PN20	20	MH-LH20	20

Figure 3. 5 A photograph of all 24 doped samples.

3.3 Materials characterization

Characterization is the final step in the materials selection process, where the developed (synthesized) materials are analyzed to understand their thermophysical properties and behaviour. These developed composite materials were characterized by methods such as X-ray diffractometry (XRD), differential scanning calorimetry (DSC), thermogravimetry analysis (TGA), scanning electron microscopy (SEM), and energy dispersive spectroscopy (EDX). Others included X-ray photoelectron spectroscopy (XPS) and Brunauer-Emmett-Teller (BET) surface area analysis, all of which have proved helpful for material selection.

3.3.1 Powder X-ray diffraction

Figure 3. 6 PaNalytical X’pert Pro diffractometer used for XRD.

Powder X-ray diffraction (XRD) was obtained at room temperature using a PANalytical X’Pert PRO diffractometer (Malvern, Worcestershire, UK) with CuK_{α} radiation (l = 1.5406 Å, 40 kV, 40 mA) for values of 2Theta (0.02 step size and 50 s step time) in the range 2^{o} and 70^{o}. XRD works by irradiating a material with X-rays and then measuring the intensities and scattering angles of the X-rays emanating from it. The primary aim of this analysis was to identify phases of the components in the doped materials based on their diffraction patterns.

3.3.2 X-ray photoelectron spectroscopy

Figure 3. 7 The Kratos LiPPS instrument used for XPS.

X-ray photoelectron spectroscopy (XPS) was performed using a Kratos Liquid Phase Photoelectron Spectrometer (LiPPS) (Kratos Analytical Ltd, UK) under ultra-high vacuum

(UHV) with a monochromated Al K_α X-ray source (1486.6 eV) at 10 mA emission current and 12 kV anode potential. Surface charging was prevented by employing a charge-neutralizer filament. The CasaXPS™ software (version 2.3.22PR1.0) was used to analyze XPS spectra; the Kratos sensitivity factors were applied to the peak areas to determine atomic percentages. The binding energies were calibrated to 284.6 eV for the high-resolution spectra using the C 1s peak as the standard. Under ultra-high vacuum, the samples were exposed to incident X-rays, leading to the emission of inner shell electrons. The emitted photoelectrons were hence detected and measured in the spectrometer, and the binding energy intensities were related to the constituent elements.

XPS was done to detect the presence of lithium ions (Li^+) since the LiOH phase was not identified in XRD. XPS is a surface-sensitive (top ~10nm) analysis technique that has the capability for the determination of the surface chemical composition of materials. The scan was done for the lower and higher doping proportions (5 wt% and 20 wt%) of LiOH, that is, CH-LH5 and CH-LH20 samples.

3.3.3 Brunauer-Emmett-Teller analysis

Figure 3. 8 The Micromeritics 3Flex analyzer used for BET analysis.

The porosity of the materials was determined using nitrogen sorption isotherms on a Micromeritics 3Flex analyzer (Micromeritics Instrument Corporation, Georgia, USA) at -

196 ℃. The samples were degassed at 150 °C for 16 hours under a vacuum before analysis. The specific surface areas were calculated using the Brunauer-Emmett-Teller method from the nitrogen adsorption data within the relative pressure (P/P_o) range of 0.02-0.20. The total pore volume was estimated using total nitrogen adsorbed at relative pressure close to saturation (P/P_o ~0.99), and the pore size distribution (PSD) was determined using non-local density functional theory (NL-DFT) applied to nitrogen isotherm data.

3.3.4 Scanning electron microscopy

Figure 3. 9 JEOL 6490LV instrument used for SEM and EDX.

The prepared samples were imaged using a JEOL 6490LV scanning electron microscope (JEOL Ltd, Tokyo, Japan) operated in high vacuum mode at 15 kV, and with a secondary electron detector. A beam of electrons is produced by an electron gun and follows a vertical path through the microscope, which is held within a vacuum. This beam excites electrons from the surface of the imaged material, and the excited electrons create differing signals of the material’s topology.

3.3.5 Energy dispersive X-ray spectroscopy

In addition, energy-dispersive X-ray spectroscopy analyses were carried out, using the extended function of the JEOL 6490LV instrument, to obtain chemical composition spectral data of the samples. To do so, X-ray emission was stimulated from the material by irradiation with a high-energy beam. The emitted radiation had energy characteristic of the atomic energy of the matched element.

3.3.6 Differential scanning calorimetry

Figure 3. 10 SDT simultaneous DSC/TGA instrument used for DSC and TGA.

Differential scanning calorimetry (DSC) measurements were performed using the SDT-Q600 Simultaneous DSC/TGA instrument (TA Instruments, Delaware, USA). A baseline measurement was taken in the range of 25 ℃ to 550 ℃ at 10 ℃/min. A 5 mg sample was heated within the same temperature range and heating rate. Nitrogen was used as the purge gas at a volumetric rate of 20 ml/min under 1 atm pressure. The DSC was carried out to measure the heat flow into the material samples as a function of temperature, while it was exposed to a controlled temperature programme.

3.3.7 Thermogravimetry analysis

Thermogravimetric analysis (TGA) was performed using the SDT-Q600 thermal instrument. The vapour pressure was set at 1 atm and a 20 mg sample was placed into the alumina crucible. This was then subjected to a temperature ramp from 25 ℃ to 600 ℃ at a heating rate of 10 ℃/min, under a nitrogen atmosphere with a volumetric rate of 20 ml/min. The analysis was done to determine the thermal stability of the materials by monitoring the weight change while the sample was heated at a constant rate.

3.4 Results and discussion

3.4.1 XRD

The developed TCES materials were characterized for phase identification of the constituents. Figure 3.11 shows the XRD diffraction patterns of pure magnesium hydroxide (MH) and its composites with different percentages of boron nitride (BN), potassium nitrate (PN), or lithium hydroxide (LH).

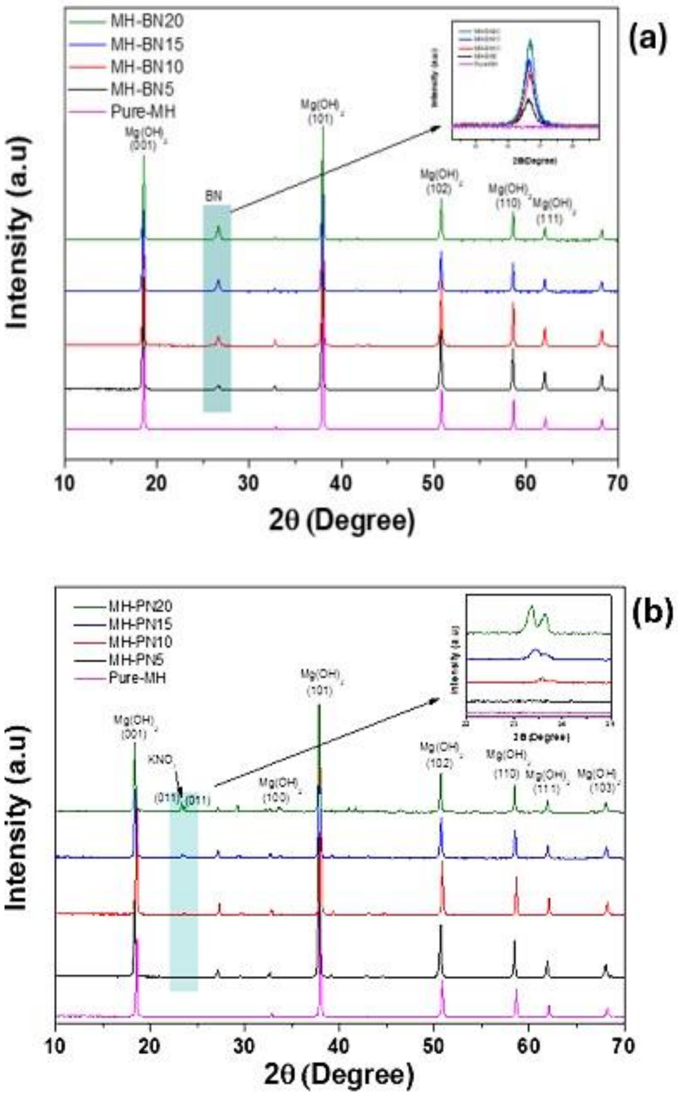

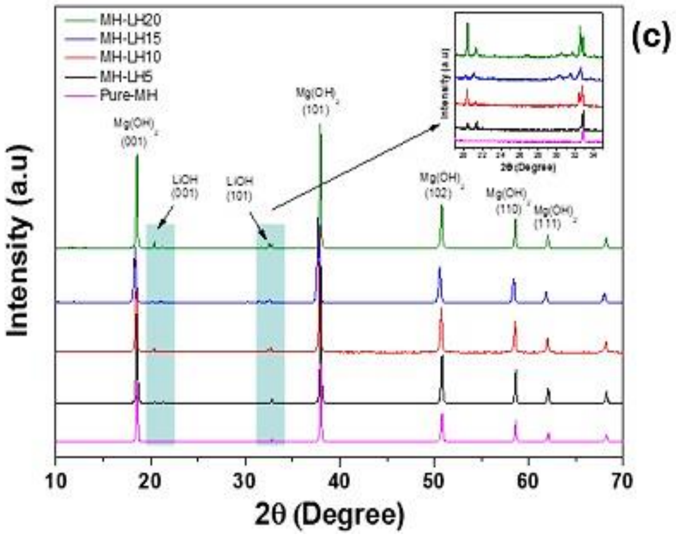

Figure 3. 11 Powder XRD spectra for pure and doped $Mg(OH)_2$.

It can be seen that pure MH shows (one phase) peaks at 001, 101, 102, 110, and 111 planes, which agree well with the brucite magnesium hydroxide crystallographic information in the Inorganic Crystal Structure Database (ICSD 01-074-2220). On the other hand, the XRD patterns of MH-composite materials show additional phases for boron nitride (Figure 3.11 (a)), potassium nitrate (Figure 3.11 (b)), and lithium hydroxide (Figure 3.11 (c)). The patterns of the composite materials show agreement with the powder diffraction form; PDF 00-045-0895 (standard BN), PDF 00-001-0493 (standard PN), and ICSD 01-085-1064 (standard LH). The intensity of the peaks increases with an increase in the dopant percentage, as illustrated in the zoomed-in part of the figures. These observations confirmed that the doping process was successful as intended.

Similarly, Figure 3.12 shows the XRD diffraction patterns of pure calcium hydroxide (CH) and its composites with different percentages of boron nitride (BN), potassium nitrate (PN), or lithium hydroxide (LH).

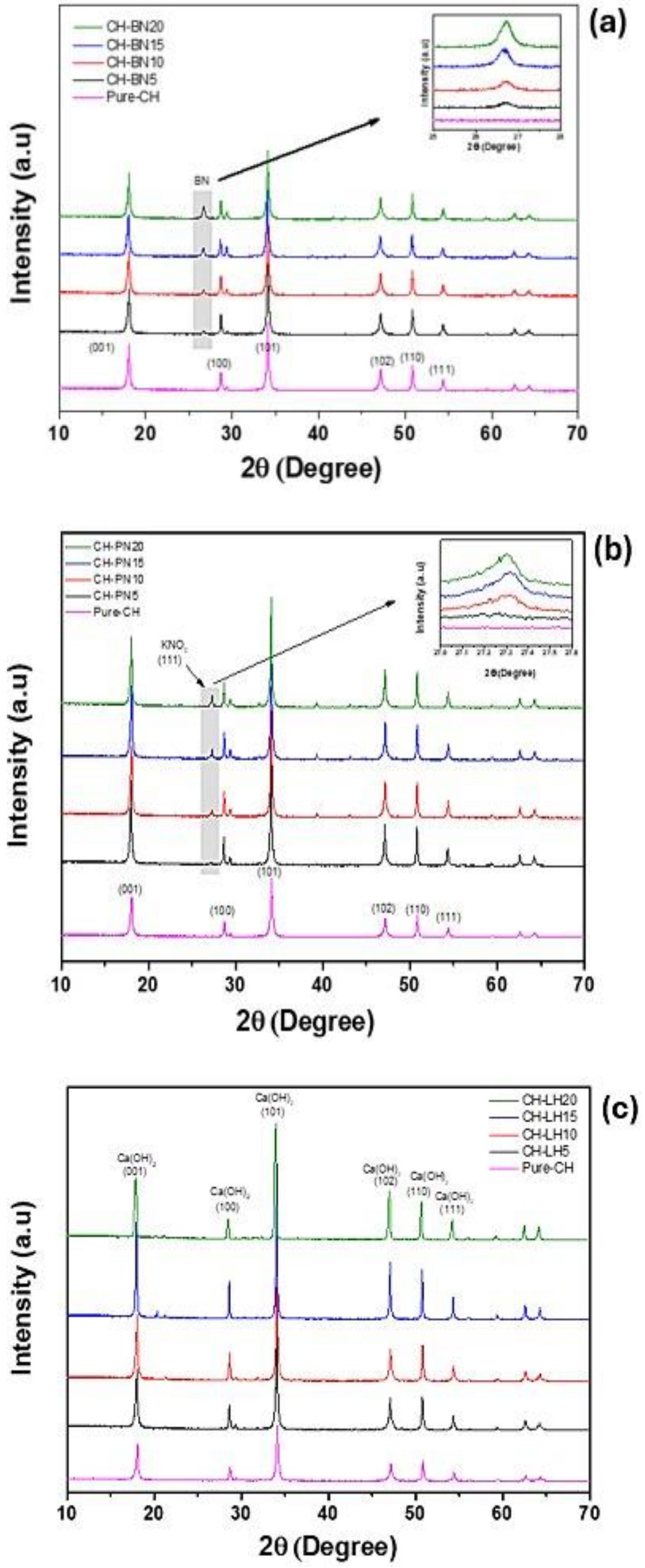

Figure 3. 12 Powder XRD spectra for pure and doped $Ca(OH)_2$.

The pure CH showed the expected XRD peak patterns according to the standard crystallographic data of the Inorganic Crystal Structure Database (ICSD 01-087-0674). For the composite materials, the XRD patterns show additional phases when doped with boron nitride (Figure 3.12 (a)) or potassium nitrate (Figure 3.12 (b)) that agree with the powder diffraction form; PDF 00-001-0493 and PDF 00-045-1171, respectively. However, for the LiOH (LH) doped composite (Figure 3.12 (c)), no peaks were observed, indicating that LiOH was undetected. This suggests that the lithium ions (Li^+) were taken into the calcium hydroxide crystal structure, as also observed in the work of Maruyama et al. [156]. For this reason, XPS was required to further confirm the success of the doping procedure.

3.4.2 XPS

Figure 3.13 shows the XPS spectra (wide scan) of composites (CH-LH5 and CH-LH20) compared to the pure lithium hydroxide (LH).

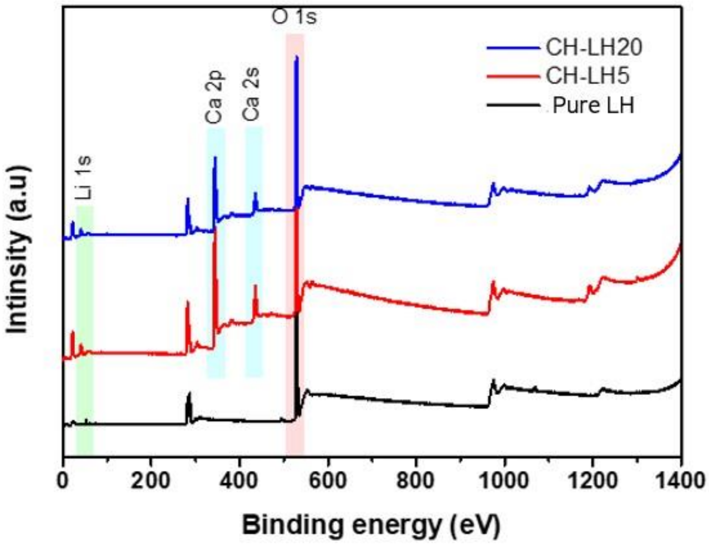

Figure 3. 13 XPS wide scan spectra for pure LiOH and LiOH-doped $Ca(OH)_2$.

The binding energy of the Li 1s core level in lithium is around 55 eV [157]. However, the exact binding energy can vary slightly depending on the chemical environment of the lithium atoms (whether lithium is in the metallic state, in an oxide or hydroxide form, or some other compound) [158]. From the XPS analysis in Figure 3.13, it can be seen that the peak detected at ~ 54.6 eV for the composites CH-LH5 and CH-LH20 aligns closely with Li 1s, which strongly suggests the presence of Li^+. In this process, lithium was detected, confirming the successful doping of LiOH in the samples.

3.4.3 BET analysis

The variation in the amount of gas adsorbed by the TCES materials with pressure at constant temperature is shown in Figure 3.14. This shows the nitrogen sorption isotherms of pure MH and its composites containing varying percentages of boron nitride (BN), potassium nitrate (PN), or lithium hydroxide (LH).

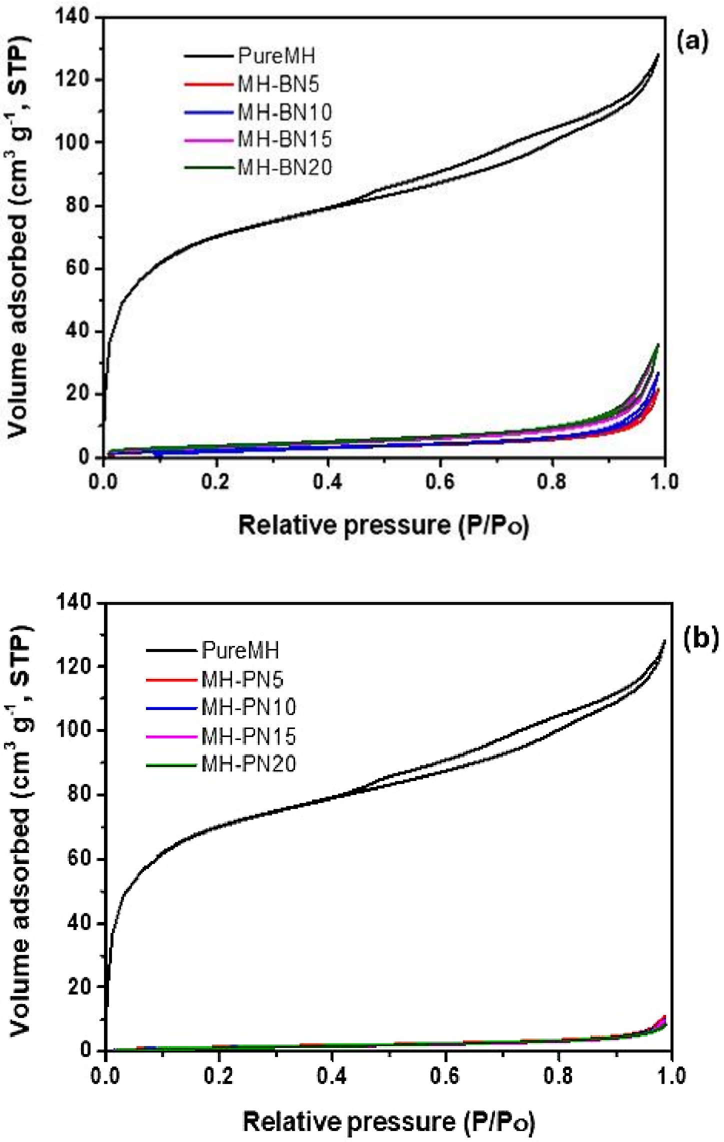

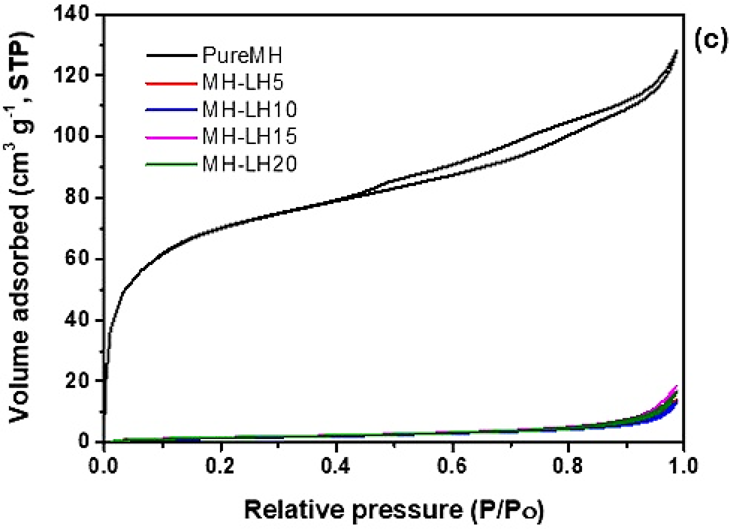

Figure 3. 14 Adsorption isotherms of pure $Mg(OH)_2$ and (a) BN, (b) KNO_3, and (c) LiOH-doped composites.

It can be seen that pure $Mg(OH)_2$ (MH) exhibits a type IV isotherm associated with gas adsorption onto mesoporous materials. Initially, there was monolayer adsorption (like Type II) on the surface of mesopores, but as pressure increased, additional multilayers of adsorbate molecules formed. Capillary condensation became significant in this region, leading to increased adsorption as the gas condensed in the mesopores, filling them with the adsorbate. However, the isotherm type changed from type IV (for pure MH) to type III for all the MH composites in Figure 3.14 (a)-(c), irrespective of the dopant type. This indicates weak adsorbate-adsorbent interactions, where adsorption increased gradually without a clear saturation point. The isotherm is concave to the pressure axis, showing a slow rise in adsorption with increasing pressure. These isotherms are often observed for non-porous materials or adsorbates with low affinity for the adsorbent surface.

On the other hand, Figure 3.15 shows the nitrogen sorption isotherms of pure CH and its composites containing varying percentages of boron nitride (BN), potassium nitrate (PN), or lithium hydroxide (LH).

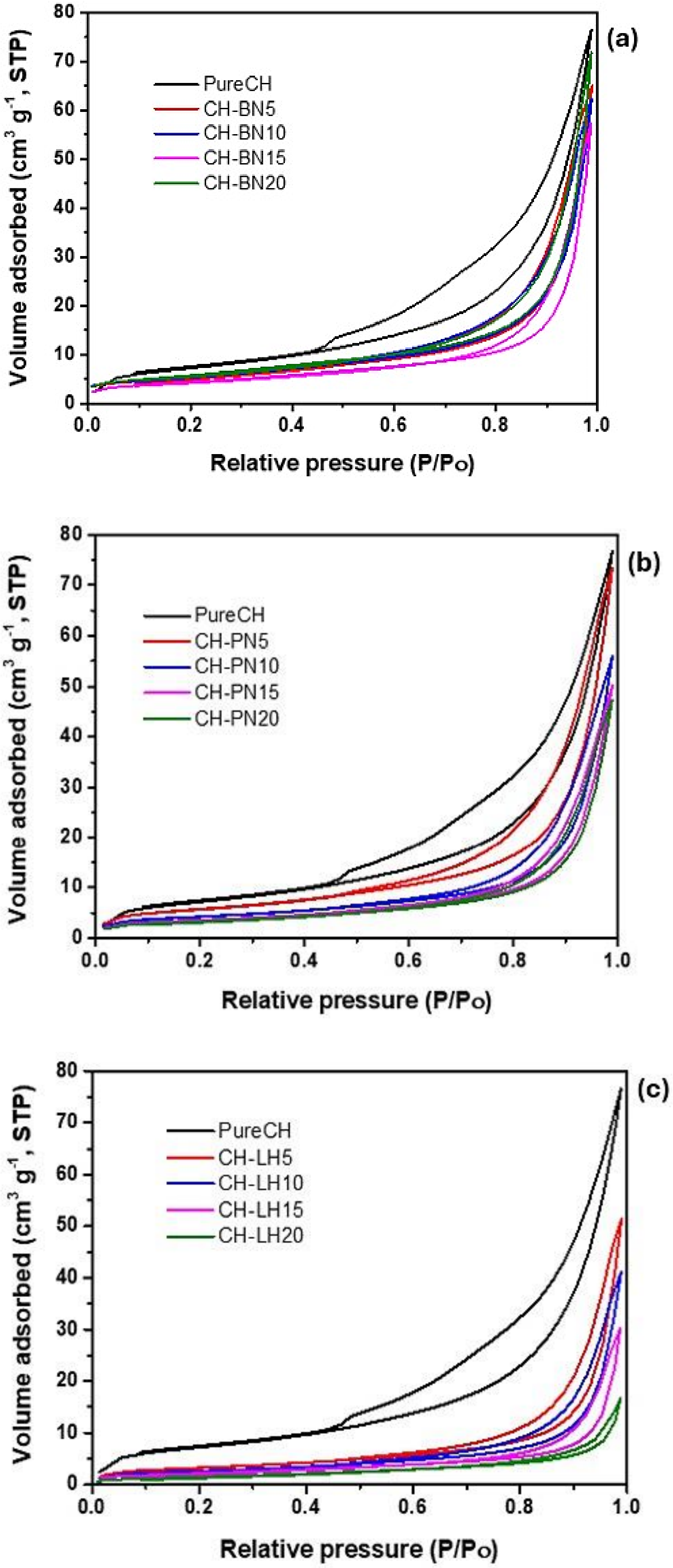

Figure 3. 15 Adsorption isotherms of pure $Ca(OH)_2$ and (a) BN, (b) KNO_3, and (c) LiOH-doped composites.

In this case, both the pure $Ca(OH)_2$ (CH) and its composites, as shown in Figure 3.15 (a)-(c), exhibit type III isotherms. As earlier explained, this indicated that the materials were essentially non-porous or possessed some macroporosity. The adsorption increased slowly with increasing pressure, reflecting the low affinity of the adsorbate for the adsorbent surface. All isotherms showed no uptake at low relative pressure; the adsorption occurred only at higher relative pressures. The BET surface area for the composite materials is given in Table 3.2.

Table 3. 2 BET surface areas for the pure and composite materials.

Sample	**BET surface area (m^2 g^{-1})**	**Sample**	**BET surface area, (m^2 g^{-1})**
Pure MH	25	Pure CH	32
MH-BN5	7	CH-BN5	19
MH-BN10	8	CH-BN10	19
MH-BN15	12	CH-BN15	15
MH-BN20	13	CH-BN20	20
MH-PN5	6	CH-PN5	21
MH-PN10	5	CH-PN10	15
MH-PN15	5	CH-PN15	13
MH-PN20	5	CH-PN20	10
MH-LH5	7	CH-LH5	12
MH-LH10	6	CH-LH10	10
MH-LH15	7	CH-LH15	8
MH-LH20	7	CH-LH20	6

The apparent BET surface area of pure MH is very high, measuring up to 25 m²/g. However, after doping with various materials, the BET surface area significantly decreased for all composites, regardless of the doping proportion. For instance, the MH-BN (boron nitride) composites have a surface area ranging between 7 and 13 m²/g, MH-PN (potassium nitrate) composites show a surface area between 5 and 6 m²/g, and MH-LH (lithium hydroxide) composites exhibit a surface area of 6 to 7 m²/g. This reduction in BET surface area could be attributed to the doping process, which likely led to pore-clogging in the pure MH structure, thereby resulting in a lower accessible surface area. That is, the doping procedure, which involved heating at 90 ℃ and subsequent crushing, may have caused fusion of the $Mg(OH)_2$ brucite particles, leading to meso/micropore formation and a pronounced collapse in surface area.

In contrast to pure MH, which has a surface area of 25 m²/g, pure CH exhibits a surface area of 32 m²/g. The surface areas of CH-based composites, irrespective of the doping percentage, show a modest reduction. Specifically, CH-BN (boron nitride) composites have surface areas ranging from 15 to 20 m²/g, CH-PN (potassium nitrate) composites exhibit surface areas between 10 and 21 m²/g, and CH-LH (lithium hydroxide) composites display the lowest surface areas, ranging from 6 to 12 m²/g. These observations suggest that doping with different materials results in a slight decrease in the surface area of CH-based composites.

The wide disparity in the BET surface area values between the pure MH or CH and their composites was further investigated by comparing their pore size distributions (PSD) with and without doping. The pore size distribution (PSD) profiles for the pure MH and its composites (at a minimal 5 wt% doping proportion) are shown in Figure 3.16, and those of pure CH and its composites are shown in Figure 3.17.

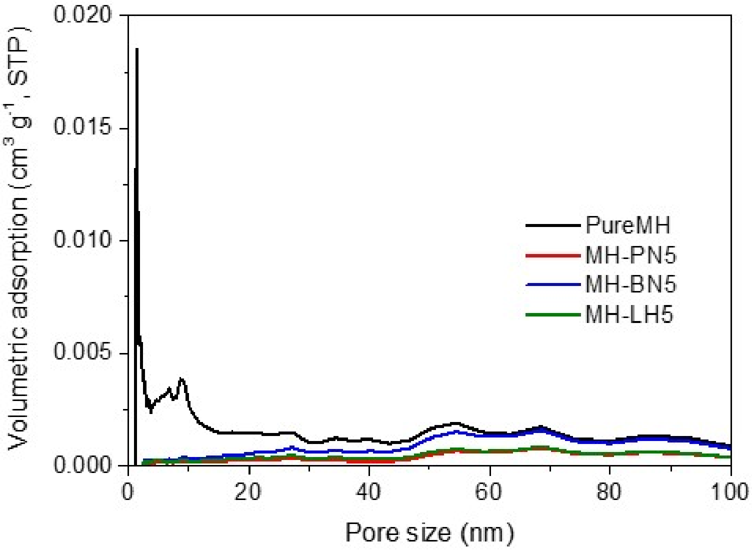

Figure 3. 16 Comparison of PSD in the pure MH and its composites.

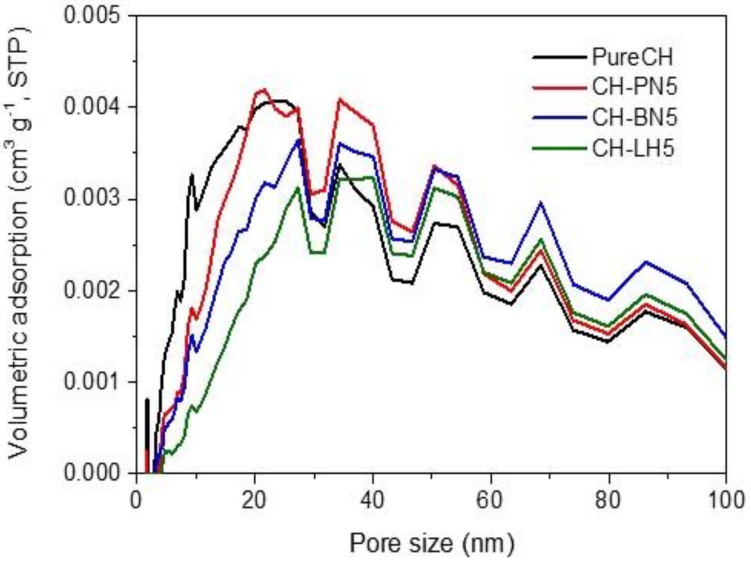

Figure 3. 17 Comparison of PSD in the pure CH and its composites.

In Figure 3.16, the curves show that pure MH has some microporosity in the pore diameters less than 2 nm, and large mesoporosity between 2 and 40 nm. Thus, the dramatic reduction in the surface area may be due to the dopant's pore-clogging effect. Again, doping may have caused particle sintering, resulting in larger aggregates with a lower overall surface area, especially at the micropores. As can be seen in Figure 3.16, pores smaller than 20 nm were present in the MH but significantly reduced after doping, which suggests that the pore size decreased after doping.

On the other hand, the profiles in Figure 3.17 show that the gradual, continuous increase in adsorption with pressure and the absence of a plateau suggest that the pores, if present, are likely very large (macropores > 50 nm) or that the material has a non-porous or low-porosity structure. Large pores do not confine the adsorbate sufficiently to cause the steep increases or saturation characteristic observed in the case of micropores or mesopores.

3.4.4 SEM imaging

Figure 3.18 is the SEM image of pure $Mg(OH)_2$, which shows a fluffy morphology with closely packed particles. The fluffy morphology indicates a potential for high surface area, as it provides more active sites for gas adsorption. This confirms the previously reported high BET surface area value of pure MH.

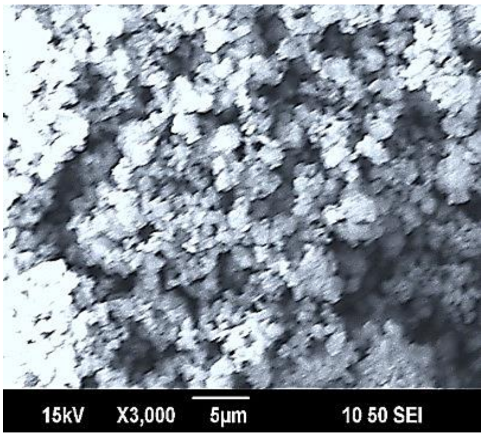

Figure 3. 18 SEM image of pure $Mg(OH)_2$.

The addition of 5, 10, and 15 wt% BN (Figure 3.19) does not make a significant difference in grain distribution or packing. At a 20 wt% BN addition, significant aggregative lumps become visible, as shown in Figure 3.19 (d).

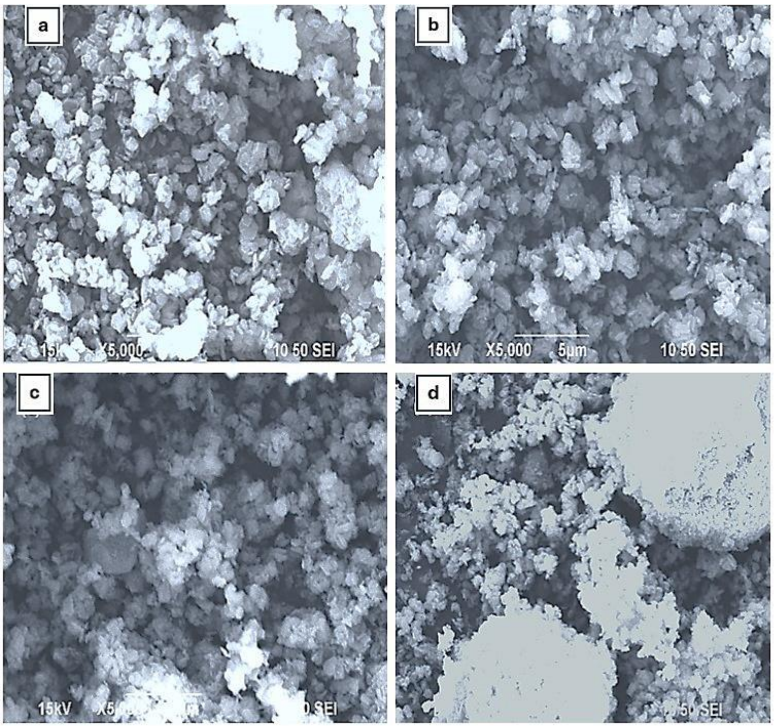

Figure 3. 19 SEM images of (a) 5%, (b) 10%, (c) 15%, and (d) 20% BN addition to $Mg(OH)_2$.

Figure 3.20 presents the SEM images of $Mg(OH)_2$ composites with KNO_3 addition. In this case, the additive proportion of 5 wt% improves particle distribution and inter-particle spaces, demonstrating a reduction in the sintering effect (Figure 3.20a). However, for proportions >5 wt%, there is a progressive increase in particle compaction resulting in coalescence at the 20 wt% mass ratio (Figure 3.20c).

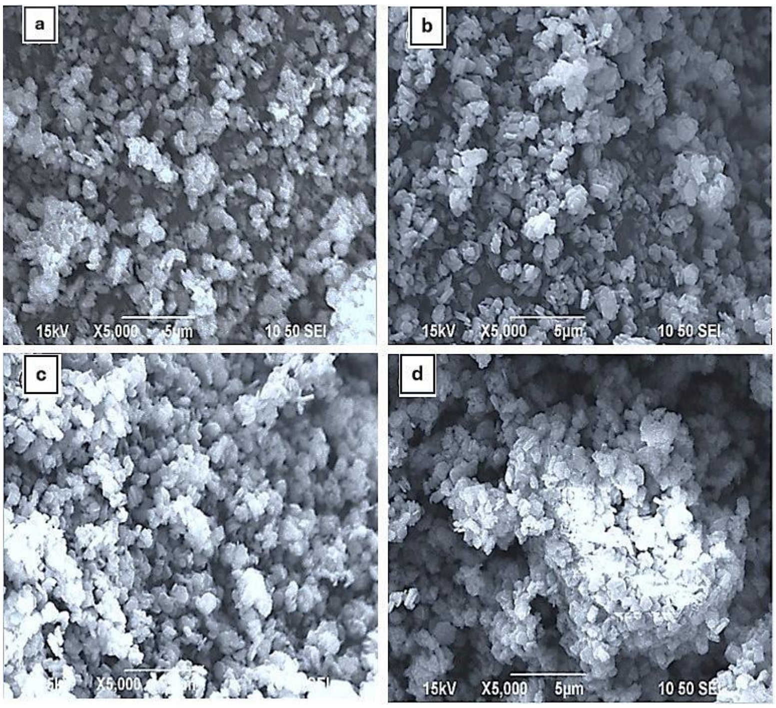

Figure 3. 20 SEM images of (a) 5%, (b) 10%, (c) 15%, and (d) 20% KNO_3 addition to $Mg(OH)_2$.

For LiOH-doped $Mg(OH)_2$ composites, the SEM images are presented in Figure 3.21. The LiOH addition leads to composites with distinct grains and needle-like morphology. Generally, all the samples appear very similar, irrespective of the dopant ratio. There is observable dense packing in morphology with closed-up intraparticle pore spaces, which is a strong indication of the prevalence of the sintering effect.

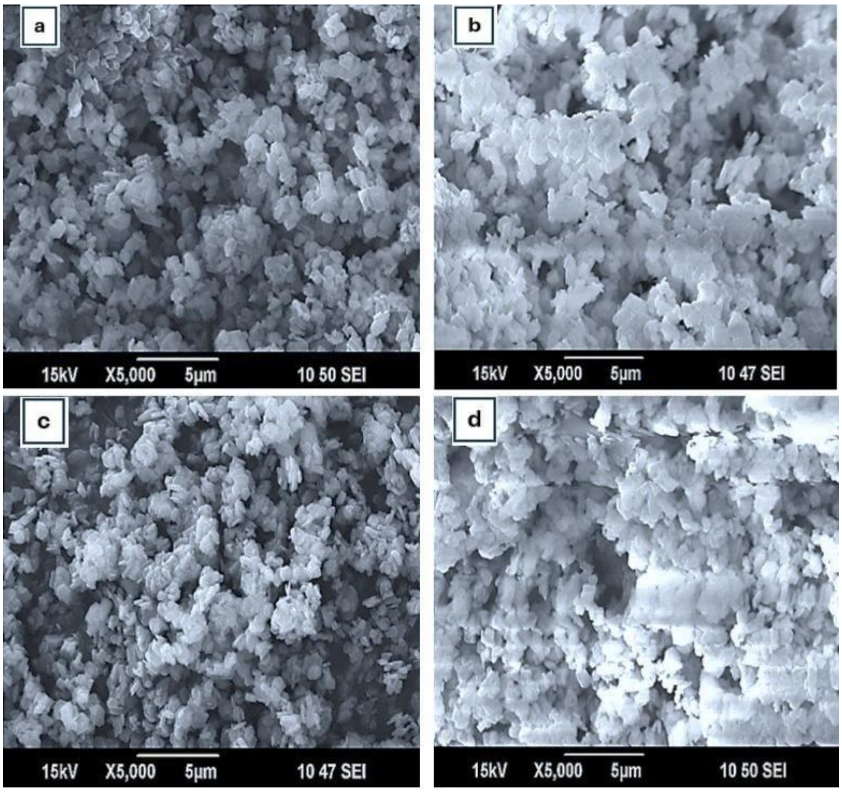

Figure 3. 21 SEM images of (a) 5%, (b) 10%, (c) 15%, and (d) 20% LiOH addition to $Mg(OH)_2$.

Figure 3.22 shows the SEM image of pure $Ca(OH)_2$ material (CH), exhibiting bulky, oval-shaped grains that tend to cluster together. The crystallites in an aggregate are more densely packed and with less intra-crystallite porosity. With the addition of BN, there is a redistribution of particles in non-homogeneous morphologies (Figure 3.23 a-d). The presence of larger voids within clusters of particles, especially for the 10 wt% ratio (Figure 3.23 b), is observed. So, the addition of 10 wt% BN improves porosity and thus demonstrates reduced particle agglomeration. Generally, the addition of BN weight ratios to $Ca(OH)_2$ produces various morphologies with non-uniform particle packing.

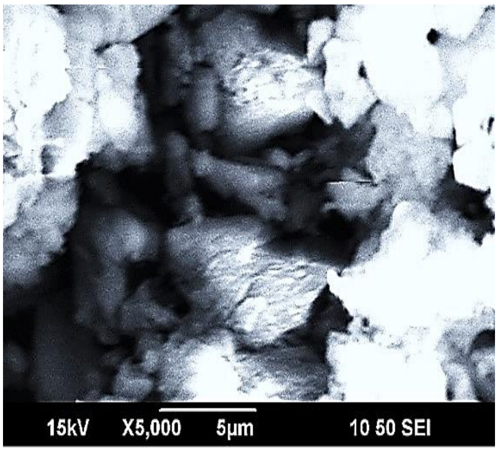

Figure 3. 22 SEM image of pure $Ca(OH)_2$.

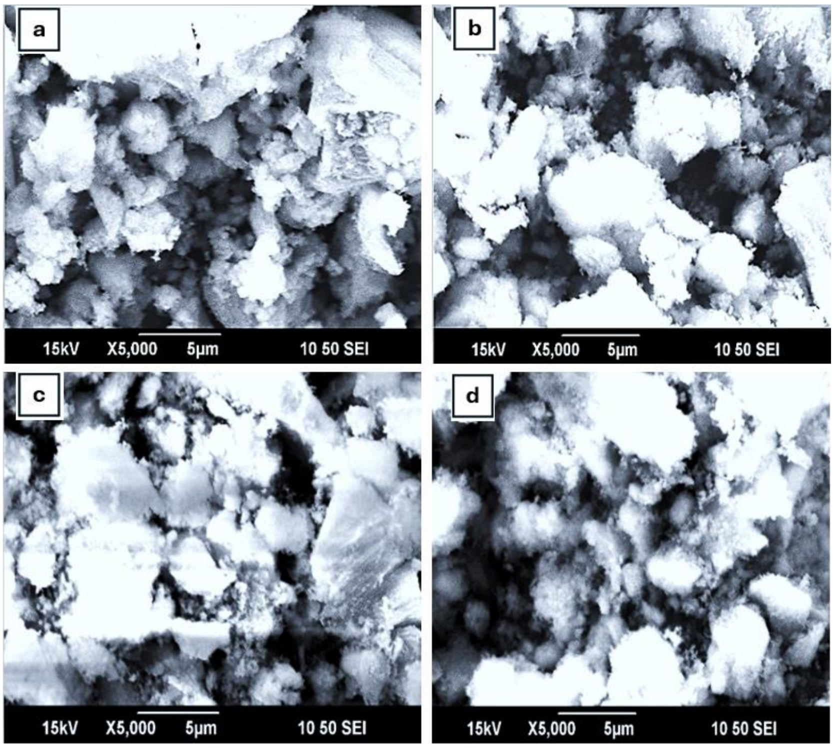

Figure 3. 23 SEM images of (a) 5%, (b) 10%, (c) 15%, and (d) 20% BN addition to $Ca(OH)_2$.

The SEM images for $Ca(OH)_2$ with KNO_3 mass proportions are shown in Figure 3.24. The 5 wt% KNO_3 additive ratio results in a reticulate morphology comprising moderate-size grains with intraparticle spaces (Figure 3.24a). Further increment in additive ratio results in the formation of lumps and close-ups on intraparticle spaces as shown in (b) and (c). At 20 wt% of KNO_3, the material's microstructure begins to flake as shown in (d).

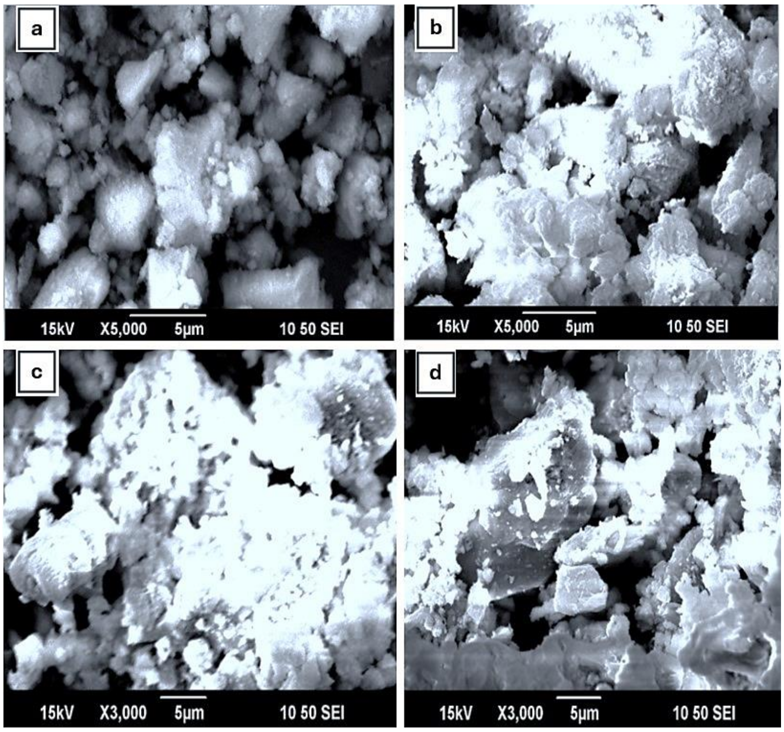

Figure 3. 24 SEM images of (a) 5%, (b) 10%, (c) 15%, and (d) 20% KNO_3 addition to $Ca(OH)_2$.

SEM images for LiOH-doped $Ca(OH)_2$ composites are presented in Figure 3.25. The initial morphology with 5 wt% LiOH addition in Figure 3.25 (a) has small grain sizes distributed around a few moderate-sized grains. These moderate-size grains increase in number with improvement in intraparticle spacing (Figure 3.25 b). Then, the appearance of massive grain sizes with dense packing is observed as the LiOH fraction increases to 20 wt%, as seen in Figure 3.25 (c)-(d).

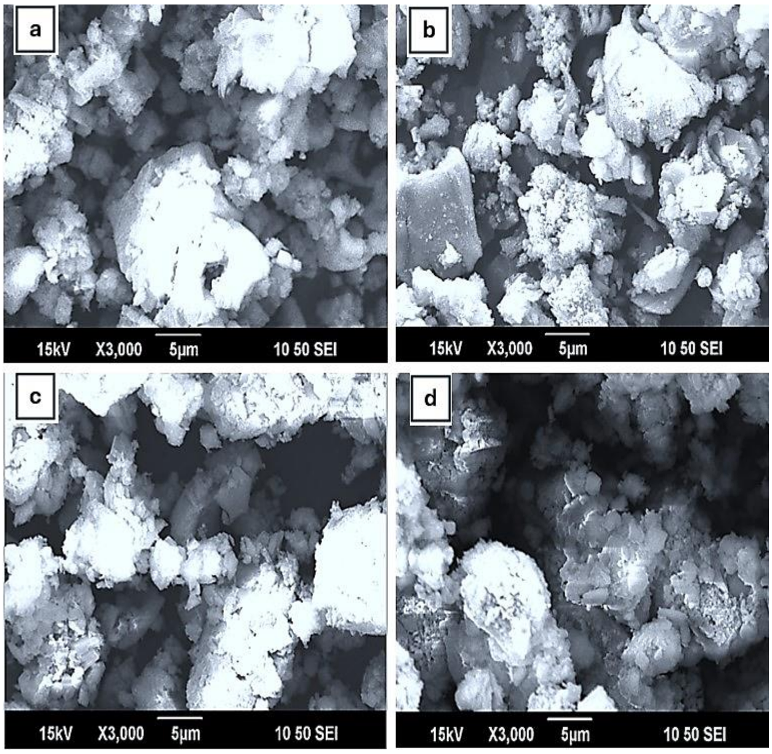

Figure 3. 25 SEM images of (a) 5% (b) 10% (c) 15% and (d) 20% LiOH addition to $Ca(OH)_2$.

Note: Further analysis with LiOH-doped materials was discontinued due to toxicity concerns.

3.4.5 EDX spectra analysis

The data generated in this procedure consists of spectra with peaks corresponding to the signal of the elements making up the sample. Figure 3.26 shows the EDX spectra and atomic weight data tables (inset) for BN-doped $Mg(OH)_2$ (MH-BN) composites, sampled at two regions (Spot 1 and Spot 2) of the materials.

The quantitative weights of Mg, O, B, and N for the composites show moderate values as seen in the standard deviation values in Figure 3.26 (a), (b), and (d). In (c), the weight percentage of B has shown uneven distribution as indicated by a surge in the value of standard deviation. This may be due to the uneven distribution of the BN dopant in the MH-BN15 sample, as the SEM confirmed an insignificant difference in grain distribution in this sample.

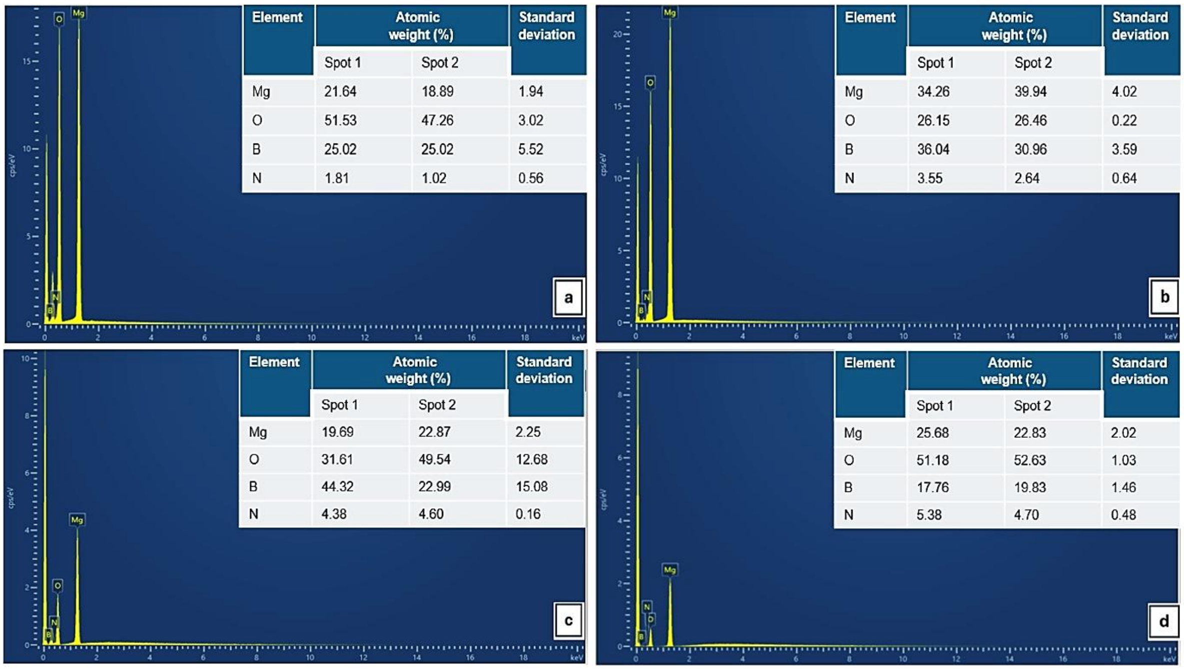

(a)

Element	Atomic weight (%)		Standard deviation
	Spot 1	Spot 2	
Mg	21.64	18.89	1.94
O	51.53	47.26	3.02
B	25.02	25.02	5.52
N	1.81	1.02	0.56

(b)

Element	Atomic weight (%)		Standard deviation
	Spot 1	Spot 2	
Mg	34.26	39.94	4.02
O	26.15	26.46	0.22
B	36.04	30.96	3.59
N	3.55	2.64	0.64

(c)

Element	Atomic weight (%)		Standard deviation
	Spot 1	Spot 2	
Mg	19.69	22.87	2.25
O	31.61	49.54	12.68
B	44.32	22.99	15.08
N	4.38	4.60	0.16

(d)

Element	Atomic weight (%)		Standard deviation
	Spot 1	Spot 2	
Mg	25.68	22.83	2.02
O	51.18	52.63	1.03
B	17.76	19.83	1.46
N	5.38	4.70	0.48

Figure 3. 26 EDX spectra of (a) 5 wt%, (b) 10 wt%, (c) 15 wt%, and (d) 20 wt% BN-doped $Mg(OH)_2$ samples.

Figure 3.27 shows the EDX spectra and atomic weights for KNO_3-doped $Mg(OH)_2$ (MH-PN) composites. For the MH-PN5 composite, the EDX spectra are seen in (a). The Mg, O, and K weights show consistency (approximately the same values) in the sampled areas, indicating uniformity in atomic distribution. This is evident in the minimal standard deviation values of 0.16, 0.13, and 0.03 for Mg, O, and K, respectively. However, it was observed that N atoms were not detected, and this is the case in Figure 3.27 (b) and (c) for the 10 and 15 wt% additive ratios of KNO_3. It is known that certain light atoms are sometimes not detected, so this might be the case with N.

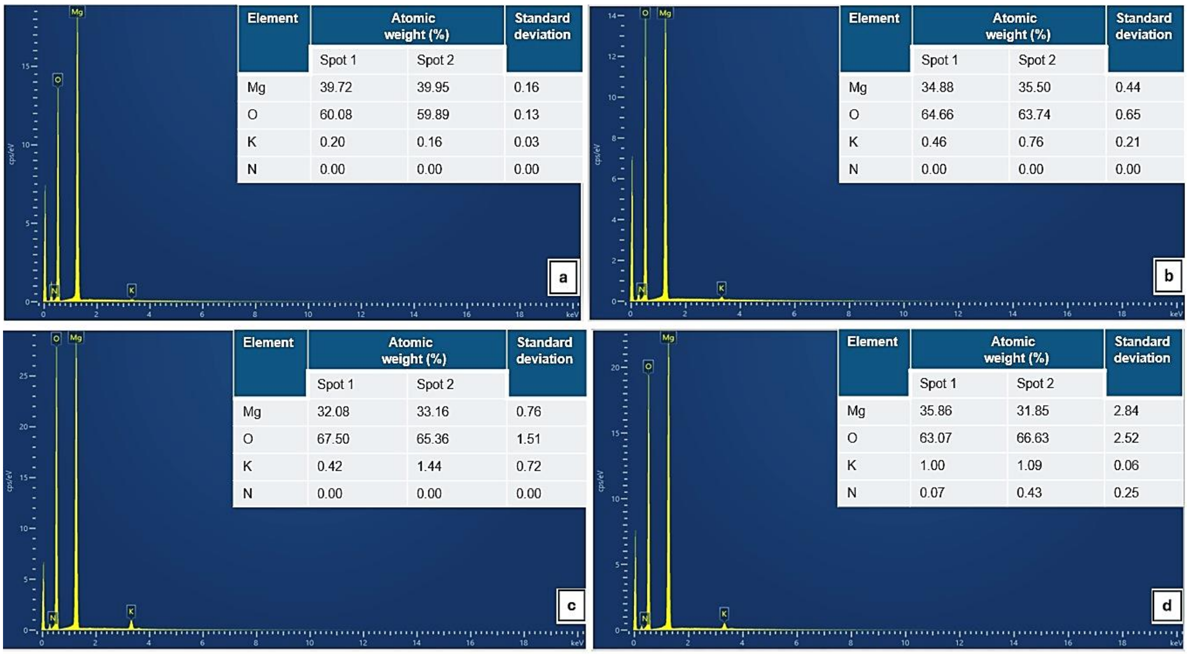

Element	Atomic weight (%)		Standard deviation
	Spot 1	Spot 2	
Mg	39.72	39.95	0.16
O	60.08	59.89	0.13
K	0.20	0.16	0.03
N	0.00	0.00	0.00

Element	Atomic weight (%)		Standard deviation
	Spot 1	Spot 2	
Mg	34.88	35.50	0.44
O	64.66	63.74	0.65
K	0.46	0.76	0.21
N	0.00	0.00	0.00

Element	Atomic weight (%)		Standard deviation
	Spot 1	Spot 2	
Mg	32.08	33.16	0.76
O	67.50	65.36	1.51
K	0.42	1.44	0.72
N	0.00	0.00	0.00

Element	Atomic weight (%)		Standard deviation
	Spot 1	Spot 2	
Mg	35.86	31.85	2.84
O	63.07	66.63	2.52
K	1.00	1.09	0.06
N	0.07	0.43	0.25

Figure 3. 27 EDX spectra of (a) 5 wt%, (b) 10 wt% (c), 15 wt%, and (d) 20 wt% KNO_3-doped $Mg(OH)_2$ samples.

For MH-PN10 in Figure 3.27 (b), the summary of the spectra values indicates standard deviation values of 0.44, 0.65, and 0.21 for Mg, O, and K, respectively, in the sampled areas. However, Mg and O showed increasing deviation in the atomic distribution in MH-PN15 and MH-PN20 samples as seen in Figure 3.27 (c) and (d). It is noticed that with a 20 wt% KNO_3 increase, the presence of N was detected.

Figure 3.28 shows the EDX of the CH-BN composites. For the CH-BN5 composite (Figure 3.28a), the weight and atomic percentages for Ca, O, B, and N in the sampling show that the weights of Ca and O varied from 22.86 to 46.51% and 37.71 to 69.16%, respectively. Both have high standard deviations, showing that the $Ca(OH)_2$ is not uniformly distributed amongst the B and N atoms.

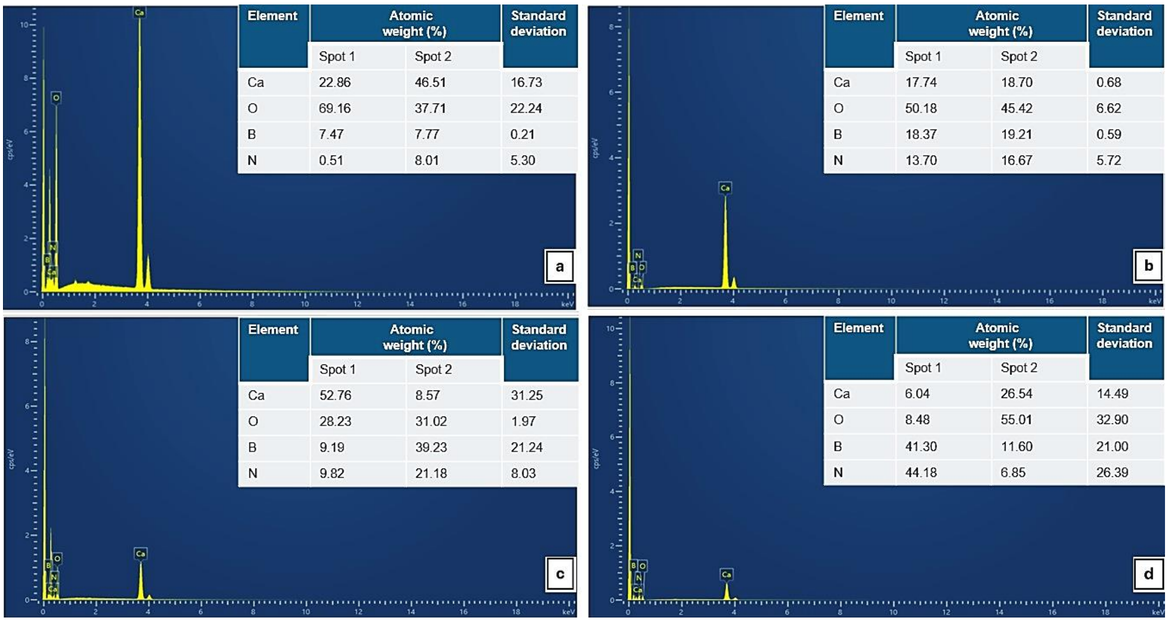

Element	Atomic weight (%)		Standard deviation
	Spot 1	Spot 2	
Ca	22.86	46.51	16.73
O	69.16	37.71	22.24
B	7.47	7.77	0.21
N	0.51	8.01	5.30

Element	Atomic weight (%)		Standard deviation
	Spot 1	Spot 2	
Ca	17.74	18.70	0.68
O	50.18	45.42	6.62
B	18.37	19.21	0.59
N	13.70	16.67	5.72

Element	Atomic weight (%)		Standard deviation
	Spot 1	Spot 2	
Ca	52.76	8.57	31.25
O	28.23	31.02	1.97
B	9.19	39.23	21.24
N	9.82	21.18	8.03

Element	Atomic weight (%)		Standard deviation
	Spot 1	Spot 2	
Ca	6.04	26.54	14.49
O	8.48	55.01	32.90
B	41.30	11.60	21.00
N	44.18	6.85	26.39

Figure 3. 28 EDX spectra of (a) 5 wt%, (b) 10 wt%, (c) 15 wt%, and (d) 20 wt% BN-doped $Ca(OH)_2$ samples.

Generally, the higher BN ratios exhibited increasing standard deviation values for the Ca, O, B, and N, suggesting increasing non-uniformity in atomic distributions. For instance, in the CH-BN15 composite (Figure 3.28c), the atomic weight of Ca, O, B, and N shows that the Ca weight varies from 8.57 to 52.76%, and O from 28.23 to 31.02%. The weights of B and N also increase from 9.19 to 39.23% and 9.82 to 39.23%, respectively. These are evident in the high standard deviation values. A similar trend also occurred in the CH-BN20 composite (Figure 3.28d), whose spectra values show that the Ca, O, B, and N weights are not uniformly distributed, as evident in their respective high standard deviation values of 14.49, 32.90, 21.00, and 26.39.

In the KNO_3-doped $Ca(OH)_2$ samples, the EDX spectra are shown in Figure 3.29. For the CH-PN5 composite in Figure 3.29 (a), the quantitative results show Ca and O weights with high standard deviation values, an indication of non-uniformity in their distribution. K weight shows a good distribution, but N was not detected. A similar trend is observed for the CH-PN10 composite in Figure 3.29 (b).

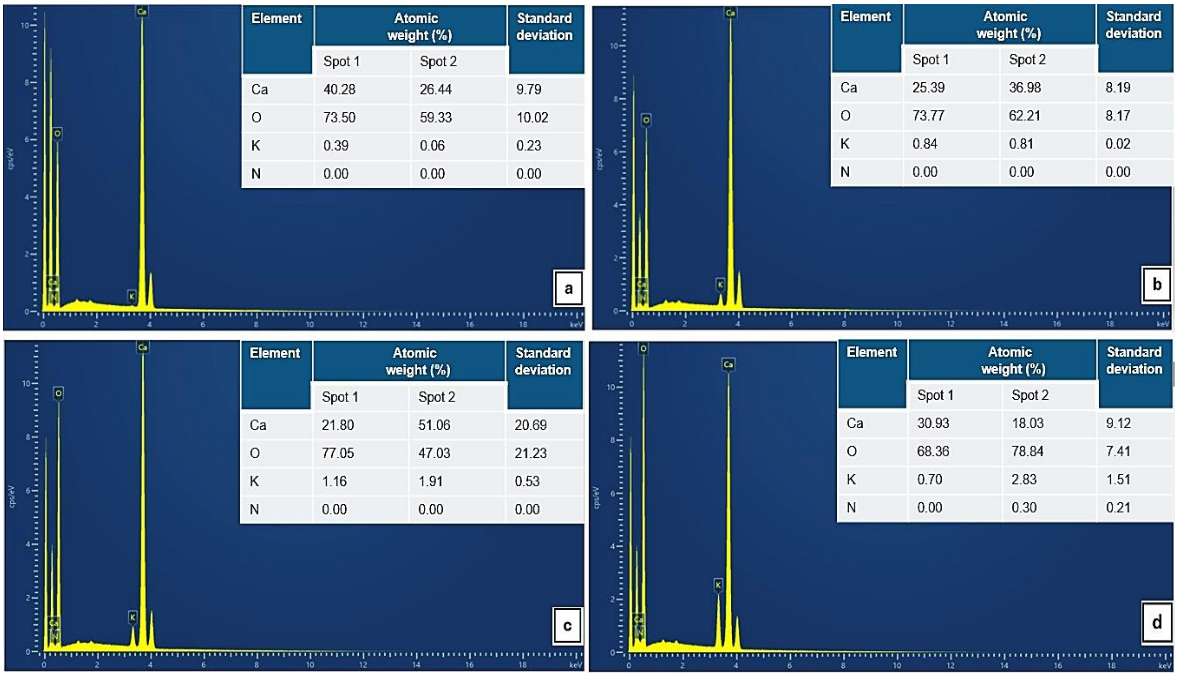

Element	Atomic weight (%)		Standard deviation
	Spot 1	Spot 2	
Ca	40.28	26.44	9.79
O	73.50	59.33	10.02
K	0.39	0.06	0.23
N	0.00	0.00	0.00

Element	Atomic weight (%)		Standard deviation
	Spot 1	Spot 2	
Ca	25.39	36.98	8.19
O	73.77	62.21	8.17
K	0.84	0.81	0.02
N	0.00	0.00	0.00

Element	Atomic weight (%)		Standard deviation
	Spot 1	Spot 2	
Ca	21.80	51.06	20.69
O	77.05	47.03	21.23
K	1.16	1.91	0.53
N	0.00	0.00	0.00

Element	Atomic weight (%)		Standard deviation
	Spot 1	Spot 2	
Ca	30.93	18.03	9.12
O	68.36	78.84	7.41
K	0.70	2.83	1.51
N	0.00	0.30	0.21

Figure 3. 29 EDX spectra of (a) 5 wt%, (b) 10 wt% (c), 15 wt%, and (d) 20 wt% KNO_3-doped $Ca(OH)_2$ samples.

The CH-PN15 sample (Figure 3.29c) shows increasing standard deviations in the Ca and O atomic weight distributions. This indicates a high disparity in the atomic weight distributions of these elements. This is similar to the CH-PN20 composite (Figure 3.29d), although it has a lower degree of disparity. Again, the N was detected due to the increasing weight of the nitrate (KNO_3).

3.4.6 DSC analysis

The DSC curves exhibited broad endothermic peaks during dehydration. The variability of the peak positions is dependent on the dopant ratios. Integrating the area under the peak yields the reaction enthalpy, ΔH. For dehydration reactions, this represents the stored heat or heat content. Another important parameter directly related to the characteristic curves of the materials is the onset temperature, T_o, which is the temperature at which a reaction starts at a measurable rate, in this case, dehydration.

The DSC overlay thermograms for the pure $Mg(OH)_2$ (MH) and its BN-doped composites (MH-BN) are shown in Figure 3.30, while the quantitative data are presented in Table 3.3.

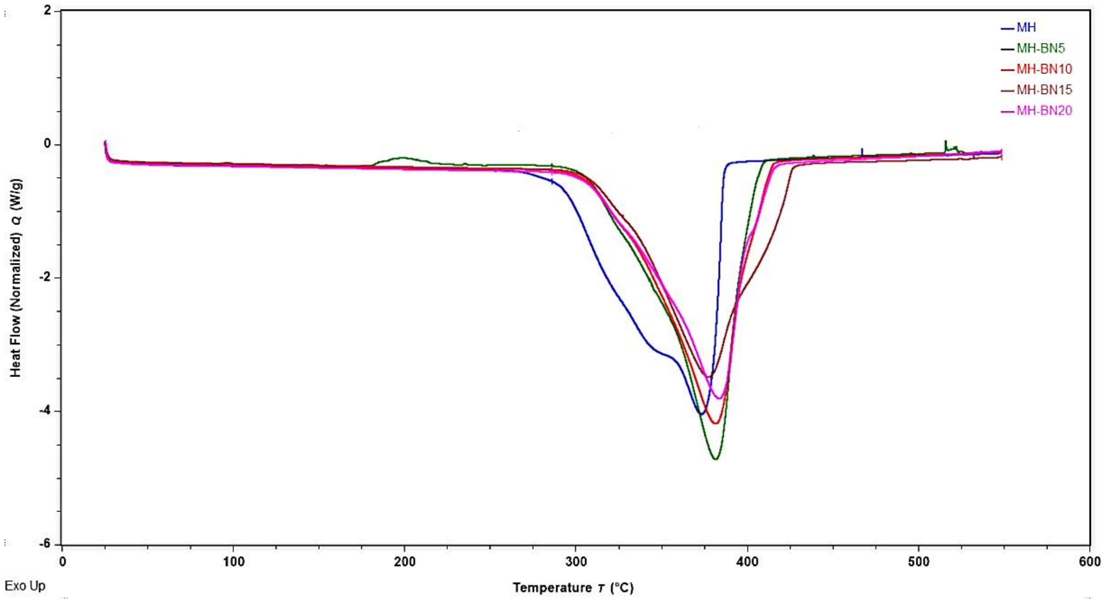

Figure 3. 30 DSC curves of pure Mg(OH)$_2$ and BN-doped composites.

Table 3. 3 Onset temperatures and heat storage in pure and BN-doped Mg(OH)$_2$.

Material	Onset temperature (℃)	Heat content (J/g)
Pure MH	317.03	1246.40
MH-BN5	336.12	1233.20
MH-BN10	328.31	1168.20
MH-BN15	321.38	1122.70
MH-BN20	331.01	1062.50

As observed in Table 3.3, the variation of onset temperature with additive mass fractions of BN in the MH-BN composites does not follow a regular pattern. For instance, at a 5 wt% BN ratio, the onset temperature increased to 336.12 ℃ compared with 317.03 ℃ of pure MH. This decreased as the BN ratio increased from 10 wt% to 15 wt% and increased again at 20 wt%. The heat contents also did not show a regular trend and remained lower than that of the pure MH. This shows that the additive proportions of BN did not positively influence the dehydration behaviour of pure Mg(OH)$_2$. It is desirable to have a lower dehydration temperature to broaden the storage temperature range, as well as a higher heat content.

For pure Mg(OH)$_2$ (MH) and its KNO$_3$-doped composites (MH-PN), the overlay thermograms are shown in Figure 3.31, while the quantitative data are presented in Table 3.4.

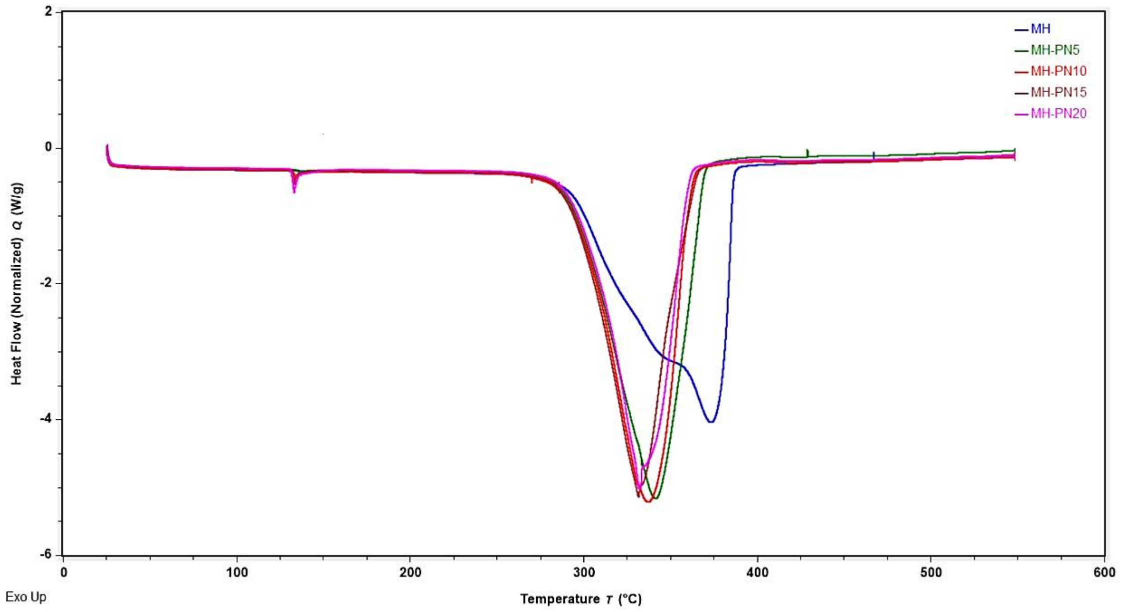

Figure 3. 31 DSC curves of pure $Mg(OH)_2$ and KNO_3-doped composites.

Table 3. 4 Onset temperatures and heat storage in pure and KNO_3-doped $Mg(OH)_2$.

Material	Onset temperature (℃)	Heat content (J/g)
Pure MH	317.03	1246.40
MH-PN5	293.88	1317.10
MH-PN10	297.82	1171.60
MH-PN15	296.47	1103.40
MH-PN20	308.20	1044.00

In Table 3.4, the dehydration temperature showed a decrease from 317.03 ℃ for pure MH to 293.88 ℃ with 5 wt% KNO_3 addition but started to increase as the proportion of KNO_3 rose above 5 wt%. The minimal onset temperature is therefore achieved with an additive fraction of 5 wt%, that is, the MH-PN5 composite. The sample's dehydration temperature was about 23 ℃ less than the dehydration temperature of the pure $Mg(OH)_2$ material (MH). In addition, its dehydration heat of 1317.10 J/g was about 6% more than the dehydration heat of pure MH. The appearance of minute peaks was observed around 132 ℃ with progressing troughs as the dopant ratio increased from 10 wt% and could be attributed to the excess unreacted nitrate salt in the matrix of the samples [44]. A similar observation was reported in the literature and was attributed to the fusion of crystalline KNO_3 around 334 ℃ [92]

On the other hand, Figure 3.32 represents the DSC overlay curves for the pure $Ca(OH)_2$ (CH) and its BN-doped composites (CH-BN), whereas Table 3.5 shows the quantitative data for the analysis.

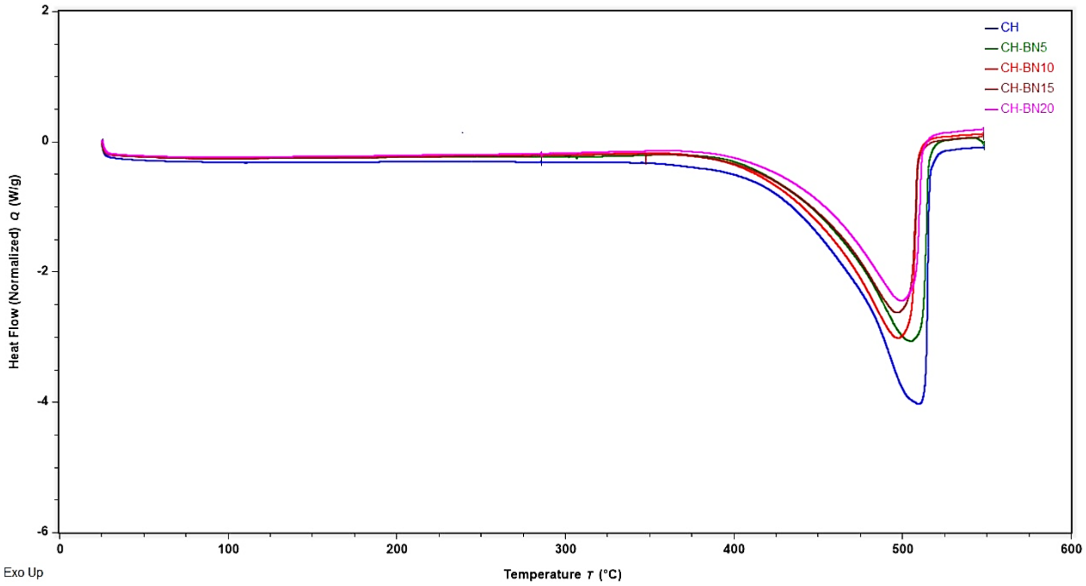

Figure 3. 32 DSC curves of pure $Ca(OH)_2$ and BN-doped composites.

Table 3. 5 Onset temperatures and heat storage in pure and BN-doped $Ca(OH)_2$.

Material	Onset temperature (℃)	Heat content (J/g)
Pure CH	451.26	1196.90
CH-BN5	441.01	1002.10
CH-BN10	433.89	1016.80
CH-BN15	434.65	853.69
CH-BN20	435.48	800.42

As seen in Table 3.5, the dehydration temperature (onset temperature) decreased as the BN content increased until the mass fraction of BN exceeded 10 wt%, and then began to increase. This demonstrates that modification of the $Ca(OH)_2$ structure by the addition of BN has a considerable effect on its dehydration. Here, the minimal dehydration temperature was 433.89 ℃ at 10 wt% of BN proportion. This means the dehydration temperature of the CH-BN10 composite could be achieved at about 17 ℃ below that of the pure material (CH). However, the dehydration heat of CH-BN10 was 1016.80 J/g, which is 15% less than the dehydration heat of pure CH.

For the KNO$_3$-doped composites (CH-PN), the overlay thermograms are shown in Figure 3.33, while the quantitative data are presented in Table 3.6.

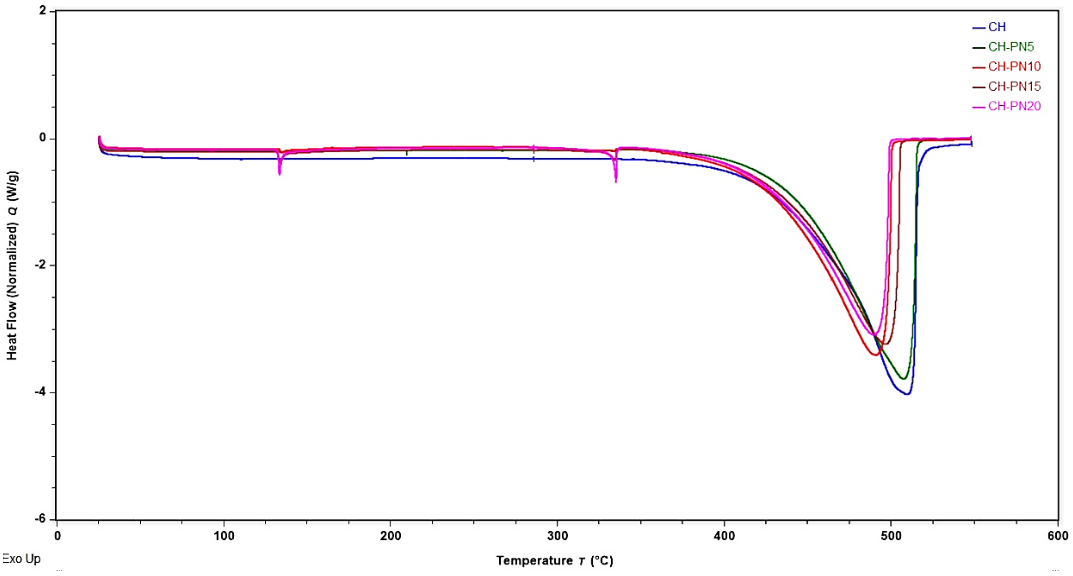

Figure 3. 33 DSC curves of pure Ca(OH)$_2$ and KNO$_3$-doped composites.

Table 3. 6 Onset temperatures and heat storage in pure and KNO$_3$-doped Ca(OH)$_2$.

Material	Onset temperature (℃)	Heat content (J/g)
Pure CH	451.26	1196.90
CH-PN5	438.87	1135.80
CH-PN10	426.96	1027.50
CH-PN15	431.18	956.30
CH-PN20	426.00	894.97

From Table 3.6, the dehydration temperature decreases as the KNO$_3$ content increases to the KNO$_3$ additive proportion of 10 wt%. The minimal dehydration temperature is 426.00 ℃ with a 20 wt% mass fraction of KNO$_3$. So, the heat storage reaction of the CH-PN20 material could be carried out at 31 ℃ lower than the pure CH material, but at 25% less dehydration heat. As previously noted, the appearance of minute endothermic peaks was observed at additive ratios >10 wt%. For the CH-PN15 composite, two peaks appeared at 133 ℃ and 331 ℃, and 132 ℃ and 333 ℃ for CH-PN20.

3.4.7 TGA

TGA was used to assess the thermal stability of the materials by determining the temperatures at which they began to lose weight, and by what percentage during the temperature ramp. This indicates how soon the dehydration reactions started when the materials began to decompose (dehydrate). Figure 3.34 presents the TGA overlay curves of pure $Mg(OH)_2$ (MH) and its BN-doped composites, and the summary is shown in Table 3.7.

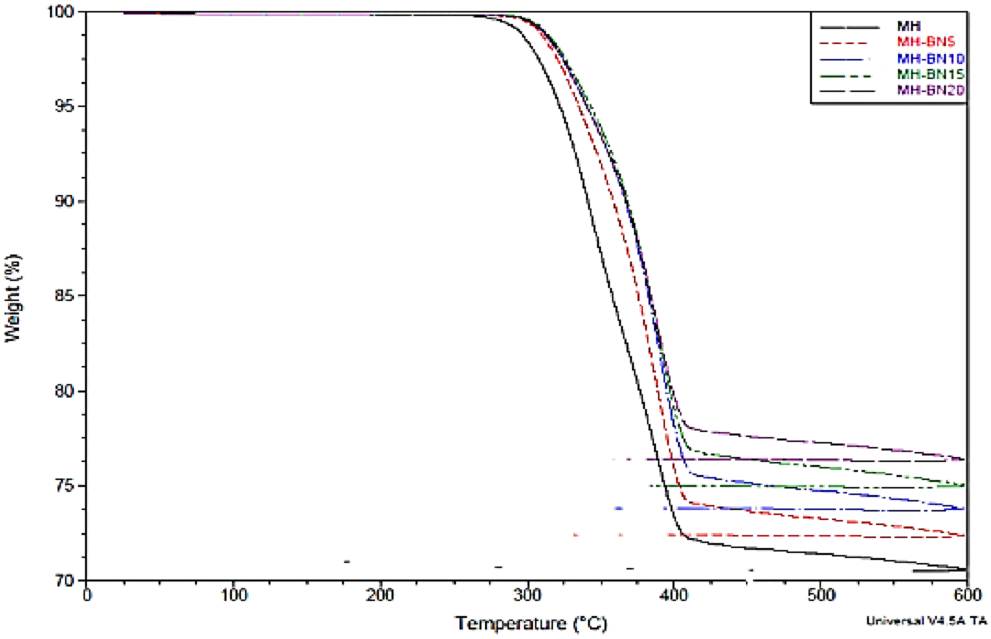

Figure 3. 34 TGA overlay curves for pure $Mg(OH)_2$ and BN-doped composites.

Table 3. 7 TG onset temperatures and weight loss in $Mg(OH)_2$ and its BN composites.

Material	**Onset temperature (℃)**	**Weight loss (%)**
Pure MH	295.25	28.79
MH-BN5	311.07	26.92
MH-BN10	312.46	25.49
MH-BN15	309.72	24.26
MH-BN20	305.52	22.94

Adding BN to the base material, MH seemed to improve thermal stability. This is evident from the increase in the onset temperature from 295.25 ℃ for MH to 312.46 ℃ for MH-BN10. A higher onset temperature suggests that the material could withstand higher temperatures before decomposition (dehydration) began. The thermal stability was highest for MH-BN10 (312.46 ℃) and decreased slightly for MH-BN15 (309.72 ℃) and MH-BN20 (305.52 ℃). The weight loss, on the other hand, decreased with the increasing BN content. MH, with no BN, had the highest weight loss of 28.79%. As the BN content increased, the weight loss decreased, with MH-BN20 showing the lowest weight loss at 22.94%. This suggests that BN not only delayed the onset of decomposition but also reduced the extent of decomposition. The results indicate that incorporating BN into MH enhances its thermal stability, with the most significant improvement observed in the MH-BN10 composition. Both onset temperature and weight loss data suggest that BN contributes positively to the material's resistance to thermal degradation. Beyond the MH-BN10 composition, the thermal stability begins to slightly decrease.

On the other hand, Figure 3.35 presents the TGA curves of pure MH and its KNO_3-doped composites, while Table 3.8 presents the obtained results.

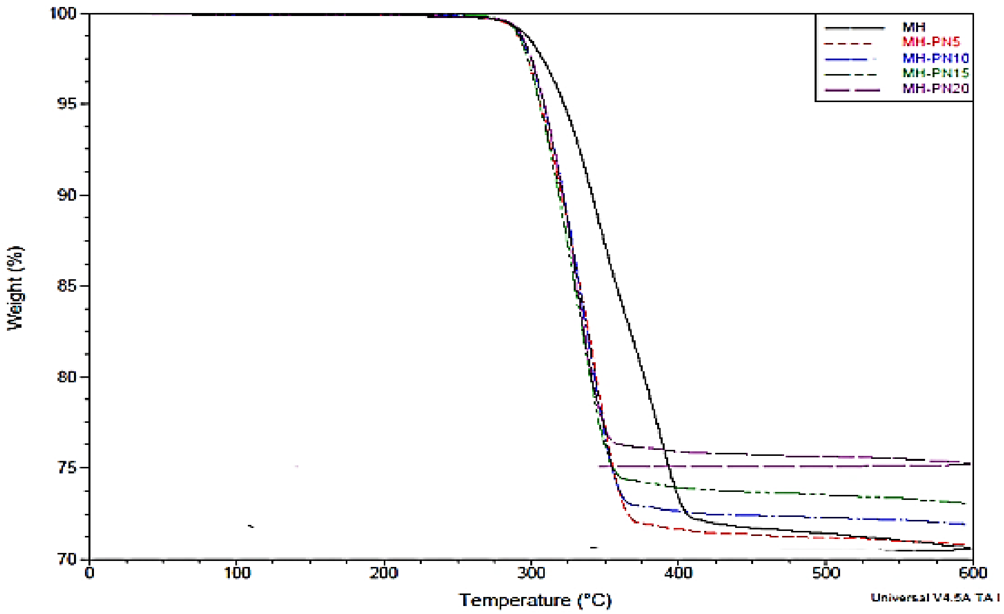

Figure 3. 35 TGA overlay curves for pure $Mg(OH)_2$ and KNO_3-doped composites.

Table 3. 8 TG onset temperatures and weight loss in $Mg(OH)_2$ and its KNO_3 composites.

Material	**Onset temperature (℃)**	**Weight loss (%)**
Pure MH	295.25	28.79
MH-PN5	291.65	28.80
MH-PN10	293.56	27.73
MH-PN15	292.00	26.56
MH-PN20	293.69	24.82

The addition of KNO_3 did not significantly enhance the thermal stability of MH. The onset temperatures for the KNO_3-modified materials (MH-PN5, MH-PN10, MH-PN15, and MH-PN20) were all slightly lower than the unmodified MH, with MH-PN5 showing the lowest onset temperature of 291.65 ℃. The thermal stability did not improve noticeably with increasing KNO_3 content, and the onset temperatures fluctuated slightly around the value for MH. For weight loss, MH had a weight loss of 28.79%. For the KNO_3-modified materials, the weight loss decreased as the nitrate content increased, similar to the trend observed with BN-modified materials. MH-PN20 showed the most significant reduction in weight loss at 24.82%, indicating that higher KNO_3 content reduced the extent of thermal decomposition.

This suggests that while KNO_3 addition did not significantly increase the onset temperature, it did contribute to reducing the overall material degradation at higher KNO_3 concentrations. The thermal stability, in terms of the onset temperature, remained relatively similar (or slightly lower) compared to the unmodified MH. This could indicate that KNO_3 doping did not delay the onset of decomposition as in the case of BN. The decrease in weight loss with increasing KNO_3 content suggests that KNO_3 did contribute to reducing the extent of decomposition, although not as effectively as BN. The reduction in weight loss might indicate that KNO_3 helped to retain more of the material mass during heating. Overall, while KNO_3 reduced the extent of material degradation (as seen by lower weight loss), it did not improve the onset temperature. This might suggest that KNO_3 acted more as a stabilizer after decomposition began rather than preventing or delaying the onset of decomposition.

Similarly, the TGA curves for pure $Ca(OH)_2$ and its BN-doped composites are shown in Figure 3.36 and the results are presented in Table 3.9.

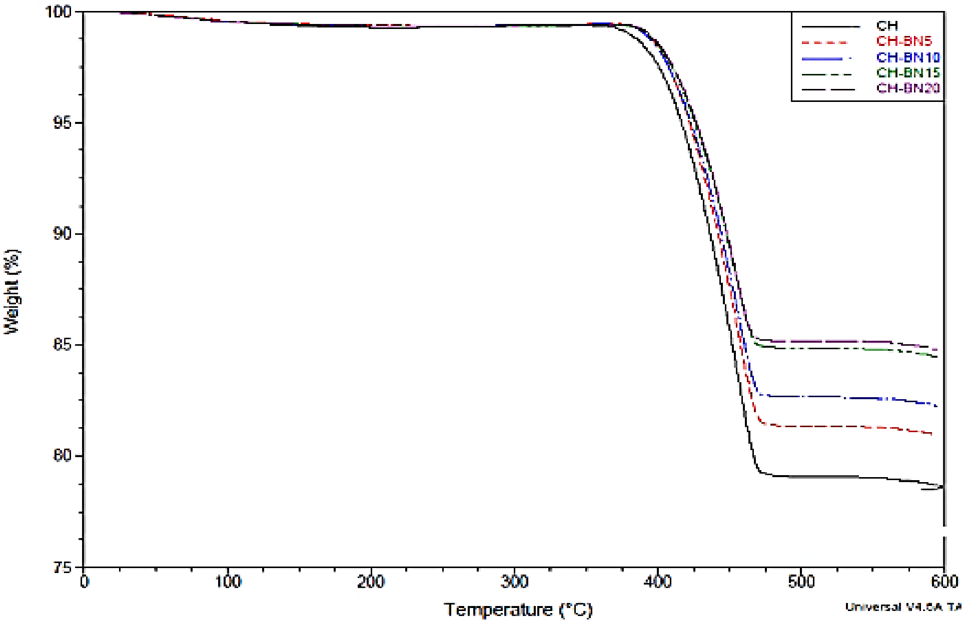

Figure 3. 36 TGA overlay curves for pure $Ca(OH)_2$ and BN-doped composites.

Table 3. 9 TG onset temperatures and weight loss in $Ca(OH)_2$ and its BN composites.

Material	Onset temperature (℃)	Weight loss (%)
Pure CH	397.30	18.40
CH-BN5	393.40	16.80
CH-BN10	393.70	14.65
CH-BN15	398.26	14.28
CH-BN20	435.48	14.28

The addition of BN has varying effects on the onset temperature. CH-BN5 and CH-BN10 showed a slight decrease in onset temperature compared to CH, with values of 393.40 ℃ and 393.70 ℃, respectively. This suggests a minor reduction in thermal stability at these lower BN concentrations. CH-BN15 showed a slight improvement in thermal stability with an onset temperature of 398.26 ℃, slightly higher than the pure CH. The most significant improvement was observed in CH-BN20, where the onset temperature dramatically increased to 435.48 ℃. This indicates a substantial improvement in thermal stability at the highest BN concentration, suggesting that CH-BN20 could withstand much higher temperatures before decomposing. The onset temperature data show that BN has a positive effect on the thermal stability of the pure material (CH), particularly at higher concentrations. While lower concentrations of BN (5% and 10%) slightly reduce the onset temperature, a significant increase is observed at 20% BN, with the onset temperature rising to 435.48 ℃. This indicates that CH-BN20 was significantly more thermally stable than the pure CH material.

Pure CH exhibits a weight loss of 18.40%. The addition of BN reduced the weight loss across all compositions. The weight loss decreased progressively with increasing BN content, with CH-BN5 showing 16.80%, CH-BN10 at 14.65%, and both CH-BN15 and CH-BN20 at 14.28%. The plateau in weight loss between CH-BN15 and CH-BN20 suggests that the reduction in weight loss stabilized at higher BN concentrations, possibly indicating that a maximum stabilization effect was reached. The lower weight loss at higher BN concentrations implies that the material retained more of its mass during heating, indicating improved thermal stability.

Overall, the results suggest that BN is an effective additive for enhancing the thermal stability of CH, particularly at higher concentrations, where it both delays the onset of decomposition and reduces the extent of degradation. The most significant improvements in thermal stability and weight retention were observed in the CH-BN20 material.

For $Ca(OH)_2$ and its KNO_3-doped composites, the TGA curves are shown in Figure 3.37, and the results are presented in Table 3.10.

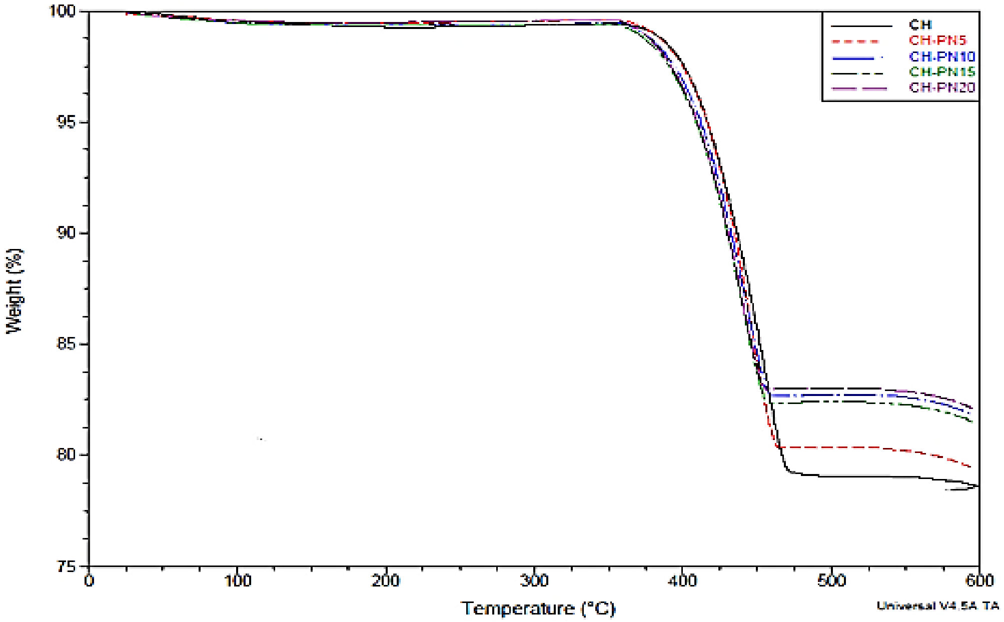

Figure 3. 37 TGA overlay curves for pure $Ca(OH)_2$ and KNO_3-doped composites.

Table 3. 10 TG onset temperatures and weight loss in $Ca(OH)_2$ and its KNO_3 composites.

Material	**Onset temperature (^{o}C)**	**Weight loss (%)**
Pure CH	397.30	18.40
CH-PN5	391.20	19.44
CH-PN10	376.35	16.82
CH-PN15	367.52	17.09
CH-PN20	372.82	16.98

The addition of KNO_3 generally decreases the onset temperature across all concentrations. CH-PN5 showed a slight decrease in onset temperature to 391.20 ℃, indicating a minor reduction in thermal stability. The onset temperature further decreased with increasing KNO_3 content, reaching the lowest value of 367.52 ℃ for CH-PN15. This suggests that KNO_3 reduced the material's thermal stability, making it decompose at lower temperatures. CH-PN20 showed a slight recovery in onset temperature to 372.82 ℃, but this value is still lower than the pure CH material. In terms of weight loss, CH had a weight loss of 18.40%. The effect of PN on weight loss is less straightforward compared to the onset temperature. For instance, CH-PN5 showed a slight increase in weight loss to 19.44%, indicating more material degradation compared to pure CH. However, with further increases in KNO_3 content, the weight loss decreased, with CH-PN10 showing 16.82% and CH-PN20 showing 16.98%. This suggests that while the addition of KNO_3 lowered the onset temperature, it did help in reducing the extent of material degradation, at least at higher concentrations.

In a nutshell, the addition of KNO_3 generally lowered the onset temperature, meaning that the CH-PN materials started decomposing at lower temperatures compared to pure CH. This indicates a reduction in thermal stability across all KNO_3 concentrations. The greatest reduction in onset temperature was observed in CH-PN15 (367.52 ℃), suggesting that this composition is the least thermally stable among those tested. The weight loss results are somewhat mixed. CH-PN5 showed a slight increase in weight loss, indicating more degradation. However, with higher nitrate content (10% and above), the weight loss decreased, with CH-PN10 having the lowest weight loss of 16.82%. This indicates that while the KNO_3 addition made the material decompose at lower temperatures, it also reduced the extent of decomposition at higher temperatures.

Overall, the results suggest that the addition of KNO_3 to $Ca(OH)_2$ (CH) generally reduced the material's thermal stability, as indicated by the lower onset temperatures. However, at higher KNO_3 concentrations, the extent of material degradation (weight loss) was reduced, which could indicate that KNO_3 helped to stabilize the material once decomposition started, but it did not prevent the onset of decomposition at higher temperatures.

3.5 Concluding remarks

In this chapter, $Ca(OH)_2$ and $Mg(OH)_2$ were used as the core materials for the development of composites TCES materials. This development process using various dopants was confirmed by XRD analysis to be successful, and their thermophysical properties were evaluated. BET surface area measurements indicated reduced surface areas and porosity in both $Ca(OH)_2$ and $Mg(OH)_2$ materials, irrespective of the dopant type used, and this was supported by SEM microstructure analysis.

DSC and TGA results both indicated that KNO_3 doping was highly effective in reducing the dehydration (onset) temperatures in $Ca(OH)_2$ and $Mg(OH)_2$. For instance, 10 wt% KNO_3 reduced the dehydration temperature in $Ca(OH)_2$ by 24 ℃, though with a 14% decrease in heat storage capacity. Whereas 5 wt% KNO_3 reduced the dehydration temperature by 23 ℃ and also enhanced the heat storage by 6% in $Mg(OH)_2$. The fact that the thermal indices of 5 wt% KNO_3-doped $Mg(OH)_2$ in TGA were very close to the base material suggests that the addition of KNO_3 did not significantly alter the thermal stability of the pure material. Again, the minimal change in thermal stability could imply good compatibility between $Mg(OH)_2$ and KNO_3, since KNO_3 incorporation into the $Mg(OH)_2$ matrix did not compromise its thermal integrity.

Overall, KNO_3 is an effective dopant for modifying the thermophysical properties of both $Ca(OH)_2$ and $Mg(OH)_2$, with 5 wt% KNO_3-doped $Mg(OH)_2$ composite (MH-PN5) showing promise for medium temperature heat storage applications between 293–400 ℃ temperature range. Further enhancement in the material's thermal transfer capabilities is therefore encouraged before testing in the rig.

Chapter 4: Thermal Enhancement Modelling of the Developed Materials

4.1 Introduction

In the preceding chapter, numerous experimental procedures were carried out on the developed TCES materials. The process ultimately narrowed the selection down to the MH-PN5 composite material due to its encouraging performance in the thermophysical tests. These tests were based on the behaviour of the materials at the macroscopic scale. However, the basic building blocks of materials are atoms, and their interactions at the microscopic level dictate the macroscopic scale behaviour of the materials. Therefore, for a fundamental understanding of TCES behaviour at the molecular level, advanced techniques are essential. Specifically, molecular dynamics (MD) simulations were used to establish appropriate conditions for the thermal enhancement of the developed material. This approach was essential for enabling the prediction of optimization parameters, thereby reducing the time spent on experiments. For thermal conductivity enhancement, aluminium oxide (alumina), Al_2O_3, nanomaterials were used as suggested by Coetzee et al. [159]. These nanomaterials possess intrinsic properties such as high thermal conductivity, compatibility with the host material, large surface area, and stability across a wide range of temperatures [160]. However, the effectiveness of nanoparticles for thermal conductivity enhancement depends on the dosage used [159]. For this reason, MD simulations were used to evaluate the dose effectiveness and the structural interactions of the particles.

MD simulation is a valuable computational tool for exploring dynamics at the atomic scale. Utilizing appropriate potential models allows for the simulation of atomic movements, and MD is particularly well-suited for studying detailed interactions between molecules or atoms, as well as their behaviour over time [161]. This makes it more appropriate than methods like Monte Carlo or coarse-grained simulations, which may not capture the intricate, time-dependent interactions that MD can provide [162].

4.2 Molecular dynamics

At the core of molecular dynamics is Newton's second law of motion, which governs the behaviour of particles under the influence of forces. By applying suitable potential models, or force fields, MD simulations can accurately predict the positions, velocities, and forces acting on each atom or molecule at every time step [162]. During an MD simulation, the trajectories of particles are determined by numerically solving Newton's equations of motion. These calculations take into account the interatomic forces and potential energies, which are derived from molecular mechanics force fields or interatomic potentials. By allowing atoms or molecules to interact over a desired period, MD provides insights into the dynamic properties of the system, revealing how it evolves over time. This makes molecular dynamics a key method in the study of complex molecular systems, offering a deep understanding of the underlying mechanisms that govern their behaviour [162].

Some of the widely used molecular dynamics (MD) software packages include GROMACS (Groningen Machine for Chemical Simulations) [163], NAMD (Nanoscale Molecular Dynamics) [164], AMBER (Assisted Model Building with Energy Refinement) [165], and CHARMM (Chemistry at Harvard Macromolecular Mechanics) [166], which are especially used in computational chemistry for simulations of biomolecular systems such as proteins, lipids, and nucleic acids with their specialized algorithms, making them ideal for researchers focused on biological systems. Again, codes with a focus on materials modelling are DL_POLY (Daresbury Laboratory Polymer)[167], HOOMD (Highly Optimized Object-oriented Molecular Dynamics) [168], and LAMMPS (Large Scale Atomic/Molecular Massively Parallel Simulator) [169].

Of all these software, LAMMPS is highly valued for its scalability and performance on large parallel computing systems, making it ideal for simulating large and complex systems. Its versatility allows it to support a wide range of force fields and models, including hybrid simulations, and its modular design enables easy customization for specific research needs [161]. LAMMPS is open-source, backed by an active development community, and offers extensive documentation and support, making it accessible and adaptable for diverse scientific applications, particularly in materials science and engineering. Besides, LAMMPS offers exceptional versatility with its ability to handle a broader range of materials and simulations, including biological molecules. For these reasons, all simulations done in this work were run using LAMMPS software.

4.3 Molecular dynamics with LAMMPS

LAMMPS, an open-source software developed at Sandia National Laboratories for conducting MD simulations, is designed to run classical MD on both single processors and parallel computers, making it highly scalable and capable of handling large, complex systems. It is versatile enough to model a wide range of physical states and systems, including liquids, solids, gases, atomic and molecular systems, polymers, metals, biological macromolecules, granular materials, and coarse-grained systems. This flexibility is supported by its extensive range of force fields, boundary conditions, and the ability to run multiple simulations simultaneously from a single input script.

Initially written in FORTRAN, LAMMPS has been rewritten in C++ to enhance its modularity and ease of use, allowing users to easily modify the code to incorporate new force fields, particle properties, boundary conditions, or diagnostics [161]. The input scripts used in LAMMPS are highly customizable, with syntax that supports variables, formulas, looping constructs, and commands for defining system geometry, atom types, force fields, and simulation parameters. The output generated by LAMMPS includes thermodynamic information and customizable data files, which can be visualized using appropriate tools or converted into formats compatible with other software for further analysis.

LAMMPS excels in simulating a wide variety of molecular systems due to its robust handling of complex interactions and its ability to scale across many processors [170]. The software is extensively used in fields such as materials science, chemistry, physics, and biology for applications ranging from phase transitions and mechanical properties to chemical reactions, diffusion processes and the behaviour of biomolecules. Its open-source nature, active development community, and comprehensive documentation make it accessible and widely used in both academic and industrial research, providing a powerful tool for understanding and predicting molecular-level phenomena.

A key advantage of LAMMPS is its scalability, as it is highly optimized for parallel computing. This allows researchers to simulate large systems with millions of particles on high-performance computing clusters [170]. It also supports hybrid simulations, combining different modelling methods such as molecular dynamics with Monte Carlo or finite element methods. Furthermore, LAMMPS is well-suited for non-equilibrium simulations, such as those involving shear flow and heat transfer, through the use of appropriate boundary conditions and thermostats.

In general, the main steps involved in LAMMPS molecular dynamics are shown in Figure 4.1, the details of which are given in the following sections.

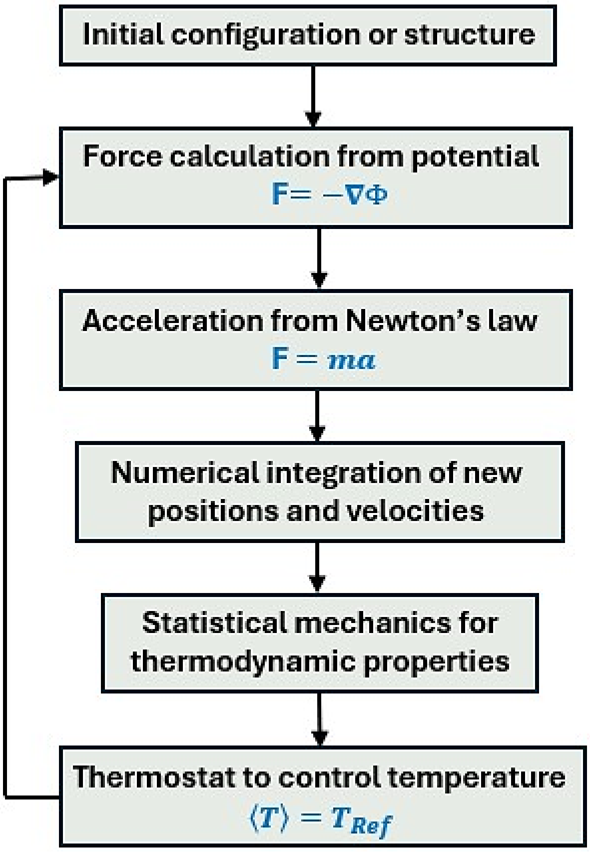

Figure 4. 1 Flow chart showing main steps in MD simulation.

4.3.1 Initial configuration

In LAMMPS, the initial configuration refers to a molecular model with positions and velocities and involves the starting arrangement and properties of the atoms or particles in the MD simulation. This setup is crucial as it defines the initial conditions from which the simulation evolves. Key aspects of the initial configuration are:

1. Atomic positions and structure:
   - The initial configuration includes the spatial coordinates of all atoms or particles in the system. These positions can represent a crystalline solid, a disordered liquid, a gas, or a desired structure.
   - Users can input these positions manually, generate them through LAMMPS commands, or import them from external files, such as data files or coordinate files in various formats.

2. Atom types and masses:
    - Each atom in the system is assigned a specific type, which corresponds to its chemical element (or particle type in coarse-grained models). The type determines the atom's mass, charge, and the interaction potentials it will use during the simulation.
3. Velocities:
    - Initial velocities can be assigned to the atoms by specifying them directly or by generating them randomly based on a desired temperature using a velocity distribution, such as the Maxwell-Boltzmann distribution.
    - The initial velocity distribution helps set the kinetic energy of the system, which corresponds to its temperature.
4. Boundary conditions:
    - LAMMPS allows users to define the boundary conditions of the simulation box, which can be periodic, fixed, or reflective. These conditions impact how atoms interact at the edges of the simulation box and are critical for mimicking bulk materials or interfaces.
5. Simulation box and dimensions:
    - The simulation box defines the overall dimensions and shape of the system. It must be specified in the initial configuration to ensure that the atoms are correctly positioned within the box and that the simulation space is properly defined.
6. Molecule or group definitions:
    - In systems with complex molecules or specific groups of atoms, these can be predefined in the initial configuration. This includes specifying bonds, angles,

dihedrals, and other molecular topology details, which LAMMPS will use to apply the correct interaction potentials.

A well-prepared initial configuration is essential, as it ensures that the simulation begins from a realistic and physically meaningful state, which is critical for achieving accurate and reliable outcomes in the simulation.

4.3.2 Force calculation from potential

In MD simulation, the atoms' movement is tracked by using the interatomic potential to measure the interaction force of the atoms, employing Newton’s equation of motion. The force on each atom is determined by taking the negative gradient of the interatomic potential as

$$\mathrm{F} = -\nabla\Phi \tag{4.1}$$

where F is the force on each particle, and Φ is the interatomic potential.

This force is then used in Newton's law of motion to calculate the acceleration of each particle as

$$\mathrm{F} = \mathrm{m}a \tag{4.2}$$

where a is the acceleration on each particle, and m is the mass of the particle.

From this acceleration, a finite difference method is required to obtain the atom’s trajectories (displacements and velocities) at every timestep of the simulation. A widely used method for this purpose is the Verlet integration (often called the velocity-Verlet algorithm), which is derived from a Taylor expansion of the atom's position and takes the form shown below. Displacement is found by

$$\mathrm{r}(\mathrm{t}+\Delta\mathrm{t}) = r(t) + v(t)\Delta t + \frac{1}{2}a(\mathrm{t})\Delta t^2 \tag{4.3}$$

and velocity is found by

$$v(\mathrm{t}+\Delta\mathrm{t}) = v(t) + \frac{1}{2}[a(t+\Delta t) + a(t)]\Delta t \qquad (4.4)$$

Figure 4.2 shows the atoms' position (r) and velocity (v) at equal times, based on the velocity-Verlet algorithm represented by Equations 4.3 and 4.4 [170].

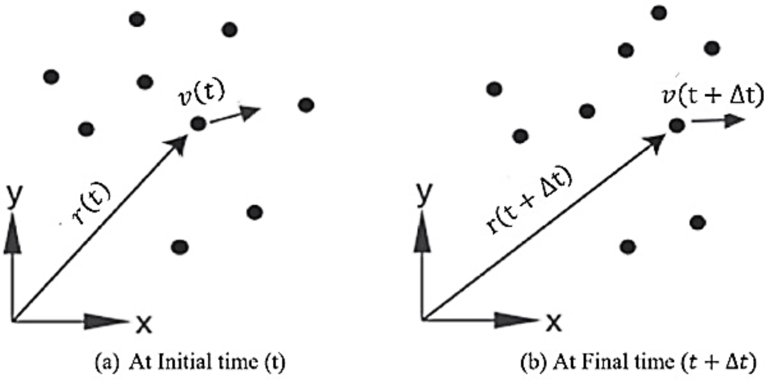

Figure 4. 2 Positions and velocities of the atoms are changed over time (This change is marked for a single atom only).

Hence, the Verlet algorithm is used to find the position and velocity of a single atom in one direction with respect to time, where t is the initial time and $\Delta\mathrm{t}$ is the timestep. By following these mathematical steps, the time evolution of the atoms can be computed, and their motion visualized using suitable software.

4.3.3 Thermodynamic properties estimation

Thermodynamic properties provide insights into the state of a system, such as its temperature, pressure, energy, and volume, which are essential for understanding phase transitions, reaction kinetics, and material properties. Key thermodynamic properties such as energy, temperature, and pressure and how LAMMPS estimates them are discussed below:

1. Energy calculations:

The potential energy in LAMMPS arises from the interactions between particles, such as bonds, angles, van der Waals, and electrostatic forces. The potential energy $(\mathrm{E_p})$ depends on the positions (r) of the particles relative to each other, expressed as

$$\mathrm{E_p} = \sum\nolimits_i^N \Phi(r) \tag{4.5}$$

where $\Phi(\mathrm{r})$ is the interatomic potential (potential function) acting on a particle i in a system of N atoms. A stable configuration typically corresponds to a local minimum in potential energy, indicating that particles are in energetically favourable positions.

Kinetic energy $(\mathrm{E_k})$ is associated with the motion of particles and is calculated based on their velocities (v_i) and masses $(\mathrm{m_i})$ as

$$\mathrm{E_k} = \sum\nolimits_i^N \frac{1}{2} \mathrm{m_i}\, v_i^2 \tag{4.6}$$

It reflects the system's temperature, as higher temperatures lead to higher particle velocities and, consequently, greater kinetic energy. It is directly related to the system's thermal state.

Users can also calculate other specific energies, such as bond, angle, dihedral, and pair interaction energies, depending on the type of force field and interactions defined in the system.

2. Temperature:

Temperature in LAMMPS is computed based on the kinetic energy of the particles using the equipartition theorem. The theorem predicts that the average total energy, $\langle \mathrm{E_T} \rangle$, of N particles or atoms in three dimensions is given as

$$\langle \mathrm{E_T} \rangle = \frac{3}{2} \mathrm{N k_B T} \tag{4.7}$$

where k_B is the Boltzmann constant and T is the absolute temperature. This formula reflects that each degree of freedom (in three dimensions: x, y, and z) contributes $1/2\, k_B T$ to the average energy per particle. Since there are three translational degrees of freedom, the total energy per particle is $3/2\, k_B T$, and for N atoms, it becomes $3/2\, N k_B T$. This total energy is equal to the kinetic energy of the system thus

$$\frac{3}{2} N k_B T = \frac{1}{2} \sum_i^N m_i v_i^2 \tag{4.8}$$

The temperature is then calculated as

$$T = \frac{\sum_i^N m_i v_i^2}{3 N k_B} \tag{4.9}$$

The temperature is a critical parameter that influences other thermodynamic properties and the behaviour of the system over time.

3. Pressure:

Pressure is calculated using the virial theorem, which accounts for both the kinetic energy of the particles and the forces acting between them. LAMMPS can compute instantaneous pressure, as well as the pressure tensor, which provides information about the stress distribution within the system. The Virial pressure (P) is given as [171]

$$P = \frac{N k_B T}{V} + \frac{1}{Vd} \langle \sum_{i<j} F_{ij} r_{ij} \rangle \tag{4.10}$$

where V is the volume, d is the dimension of the system, F_{ij} is the force on the particle i exerted by particle j, and *r* is the vector going from i to j. The angular brackets denote a time average in molecular dynamics. If Φ_{ij} is the interatomic potential between i and j then the force is $F_{ij} = -\nabla \Phi_{ij} = -\frac{\partial \Phi_{ij}}{\partial r_{ij}}$ and Equation (4.10) becomes

$$P = \frac{N k_B T}{V} - \frac{1}{Vd} \langle \sum_{i<j} \frac{\partial \Phi_{ij}}{\partial r_{ij}} r_{ij} \rangle \tag{4.11}$$

4. Ensemble simulations:

LAMMPS supports various statistical ensembles, such as microcanonical or NVE (constant number of particles, volume, and energy), canonical or NVT (constant number of particles, volume, and temperature), isothermal-isobaric or NPT (constant number of particles, pressure, and temperature), and grand canonical or μVT (constant chemical potential, volume, and temperature). Each ensemble corresponds to different thermodynamic conditions and is used to simulate specific physical scenarios.

The choice of ensemble affects the thermodynamic properties estimated during the simulation. For instance, in an NPT ensemble, both temperature and pressure are controlled, allowing for the estimation of properties like enthalpy.

Thermodynamic properties in LAMMPS are often averaged over time to obtain meaningful values, especially for properties like temperature and pressure, which may fluctuate during a simulation. These time-averaged values provide a more accurate representation of the system's equilibrium state. LAMMPS also allows for the calculation of fluctuations, such as the variance in energy or pressure, which can be related to other thermodynamic quantities like heat capacity.

4.3.4 Thermostat and barostat

Thermostats and barostats are essential tools in LAMMPS for maintaining the desired thermodynamic conditions during simulations. The choice of the specific thermostat or barostat depends on the ensemble required and the characteristics of the system under study.

Thermostats adjust particle velocities to control temperature. In the NVE ensemble, energy is conserved, so a thermostat is optional and primarily used to stabilize temperature. In the NVT ensemble, which maintains constant temperature, volume, and particle number, thermostats like the Nose-Hoover, Langevin, and Berendsen are commonly used. The Nose-Hoover thermostat accurately couples the system to a thermal reservoir, while the Langevin thermostat introduces random forces to mimic a heat bath, useful for precise temperature control. Though less accurate, the Berendsen thermostat is often employed for initial equilibration due to its simplicity [172].

Barostats control pressure by adjusting system volume or particle forces, critical in the NPT ensemble. The Nose-Hoover barostat, often paired with a thermostat in NPT simulations, modifies system volume to maintain target pressure. The Parrinello-Rahman barostat is ideal for systems where the simulation box shape needs to change, such as in anisotropic systems. The Berendsen barostat, like its thermostat counterpart, is used for equilibration but doesn't accurately reproduce pressure fluctuations [172].

4.4 Computational resources and software

The molecular dynamics (MD) simulations discussed in this thesis involved thousands of atoms making millions of timesteps. These simulations required significant computational power and were carried out on the Augusta High-Performance Computing (HPC) system, provided by Digital and Technology Services at the University of Nottingham. Augusta comprises 115 compute nodes, each equipped with dual 20-core Intel Skylake 6138 processors (2.0 GHz), 192 GB of RAM, and 1 TB of local storage. The system runs on Linux CentOS 7.7. For the simulations, the Large-scale Atomic/Molecular Massively Parallel Simulator (LAMMPS), the October 2020 version, developed by Sandia National Laboratories, was utilized.

4.5 Simulation model

The simulated materials were the 5 wt% potassium nitrate-doped magnesium hydroxide [$Mg(OH)_2/KNO_3$], designated as MH-PN5, nano alumina-enhanced doped magnesium hydroxide [$Mg(OH)_2/KNO_3/Al_2O_3$], designated as MH-PN5AO, and pure $Mg(OH)_2$ as MH. An average of 11000 atoms were randomly distributed in a 50 x 50 x 50 $Å^3$ periodic cubic cell using the PACKMOL package [173]. The periodic boundary condition (PBC) was used to minimize edge effects in the finite-sized simulation box and approximate an infinite system in real-world situations. The PBC required atoms to be placed inside a cubic simulation box that was periodically repeated in all directions. A two-dimensional illustration of PBC is shown in Figure 4.3, where the particle trajectories in the central simulation box are mirrored in every surrounding direction.

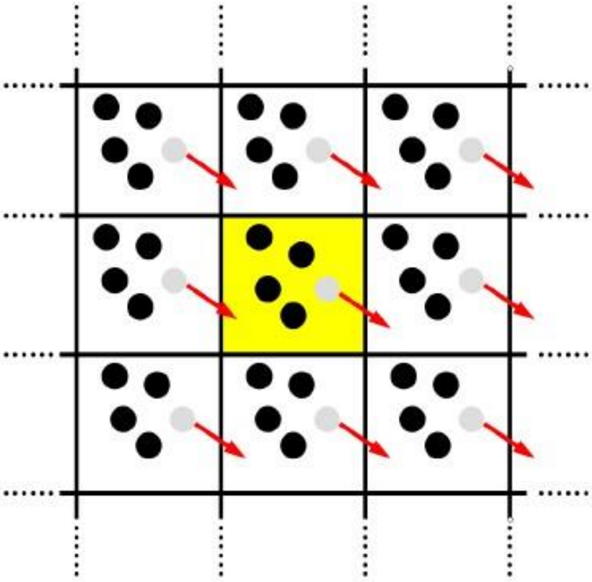

Figure 4. 3 A two-dimensional illustration of PBC.

If, during the simulation, a particle moved out of the central simulation box, an identical image of that particle entered the central box from the opposite side, creating the illusion of a continuous, infinite system (mimicking bulk materials or interfaces). Thus, PBC enabled the simulation of bulk properties in the system with relatively few atoms.

Figure 4.4 shows the schematic view of the interaction between the constitutive atoms of $Mg(OH)_2$, KNO_3, and the doped $Mg(OH)_2$ material. Similarly, Figure 4.5 represents the schematic of the interaction between the constitutive atoms of $Mg(OH)_2$, KNO_3, Al_2O_3, and the enhanced doped $Mg(OH)_2$ material. The randomly distributed initial configurations of the MH-PN5 and MH-PN5AO materials, in the simulation box with periodic boundary conditions, are shown in Figure 4.6.

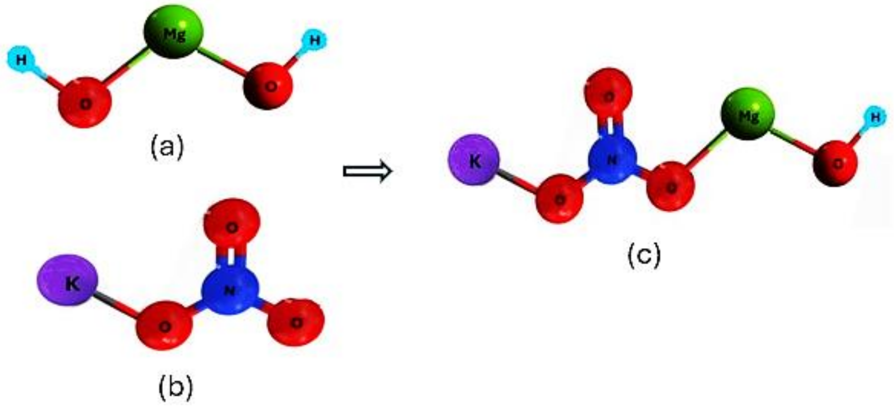

Figure 4. 4 The molecular structures of (a) $Mg(OH)_2$ (b) KNO_3, and (c) doped $Mg(OH)_2$.

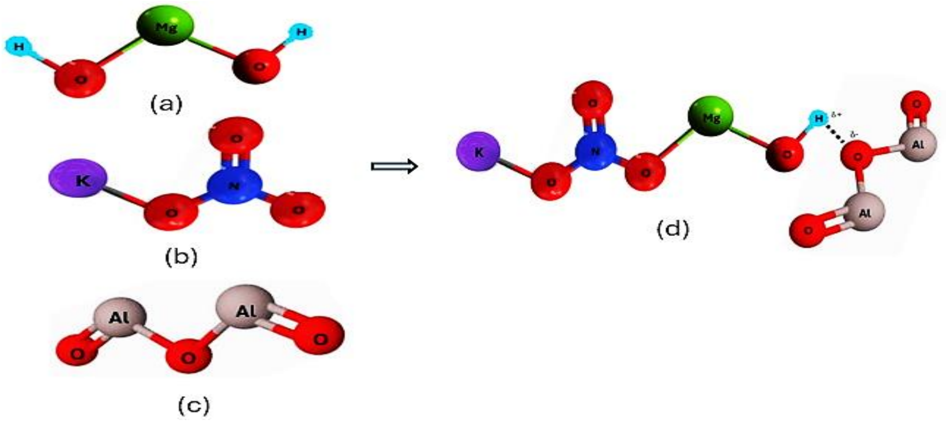

Figure 4. 5 The molecular structures of (a) $Mg(OH)_2$ (b) KNO_3, (c) Al_2O_3, and (d) the enhanced doped $Mg(OH)_2$.

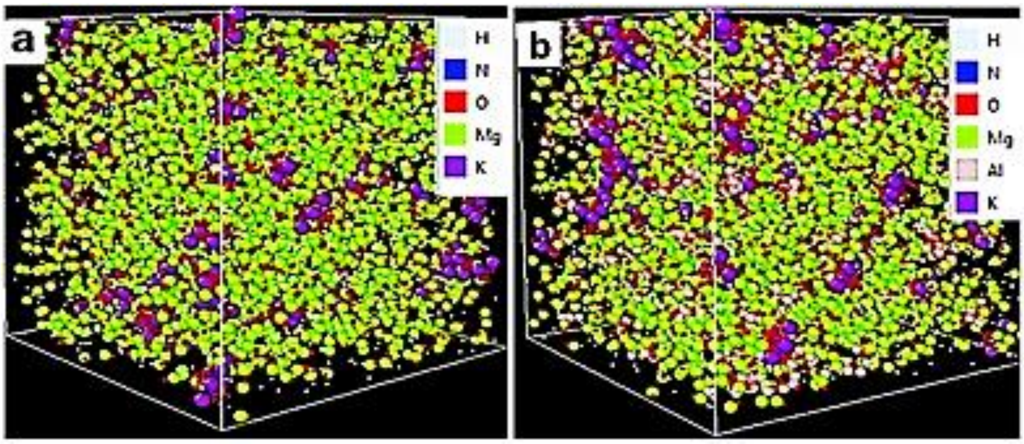

Figure 4. 6 Initial configuration of (a) MH-PN5 and (b) MH-PN5AO in cubic simulation box with PBC.

The initial configuration of MH-PN5 (Figure 4.6a) indicates the atomic distribution within the 5 wt% KNO_3-doped $Mg(OH)_2$ matrix in which green, red, and purple spheres represent Mg, O, and K atoms, respectively, while the light blue and dark blue spheres indicate H and N atoms, respectively. In the configuration of MH-PN5AO (Figure 4.6b), nano-aluminium oxide (Al_2O_3) is introduced, with Al atoms represented by grey spheres dispersed throughout the matrix. This configuration highlights the distribution and interaction sites of nano-aluminium oxide within the $Mg(OH)_2/KNO_3$ composite, which aimed to enhance its thermal conductivity. The MH-PN5 material was simulated along with a varying proportion (5, 10, 15, and 20 wt%) of Al_2O_3, designated as MH-PN5AO5, MH-PN5AO10, MH-PN5AO15, and MH-PN5AO20, respectively, to find the optimal dose of the nanomaterials in terms of thermal conductivity enhancement.

4.6 Force field

As previously seen in Section 4.3.2, interactions between atoms are approximated with a simple empirical potential energy function, which allows for calculating forces. Therefore, a force field can be defined as a combination of potential functions that account for various forces acting between particles within molecules [174]. Force fields define the rules that govern how atoms in a molecule or a collection of molecules interact with each other, dictating their movement and behaviour over time. They are composed of a set of equations and parameters that represent different types of interactions within a system, including bonded (bonds, angles, and dihedrals) and non-bonded Van der Waals and Coulombic) interactions. The force between two atoms is defined by a so-called “two-body” potential (often referred to as a “pair” potential). This proposes that the interaction is determined solely by the properties and relative positions of the two particles involved, independent of any other particles in the system.

The force on a particle can be determined from the potential, viz: $\mathrm{F} = -\nabla\Phi_{\mathrm{i}}$, where Φ_{i} is the sum of atom-atom pair potentials with all surrounding atoms: $\Phi_{\mathrm{i}} = \sum_{\mathrm{j}\neq\mathrm{i}} \Phi_{\mathrm{ij}}$.

4.6.1 Interatomic potential

All the simulations in this thesis are based on a combination of the Lennard-Jones (LJ) potential and Coulombic interactions. The LJ potential is a pair potential model that is well-accepted for explaining the behaviour of non-bonded interactions, especially the van der Waals forces, which are weak attractive forces, and the repulsive forces that prevent atoms or molecules from overlapping. The LJ potential is given as

$$\Phi_{\mathrm{LJ}} = 4\epsilon\left[\left(\frac{\sigma}{r}\right)^{12} - \left(\frac{\sigma}{r}\right)^{6}\right] \tag{4.12}$$

where Φ_{LJ} is the potential energy as a function of distance r between two atoms, ϵ is the depth of the potential well, and σ is the finite distance at which the inter-particle potential is zero. The first term of Equation (4.12) represents the short-range repulsive force, and the second describes the attraction. The ϵ and σ parameters have values specific to each atom species and are relevant to pairwise interactions between atoms of the same kind. However, the Lorentz-Berthelot rules estimate the cross-term interactions between unlike species viz

$$\epsilon_{ij} = \sqrt{\epsilon_i \epsilon_j} \tag{4.13}$$

$$\sigma_{ij} = \frac{1}{2}\left(\sigma_i + \sigma_j\right) \tag{4.14}$$

The form of LJ potential in LAMMPS uses a cutoff radius r_c such that $r \leq r_c$ to limit the computational and simulation time so that $\Phi_{\mathrm{LJ}} = 0$ if $r > r_c$. It is therefore required to provide these LJ parameters ϵ, σ, and r_c as arguments for the potential function in LAMMPS.

For the Coulombic interactions, the potential function is given as

$$\Phi_{\mathrm{Coul}} = \frac{1}{4\pi\epsilon_0}\frac{q_i q_j}{r} \tag{4.15}$$

with q_i, q_j being the charges on atoms of types i and j respectively, and ϵ_0 is the dielectric constant. Since r varies inversely, it means that the potential does not approach zero quickly enough as the distance increases. This implies that particles far apart can have much influence on the interaction, so r_c would have to be very large to prevent large errors. This would be computationally prohibitive in periodic boundary conditions. However, a solution to this problem was to make use of the Particle-Particle Particle-Mesh (PPPM) method to ensure that the long-range interactions are properly accounted for.

4.6.2 Simulation input parameters

The force field parameters in this study were taken from existing literature [175–177]. The complete set of input parameters for the particles is as follows:

Table 4. 1 Lenard-Jones parameters and partial charges for atom pairs.

Material	Atomic pair	ε (eV)	σ (Å)	Charge
$Mg(OH)_2$	Mg-Mg	2.2533199	1.501	+2
	O-O	0.0050208	3.369	-2
	H-H	0.0008673	1.780	+1
KNO_3	K-K	0.0043364	3.188	+1
	N-N	0.0073719	3.107	+0.95
	O-O	0.0069383	3.009	- 0.65
Al_2O_3	Al-Al	0.0017346	4.053	+1.5
	O-O	0.0098870	2.860	- 1.0

Additional input parameters used include a timestep of 0.001 ps, a cutoff radius (r_c) of 11.0 Å, a thermostat damping time of 0.1 ps, and a barostat damping time of 1 ps. For the thermostat and barostat damping times, these values are generally good starting points for maintaining temperature and pressure control during simulations, as recommended in the LAMMPS documentation [172] for many models.

4.7 Annealing, minimization, and equilibration

To ensure the loss of memory of the initial configuration and achieve a more realistic and stable one, the first step involves optimizing the configurations through a series of temperature changes. Initially, the system was slowly heated at 2.65 x 10^{-1} K/ps from 293 K to 823 K over 2 x 10^{6} steps, then cooled back to 293 K under the same conditions. The simulation was performed in the isothermal-isobaric (NPT) ensemble using a Nosé-Hoover thermostat with a timestep of 1 fs.

Subsequently, an energy minimization process was conducted to redistribute the atoms, aiming for a configuration with minimal energy. These iterative procedures were crucial for resetting the system's initial configuration and resolving any potential atom overlaps. This process was essential to stabilize the randomly placed atoms in the system, thus resolving unrealistic atom interactions or high-energy configurations that would otherwise distort the results of subsequent simulations. The '*minimize'* command was set with the following stopping criteria:

- stopping tolerance for energy = 1.0e-6.
- stopping tolerance for force = 1.0e-10.
- maximum iterations for minimizer = 10000.
- maximum number of force/energy evaluations = 100000.

LAMMPS therefore performed an energy minimization of the system by iteratively adjusting atom coordinates until the iterations were terminated when one of the stopping criteria was satisfied. At that point, the configuration was assumed to be in a local potential energy minimum with the temperature near absolute zero Kelvin. Essentially, the objective function minimized was the total potential energy (Φ) of the system as a function of N atom coordinates [172]:

$$\Phi(\mathrm{r}_{1,}\mathrm{r}_{2,} \dots, \mathrm{r}_{\mathrm{N}}) = \sum\nolimits_{\mathrm{i,j}} \Phi_{\mathrm{pair}}(\mathrm{r}_{\mathrm{i}}, \mathrm{r}_{\mathrm{j}}) + \cdots + \sum\nolimits_{\mathrm{i}} \Phi_{\mathrm{fix}}(\mathrm{r}_{\mathrm{i}}) \qquad (4.16)$$

where the first term on the right is the pairwise interactions and the last term is energy due to the 'fixed' constraint, such as boundary conditions or interactions of particles with the wall. So, the system was relaxed to a local minimum energy state, which represented a more physically realistic configuration, before the equilibration run was started. `

Following this, the system underwent an NPT equilibration run at 293 K and 1 atm during 1000 ps to allow the system to relax to the target temperature and pressure. This ensured that the systems' densities and internal energies stabilized around values consistent with the desired ensemble conditions. At equilibrium, a system's thermodynamic potential reaches a minimum, indicating a balanced state of energy and interactions within the system. To check for equilibration in all the configurations, the energy was plotted against time (or run steps), using the open-source software, Gnuplot, to observe when the energy becomes largely stable after fluctuating around stable mean values, as shown in Figure 4.7. The energy stabilization around –250000 eV signifies that the system's atoms settled into a low-energy configuration, where their interactions were balanced. This value indicates the cumulative potential energy of all interactions within the system (including van der Waals forces and electrostatic interactions). Furthermore, the temperature and volume profiles (in Figure 4.7b,c) also show stability over 1000000 timesteps, confirming that the system was adequately equilibrated before proceeding with further simulations.

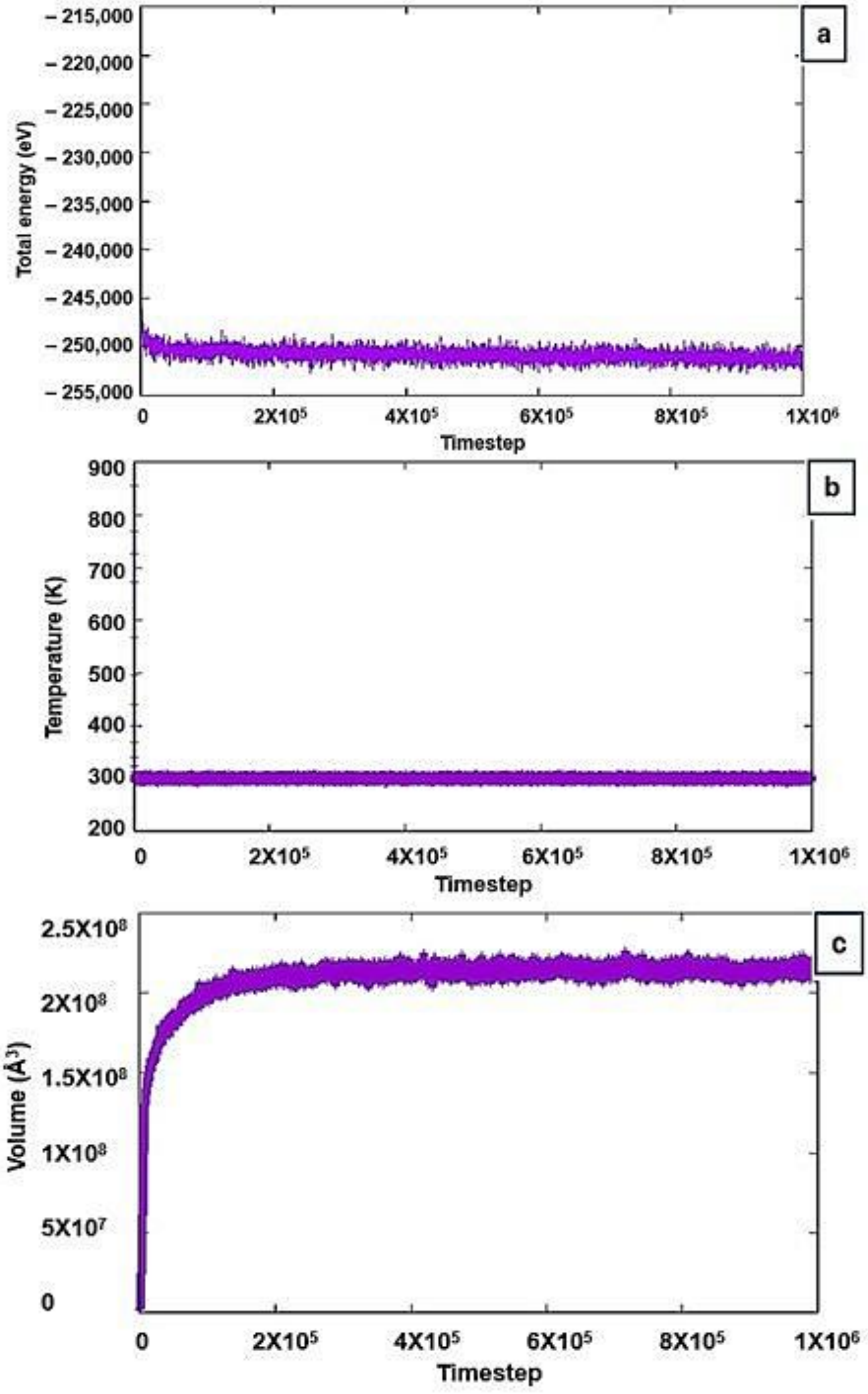

Figure 4. 7 Stable equilibrium profiles for (a) total energy, (b) temperature, and (c) volume.

Following equilibration, the optimized configurations of the simulated materials are obtained, as shown in Figure 4.8. In Figure 4.8(a), the configuration of MH-PN5 (5 wt% KNO_3-doped $Mg(OH)_2$) is shown. The atoms are distributed uniformly throughout the cubic cell, reflecting a stable and homogeneous mixture. Similarly, Figure 4.8(b) displays the optimized configuration of MH-PN5AO ($Mg(OH)_2/KNO_3$ with the addition of nano-Al_2O_3), also showing atoms well-dispersed within the matrix, indicating good mixing and interaction with the base material. The densities of MH-PN5 and MH-PN5AO were obtained as an average over the entire simulation time.

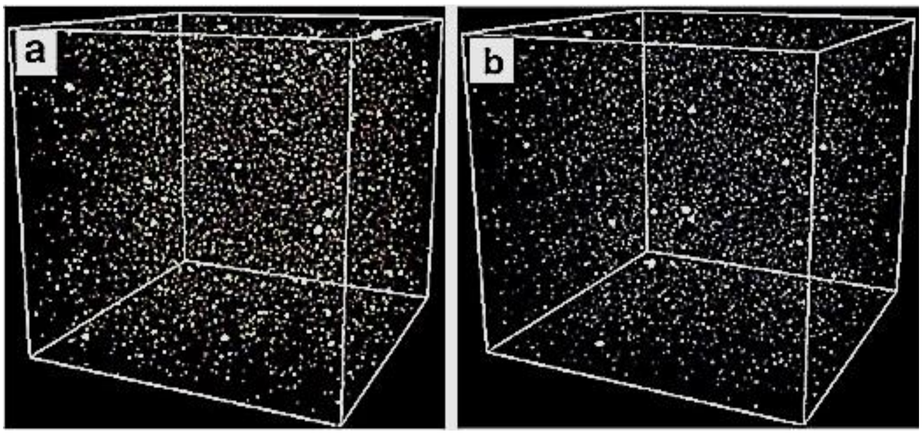

Figure 4. 8 The optimized configuration of (a) MH-PN5 and (b) MH-PNAO.

4.8 Calculation of desired quantities

4.8.1 Calculation of thermal conductivity

4.8.1.1 EMD method

Equilibrium Molecular Dynamics (EMD), employing the Green-Kubo (G-K) method, was used to determine the optimal dose of nanomaterials added to the doped material. The G-K method given in Equation (4.17) was used to calculate the thermal conductivity κ directly from the ensemble-averaged autocorrelation of the spontaneous heat flux J_X that occurred during the simulation.

$$\kappa = \frac{1}{K_B T^2 V} \int_0^\infty \langle J_X(t) J_X(0) \rangle \, dt \tag{4.17}$$

where V is the system volume, T is the temperature, K_B is the Boltzmann constant, and $\langle J_X(t) J_X(0) \rangle$ indicates the ensemble average. Thermal conductivity in the G-K method is related to the elapsed time, which dissipates the fluctuations [178]. The EMD simulation was performed following the method described in Alexander et al. [179]. A small NVT equilibration run was performed for 100 ps with the help of a Nosé–Hoover thermostat to relax the system before calculating the thermal conductivity. An NVE simulation was then performed to thermalize the system by allowing the evolution of phonons. By removing the thermostat and barostat, atomic motions were freed from artificial rescaling, enabling a more realistic equilibration before thermal conductivity computation.

4.8.1.2 NEMD method

The Non-Equilibrium Molecular Dynamics (NEMD) method was then employed to estimate the thermal conductivity of the material sample with the optimal nanomaterial dose obtained from Section 4.8.1.1. The NEMD method is a steady-state approach based on Fourier's law. Thermal conductivity κ was calculated from the steady-state heat flux J_X through the material and the resulting temperature gradient ${}^{\partial T}/_{\partial x}$, expressed as [180]:

$$\kappa = -\frac{J_X}{{}^{\partial T}/_{\partial x}} \tag{4.18}$$

The NEMD method was now employed because of its analogy with the transient hot wire (THW) method used in this study for the experimental thermal conductivity measurements. Specifically, the fundamental principle in both methods is Fourier's law, used to relate the thermal conductivity to the observed heat transfer characteristics [180,181].

At first, the system was simulated during the NVT ensemble for 10 ps to thermalize. Next, the simulation cell was divided into three distinct regions to establish a thermal gradient: a central region and two boundary regions. The boundary regions were maintained at different temperatures using Langevin thermostats, creating a heat flux from the hot region to the cold region, as summarized in the schematic of Figure 4.9. The NVE ensemble was utilized for 50 ps in the central region, whilst heat was added to the hot region and removed from the cold region, facilitating a continuous heat flow through the system.

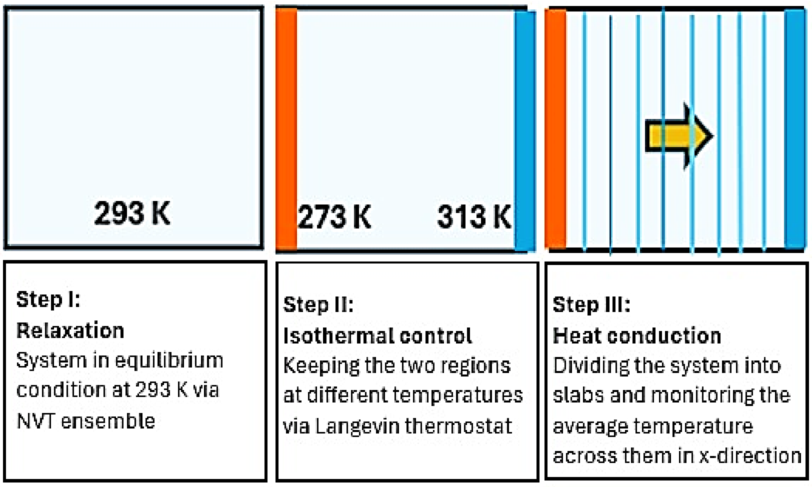

Figure 4. 9 The three steps involved in the NEMD simulation of thermal conductivity at 293 K using the two-region method.

Once the system reached a non-equilibrium steady state, the steady-state heat flux and the resulting temperature gradient were derived, and the thermal conductivity was determined based on Fourier's law. The heat flux was calculated from the rate of heat exchange between the hot and cold regions. This was done by extracting the data from the output file for both regions and plotting on the same axes, as demonstrated in the work of Winczewski and Muna [182]. The average of the two slope values (absolute) of the curves gave the heat flux. A linear fit was performed on the temperature profile along the direction of heat flow within the central region to obtain the temperature gradient. This direct calculation method allowed for the estimation of the thermal conductivity of the materials.

4.8.2 Calculation of radial distribution function

The radial distribution function (RDF), $g(r)$, measures the likelihood of finding a particle at a distance r from a reference particle in a system. RDF is determined by calculating the distance between all particle pairs (Figure 4.10) and binning them into a histogram [183]. The histogram is then normalized with respect to the bulk density of the particles.

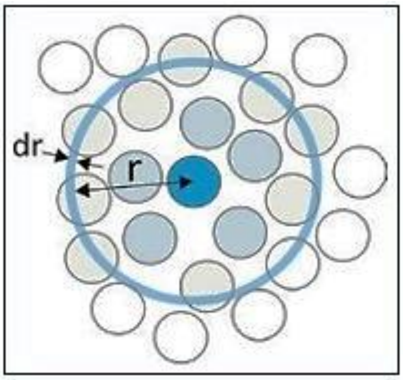

Figure 4. 10 Calculation of the radial distribution function in an atomic system.

In LAMMPS, RDF was calculated by invoking the '*compute rdf*' command in combination with others to compute the RDF, using an algorithm defined by

$$\boldsymbol{g}(\boldsymbol{r}) = \frac{\mathrm{V}}{\mathrm{N}} \frac{\langle n_{ij}(\mathrm{r}) \rangle}{4\pi \mathrm{r}^2 \, \Delta \mathrm{r}} \tag{4.19}$$

where V is the volume of the simulation box, N is the total number of particles in the system, $\langle n_{ij}(\mathrm{r}) \rangle$ is the average number of particles j in a spherical shell of radius r and thickness $\Delta\mathrm{r}$ centred on particle i [184] This function is a scaled histogram of every interatomic distance and is implemented by dividing the space around each particle into spherical shells of thickness $\Delta\mathrm{r}$. So, the algorithm was implemented to calculate the number of particles located within a distance r from a reference particle at each bin.

In summary, the RDF was calculated using the *compute rdf* command, which internally follows the above formula in Equation (4.19), and the steps are outlined in Figure 4.11. The command divides the range of interest into specified bins. LAMMPS efficiently counted the number of particles in each shell for each bin and averaged these counts of overall reference particles and simulation timesteps. The output includes the distance r and the corresponding g(r) values for each bin, giving a detailed view of how particle density varies radially.

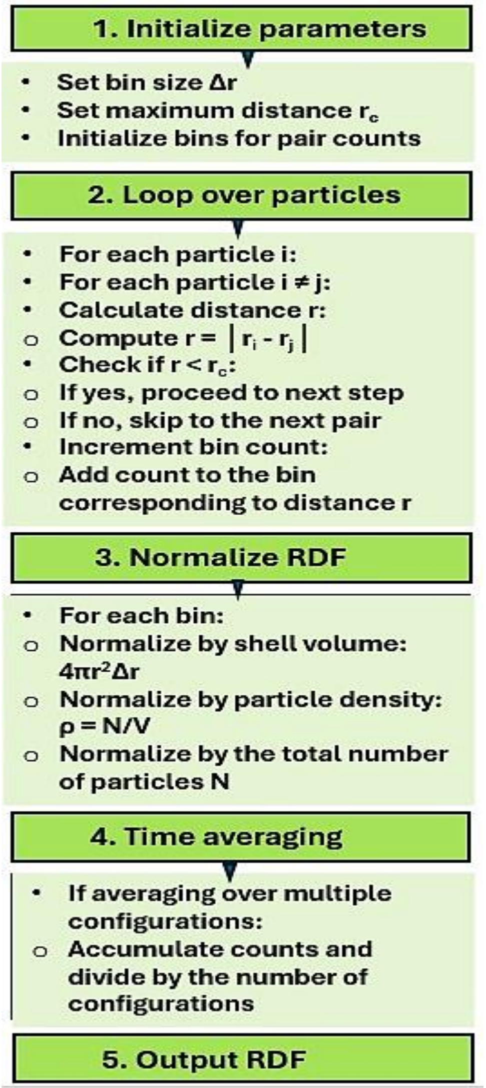

1. Initialize parameters

- Set bin size Δr
- Set maximum distance r_c
- Initialize bins for pair counts

2. Loop over particles

- For each particle i:
- For each particle i ≠ j:
- Calculate distance r:
  - Compute $r = |r_i - r_j|$
- Check if $r < r_c$:
  - If yes, proceed to next step
  - If no, skip to the next pair
- Increment bin count:
  - Add count to the bin corresponding to distance r

3. Normalize RDF

- For each bin:
  - Normalize by shell volume: $4\pi r^2 \Delta r$
  - Normalize by particle density: $\rho = N/V$
  - Normalize by the total number of particles N

4. Time averaging

- If averaging over multiple configurations:
  - Accumulate counts and divide by the number of configurations

5. Output RDF

Figure 4. 11 The algorithm used in calculating RDF.

4.9 Results and discussion

4.9.1 Simulation results for thermal conductivity

4.9.1.1 Optimal proportion of nanomaterials addition

The EMD method (Equation 4.17) was used to obtain these results. Here, the autocorrelation function of the heat flux, $\langle J_x(t) J_x(0) \rangle$, was shown to describe how the heat flux at time t is related to the heat flux at time t = 0. Figure 4.12 shows the graphical profiles of the autocorrelation function over time for the simulated materials. Similar curves were obtained by Schelling et al. [185].

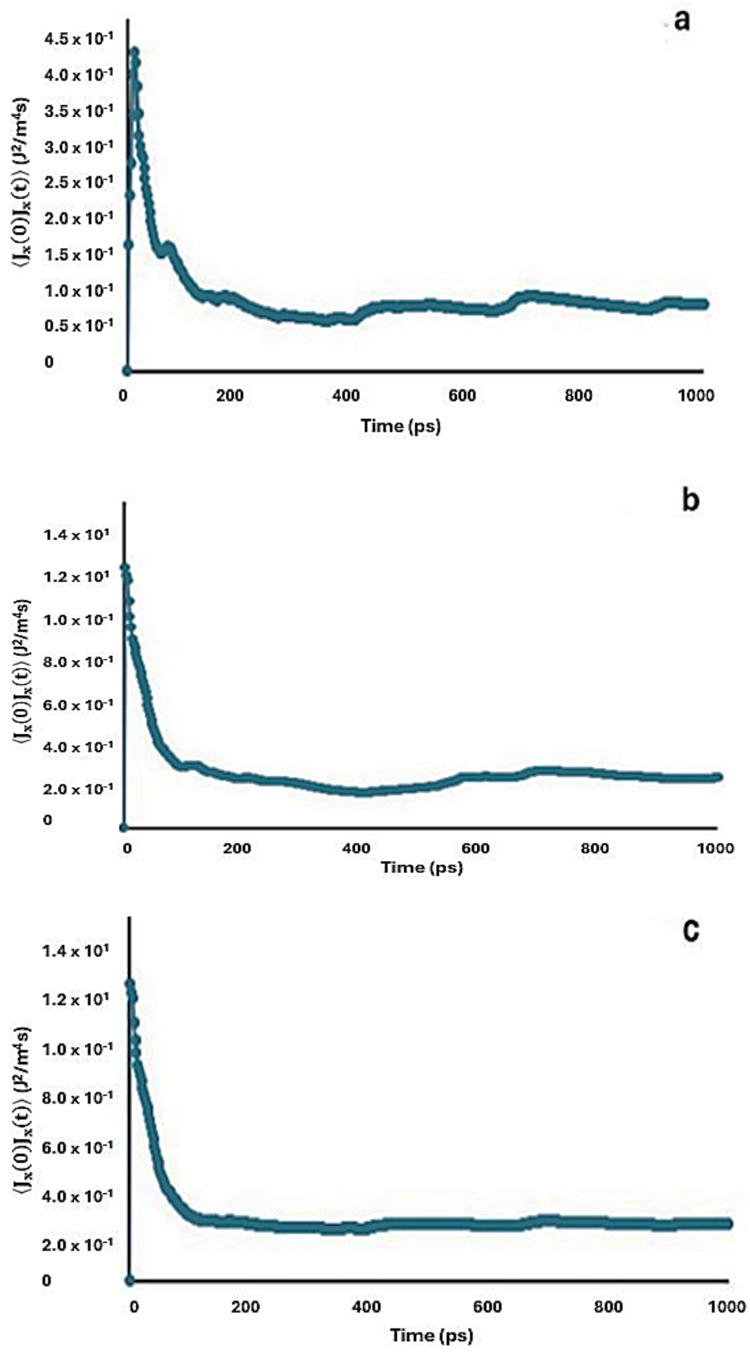

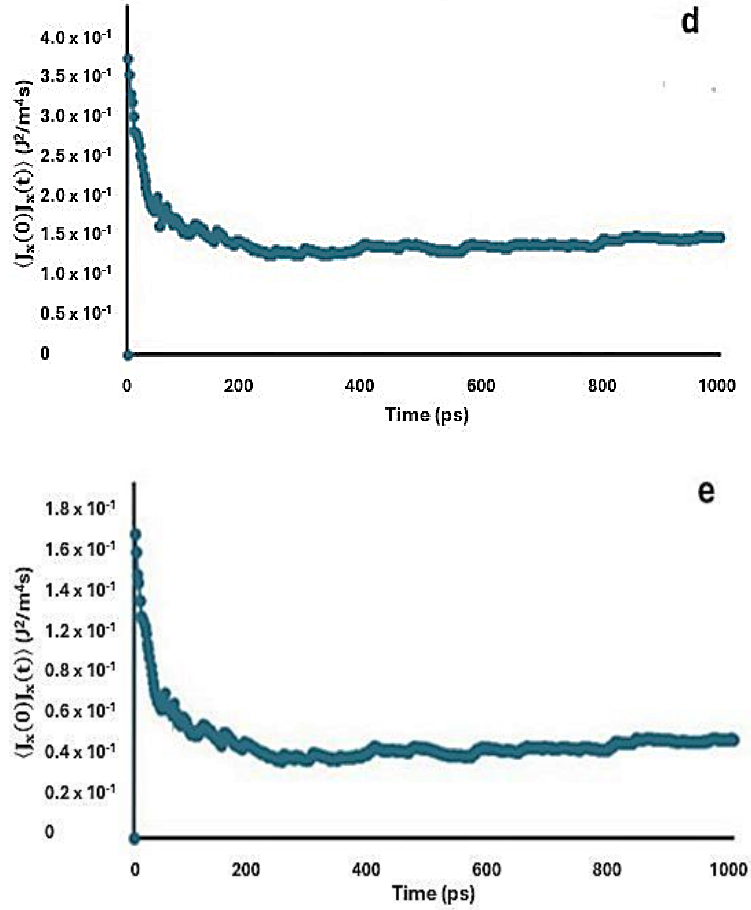

Figure 4. 12 Profiles of the autocorrelation function over time for (a) MH-PN5, (b) MH-PN5AO5, (c) MH-PN5AO10, (d) MH-PN5AO15, and (e) MH-PN5AO20.

As shown in Figure 4.12, the autocorrelation function typically reaches a maximum value at t = 0 and then decays over time. Thus, the function approximates an exponential decay model; $\langle J_X(t)J_X(0)\rangle \sim e^{-t/\tau,}$ where τ is the correlation time [185]. The thermal conductivity was calculated as the integral of the function over time. That is, the area under the curve corresponds to the value of κ. The initial value and the shape of the curve determined how quickly the thermal conductivity integral converged. In Figure 4.12(a), the function decayed from a value of 0.437 to 0.0709 J^2/m^4s with a calculated decay constant of 1.82 s^{-1}. Thus, the decay constant measured the rate of decrease of the autocorrelation function over time. Similarly, the functions in Figure 4.12 b, c, d, and e decayed from 1.22 to 0.171, 1.26 to 0.221, 0.372 to 0.127, and 0.165 to 0.042 J^2/m^4s, respectively, with decay constants 1.96 s^{-1}, 1.74 s^{-1}, 1.07 s^{-1}, and 1.37 s^{-1}. The higher the decay constant, the faster the decay rate of the autocorrelation function. Conversely, if the decay constant is small, the decay rate of the autocorrelation function is slow. This has implications for the interpretation of the results.

It was, however, noted that the autocorrelation functions in Figure 4.12 did not approach zero at large t. This behaviour is commonly attributed to either inadequate equilibration or the presence of background noise in simulations of finite duration. Given that the system had already been demonstrated to be well equilibrated, the observed behaviour was likely a result of background noise. To correct for this, the background noise was estimated by averaging the autocorrelation function over a time range where no significant decay was observed. This average value was subsequently subtracted from the computed thermal conductivity.

The results of the thermal conductivities of the MH-PN5 and the various proportions of Al_2O_3-added materials obtained by EMD simulations are presented in Figure 4.13.

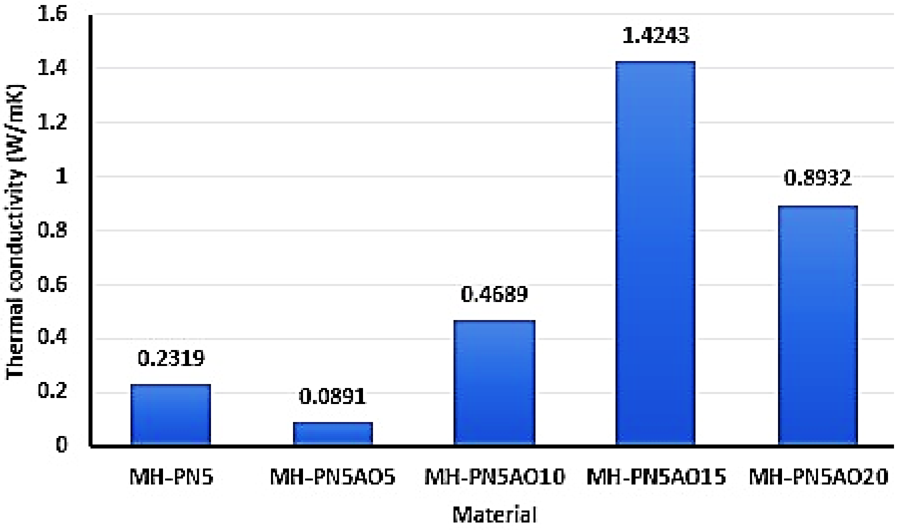

Figure 4. 13 Thermal conductivity of the doped and the enhanced doped samples.

As seen in Figure 4.13, increasing the Al_2O_3 ratio in MH-PN5 results in variation in the thermal conductivities of the samples. This agrees with the proposition of Coetzee et al. [159] that adding nanoparticles to a material could increase or decrease its thermal conductivity with respect to the dosage. The thermal conductivity of the doped material with 15 wt% Al_2O_3 addition (that is, MH-PN5AO15) showed the highest thermal conductivity value of 1.4243 W/mK compared with 0.0891, 0.4689, 0.8932, and 0.2319 W/mK for MH-PN5AO5, MH-PN5AO10, MH-PN5AO20, and MH-PN5, respectively. In the context of the Green-Kubo theory, the autocorrelation function $\langle J_x(t)J_x(0)\rangle$ decayed more slowly in the MH-PN5AO15 sample, as previously seen in the lowest decay constant value of 1.07 s^{-1}, meaning that heat flux fluctuations persisted longer. This indicates that the material has more efficient energy transfer mechanisms, allowing heat flux to remain correlated over longer times, thus facilitating better heat conduction.

4.9.1.2 Results for enhanced doped material

The NEMD results for comparison of thermal conductivity of samples MH (pure magnesium hydroxide), MH-PN5, and MH-PN5AO15 were determined as follows. For the pure MH, the plot to obtain the heat flux is shown in Figure 4.14a. The heat flux value was calculated as the average of the absolute values of the slopes (of the fitted lines), representing the heat extracted from the hot (pink) and the heat added to the cold (blue) regions. This gives a value of 0.2454. On the other hand, Figure 4.14b represents the temperature gradient as a plot of the temperature averaged over all the chunks of the simulation box, across the direction of heat transmission. Here, the value is 3.8755, the absolute value of the slope of the fitted line. Using Equation (4.18), the thermal conductivity was calculated to be 0.0633 W/mK. To evaluate the variability around the target temperature (293 K), a standard error of 1.8741 was obtained for Figure 4.14b (See Appendix A.1b). The small standard error indicates that the data points were fairly representative of the true mean temperature. It can be seen that more data points cluster closer to the line than away.

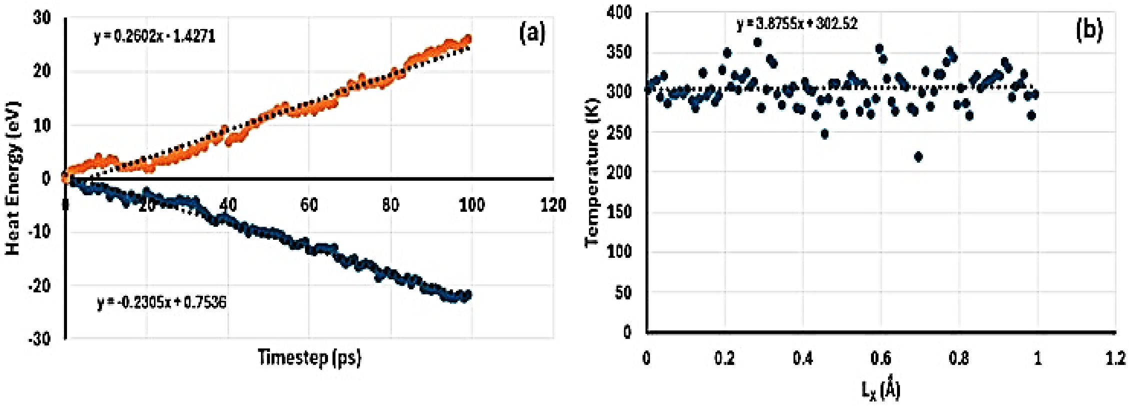

Figure 4. 14 A plot of (a) heat energy against timestep to derive heat flux, (b) temperature against coordinate to derive temperature gradient for MH material.

Similarly, the plots for deriving the heat flux and temperature gradient for the doped material (MH-PN5) are shown in Figure 4.15. For the heat flux value, the average of the absolute values of the slopes of the fitted lines in Figure 4.15a gives 0.6051, whereas the coefficient for the temperature gradient curve in Figure 4.15b gives 10.9950. Therefore, using Equation (4.18) resulted in a thermal conductivity of 0.0550 W/mK. A standard error value of 1.7286 was obtained for the scatter plot in Figure 4.15b (See Appendix A.2b), indicating a small degree of variability in the data points. It can be observed that the thermal conductivity of the doped material (MH-PN5) is slightly lower than that of the pure magnesium hydroxide material (MH) by 0.0083 W/mK.

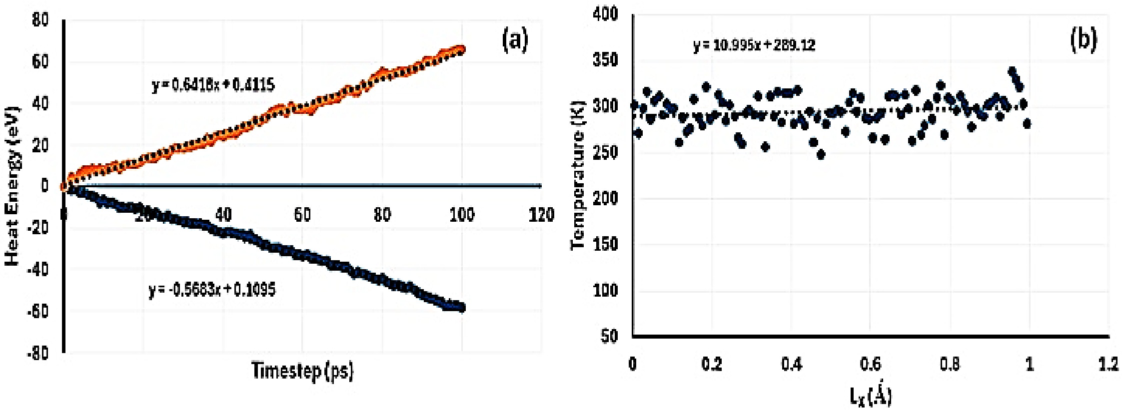

Figure 4. 15 A plot of (a) heat energy against timestep to derive heat flux, (b) temperature against coordinate to derive temperature gradient for MH-PN5 material.

For the enhanced material (MH-PN5AO15), the heat flux and temperature gradient are deduced from Figure 4.16(a) and (b), respectively, wherein the thermal conductivity is calculated as 0.7084 W/mK. In this case, a standard error value of 2.0479 was obtained for Figure 4.16b (See Appendix A.3b), showing a small variability in the data distribution around the line. Therefore, by comparison, the theoretical thermal conductivity of MH-PN5AO15 was 0.6534 W/mK higher than MH-PN5 material. This showed that the addition of Al_2O_3 nanomaterials had the potential to enhance the thermal conductivity of the doped material.

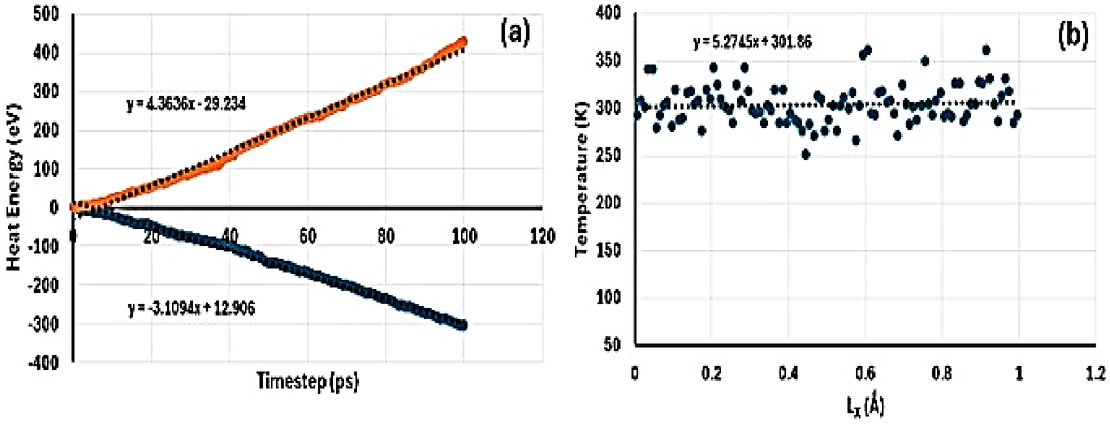

Figure 4. 16 A plot of (a) heat energy against timestep to derive heat flux, (b) temperature against coordinate to derive temperature gradient for MH-PN5AO15 material.

4.9.2 Simulation results for RDF

The radial distribution functions (RDFs) of MH-PN5 and MH-PN5AO15 were analyzed to investigate the structural characteristics of each material. Figure 4.17 shows the RDF curves of the materials.

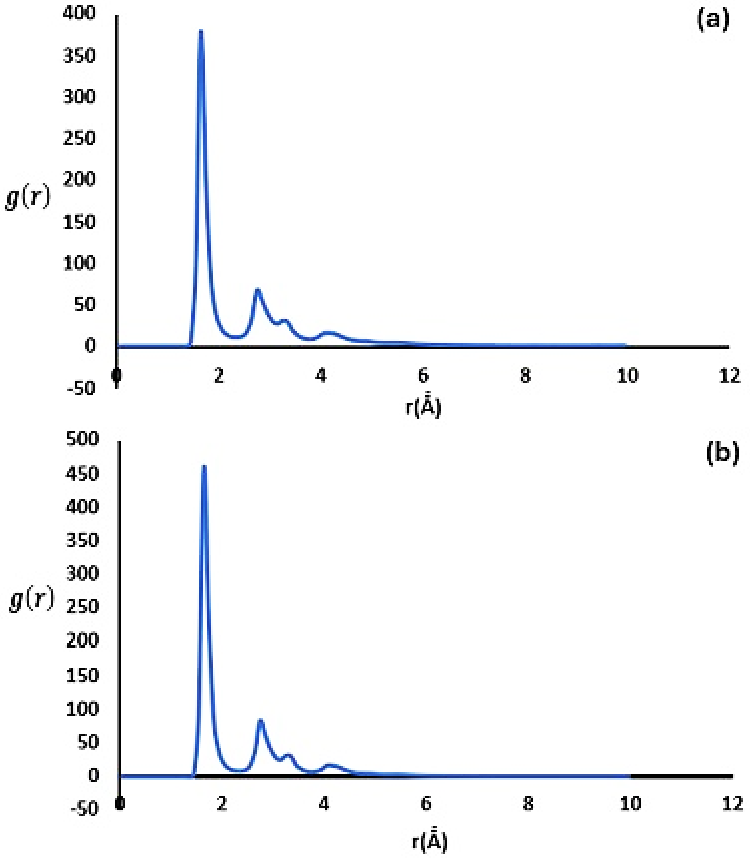

Figure 4. 17 RDF of (a) MH-PN5 and (b) MH-PN5AO15 materials.

The RDFs revealed the distribution of Mg atoms over a range of interatomic distances, providing insights into the local and medium-range ordering in these systems. For MH-PN5, the first peak in the Mg–Mg RDF appeared at r = 1.65 Å with a peak height g(r) = 378. This peak corresponds to the nearest-neighbour Mg–Mg distance, indicating a strong short-range correlation between magnesium atoms. A second, smaller peak was observed at r = 2.75 Å, with g(r) = 67, followed by a small shoulder at r = 3.35 Å. Additionally, a diminished peak was observed at r = 4.25 Å, suggesting weaker structural correlations at larger distances. A well-defined minimum appeared between the first and second peaks at r = 2.35 Å, separating the first and second coordination shells of Mg atoms.

In the case of MH-PN5AO15, a similar trend was observed, with the first peak also appearing at r = 1.65 Å, but with a significantly higher intensity of g(r) = 458. This increased peak height indicated a denser local Mg–Mg packing in MH-PN5AO15 compared to MH-PN5. The second peak, located at r = 2.75 Ǻ, exhibited a slightly larger g(r) = 83, again pointing to enhanced medium-range order in MH-PN5AO15. A small shoulder was noted at r = 3.35 Ǻ, similar to that in MH-PN5, and the diminished peak was shifted slightly to r = 4.15 Ǻ. The first minimum also appeared at r = 2.35 Ǻ, indicating a comparable separation between coordination shells in both materials.

It is important to observe that the position of the first peak signified the average nearest-neighbour distance, which could help in identifying interatomic or intermolecular bond lengths. In both MH-PN5 and MH-PN5AO15, this distance was 1.65 Ǻ, which is very close to 1.7670 Ǻ, the Mg–Mg interatomic distance in $Mg(OH)_2$ [186]. This implied that the structure of the core material was not adversely altered by doping processes.

These results suggested that, while the overall Mg–Mg structural framework was similar in both materials, MH-PN5AO15 exhibited a more pronounced short- and medium-range order. The higher RDF values in MH-PN5AO15 at both the first and second peaks indicated a more densely packed local structure compared to MH-PN5. This could be attributed to the additional nanomaterials in MH-PN5AO15, which likely influenced the packing and overall atomic arrangement of the material, thereby promoting a more stable and thermally conductive framework.

4.10 Concluding remarks

The thermophysical properties of doped and enhanced-doped $Mg(OH)_2$ were systematically investigated using molecular dynamics (MD) simulations. The simulation results revealed that doping with 5 wt% KNO_3 led to a slight reduction in the thermal conductivity of $Mg(OH)_2$, indicating a potential disruption in heat transport pathways. However, the enhanced-doped configuration (MH-PN5AO15) demonstrated a recovery and improvement in thermal conductivity, suggesting that the additional 15 wt% Al_2O_3 nanomaterials counteract the negative thermal effects introduced by doping alone.

Radial distribution function (RDF) analysis provided further insight into the structural changes resulting from doping. Both the doped and enhanced-doped systems exhibited prominent peaks at 1.65 Å, closely matching the known Mg–Mg interatomic distance in pristine $Mg(OH)_2$, which is approximately 1.7670 Å. This minor shift indicates subtle structural rearrangements due to doping, without significant disruption of the material's lattice integrity.

Overall, the MD simulations offer valuable predictive insight into the thermal and structural behaviour of the modified $Mg(OH)_2$ system. The findings highlight the potential of doping procedures to tailor thermal properties, making them promising candidates for target-temperature heat storage applications.

Chapter 5: Experimental Thermal Enhancement of the Developed Material

5.1 Introduction

This chapter details the experimental approach undertaken to enhance the thermal performance of the developed material. Guided by the predictions and insights gained from earlier theoretical modelling, the experimental phase serves to implement the predicted optimization parameters for thermal enhancement, while also serving to validate the computational model. A series of controlled laboratory tests was conducted with a focus on thermal conductivity measurement. The chapter outlines the experimental setup and procedures, followed by a presentation and discussion of the observed results. Emphasis is placed on the correlation between the theoretical and experimental outcomes, highlighting both consistencies and deviations.

5.2 Development of enhanced doped material

The enhanced doped material was developed by incorporating the optimal proportion of Al_2O_3 nanomaterials estimated in the EMD simulation (Section 4.8.1.1) into the $Mg(OH)_2/KNO_3$ material. The experimental procedure used was similar to that previously described in Section 3.2.2 for the development of KNO_3-doped composites. The materials used included 95.0% pure magnesium hydroxide ($Mg(OH)_2$), 99.0% potassium nitrate (KNO_3), and nano-sized aluminium oxide (Al_2O_3), all sourced from Sigma-Aldrich (Gillingham, UK). To prepare the enhanced doped $Mg(OH)_2$ composite, 5 g of KNO_3 and 15 g of Al_2O_3 were incorporated into 80 g of $Mg(OH)_2$. The powders were initially blended thoroughly in an agate mortar to achieve a homogeneous mixture, then transferred to a beaker for wet mixing with 100 mL of distilled water. The suspension was stirred continuously at moderate speed and heated to 90 ℃ for 1.5 hours. After cooling to room temperature, the mixture was dried in an oven at 120 ℃ for 12 hours to yield the enhanced doped composite. Figure 5.1 illustrates the procedural steps used in the material development.

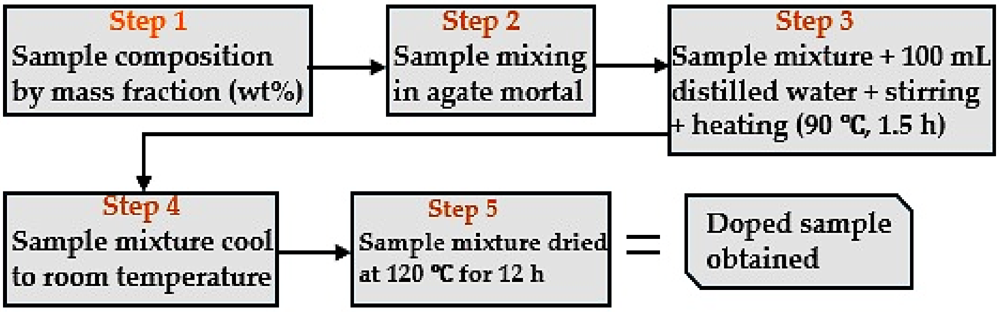

Figure 5. 1 Procedure for the development of enhanced doped material.

For ease of reference, the labels MH-PN5 and MH-PN5AO15 represent the KNO_3-doped and Al_2O_3-enhanced samples, respectively. A photograph of the samples prepared for testing is shown in Figure 5.2.

Figure 5. 2 A photo showing the doped and enhanced doped materials.

5.2.1 Powder X-ray diffraction test on enhanced doped material

The Powder X-ray Diffraction (XRD) analysis was also conducted to identify the composition of phases in the enhanced doped material. This investigation was carried out using the same instrument and procedure previously reported in Section 3.3.1.

5.2.2 Thermal conductivity measurement

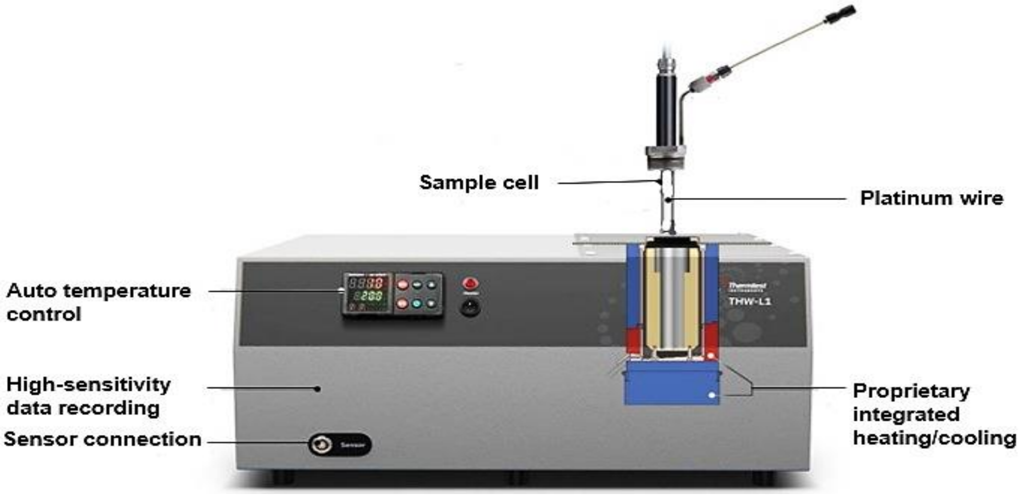

Figure 5. 3 Thermtest THW-L1 thermal conductivity meter used for the measurements.

The thermal conductivities of the samples were measured using the Thermtest transient hot wire (THW-L1) thermal conductivity meter (shown in Figure 5.3). Initially, the samples were dried in the oven at 110 ℃ for 6 hours to drive off any moisture that could affect measurements and allowed to cool to room temperature. Each sample was then filled into the instrument's sample holder, and the sensor wire (a thin platinum heating wire) was completely immersed in the sample. The sensor wire was heated (using a constant current source) to 20 ℃ as specified in the materials' datasheets for characterization. The instrument's software then calculated and displayed the thermal transfer through the samples.

To ensure the reliability of results, each sample was tested 10 times, and a standard error was determined at a 95% confidence level. The following relations were used to determine the confidence level (CL) used to estimate the accuracy range (AR) of the results, as shown in Appendix B.

Step one: The mean ($\bar{x}$) of individual data points (x_i) for the total number of points (n) was found using the formula

$$\bar{x} = \sqrt{\frac{\sum x_i}{n}} \tag{5.1}$$

Step two: The standard deviation (s) was calculated from the formula

$$s = \sqrt{\frac{\sum(x_i - \bar{x})^2}{n}} \tag{5.2}$$

Step three: The standard error (SE) was then calculated from the formula

$$SE = \frac{s}{\sqrt{n}} \tag{5.3}$$

Step four: The confidence level (CL), at 95%, was determined from the expression

$$\mathrm{CL} = (\mathrm{SE}).(\mathrm{t_{value}}) \tag{5.4}$$

Step five: The confidence interval (CI) and accuracy range (AR) were obtained from

$$\mathrm{CI} = \pm \mathrm{CL} \tag{5.5}$$

$$AR = \bar{x} \pm \mathrm{CL} \tag{5.6}$$

Measurements were taken at 20 ℃ (room temperature) and with 15 min between each of the 10 experiments. Subsequently, the percentage error between the theoretical (MD simulated) and the experimental values was determined using the formula

$$\text{Percentage Error} = \left|\frac{\text{Theoretical} - \text{Experimental}}{\text{Theoretical}}\right| \times 100 \tag{5.7}$$

5.3 Experimental results

5.3.1 XRD

The enhanced doped material was analyzed for phase identification of the composite elements using X-ray diffraction (XRD). The XRD spectra for pure $Mg(OH)_2$ (MH), doped $Mg(OH)_2$ (MH-PN5), and enhanced $Mg(OH)_2$ (MH-PN5AO15) are displayed in Figure 5.4. MH exhibited a single phase (peak), whereas the composites MH-PN5 showed two distinct peaks corresponding to $Mg(OH)_2$ and KNO_3, with MH-PN5AO15 additionally displaying a third peak for Al_2O_3. The observed planes match the standard Powder

Diffraction File (PDF) from the Inorganic Crystal Structure Database (ICSD), with references 01-074-2220 for pure $Mg(OH)_2$ brucite, 00-001-0493 for standard KNO_3, and JCPDS card No. 35-0121 for Al_2O_3.

These results demonstrated the successful incorporation of KNO_3 and Al_2O_3 into the $Mg(OH)_2$ matrix, resulting in composite materials with distinct phases. Multiple peaks in the XRD spectra indicated that the doping process did not alter the fundamental structure of $Mg(OH)_2$ but revealed additional phases corresponding to the dopants. By carefully analyzing the XRD spectra and matching the observed peaks to standard references, the study confirmed the successful synthesis of the composite materials via phase identification. This step was crucial for validating the doping the effectiveness of the doping processes and ensuring the desired material properties for further analysis.

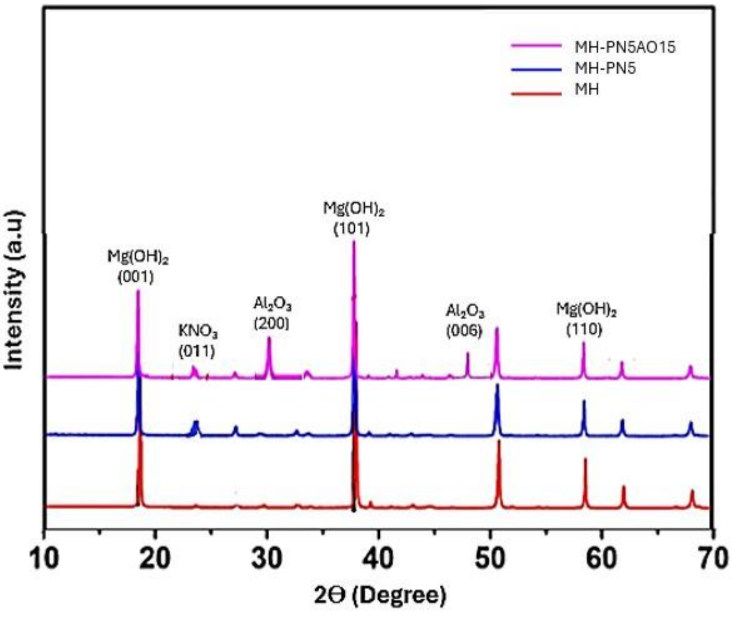

Figure 5. 4 XRD spectra of MH, MH-PN5, and MH-PN5AO15.

5.3.2 Thermal conductivity

The results of thermal conductivity measurements for the three materials are summarized in Table 5.1.

Table 5. 1 Results of experimental measurement of thermal conductivity for the materials.

Material	MH	MH-PN5	MH-PN5AO15
Mean	0.06562	0.04936	0.64841
Standard deviation	0.0008661	0.0000549	0.0099096
Standard error	0.0002739	0.0000174	0.0031337
Confidence interval	± 0.000537	± 0.000034	± 0.006142
Accuracy	0.06562±0.000537	0.04936±0.000034	0.64841±0.006142

As shown in Table 5.1, the small values of the standard error signified that the sample mean was a reliable estimate of the measurements, and the narrower confidence interval indicated a higher confidence in the measured parameters. Therefore, it is reasonable to conclude that the thermal conductivity values lie within a good accuracy range. The thermal conductivities of the materials are presented in Figure 5.5. As seen in this Figure, the thermal conductivity of the pure magnesium hydroxide material (MH) was 0.06562 W/mK. Doping MH with KNO_3 (as in MH-PN5 material) appeared to have a small impact on the thermal conductivity of the MH, as the thermal conductivity of the doped material was 0.0494 W/mK. However, incorporating nano Al_2O_3 (MH-PN5AO15) enhanced the thermal conductivity of the doped material by 0.5990 W/mK. This was likely due to the well-dispersed Al_2O_3 nanoparticles forming an efficient network within the composite matrix. This configuration could have created sufficient thermal conduction pathways, similar to what has been seen in other polymer composite studies [187].

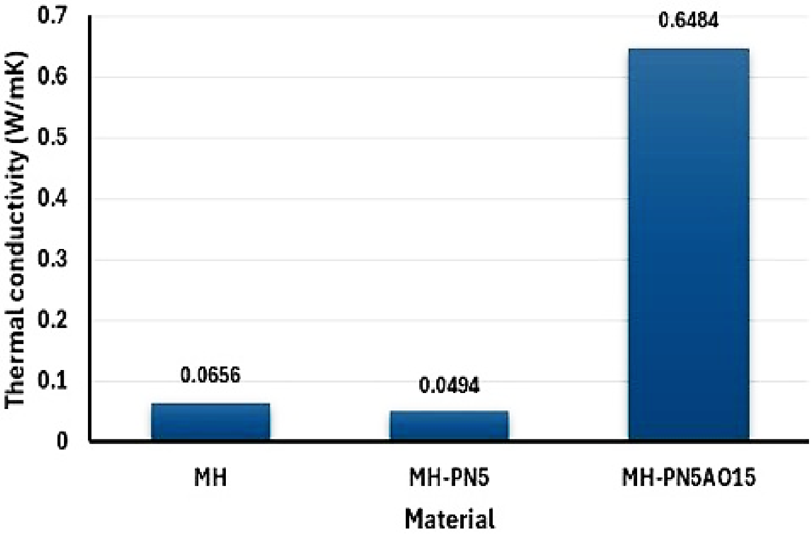

Figure 5. 5 Chart showing the experimental thermal conductivity values of the materials.

Table 5.2 shows a comparison of the theoretical and experimental results of the thermal conductivity of the materials.

Table 5. 2 Comparison of theoretical and experimental thermal conductivity results.

Material	**Theoretical (W/mK)**	**Experimental (W/mK)**	**Percentage Error (%)**
MH	0.0633	0.0656	4
MH-PN5	0.0550	0.0494	10
MH-PN5OA15	0.7084	0.6484	9

As seen in Table 5.2, the theoretical value for MH was lower than the experimental value with an error margin of 4%. The marginal discrepancy suggested that the theoretical model for this material was fairly accurate. However, for the MH-PN5 and MH-PN5AO15 materials, the theoretical values exceeded the experimental results with errors of 10% and 9%, respectively. This suggested that while the theoretical models for these materials were reasonably accurate, they still have room for refinement. The observed discrepancies could stem from various factors, including simplifications or assumptions of the theoretical model that failed to fully capture the materials' microstructural complexities and the intricate interactions among its multiple components. For example, theoretical models often rely on parameters such as force field potentials or lattice constants, which may be estimated or sourced from existing literature, potentially introducing inaccuracies. Experimental errors may have also contributed to the observed differences. Nonetheless, the theoretical results aligned well with the experimental data, indicating that the theoretical approach was generally valid but could benefit from further refinement to better account for more complex interactions.

5.4 Concluding remarks

This chapter presented an experimental investigation into the thermal enhancement of the doped $Mg(OH)_2$ material, guided by prior theoretical modelling. Doping with KNO_3 and further enhancement with Al_2O_3 nanoparticles were employed to improve thermal performance, and the resulting materials were analyzed using X-ray diffraction (XRD) and thermal conductivity measurements.

XRD analysis confirmed successful incorporation of the dopants, with additional diffraction peaks indicating the presence of KNO_3 and Al_2O_3 phases, while the core structure of $Mg(OH)_2$ was preserved. Thermal conductivity testing revealed that doping with KNO_3 slightly reduced thermal performance, whereas the addition of Al_2O_3 significantly improved it. This enhancement was attributed to the formation of efficient thermal pathways through the well-dispersed nanoparticles.

Comparison with the results of molecular dynamics (MD) simulations showed a strong alignment. While pure $Mg(OH)_2$ exhibited only a 4% error between predicted and measured thermal conductivity, the doped and enhanced materials showed discrepancies of 10% and 9%, respectively. These differences likely stem from simplifications in the simulation model and/or experimental limitations, yet the overall agreement confirms the value of MD as a strong predictive tool.

The combination of theoretical modelling and experimentation provides a solid basis for the development of thermally efficient composite for heat storage applications.

Chapter 6: Numerical Evaluation of the Developed Material in a Model Agitated Fluidized Bed Reactor

6.1 Introduction

In this chapter, a numerical modelling approach is used to evaluate the performance of the developed $Mg(OH)_2$ material, that is, the enhanced-doped material, in a model agitated fluidized bed reactor. The primary focus is on using numerical evaluation to derive key operating parameters, the MFV and the heat and mass transfer conditions. Aspen Plus, a robust process simulation software, is employed to develop and simulate the model. By using Aspen Plus, complex physical and chemical processes within the reactor can be represented, enabling a detailed investigation of the reactor's behaviour under various operating conditions.

6.2 Overview of the model agitated fluidized bed reactor

The model fluidized bed reactor is a cylindrical vessel measuring 100 mm in diameter and 500 mm in height, as shown in Figure 6.1.

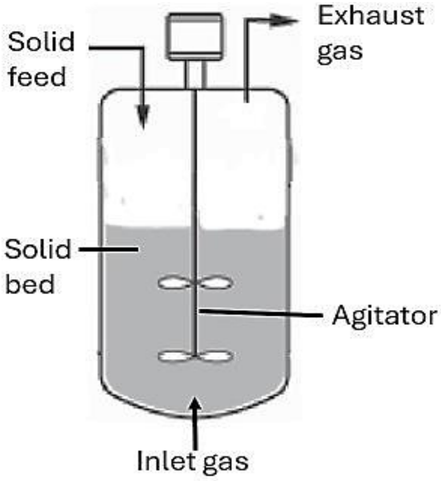

Figure 6. 1 Schematic of the model agitated fluidized bed reactor.

A fluidized bed reactor rig is constructed for experimental purposes, with a designed thermal output of up to 5 kW. To achieve this power output, the reactor is expected to operate for approximately 606 seconds, using 1.5 kg of MgO to discharge heat at the specified rate. Accordingly, the geometry and material mass used in this numerical model were based on those of the experimental rig, ensuring consistency between the simulation and the physical setup.

Gas enters the reactor after being preheated by a heater. The reactor contains 1.5 kg of thermochemical material, occupying one-third of the vessel's height. A stirrer is mounted within the bed to agitate both the particles and the gas, enhancing heat and mass transfer via enhanced particulate interactions. This agitation improves dehydration efficiency during charging by exposing more particles to the hot drying gas, and promotes better reactant interaction during discharging. Heat generated by exothermic reactions within the bed is removed via a coupled heat exchanger. The reactor's exhaust, comprising fluidizing gas, water vapour, and entrained bed particles, exits through an exhaust (outlet) stream connected to a cyclone filter, where larger particles are separated and removed.

6.3 Mathematical modelling of fluidized bed reactor

6.3.1 Governing equations

In the context of a fluidized bed, the governing equations describe the complex interactions between the fluid (gas) phase and the particle (solid) phase. These equations are derived separately for each phase (gas and solid) and often involve interphase interactions. Below are the fundamental governing equations in the order of mass balance, momentum balance, and energy balance [188].

6.3.1.1 Mass balance equations

For gas phase:

$$\frac{\partial(\epsilon_g \rho_g)}{\partial \mathrm{t}} + \nabla\cdot\left(\epsilon_g \rho_g \bar{\mathrm{u}}_g\right) = 0 \qquad (6.1)$$

where ϵ_g is the gas volume fraction, $\bar{\mathrm{u}}_g$ is the gas velocity vector, and t is the time.

For solid phase:

$$\frac{\partial(1-\epsilon_s)\mathrm{\rho_s}}{\partial \mathrm{t}} + \nabla\cdot((1-\epsilon_s)\mathrm{\rho_s}\bar{\mathrm{u}}_s = 0 \qquad (6.2)$$

where $\bar{\mathrm{u}}_s$ is the particle velocity vector.

6.3.1.2 Momentum balance equations

For gas phase:

$$\frac{\partial(\epsilon_g\rho_g\bar{\mathrm{u}}_g)}{\partial t} + \nabla\cdot\left(\epsilon_g\rho_g\bar{\mathrm{u}}_g\bar{\mathrm{u}}_g\right) = -\epsilon_g\nabla P + \epsilon_g\rho_g g - \mathrm{F} + \nabla\cdot\left(\epsilon_g\tau_g\right) \qquad (6.3)$$

where P is the pressure, F is the interphase drag force acting on the gas due to the particles, and τ is the gas stress tensor.

For solid phase:

$$\frac{\partial((1-\epsilon_s)\rho_s\bar{\mathrm{u}}_s)}{\partial t} + \nabla\cdot\left((1-\epsilon_s)\rho_s\bar{\mathrm{u}}_g\bar{\mathrm{u}}_g\right)$$

$$= -((1-\epsilon_s)\nabla P + (1-\epsilon_s)\rho_s g + \mathrm{F} + \nabla\cdot(\tau_s) \qquad (6.4)$$

where τ_s is the solid phase stress tensor representing particle-particle and particle-wall interactions.

6.3.1.3 Energy balance equations

For gas phase:

$$\frac{\partial(\epsilon_g\rho_g c_g T_g)}{\partial t} + \nabla\cdot\left(\epsilon_g\rho_g c_g T_g\bar{\mathrm{u}}_g\right) = \nabla\cdot\left(\epsilon_g\kappa_g\nabla T_g\right) + \mathrm{Q} \qquad (6.5)$$

where c_g is the specific heat capacity of the gas, T_g is the gas temperature, κ_g is the gas thermal conductivity, and Q is the heat exchange term between the fluid and particles.

For solid phase:

$$\frac{\partial((1-\epsilon_s)\rho_s c_s T_s)}{\partial t} + \nabla\cdot((1-\epsilon_s)\rho_s \mathrm{c_s u_s T_s}) = \nabla\cdot(\kappa_s\nabla T_s) - \mathrm{Q} \qquad (6.6)$$

where c_s is the specific heat capacity of the solid particles, $\mathrm{T_s}$ is the particle temperature, and κ_s is the thermal conductivity of the solid phase.

The key interaction terms, for instance, the interphase drag force (F), captures the momentum exchange between gas and solid particles, and is typically modelled using empirical relations such as the Ergun equation or drag laws. The interphase heat transfer (Q) describes the energy exchange between the gas and solid particles, proportional to the temperature difference and heat transfer coefficient. Again, the stress tensors (τ_g, τ_s) account for the viscous or granular flow stresses within each phase. The foregoing equations form the basis for analyzing fluidized beds, though further simplifications (such as steady-state, 1D flow) or numerical methods are typically required for practical solutions.

The mass balance, momentum balance, and energy balance equations represent the theoretical foundation for modelling fluidized beds. While Aspen Plus software does not explicitly require the user to input these equations, its underlying models and solvers implement simplified or adapted versions of these principles, depending on the chosen configuration and unit operations [189]. The various pre-defined models provided by Aspen Plus for modelling fluidized beds include the ‘Fluidbed’ in the Aspen Plus model palette. This model is a parameterized version of the fundamental governing equations, tailored to engineering and process design contexts. The following is a concise representation of how Aspen Plus implemented fluidized bed modelling, in terms of mass, momentum, and energy balances.

For mass balance, Aspen Plus solves the mass balance equation, ensuring the conservation of mass for both gas and solid phases. In fluidized beds, the software accounts for:

- Multiphase interactions (gas and solid mass fractions),

  - Reaction stoichiometry,
  - Solids holdup and fluid (gas) holdup.

For momentum balance, Aspen Plus uses simplified momentum balance equations for practical fluidized bed modelling:

  - The Ergun equation or similar correlations were used to model pressure drops across the bed.
  - Drag force correlations (Wen-Yu model) approximated the interaction between gas and solid phases.
  - The detailed Navier-Stokes equations or complex solid-phase momentum balances were not explicitly solved in standard configurations, but their effects were incorporated into drag force or empirical terms.
  - Parameters like particle sizes were specified to match experimental conditions.

For energy balance,

  - The software solved heat transfer equations, accounting for conduction, convection, and radiation between the solid and fluid phases.
  - It included interphase heat transfer using empirical or semi-empirical correlations.
  - Reaction heat was included in the energy balance.

6.4 Development of multicomponent mathematical models

The Aspen Plus fluidized bed model represents a bubbling or circulating fluidized bed and accounts for five key aspects [190]

- Particle entrainment: The model incorporates the vessel geometry and gas supply, allowing for the calculation of parameters such as minimum fluidization velocity, transport disengagement height, and distributor pressure drop for either porous plates or bubble caps.

- Chemical reactions: Reaction stoichiometry and kinetics are defined, and the calculation method treats the gas as plug flow, solids as ideally mixed, and each balance cell is treated as a continuously stirred tank reactor (CSTR) with uniform properties.
- Fluid mechanics: The model assumes one-dimensional fluid mechanics and considers the impact of volume and heat exchange on fluid mechanics.
- Particle size distribution (PSD): Various methods are available to determine the PSD based on the inlet PSD data.
- Thermodynamics: The system assumes thermodynamic equilibrium between solids and vapours while accounting for heat effects and heat exchange on the bed temperature.

6.4.1 Multiphase reactions

Reversible chemical reaction

The enhanced doped magnesium hydroxide ($Mg(OH)_2$) and magnesium oxide (MgO) pair served as the working material in the TCES system. The reversible reaction governing this system is expressed as

$$\mathrm{M}g(\mathrm{OH})_2(\mathrm{s}) \rightleftharpoons \mathrm{M}g\mathrm{O} + \mathrm{H}_2\mathrm{O}(g) \tag{6.7}$$

1. Dehydration (heat storage process):

$$\mathrm{M}g(\mathrm{OH})_2(\mathrm{s}) \rightleftharpoons \mathrm{M}g\mathrm{O} + \mathrm{H}_2\mathrm{O}(g), \Delta\mathrm{H} > 0 \tag{6.8}$$

This process is an endothermic reaction in which $Mg(OH)_2$ was decomposed into MgO and water vapour, H_2O (g), and typically occurred at elevated temperatures under a stream of hot, dry air. The enthalpy change of the reaction is represented by $\Delta\mathrm{H}$.

2. Hydration (heat recovery process):

$$\mathrm{M}g\mathrm{O(s)} + \mathrm{H_2O}(g) \rightleftharpoons \mathrm{M}g\mathrm{(OH)_2}(s), \Delta\mathrm{H} < 0 \tag{6.9}$$

The hydration of MgO is an exothermic reaction in which $Mg(OH)_2$ was reformed. The reaction was carried out at lower temperatures with a humidified air stream.

Species involved and chemical reaction at the gas-solid interface

The thermochemical processes in the fluidized bed reactor (FBR) involved interactions between multiple species across both the solid and gas phases. In the solid phase, key reactants and products included $Mg(OH)_2$ and MgO. $Mg(OH)_2$ is a hydrated solid form of Mg that underwent a dehydration process to produce MgO, which is the anhydrous solid product.

In the gas phase, water vapour, H_2O (g), played a dual role as a product of the dehydration reaction and a reactant in reverse hydration. Additionally, air acted as a carrier gas within the reactor, facilitating the transfer of heat and supporting the removal or addition of water vapour as needed to drive the reactions.

The chemical reactions occurred at the interface between the solid particles and the surrounding gas:

- H_2O (g) adsorbed onto the MgO surface for hydration to occur.
- H_2O (g) desorbed from $Mg(OH)_2$ during dehydration and released into the gas phase.

6.4.2 General framework for species conservation

The conservation of species i in a multiphase system (solid and gas phases) can be expressed as

$$\frac{\partial \mathrm{C}_i}{\partial t} + \nabla\cdot \mathrm{J}_i = R_i \tag{6.10}$$

where C_i is the concentration of species i, J_i is the flux of species i, and R_i is the reaction rate.

For the gas phase, species conservation for H_2O (g) is crucial because it acts as the reactant/product for the hydration/dehydration processes. In FBR, the conservation equation for gas species i is

$$\frac{\partial \mathrm{C}_\mathrm{i}^g}{\partial t} + \nabla\cdot\left(\mathrm{u}_g C_i^g\right) - \nabla\cdot\left(D_i^g C_i^g\right) = -\mathrm{R}_i^g \tag{6.11}$$

where C_i^g is the concentration of the gas species i, D_i^g is the diffusion coefficient of species i, and R_i^g is the rate of mass transfer or reaction involving species i.

For the solid phase, the species conservation equation describes the evolution of the concentration of $Mg(OH)_2$ or MgO, accounting for reaction rates. The solid phase conservation for species j is

$$\frac{\partial \mathrm{C}_j^s}{\partial t} = -\mathrm{R}_j^s \tag{6.12}$$

where C_j^s is the concentration of solid species j, R_j^s is the rate of reaction of solid species j. The reaction rate R_j^s can be expressed using a reaction kinetic model, such as

$$R_j^s = k_j f\left(\mathrm{C}_j^s, \mathrm{T}\right) \tag{6.13}$$

So that,

During dehydration: $R_{\mathrm{Mg(OH)_2}}^s = -k_{\mathrm{deh}} \exp\left(-\frac{E_a}{\mathrm{RT}}\right)\cdot C_{Mg(OH)_2}^s$ (6.14)

During hydration: $R_{MgO}^s = -k_{\mathrm{hyd}} \exp\left(-\frac{\mathrm{E}_a}{RT}\right)\cdot C_{MgO}^s \cdot C_{H_2O}^g$ (6.15)

where E_a is the activation energy.

The coupling between the gas and solid phases is governed by the rate of reaction (R_i) and mass transfer (J_i) at the interface. For the vapour,

$$R_{\mathrm{H_2O}}^{g} = \frac{a_s}{\epsilon_g} R_{\mathrm{Mg(OH)_2}}^{s} \tag{6.16}$$

where a_s is the specific surface area of the solid particles, and ϵ_g is the void fraction of the gas phase. The reaction rate can also include mass transfer effects, such as

$$R_{H_2O}^{g} = k_{\mathrm{mass}}(\mathrm{C}_{\mathrm{H_2O,bulk}} - C_{\mathrm{H_2O,surface}}) \tag{6.17}$$

where k_{mass} is the gas-side mass transfer coefficient.

Therefore, the resulting mathematical model for the gas phase would be

$$\frac{\partial C_{H_2O}^{g}}{\partial t} + \nabla\cdot\left(\mathrm{u}_g C_{H_2O}^{g}\right) - \nabla\cdot(D_{H_2O}^{g} \nabla C_{H_2O}^{g}) = -\frac{a_s}{\epsilon_g} R_{\mathrm{Mg(OH)_2}}^{s} \tag{6.18}$$

For the solid phase,

$$\frac{\partial \mathrm{C}_{\mathrm{Mg(OH)_2}}^{s}}{\partial \mathrm{t}} = -R_{\mathrm{Mg(OH)_2}}^{s} \tag{6.19}$$

$$\frac{\partial \mathrm{C}_{\mathrm{MgO}}^{s}}{\partial \mathrm{t}} = -R_{\mathrm{MgO}}^{s} \tag{6.20}$$

These equations could be solved simultaneously with appropriate boundary and initial conditions for the reactor geometry and process dynamics. To derive the boundary conditions for the mathematical model, the system's behaviour at the inlet, outlet, and walls was considered. These conditions were critical for solving the governing equations.

6.4.2.1 Gas phase conservation: Boundary conditions

The boundary conditions for Equation (6.18) depend on the geometry and flow characteristics of the FBR system.

Inlet boundary condition (z=0, reactor bottom)

- Species concentration: For water vapour,

$$C^{g}_{H_2O}(z = 0, r, t) = C^{g}_{H_2O,in} \tag{6.21}$$

where $C^{g}_{H_2O,in}$ is the inlet concentration of H_2O (g), which could depend on the process (dry air for dehydration or humidified air for hydration).

- Velocity profile: For the gas velocity,

$$u_g(z = 0, r, t) = u_{g,in} \tag{6.22}$$

A uniform or parabolic velocity profile is often assumed for fluidized beds, depending on whether the flow is turbulent or laminar.

Outlet boundary condition (z=L, reactor top)

- Convective outflow: A convective outflow was assumed to dominate at the reactor outlet. A common assumption is that the concentration gradient normal to the boundary is zero.

$$\left.\frac{\partial C^{g}_{i}}{\partial t}\right|_{z=L} = 0 \tag{6.23}$$

Alternatively, the outlet concentration could be set to reflect the reactor performance, based on experimental or design criteria.

Wall boundary condition (r=R, reactor wall)

- Impermeable walls: At the reactor walls, no gas flux occurred normal to the surface.

$$C^{g}_{i}\cdot\hat{n} = 0 \quad \Rightarrow \quad \nabla C^{g}_{i}\cdot\hat{n} = 0 \tag{6.24}$$

where $\hat{n}$ is the unit vector normal to the reactor wall.

- Velocity boundary condition: The gas velocity at the walls would often satisfy the no-slip condition,

$$u_g(r = R) = 0 \qquad (6.25)$$

6.4.2.2 Solid phase conservation: Boundary conditions

Equations (6.19) and (6.20) describe the boundary conditions for the solid phase, which represent its confinement and interaction with the gas phase.

Surface interaction boundary condition

- The reaction at the gas-solid interface coupled the solid phase and gas phase, so that the rate of reaction typically depended on the temperature and species concentrations.
- For vapour adsorption or desorption,

$$R_j^s = k \cdot C_{H_2O}^g \qquad (6.26)$$

Initial conditions

- At t=0, the concentrations of solid species would typically be known, viz

$$C_{Mg(OH)_2}^s(z, r, t = 0) = C_{Mg(OH)_{2,init}}^s \qquad (6.27)$$

$$C_{MgO}^s(z, r, t = 0) = C_{MgO,init}^s \qquad (6.28)$$

The initial concentrations reflected the bed's starting composition, which would either be fully/partially hydrated ($Mg(OH)_2$) or dehydrated (MgO).

6.4.2.3 Thermal boundary conditions

Since reaction rates depended on temperature, thermal boundary conditions were also required.

Inlet temperature (z=0)

- The gas inlet temperature was specified as

$$T_g(z = 0, r, t) = T_{in} \qquad (6.29)$$

Wall heat transfer

- For insulated reactor walls, no heat flux condition would apply, so

$$\left.\frac{\partial \mathrm{T}}{\partial \mathrm{r}}\right|_{\mathrm{r=R}} = 0 \tag{6.30}$$

- For heat exchange between the reactor and the surroundings (such as through cooling/heating coils or jacket), a heat transfer coefficient $\mathrm{h_w}$ would be required.

$$-k_g \frac{\partial \mathrm{T}}{\partial \mathrm{r}} = \mathrm{h_w}\left(\mathrm{T}_w - \mathrm{T}_g\right) \tag{6.31}$$

where T_w is the wall temperature, and k_g is the thermal conductivity of the gas phase.

6.4.3 Steady-state reactions

The general framework for species conservation, gas, and solid phase conservations, as well as phase coupling, were adapted to describe the steady-state situation in Aspen Plus. However, certain assumptions and simplifications were applied to tailor these equations to steady-state conditions since Aspen Plus inherently solves steady-state models unless explicitly configured for dynamic simulations (Aspen Plus Dynamics or custom ODE models).

6.4.4 General framework for species conservation in steady-state

In steady-state conditions, the time-derivative term is eliminated ($^{\partial}/_{\partial t} = 0$) from the conservation equations.

Gas phase conservation (steady-state)

$$\nabla\cdot\left(\mathrm{u}_g C_i^g\right) - \nabla\cdot\left(D_i^g \nabla C_i^g\right) = -\frac{a_s}{\epsilon_g} R_\mathrm{i}^s \tag{6.32}$$

The convective term ($\mathrm{u}_g C_i^g$) remains, as the gas flows through the reactor, whereas the diffusive term ($D_i^g \nabla C_i^g$) is often negligible in bulk flow compared to convection, unless significant gradients exist. The reaction term (R_i^s) represents the coupling between the gas and solid phases. Aspen Plus directly handles such relationships using built-in reactor models, where R_{i}^{s} is specified through reaction kinetics or equilibrium expressions.

Solid phase conservation (steady-state)

$$0 = -R_j^s \tag{6.33}$$

This equation states that the rate of production or consumption of solid-phase species is balanced by the reaction rate. For steady-state systems, the solid-phase species concentrations are constant in time (but can vary spatially if axial gradients are considered).

Coupling between phases in Aspen Plus

Aspen Plus uses the film resistance model or the overall mass transfer coefficient approach to model gas-solid interactions. Coupling terms are expressed as

$$R_i^s = k_{\mathrm{i}} a_s (\mathrm{C}_i^g - \mathrm{C}_i^{g,eq}) \tag{6.34}$$

where the mass transfer coefficient k_{i} can be user-defined or calculated by Aspen Plus, a_s is the specific surface area for reaction or mass transfer, and $\mathrm{C}_i^{g,eq}$ is the equilibrium concentration of the gas species at the solid surface. Aspen Plus allows input for both reaction rates (R_i^s) and equilibrium conditions via reaction kinetics and thermodynamics models.

Simplification of the mathematical model for steady-state

The resulting mathematical model for steady-state in Aspen Plus typically involves the following

- Mass balance: Conservation of mass for all species.
- Energy balance: Conservation of enthalpy or heat transfer rates.

- Momentum balance: For detailed hydrodynamics, but typically replaced with empirical or semi-empirical flow models.
- Reaction kinetics: User-defined or from the Aspen Plus library.

For a FBR in steady-state, the final governing equations simplify as

$$\nabla\cdot\left(\mathrm{u}_g C_i^g\right) = -\frac{a_s}{\epsilon_g} R_{\mathrm{i}}^s \tag{6.35}$$

These equations are embedded in the Aspen Plus fluidized bed reactor model.

6.4.5 Thermodynamic model

The selection of a thermodynamic model in Aspen Plus for the $Mg(OH)_2$/MgO system needed to account for the behaviour of solid and gas phases. This system involved a gas-solid reaction and, possibly, non-ideal behaviour of water vapour at higher temperatures. For instance, the dehydration and hydration processes involved the following key phenomena:

- Phase equilibrium: The interconversion between solid phases ($Mg(OH)_2$ and MgO) and the gas phase (water vapour).
- Reaction chemistry: The endothermic dehydration reaction and the exothermic hydration reaction.
- Gas-phase interaction: The behaviour of water vapour in the presence of solids (or other gases).

For such solid-gas systems, the "SOLIDS" Base Method in Aspen Plus was used. This allowed the software to appropriately account for solid behaviour by incorporating the properties of solid species into equilibrium calculations. To complement this, the Peng-Robinson (PR) Equation of State (EOS) was used as a suitable model to effectively capture phase equilibrium and describe the non-ideal effects (such as deviations from ideal gas behaviour) that may occur at conditions of high temperature and pressure. The justification for the choice was based on the multicomponent nature of the system.

The reaction stoichiometry for the dehydration reaction, for instance, indicates that one mole of $Mg(OH)_2$ produces one mole of MgO and one mole of H_2O (g). The reaction rate (r) is described by the first derivative equation, which characterizes the rate of conversion. Aspen Plus provides a built-in power law method for calculating the rate of reaction, expressed as

$$\mathrm{r} = \mathrm{k}(\mathrm{T}/\mathrm{T_o})^{n}\mathrm{e}^{-(\mathrm{E}/\mathrm{R})[1/\mathrm{T}-1/\mathrm{T_o}]}\prod_{\mathrm{i}=1}^{\mathrm{N}}\mathrm{C_i}^{a_\mathrm{i}} \qquad (6.36)$$

where k is the pre-exponential factor, T and $\mathrm{T_o}$ the absolute and reference temperatures, n the temperature exponent, $\mathrm{E_a}$ the activation energy, R the universal gas constant, Π, the product operator, N, the number of components, $\mathrm{C_i}$ the concentration of the ith component, and a_i the exponent of the ith component. If no reference temperature is considered, the reduced form of the power law becomes

$$\mathrm{r} = \mathrm{k}\mathrm{T}^{\mathrm{n}}\mathrm{e}^{-\mathrm{E}/\mathrm{RT}}\prod_{\mathrm{i}=1}^{\mathrm{N}}\mathrm{C_i}^{a_\mathrm{i}} \qquad (6.37)$$

6.5 Simulation inputs and boundary conditions

The modelling and simulation followed two main steps: the thermodynamics properties method (components and methods specifications) and the process flowsheet simulation (unit operations selection). The summary of the modelling and simulation procedure in this thesis is presented in Figure 6.2.

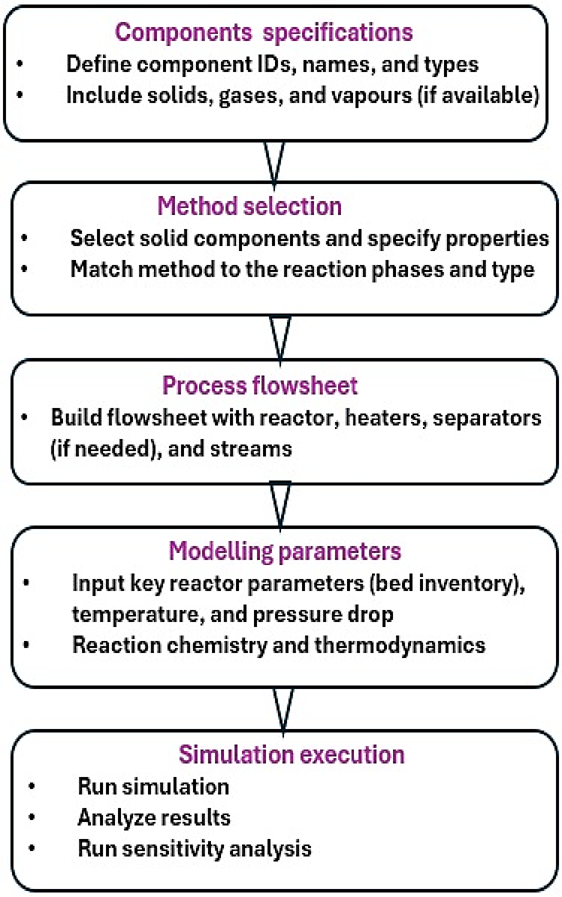

Figure 6. 2 Aspen Plus modelling and simulation flowsheet.

Components and methods specifications

Figure 6.3 shows the components and method specifications for the enhanced doped $Mg(OH)_2/MgO$ system.

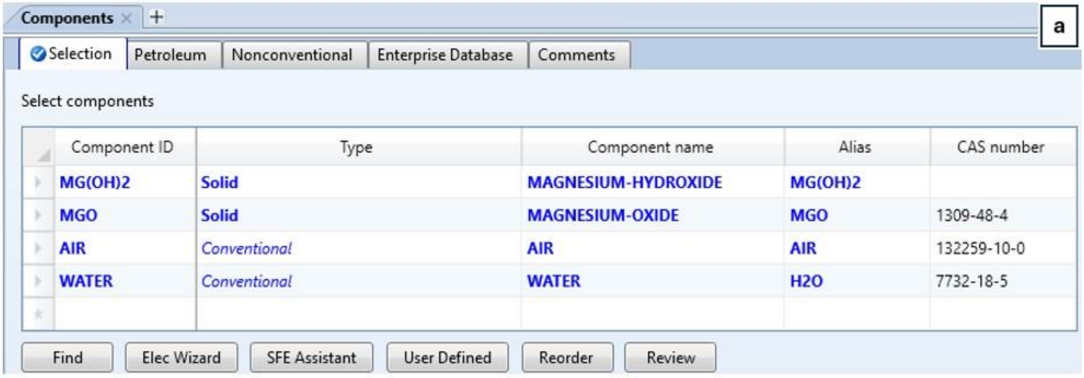

Select components

Component ID	Type	Component name	Alias	CAS number
MG(OH)2	Solid	MAGNESIUM-HYDROXIDE	MG(OH)2	
MGO	Solid	MAGNESIUM-OXIDE	MGO	1309-48-4
AIR	*Conventional*	AIR	AIR	132259-10-0
WATER	*Conventional*	WATER	H2O	7732-18-5

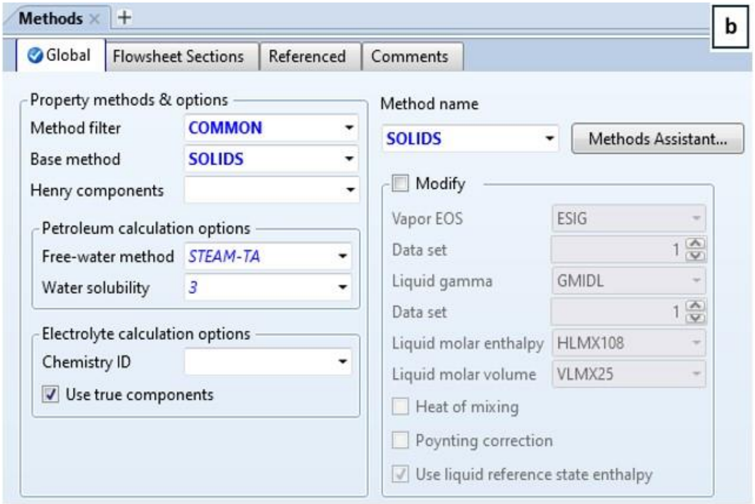

Property methods & options
Method filter COMMON
Base method SOLIDS
Henry components

Petroleum calculation options
Free-water method STEAM-TA
Water solubility 3

Electrolyte calculation options
Chemistry ID
☑ Use true components

Method name SOLIDS

☐ Modify
Vapor EOS ESIG
Data set 1
Liquid gamma GMIDL
Data set 1
Liquid molar enthalpy HLMX108
Liquid molar volume VLMX25
☐ Heat of mixing
☐ Poynting correction
☑ Use liquid reference state enthalpy

Figure 6. 3 (a) Components and (b) Method entries for the enhanced doped $Mg(OH)_2$/MgO system.

Afterwards, a physical methods analysis was run before the unit operations selection.

Unit operations selection

The simulation flowsheets were created using the graphical user interface (GUI). The flowsheets for the (de)hydration consisted of different unit operations and streams that are available in the Aspen Plus model palette. For the dehydration process, the system comprised two inlet streams: the doped $Mg(OH)_2$ feed (SOLIDIN) into the FBR (FLUIDBED), and the dry air (AIRIN) via a compressor (COMPR) functioning as a pressure controller. Other blocks included a heater (HEATER) to generate the needed inlet gas temperature (GASIN) and a solid splitter (SSPLIT) for separating output solids from any gas residue. Figure 6.4 shows the Aspen Plus dehydration model.

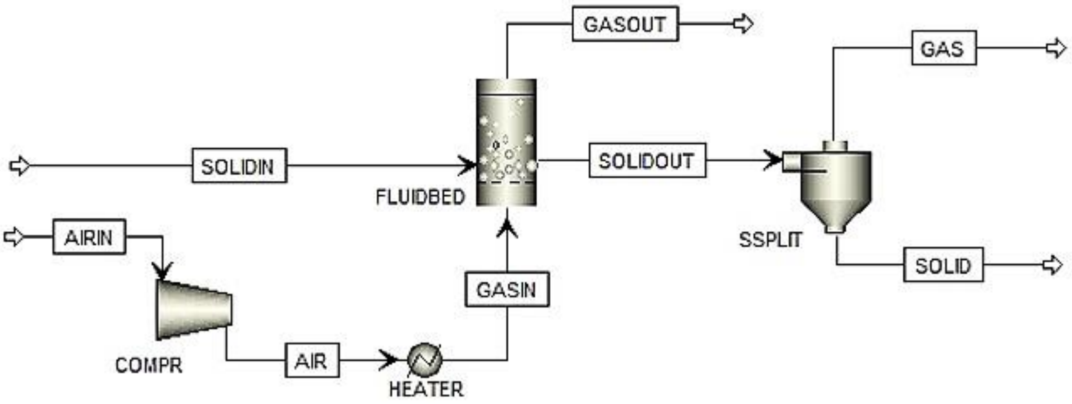

Figure 6. 4 The Aspen Plus dehydration model used in this work.

For the hydration process, a mixer (MIXER) was added to the system to enable the mixing of input air with the generated water vapour (WAT-V) before feeding it into the FBR. The heater, designated HEATER1, was used to heat the fed-in liquid water (WAT-L) to vaporize it before mixing it with the carrier air, and HEATER2 was used to feed the gas mixture into the bed at the required hydration temperature. Figure 6.5 shows the Aspen Plus hydration model.

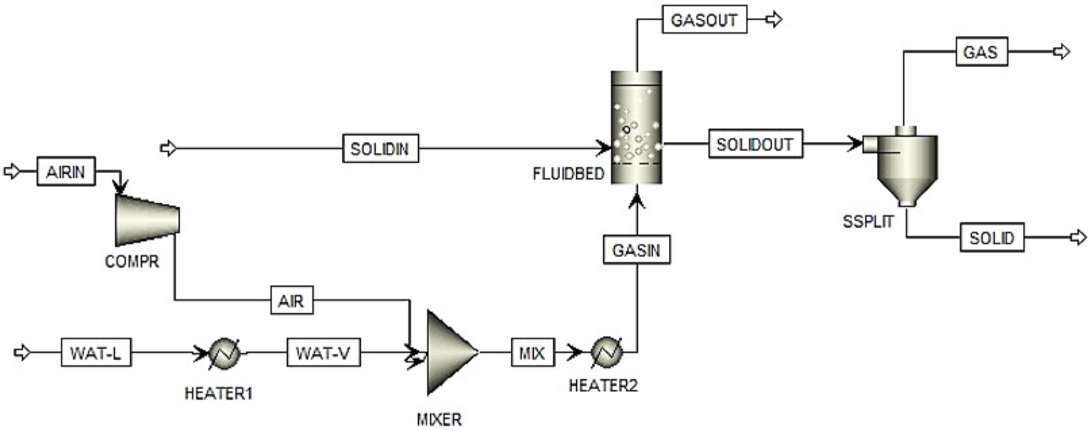

Figure 6. 5 The Aspen Plus hydration model used in this work.

Simulation setup

The enhanced doped $Mg(OH)_2/MgO$ system was specified as “MIXNCPSD” sub-stream in the simulation setup pane (Figure 6.6). In Aspen Plus, MIXNCPSD stands for Mixed Nonconventional Particle Size Distribution, which is used to model nonconventional solid materials with a specified particle size distribution. This property method defines particle size distribution (PSD) and other physical properties of solids that do not conform to standard thermodynamic models.

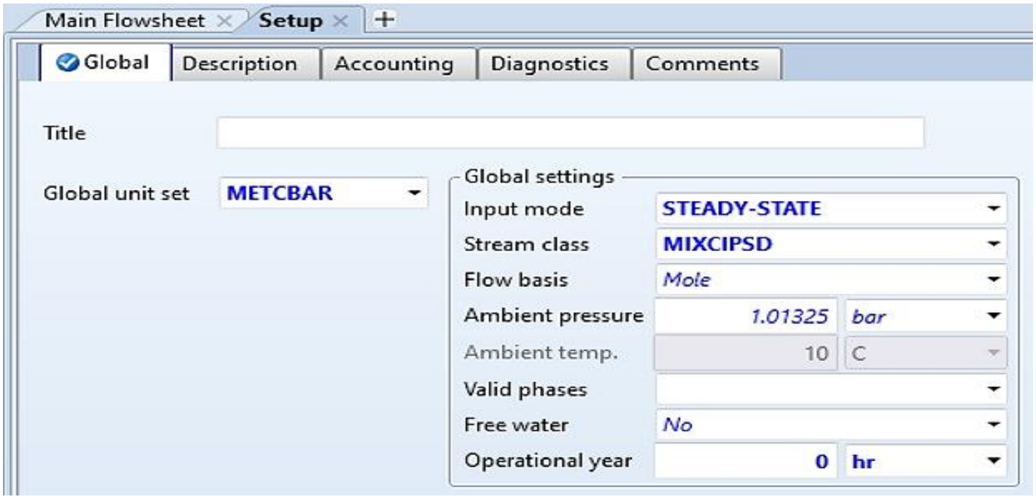

Title

Global unit set: METCBAR

Global settings

Input mode: STEADY-STATE

Stream class: MIXCIPSD

Flow basis: Mole

Ambient pressure: 1.01325 bar

Ambient temp.: 10 C

Valid phases:

Free water: No

Operational year: 0 hr

Figure 6. 6 Aspen Plus specification for nonconventional solids.

The boundary conditions for the dehydration process given two inlet streams, SOLIDIN and AIRIN, are shown in Table 6.1.

Table 6. 1 Boundary conditions for the dehydration process.

Stream name: SOLIDIN				
State variables			**Composition**	
Temperature	25	℃	Mole-Flow	kmol/hr
Pressure	1	bar	Component	Value
Total flow basis	Mole		MG(OH)2	1
Total flow rate		kmol/hr	MGO	
Stream name: AIRIN				
State variables			**Composition**	
Temperature	25	℃	Mole-Flow	kmol/hr
Pressure	1	bar	Component	Value
Total flow basis	Mole		MG(OH)2	
Total flow rate		kmol/hr	MGO	
		Total	AIR	1
			WATER	

In Figure 6.4, the HEATER in the compressor outlet raised the temperature of the bed inlet gas (GASIN) to 300 ℃ at a pressure of 2 bar. The PSD of the bed material is another important boundary condition for the FBR [191]. Here, the material's PSD was specified as 150 μm. The normal distribution option was used. The median value and the standard deviation completely characterize this distribution function.

Similarly, Table 6.2 shows the boundary conditions for the two inlet streams, SOLIDIN and AIRIN, for the hydration process shown in Figure 6.5. In this case, the GASIN was a mixture of dry air and water vapour fed into the bed at 200 ℃ and 2 bar, with the aid of HEATE2. The PSD of the material was also specified as 150 μm.

Table 6. 2 Boundary conditions for the hydration process.

Stream name: SOLIDIN				
State variables			**Composition**	
Temperature	25	℃	Mole-Flow	kmol/hr
Pressure	1	bar	Component	Value
Total flow basis	Mole		MG(OH)2	
Total flow rate		kmol/hr	MGO	1
Stream name: AIRIN				
State variables			**Composition**	
Temperature	25	℃	Mole-Flow	kmol/hr
Pressure	1	bar	Component	Value
Total flow basis	Mole		MG(OH)2	
Total flow rate		kmol/hr	MGO	
		Total	AIR	1
			WATER	

The main operating conditions required for the fluidized bed include the bed inventory, column geometry, gas distributor plate, reactions, and convergence. Ideally, the simulation should converge when all boundary and operation conditions are satisfied. The “Newton” mass balance convergence solver was used. Table 6.3 presents a summary of the fluidized bed reactor specifications.

It is important to note that the geometry and input parameters selected for this fluidized bed reactor model are based on a lab-scale rig proposed for the experimental studies.

Table 6. 3 Specifications for fluidized bed reactor.

Bed inventory			**Geometry**		
Bed mass	1.5	kg	**Dimensions**		
Voidage	0.5		Height	500	mm
Geldart classification	Geldart B		Solids discharge location	0	
Minimum fluidization velocity			Cross section	Circular	
Calculate from correlation	Ergun		Constant diameter	100	mm
Transport disengagement height			**Gas Distributor**		
TDH model	George & Grace		Type	Perforated plate	
Maximum dC_V/dh	1e-05		Number of orifices	1000	
Elutriation			Orifice diameter	1e-05	mm
Model	Tasirin & Geldart				

In addition, the respective dehydration and hydration reactions were set up as seen in Figure 6.7.

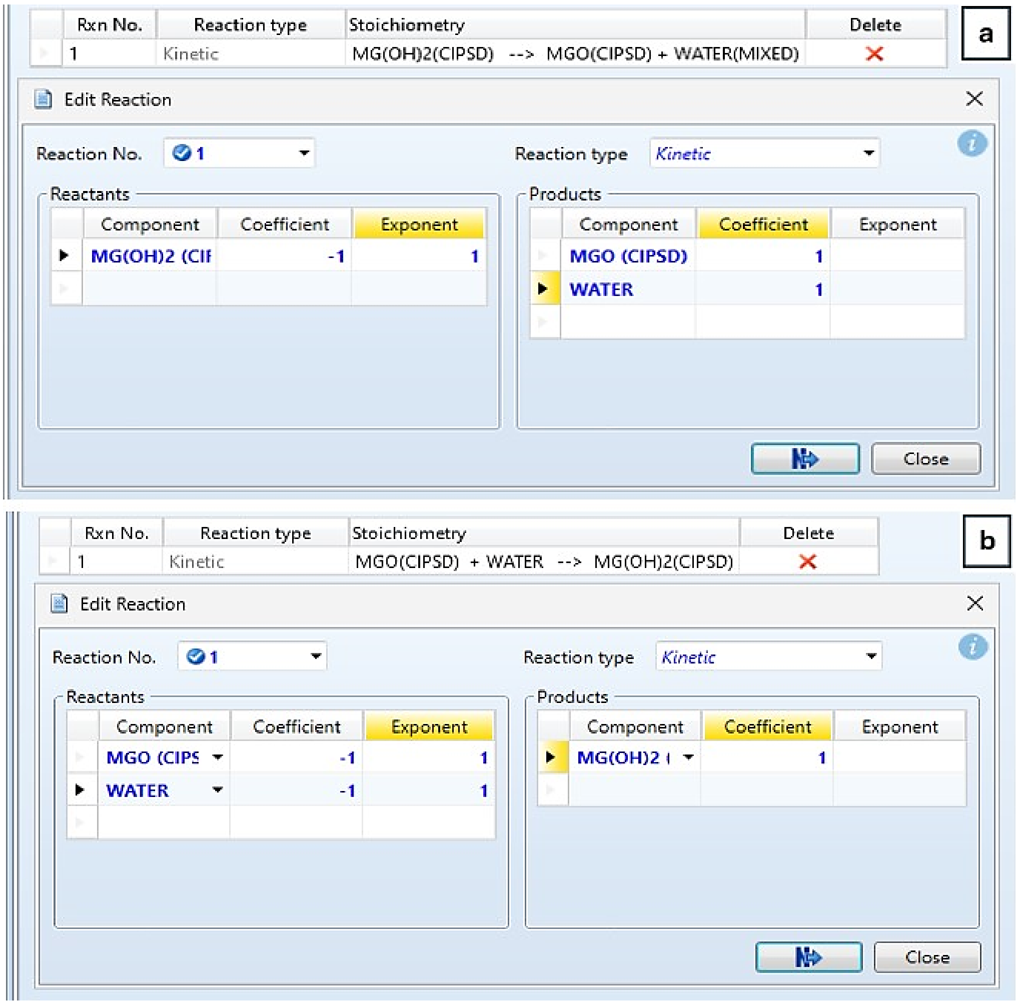

Rxn No.	Reaction type	Stoichiometry	Delete
1	Kinetic	MG(OH)2(CIPSD) --> MGO(CIPSD) + WATER(MIXED)	✕

Reaction No. 1

Reaction type Kinetic

Reactants

Component	Coefficient	Exponent
MG(OH)2 (CIF	-1	1

Products

Component	Coefficient	Exponent
MGO (CIPSD)	1	
WATER	1	

Rxn No.	Reaction type	Stoichiometry	Delete
1	Kinetic	MGO(CIPSD) + WATER --> MG(OH)2(CIPSD)	✕

Reaction No. 1

Reaction type Kinetic

Reactants

Component	Coefficient	Exponent
MGO (CIPS	-1	1
WATER	-1	1

Products

Component	Coefficient	Exponent
MG(OH)2 (	1	

Figure 6. 7 Reaction stoichiometry specification for the (a) dehydration and (b) hydration processes.

6.6 Simulation results and discussion

After completing the modelling and simulation, the results are analyzed and discussed. Aspen Plus outputs results in two categories: stream results and unit operation results. This section provides an analysis of these results, focusing on the stream results and a summary of the fluidized bed unit operation. Aspen Plus presents these results in a tabular format.

6.6.1 Dehydration of enhanced doped magnesium hydroxide

The stream results of the $Mg(OH)_2$ dehydration are presented in Table 6.4.

Table 6. 4 Stream results for dehydration of enhanced doped $Mg(OH)_2$.

Process variables	**Units**	GASIN	SOLIDIN	GASOUT	SOLIDOUT
Temperature	℃	293	25		
Pressure	bar	2	1	1.9469	1.9469
Molar Vapour Fraction		1	0	0.9987	0
Molar Solid Fraction		0	1	0.0013	1
Mass Vapour Fraction		1	0	0.9979	0
Mass Solid Fraction		0	1	0.0022	1
Mole flows	kmol/hr	1	1	2.0025	0.9974
Mass flows (Total)	kg/hr	28.9509	58.3197	47.0692	40.2014
• MG(OH)2	kg/hr	0	58.3197	6.647e-06	0.0029
• MGO	kg/hr	0	0	0.1038	40.1988
• AIR	kg/hr	28.9509	0	28.9509	0
• WATER	kg/hr	0	0	18.0145	0
Mass Fractions					
• MG(OH)2		0	1	1.412e-07	6.404e-05
• MGO		0	0	0.0022	0.9999
• AIR		1	0	0.6151	0
• WATER		0	0	0.3827	0

A feed stream containing 58.32 kg/hr of magnesium hydroxide ($Mg(OH)_2$) was introduced into the fluidized bed reactor (FBR) for thermal dehydration. To promote effective heat transfer and ensure efficient removal of water vapour produced during the decomposition process, hot compressed air was supplied at a mass flow rate of 28.95 kg/hr and maintained at an operating pressure of 2 bar. As shown in Table 6.4, the thermal decomposition reaction yielded 40.19 kg/hr of magnesium oxide (MgO) and 18.00 kg/hr of water vapour. This corresponds to a conversion efficiency of 99.99%, indicating that nearly all of the $Mg(OH)_2$ fed into the reactor was successfully converted into MgO. The reaction conversion efficiency (χ) was calculated from the formula

$$\chi = \frac{M_{fi} - M_{fo}}{M_{fi}}.100\% \tag{638}$$

where M_{fi} is the mass flow rate of the input feed (the hydroxide) and M_{fo} is the mass flow rate of the feed (the hydroxide) at the outlet.

The dehydration reaction proceeds according to the stoichiometry given in Equation (6.8), which is endothermic and typically requires temperatures in the range of 350–400 ℃ for the typical material. The mass flow rates of the species align closely with stoichiometric predictions based on molecular weights (58.32 g/mol for $Mg(OH)_2$, 40.30 g/mol for MgO, and 18.02 g/mol for H_2O), confirming both the consistency of the mass balance and the accuracy of the simulation. The slight deviation between the theoretical and actual MgO yield, that is, 0.11 kg/hr, may be attributed to rounding off, model assumptions, or minor unreacted residue, though this remains within acceptable engineering tolerance. A similar approach was used by Debtera et al. [192] to model a fluidized bed reactor in Aspen Plus for aluminum hydroxide, $Al(OH)_3$, dehydration. Using Geldart B particles, the GGC (Gates-Gaudin-Schuhmann) method for particle size distribution, and the Ergun equation for fluidization parameters, the simulation showed 94.4% conversion of 275 kg/hr $Al(OH)_3$ into 169.6 kg/hr Al_2O_3 and 89.9 kg/hr H_2O, which aligned well with their reported experimental results.

The use of compressed air in the reactor served a dual purpose. Thermally, it delivered the energy required to drive the endothermic decomposition. Hydrodynamically, it ensured that the bed remained fluidized, thus facilitating excellent solid-gas contact, uniform temperature distribution, and continuous removal of generated water vapour. This continuous removal was critical, as it shifted the equilibrium towards the products, enhancing conversion. Furthermore, the selected air-to-solids mass flow ratio (approximately 0.5) appears sufficient to maintain stable bubbling fluidization under the given pressure, assuming appropriate particle characteristics and superficial gas velocity.

The near-complete conversion reported suggests that the simulation captured the key aspects of fluidized bed operation with high fidelity, including appropriate residence time, thermal equilibrium, and efficient phase separation. These results strongly support the suitability of the FBR configuration for solid-state dehydration processes and demonstrate that, with proper thermal integration and particle sizing, the process can be efficiently scaled up.

The fluidized bed model results from the process variables and parameters are given in Table 6.5.

Table 6. 5 Results of fluidized bed parameters for enhanced doped $Mg(OH)_2$ dehydration.

Parameter	**Value**	**Units**
Height of bottom zone	0.00189	meter
Height of freeboard	4.9981	meter
TDH from correlation	0.3097	meter
TDH based on solids volume profile	3.9485	meter
Solids holdup	0.5000	kg
Distributor pressure drop	6.741e-06	bar
Bottom zone pressure drop	0.0003	bar
Freeboard pressure drop	0.0528	bar
Fluidized bed pressure drop	0.0531	bar
Heat duty	1195.03	cal/sec
Minimum fluidization velocity	0.1850	m/sec

A plot of the bed height versus gas flow velocity during the dehydration process simulation is shown in Figure 6.8.

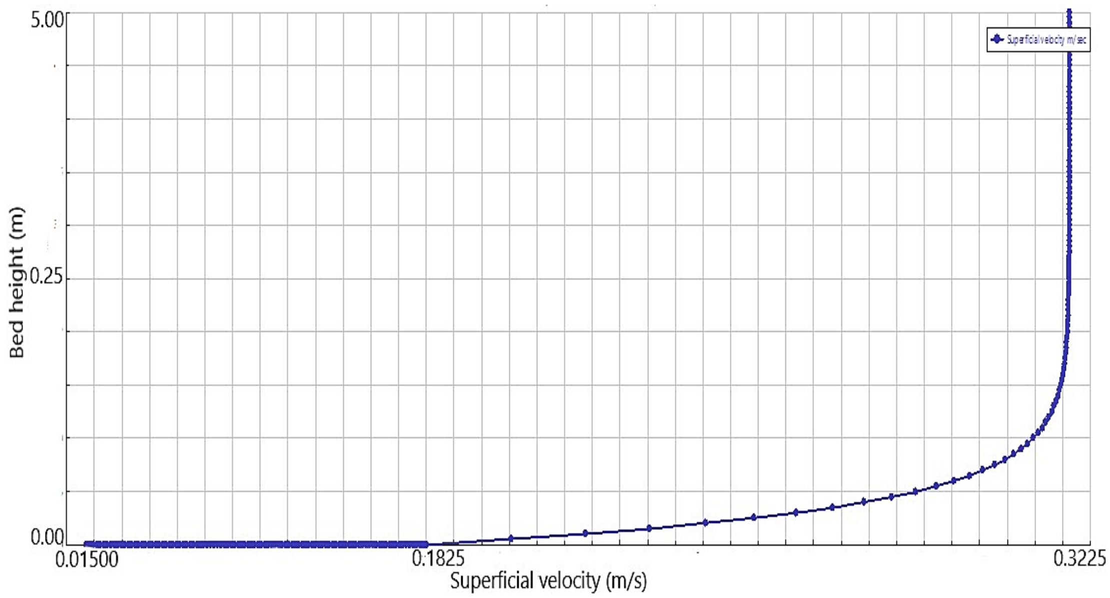

Figure 6. 8 Bed height versus superficial velocity for the enhanced doped $Mg(OH)_2$ dehydration.

In the fixed bed regime, the bed height remained constant, and the gas simply flowed through the voids between stationary particles. Once the minimum fluidization velocity was reached at around 0.1850 m/s, the bed began to expand as particles were suspended by the gas flow. At this point, further increases in gas flow resulted in the bed expanding more rapidly around 0.3225 m/s.

The pressure drop across the bed, on the other hand, reflects the balance between the upward drag force exerted by the gas and the weight of the particle bed. As the gas velocity increased from the fixed bed regime, the pressure drop across the bed rose until fluidization began. At the point of minimum fluidization, the pressure drop reached a maximum and then began to decrease exponentially despite further increases in gas velocity (Figure 6.9). This may be because additional gas flow primarily expanded the bed and increased porosity rather than adding to the drag force.

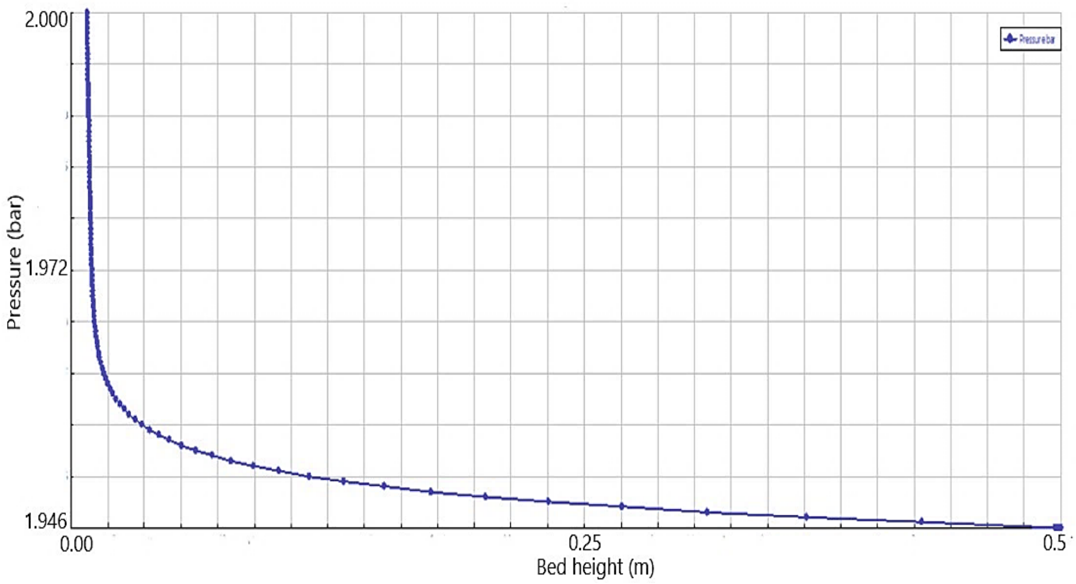

Figure 6. 9 Bed pressure drop against bed height for the enhanced doped $Mg(OH)_2$ dehydration.

The sensitivity analysis result in Figure 6.10 shows how the airflow rate influences the heat supply for the dehydration process, hence the product yield (by mass fraction of MgO).

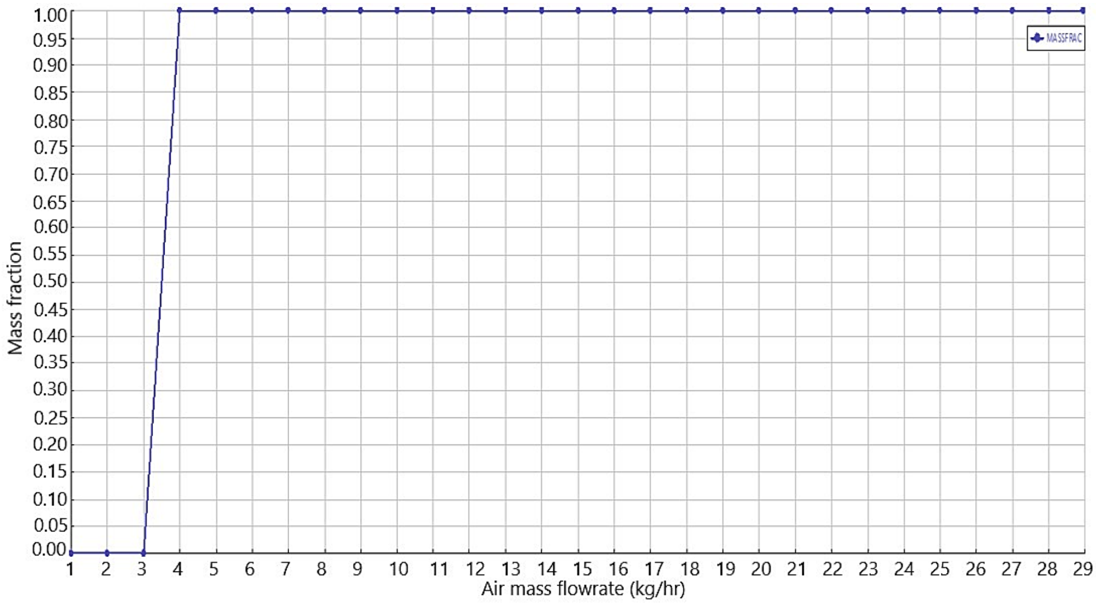

Figure 6. 10 Sensitivity analysis of the influence of airflow rate on the enhanced doped $Mg(OH)_2$ dehydration reaction.

At very low airflow rates close to 3 kg/hr, the gas velocity was insufficient to properly fluidize the bed, and the solid particles remained in a packed bed. So, a significant portion of $Mg(OH)_2$ remained unreacted in bed. Consequently, the mass fraction of the MgO product was low. When the airflow rate reached the minimum fluidization velocity, the particles became fully fluidized, leading to improved mixing. This created optimal conditions for the dehydration reaction, ensuring that $Mg(OH)_2$ was effectively converted to MgO at a mass fraction near 1.00. With better contact between the hot air and the solid particles, the reaction proceeded more efficiently, and the MgO mass fraction in the final product increased. This was the ideal operating range where the process achieved high conversion rates with minimal unreacted $Mg(OH)_2$ material.

Furthermore, Table 6.6 represents a summary of the temporal variation in temperature and heat during the endothermic thermal decomposition of the developed material, whilst Figure 6.10 illustrates the temporal evolution of temperature and heat during the process, suggesting the continuous heat input requirement for the decomposition. The temperature profile showed a steady increase from around 300 ℃, gradually reaching approximately 320 ℃ over 600 seconds. This temperature rise is attributable to the sustained supply of thermal energy required to break the hydroxide bonds and drive off water vapour. Simultaneously, the heat duty increased proportionately, peaking at approximately +1195 cal/s (+5 kW) by the end of the reaction time. Heat duty refers to the amount of heat energy added to (or removed from) a unit operation, such as a heat exchanger or reactor, in given process conditions. This positive heat duty reflects the energy absorbed by the process, according to the efficiency of the air preheater in delivering the required thermal input.

Table 6. 6 Representative temperatures and heat over time for the enhanced doped material dehydration.

Time (s)	Temperature (℃)	Heat duty (kW)
0	300	0
60	304	0.8
120	308	1.6
180	312	2.4
240	316	3.6
300	318	4.3
360	320	5
420	320	5
480	320	5
540	320	5
600	320	5

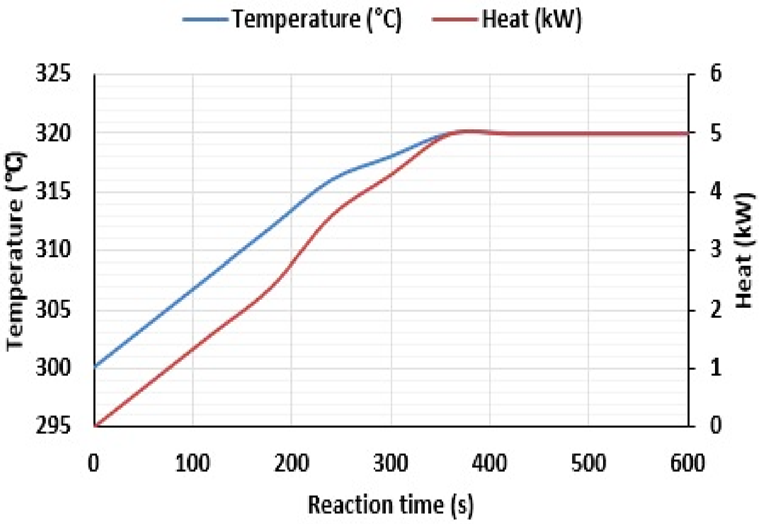

Figure 6. 11 Graphical illustration of temperature and heat profiles during the dehydration process.

In conclusion, the Aspen Plus simulation of $Mg(OH)_2$ dehydration in a fluidized bed reactor demonstrates good alignment with stoichiometric, thermodynamic, and hydrodynamic expectations. The temporal temperature and heat profiles confirm the energy-intensive nature of dehydration. The high conversion rate and accurate mass balance underscore the effectiveness of the reactor model, providing a solid foundation for further optimization and potential scale-up.

6.6.2 Hydration of doped magnesium oxide

The stream results for the reversible hydration of MgO are presented in Table 6.7.

Table 6. 7 Stream results for hydration of enhanced doped MgO.

Process variables	**Units**	GASIN	SOLIDIN	GASOUT	SOLIDOUT
Temperature	℃	293	25		
Pressure	bar	2	1	1.9651	1.9651
Molar Vapour Fraction		1	0	0.9998	0
Molar Solid Fraction		0	1	0.0001	1
Mass Vapour Fraction		1	0	0.9997	0
Mass Solid Fraction		0	1	0.0003	1
Mole flows	kmol/hr	2	1	1.0079	0.9999
Mass flows (Total)	kg/hr	46.9662	40.3044	29.0999	58.1707
• MG(OH)2	kg/hr	0	0	0.0086	57.8568
• MGO	kg/hr	0	40.3044	4.689e-05	0.3139
• AIR	kg/hr	28.9509	0	28.9509	0
• WATER	kg/hr	499.9999	0	0.1403	0
Mass Fractions					
• MG(OH)2		0	0	0.0003	0.9946
• MGO		0	1	1.611e-06	0.0054
• AIR		0.6164	0	0.9949	0
• WATER		0.3836	0	0.0048	0

In a reverse operation to thermal dehydration, the material (MgO) was rehydrated in a fluidized bed reactor (FBR) under controlled conditions. A solid feed stream of 40.30 kg/hr MgO was introduced into the reactor, and the reaction was initiated by mixing water vapour with dry compressed air flowing at 28.95 kg/h. This configuration provided the necessary reactant and thermal medium to facilitate the solid-gas phase hydration of MgO. As reported in Table 6.7, the hydration reaction produced 57.86 kg/hr of magnesium hydroxide ($Mg(OH)_2$).

The hydration reaction proceeds according to Equation (6.9). This reaction is characteristically exothermic, releasing heat as the magnesium oxide absorbs water molecules and forms the more thermodynamically stable hydroxide compound. The molar masses, 40.30 g/mol for MgO and 58.32 g/mol for $Mg(OH)_2$, suggest that the observed product flow rate is nearly stoichiometrically consistent with the mass input of MgO. The theoretical yield for complete conversion of 40.30 kg/hr of MgO would approximately be 58.32 kg/hr of $Mg(OH)_2$. Therefore, the reported yield of 57.86 kg/hr is a reasonably close value, affirming the reaction's completeness and the accuracy of simulation results. This represents a conversion efficiency of approximately 99.21%.

The fluidized bed model results from the process variables and parameters are given in Table 6.8.

Table 6. 8 Results of fluidized bed parameters for enhanced doped MgO hydration.

Parameter	**Value**	**Units**
Height of bottom zone	1e-10	meter
Height of freeboard	5.0000	meter
TDH from correlation	0.4211	meter
TDH based on solids volume profile	3.9500	meter
Solids holdup	0.5000	kg
Distributor pressure drop	0.0029	bar
Bottom zone pressure drop	9.414e-12	bar
Freeboard pressure drop	0.0349	bar
Fluidized bed pressure drop	0.0349	bar
Heat duty	-1147.3	cal/sec
Minimum fluidization velocity	0.01598	m/sec

In the fixed bed regime, the bed height stayed relatively unchanged as the gas flowed through the spaces between the stationary particles. When the gas flow reached a velocity close to 0.01598 m/s, the particles became suspended, causing the bed to expand. As the gas flow rate increased, the bed continued to expand rapidly afterwards.

A plot of the bed height versus gas flow velocity during the hydration process simulation is shown in Figure 6.12.

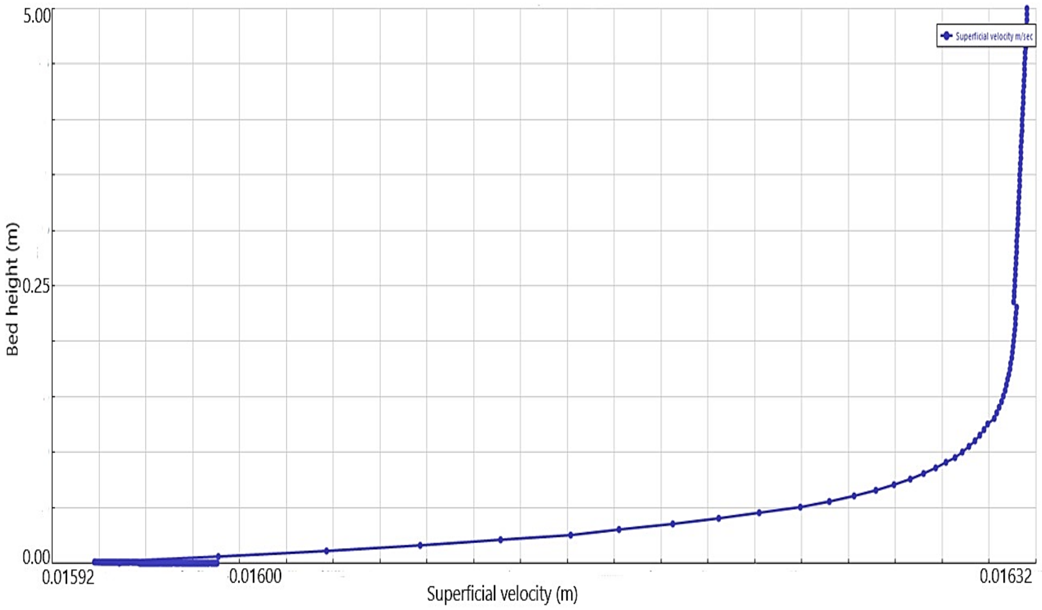

Figure 6. 12 Bed height versus superficial velocity for the enhanced doped MgO hydration.

The pressure drop decreased as the bed expanded further after reaching the minimum fluidization, as shown in Figure 6.13. The pressure drop reached a maximum of 1.977 bar and then decreased exponentially despite further gas velocity increases.

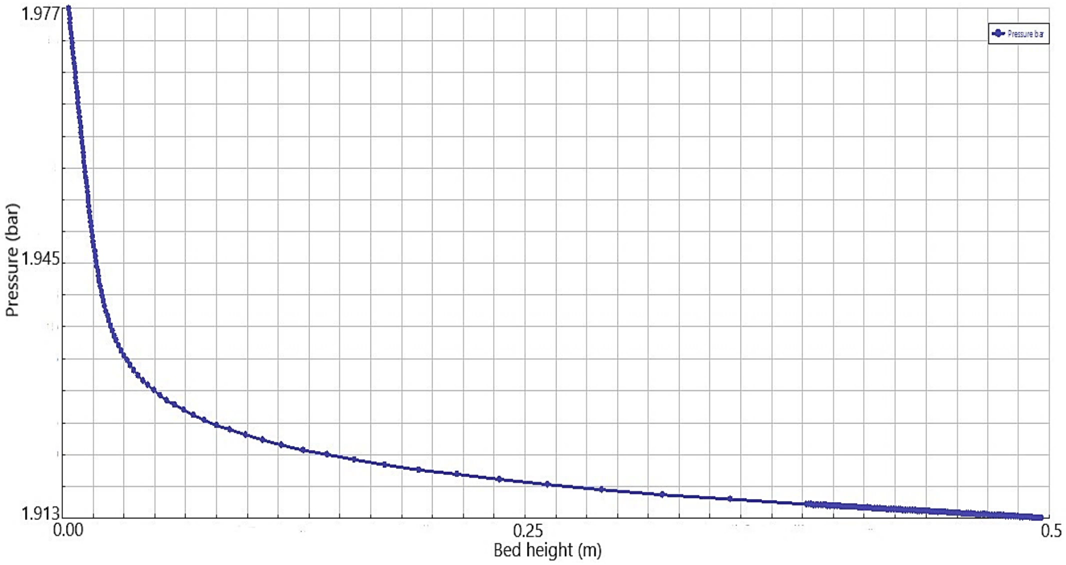

Figure 6. 13 Bed pressure drop against bed height for the enhanced doped MgO hydration.

Sensitivity analysis showed that the reaction conversion efficiency varied with the moles of water vapour in the inlet gas (Figure 6.14). The process produced about 99.78% $Mg(OH)_2$ with four times the moles of water vapour available to react with MgO, as against 99.44% with one mole. Further increases in the amount of water did not show any appreciable change.

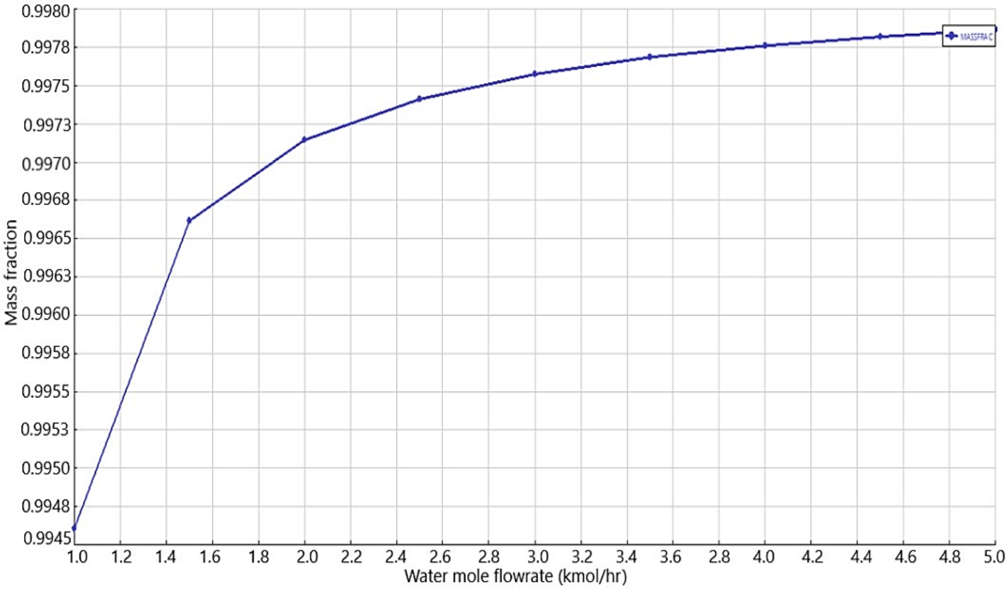

Figure 6. 14 Sensitivity analysis of the influence of water mole-flow rate on the enhanced doped MgO hydration reaction.

This observation highlights the significance of water vapour availability as a driver of the reaction equilibrium and kinetics within the fluidized bed system. According to Le Chatelier's Principle, increasing the concentration (or partial pressure) of water vapour shifted the equilibrium towards the product side, thereby favouring the formation of $Mg(OH)_2$. At low water vapour availability, the forward reaction was impacted both kinetically and thermodynamically. As water availability increased, the equilibrium was increasingly driven forward, and surface reaction rates improved due to greater reactant solid-gas contact. However, the observed plateau in conversion beyond a 4:1 water-to-MgO molar ratio suggests that saturation of reactive sites or equilibrium limitations began to dominate. At this point, the system likely approached its thermodynamic conversion limit under the prevailing temperature and pressure conditions. Additional water vapour no longer contributed meaningfully to conversion, as the reaction either neared completion or was constrained by other rate-limiting factors (such as diffusion or solid-gas mass transfer).

On the other hand, Figure 6.15 shows the inlet air-vapour flow rates for the hydration process. The MgO was rapidly converted to $Mg(OH)_2$ as the flow rate increased from 15 kg/hr to 175 kg/hr, leading to improved mixing and enhanced heat transfer.

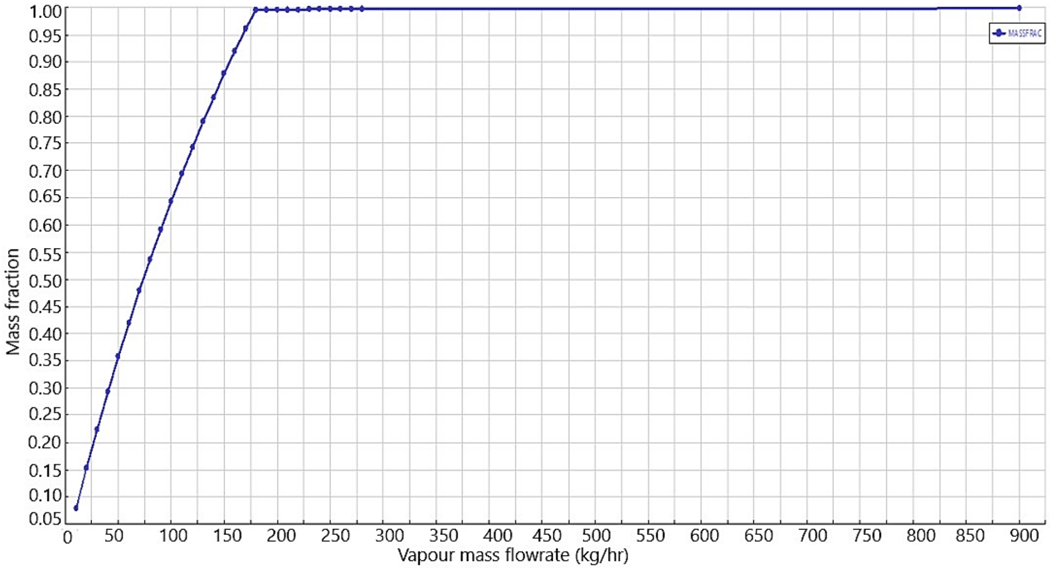

Figure 6. 15 Sensitivity analysis of the influence of airflow rate on the enhanced doped MgO hydration reaction.

This trend reinforces the critical role of solid-gas hydrodynamics in the overall performance of the fluidized bed reactor. As the inlet vapour/air flow rate increases, the fluidizing medium becomes more rigorous, promoting more solid particle suspension and increased interfacial contact between gas and solids. These factors contribute to faster reaction rates and higher conversion efficiency. This observation complements the earlier sensitivity analysis on water vapour concentration, further demonstrating that both composition and velocity of the fluidizing gas must be jointly optimized. Together, they define the reactive environment within the FBR, controlling not only chemical transformation but also the physical behaviour of particles and solid-gas contact dynamics.

In contrast to dehydration, hydration is an exothermic reaction involving heat release. Table 6.9 represents a summary of the temporal variation in temperature and heat during the exothermic rehydration of the developed material. The temperature profile (Figure 6.16) began at 200 ℃ and showed a steep decline to around 170 ℃, indicating that heat was being released and removed from the system. The associated heat duty was negative throughout the process, reaching −4.8 kW at its peak, clearly reflecting the exothermic character of the reaction. The magnitude of the heat duty during rehydration indicates a substantial energy release, which must be carefully managed to avoid temperature excursions that could affect fluidization stability. Notably, the heat released during hydration (−4.8 kW) is nearly equal in magnitude to the heat absorbed during dehydration (+5 kW). This near equivalence underscores the energy-conserving nature of the thermochemical storage system, affirming its potential for efficient thermal energy storage.

Table 6. 9 Representative temperatures and heat over time for the enhanced doped material hydration.

Time (s)	**Temperature (℃)**	**Heat duty (kW)**
0	25	0
60	84	0.96
120	143	1.92
180	202	2.88
240	261	3.84
300	320	4.8
360	220.7385599	2.634295853
420	166.2627266	1.445732217
480	136.3657554	0.793434663
540	119.9579497	0.435446176
600	110.953155	0.238977928

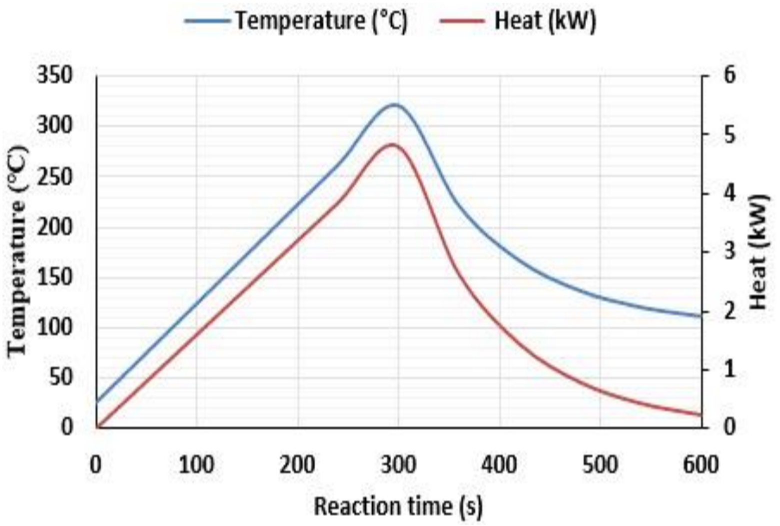

Figure 6. 16 Graphical presentation of **t**emperature and heat profiles during the hydration process.

In summary, the simulation of MgO hydration in the FBR demonstrates excellent conversion efficiency and highlights the importance of thermal control in exothermic solid-gas reactions. The alignment between stoichiometric predictions and simulated outputs validates the robustness of the Aspen Plus model used. At the same time, the reported heat duty offers critical insight for effective heat removal mechanisms or reactor thermal management strategies. This could involve the design of internal heat exchangers or external cooling loops. These findings affirm the FBR's viability for reactive solid-gas processing and provide a strong basis for further experimental validations towards industrial scale-up.

6.7 Potential impact of model simplifications and assumptions

Although Aspen Plus provides a robust platform for steady-state process simulation, its application to the modelling of complex fluidized bed reactors (FBRs) involves several simplifications and assumptions that may limit the accuracy and detail of its predictions. These limitations are especially relevant when simulating multiphase systems where fluid dynamics, heat and mass transfer, and particle-scale interactions are critical.

6.7.1 Mass balance simplifications

Aspen Plus implements mass conservation by averaging phase interactions across the reactor bed, accounting for gas and solid mass fractions, reaction stoichiometry, and phase holdups. However, it does not resolve spatial or temporal variations in flow fields. In real fluidized beds, phenomena such as bubble formation, slug flow, and channelling lead to significant non-uniformities in phase distribution and reactant contact. This homogenization in the model may lead to overprediction of conversion efficiency and an inability to detect zones of poor mixing or dead space within the reactor.

6.7.2 Momentum balance approximations

Momentum balance within the fluidized bed is approximated using empirical correlations such as the Ergun equation for pressure drop and the Wen-Yu drag model for solid-gas interactions. These correlations assume steady-state, ideal fluidization with spherical particles and uniform flow regimes. However, in industrial reactors, the presence of broad particle size distributions, non-spherical particles, and varying bed dynamics (such as bubbling or turbulent flow) can significantly alter pressure profiles and solid-gas contact behaviour, which Aspen Plus does not capture. This may result in limited reliability in predicting bed expansion, fluidization quality, and pressure drop under realistic conditions.

6.7.3 Energy balance simplifications

The energy balance is similarly treated with bulk-phase heat transfer models, using lumped parameters and semi-empirical interphase heat transfer coefficients. While suitable for steady-state analysis, this approach fails to resolve intra-particle temperature gradients or transient heat transfer effects, particularly in highly endothermic or exothermic reactions. Consequently, local thermal effects such as hot spots, temperature stratification, or heat transfer bottlenecks may be overlooked, potentially impacting safety or scale-up reliability.

6.7.4 Lack of detailed hydrodynamics and particle behaviour

Aspen Plus does not simulate detailed hydrodynamic structures such as bubble coalescence, wake regions, or particle-particle interactions. Additionally, phenomena such as entrainment, segregation, or agglomeration are not explicitly modelled. These features are critical in industrial-scale FBRs and directly influence reactor performance, residence time distribution, and separation requirements.

6.7.5 Static operation and limited dynamic response

The standard Aspen Plus environment is based on steady-state assumptions and does not simulate dynamic reactor behaviour. This limitation hinders the analysis of start-up and shutdown processes, transient disturbances, or process control strategies that are essential for industrial operations.

6.8 Justification for use of Aspen Plus simulation software

While next-level simulation tools such as Computational Fluid Dynamics (CFD) and Discrete Element Method (DEM) may offer significantly higher spatial and temporal resolution for modelling the complex hydrodynamics and particle behaviour in fluidized bed systems, these tools were not employed in the present study for the following reasons.

The primary aim in this chapter was to develop a process-level understanding of the dehydration and hydration of the developed magnesium hydroxide material in a fluidized bed reactor, with particular focus on reaction thermodynamics, mass transfer, and overall conversion efficiency. The level of resolution provided by Aspen Plus was deemed sufficient to meet these objectives, especially for preliminary design, sensitivity analysis, and performance evaluation. Incorporating CFD or DEM would have required a shift toward fluid mechanics-centric goals, which was beyond the intended scope of this thesis.

Additionally, Aspen Plus provides a unified environment for integrating reaction modelling with thermodynamics, heat integration, and downstream separation—essential for early-stage design and techno-economic assessment. While CFD and DEM are powerful for analyzing local bed dynamics, they are less suited for simulating integrated process flows or performing mass and energy balances across multiple units.

6.9 Concluding remarks

The numerical simulation study using Aspen Plus software provided key insights into the behaviour of the fluidized bed reactor for $Mg(OH)_2$ dehydration and hydration. The results demonstrate that fluidization began at 0.1850 m/s for dehydration and 0.01598 m/s for hydration, with the bed expanding as gas velocity increased. The pressure drop peaked before decreasing exponentially once fluidization was established. Sensitivity analysis indicated that low airflow rates resulted in low reaction conversion. Similarly, MgO hydration efficiency was found to depend on adequate availability of water vapour, with four times the stoichiometric moles achieving 99.78% $Mg(OH)_2$, while increasing the inlet air/vapour flow rate from 15 kg/hr to 175 kg/hr improved mixing and reaction enhancement. These findings emphasize the importance of optimal gas/vapour inlet flow rate and nearly 4:1 water vapour-$Mg(OH)_2$ mole flow rates in maximizing reaction and conversion efficiency in the fluidized bed reactor at ~300 °C and 2 bar.

The use of Aspen Plus facilitated the evaluation of key performance factors, offering valuable insights for optimizing the reactor operation. However, despite its advantages, the model relies on simplified fluid mechanics, idealized reaction conditions, and thermodynamic equilibrium assumptions, which may not fully capture real-world complexities.

Chapter 7: Conclusion and Recommendations for Future Work

7.1 Conclusion

The thesis was aimed at developing and evaluating a novel thermochemical energy storage (TCES) material suitable for medium-grade waste heat storage application in the buildings sector. Through a comprehensive and multidisciplinary approach, combining material synthesis, characterization, molecular-level simulation, and system-scale modelling, the research has addressed some of the key limitations of current TCES materials.

A significant contribution of this work is the development of an enhanced $Mg(OH)_2$-based composite with improved thermophysical properties, which are critical for practical TCES deployment. Evaluation of the developed material demonstrated lower dehydration temperatures and an increase in energy storage capacity, positioning it as a viable candidate for medium-grade waste heat storage applications.

The molecular dynamics simulations provided further validation of material performance, offering a predictive understanding of thermophysical properties and informing precise experimental direction. Meanwhile, the numerical evaluation of the material in a model agitated fluidized bed reactor using Aspen Plus allowed for detailed analysis of system behaviour, identifying key operating conditions necessary for achieving high conversion efficiency and stable reactor performance.

The key findings of this research may therefore be summarized as follows:

- Material performance
    - 5 wt% KNO_3-doped $Mg(OH)_2$ material showed a reduction in the dehydration temperature from ~317 ℃ to 293 ℃, enabling more waste heat capture within the temperature range of 293–400 ℃.

    - The heat storage capacity increased from 1246 J/g (pure $Mg(OH)_2$) to 1317 J/g in the doped composite.
- Thermal conductivity enhancement
    - Molecular simulation predicted a thermal conductivity of 0.708 W/mK with 15 wt% Al_2O_3 nanomaterials—an enhancement of 12.9%—compared to the experimental value of 0.6484 W/mK.
- Numerical modelling of a 1.5 kg material in a model agitated fluidized bed reactor showed
    - The dehydration reaction progressed from 300 ℃ at an airflow rate of 28.95 kg/hr, achieving a minimum fluidization velocity of 0.1850 m/s.
    - A 99.99% dehydration reaction efficiency was achieved with a desorption heat of +5 kW.
    - Hydration began at 200 ℃ with airflow mixed with water vapour, attaining a minimum fluidization velocity of 0.01598 m/s.
    - A 99.21% hydration reaction efficiency was achieved, releasing −4.8 kW of heat.
    - Water vapour was a limiting factor for MgO hydration beyond a 4:1 molar ratio, indicating equilibrium saturation.

In summary, the combined findings from material synthesis, molecular modelling, and reactor simulation demonstrate that the newly developed $Mg(OH)_2$-KNO_3-Al_2O_3 composite exhibits:

- Suitable thermal characteristics for medium-temperature TCE storage.
- Enhanced thermal conductivity for improved heat transfer.
- High reaction conversion when deployed in an agitated fluidized bed rig under suitable conditions.

7.2 Recommendations for future work

Building on the insights gained from this research, several opportunities exist for further development and refinement of thermochemical energy storage systems and materials. The following recommendations are aimed at ensuring that the advances made in this study can be translated into robust, scalable, and commercially viable energy storage solutions, addressing both technical and practical challenges in the transition to low-carbon energy systems.

1. Long-term cyclability and material stability.

While the developed $Mg(OH)_2$–KNO_3–Al_2O_3 composite showed promising performance in terms of dehydration temperature and energy storage capacity, future work should focus on:

- Long-term cyclic testing (charging/discharging over many cycles) to assess thermal and chemical stability under repeated operation.
- Investigating potential degradation mechanisms, including surface topology or phase changes in constituent materials over time.

2. Material composition and optimization.

The current study optimized material performance with a specific ratio of KNO_3 and Al_2O_3. Further work could explore:

- Alternative dopants or composite structures, such as other nitrates, and evaluate their characteristics and performance.
- The use of binders, coatings, or encapsulation methods to improve cyclic durability and prevent particle agglomeration or sintering.

3. Experimental validation of reactor performance.

The Aspen Plus model provided valuable thermodynamic insights that relied on simplified fluid flow assumptions. To close the gap between modelling and reality:

- A lab-scale fluidized bed reactor should be designed and implemented to validate the model’s assumptions and results.
- Parameters such as pressure drop, fluidization behaviour, heat transfer, and reaction conversion should be measured under realistic conditions.

4. Advanced reactor modelling.

For a more accurate and detailed understanding of heat and mass transfer phenomena:

- Computational fluid dynamics (CFD) simulations could be employed to capture non-ideal flow patterns and spatial temperature gradients.
- Coupling CFD with reaction kinetics would support the optimization of reactor geometry and operating conditions.

5. System integration and techno-economic analysis.

For the technology to transition from laboratory research to practical deployment:

- Integration studies should be conducted to assess how the developed material and reactor can be incorporated into real waste heat recovery systems (e.g., industrial furnaces, power plants, or HVAC systems).
- Techno-economic assessments are needed to evaluate cost, scalability, return on investment, and lifecycle performance in comparison to competing storage technologies (e.g., sensible or latent heat storage).

References

1. Abergel, T.; Delmastro, C.; Janoska, P.; Lane, K.; Prag, A. *Perspectives for the Clean Energy Transition: The Critical Role of Buildings*; 2019;

2. Eames P; Loveday D; Haines V; Romanos P The Future Role of Thermal Energy Storage in the UK Energy System | UKERC | The UK Energy Research Centre Available online: https://ukerc.ac.uk/publications/the-future-role-of-thermal-energy-storage-in-the-uk-energy-system/ (accessed on 4 January 2022).

3. Friedlingstein, P.; Le Quéré, C.; Pongratz, J.; O'Sullivan, M.; Peters, G.; Ciais, P. Global Carbon Budget Report 2023 Available online: https://globalcarbonbudget.org/fossil-co2-emissions-at-record-high-in-2023/ (accessed on 26 December 2023).

4. CCC The Sixth Carbon Budget--Buildings Available online: https://www.theccc.org.uk/wp-content/uploads/2020/12/Sector-summary-Buildings.pdf (accessed on 11 January 2024).

5. Albert, M.D.A.; Bennett, K.O.; Adams, C.A.; Gluyas, J.G. Waste Heat Mapping: A UK Study. *Renewable and Sustainable Energy Reviews* **2022**, *160*, doi:10.1016/j.rser.2022.112230.

6. Papapetrou, M.; Kosmadakis, G.; Cipollina, A.; La Commare, U.; Micale, G. Industrial Waste Heat: Estimation of the Technically Available Resource in the EU per Industrial Sector, Temperature Level and Country. *Appl Therm Eng* **2018**, *138*, 207–216, doi:10.1016/j.applthermaleng.2018.04.043.

7. Bauer, T. Fundamentals of High-Temperature Thermal Energy Storage, Transfer, and Conversion. In *Ultra-High Temperature Thermal Energy Storage, Transfer and Conversion*; Elsevier, 2021; pp. 1–34.

8. Behzadi, A.; Holmberg, S.; Duwig, C.; Haghighat, F.; Ooka, R.; Sadrizadeh, S. Smart Design and Control of Thermal Energy Storage in Low-Temperature Heating and High-Temperature Cooling Systems: A Comprehensive Review. *Renewable and Sustainable Energy Reviews* 2022, *166*.

9. N'Tsoukpoe, K.E.; Kuznik, F. A Reality Check on Long-Term Thermochemical Heat Storage for Household Applications. *Renewable and Sustainable Energy Reviews* 2021, *139*.

10. Lizana, J.; Chacartegui, R.; Barrios-Padura, Á.; Valverde, J.M. Characterization of Thermal Energy Storage Materials for Building Applications. In Proceedings of the Proceedings of the 3rd International Congress on Sustainable Construction and Eco-Efficient Solutions; Mercader-Moyano, P., Ed.; Seville, March 27 2017; pp. 606–620.

11. Wu, S. Heat Energy Storage and Cooling in Buildings. In *Materials for Energy Efficiency and Thermal Comfort in Buildings*; Hall, M.R., Ed.; Woodhead Publishing, 2010; pp. 101–126 ISBN 9781845695262.

12. Sun, M.; Liu, T.; Wang, X.; Liu, T.; Li, M.; Chen, G.; Jiang, D. Roles of Thermal Energy Storage Technology for Carbon Neutrality. *Carbon Neutrality* 2023, *2*.

13. Furbo, S. Using Water for Heat Storage in Thermal Energy Storage (TES) Systems. In *Advances in Thermal Energy Storage Systems: Methods and Applications*; 2015.

14. Bauer, T.; Pfleger, N.; Breidenbach, N.; Eck, M.; Laing, D.; Kaesche, S. Material Aspects of Solar Salt for Sensible Heat Storage. *Appl Energy* **2013**, *111*, doi:10.1016/j.apenergy.2013.04.072.

15. Alva, G.; Liu, L.; Huang, X.; Fang, G. Thermal Energy Storage Materials and Systems for Solar Energy Applications. *Renewable and Sustainable Energy Reviews* 2017, *68*, 693–706.

16. Danehkar, S.; Yousefi, H. A Comprehensive Overview on Water-Based Energy Storage Systems for Solar Applications. *Energy Reports* 2022, *8*, 8777–8797.

17. Tatsidjodoung, P.; Le Pierrès, N.; Luo, L. A Review of Potential Materials for Thermal Energy Storage in Building Applications. *Renewable and Sustainable Energy Reviews* 2013, *18*, 327–349.

18. Hauer, A. Thermal Energy Storage Available online: https://www.irena.org/-/media/Files/IRENA/Agency/Publication/2013/IRENA-ETSAP-Tech-Brief-E17-Thermal-Energy-Storage.pdf (accessed on 27 May 2024).

19. Kemna, R.; van Elburg, M.; Aarts, S. Water Heaters and Storage Tanks Available online: https://www.eceee.org/static/media/uploads/site-2/ecodesign/products/Water%20heaters%20ENER%20Lot%202/water_heaters_task_1_final_report_july_2019.pdf (accessed on 28 May 2024).

20. Sarbu, I.; Sebarchievici, C. A Comprehensive Review of Thermal Energy Storage. *Sustainability (Switzerland)* 2018, *10*.

21. Bespalko, S.; Miranda, A.M.; Halychyi, O. Overview of the Existing Heat Storage Technologies: Sensible Heat. *Acta Innovations* **2018**, 82–113, doi:10.32933/ActaInnovations.28.8.

22. Al-Yasiri, Q.; Szabó, M. Incorporation of Phase Change Materials into Building Envelope for Thermal Comfort and Energy Saving: A Comprehensive Analysis. *Journal of Building Engineering* 2021, *36*.

23. Sharma, S.D.; Sagara, K. Latent Heat Storage Materials and Systems: A Review. *Int J Green Energy* **2005**, *2*, doi:10.1081/ge-200051299.

24. Jouhara, H.; Żabnieńska-Góra, A.; Khordehgah, N.; Ahmad, D.; Lipinski, T. Latent Thermal Energy Storage Technologies and Applications: A Review. *International Journal of Thermofluids* **2020**, *5–6*, doi:10.1016/j.ijft.2020.100039.

25. Mabrouk, R.; Naji, H.; Benim, A.C.; Dhahri, H. A State of the Art Review on Sensible and Latent Heat Thermal Energy Storage Processes in Porous Media: Mesoscopic Simulation. *Applied Sciences (Switzerland)* 2022, *12*.

26. Du, K.; Calautit, J.; Wang, Z.; Wu, Y.; Liu, H. A Review of the Applications of Phase Change Materials in Cooling, Heating and Power Generation in Different Temperature Ranges. *Appl Energy* 2018, *220*.

27. Masood, U.; Haggag, M.; Hassan, A.; Laghari, M. A Review of Phase Change Materials as a Heat Storage Medium for Cooling Applications in the Built Environment. *Buildings* 2023, *13*.

28. Phase Change Materials Available online: https://thermalds.com/phase-change-materials/ (accessed on 30 July 2025).

29. da Cunha, S.R.L.; de Aguiar, J.L.B. Phase Change Materials and Energy Efficiency of Buildings: A Review of Knowledge. *J Energy Storage* 2020, *27*.

30. Podara, C. V.; Kartsonakis, I.A.; Charitidis, C.A. Towards Phase Change Materials for Thermal Energy Storage: Classification, Improvements and Applications in the Building Sector. *Applied Sciences (Switzerland)* **2021**, *11*, 1–26, doi:10.3390/app11041490.

31. Sevault, A.; Vullum-Bruer, F.; Tranås, O.L. Active PCM-Based Thermal Energy Storage in Buildings. In *Encyclopedia of Energy Storage: Volume 1-4*; 2022; Vol. 1–4.

32. Ghadim, H.B.; Shahbaz, K.; Al-Shannaq, R.; Farid, M.M. Binary Mixtures of Fatty Alcohols and Fatty Acid Esters as Novel Solid-Liquid Phase Change Materials. *Int J Energy Res* **2019**, *43*, doi:10.1002/er.4852.

33. Zahir, M.H.; Irshad, K.; Shafiullah, M.; Ibrahim, N.I.; Kausarul Islam, A.K.M.; Mohaisen, K.O.; Sulaiman, F.A.A. Challenges of the Application of PCMs to Achieve Zero Energy Buildings under Hot Weather Conditions: A Review. *J Energy Storage* 2023, *64*.

34. RESTORE Thermochemical Energy Storage Available online: https://www.restore-dhc.eu/about-restore/thermochemical-energy-storage/# (accessed on 9 January 2024).

35. Chen, X.; Zhang, Z.; Qi, C.; Ling, X.; Peng, H. State of the Art on the High-Temperature Thermochemical Energy Storage Systems. *Energy Convers Manag* 2018, *177*, 792–815.

36. Pardo, P.; Deydier, A.; Anxionnaz-Minvielle, Z.; Rougé, S.; Cabassud, M.; Cognet, P. A Review on High Temperature Thermochemical Heat Energy Storage. *Renewable and Sustainable Energy Reviews* 2014, *32*, 591–610.

37. Farulla, G.A.; Cellura, M.; Guarino, F.; Ferraro, M. A Review of Thermochemical Energy Storage Systems for Power Grid Support. *Applied Sciences (Switzerland)* 2020, *10*.

38. André, L.; Abanades, S. Recent Advances in Thermochemical Energy Storage via Solid–Gas Reversible Reactions at High Temperature. *Energies (Basel)* 2020, *13*.

39. Yan, Y.; Wang, K.; Clough, P.T.; Anthony, E.J. Developments in Calcium/Chemical Looping and Metal Oxide Redox Cycles for High-Temperature Thermochemical Energy Storage: A Review. *Fuel Processing Technology* 2020, *199*.

40. Scapino, L.; Zondag, H.A.; Van Bael, J.; Diriken, J.; Rindt, C.C.M. Sorption Heat Storage for Long-Term Low-Temperature Applications: A Review on the Advancements at Material and Prototype Scale. *Appl Energy* 2017, *190*, 920–948.

41. Kur, A.; Darkwa, J.; Calautit, J.; Boukhanouf, R.; Worall, M. Solid–Gas Thermochemical Energy Storage Materials and Reactors for Low to High-Temperature Applications: A Concise Review. *Energies (Basel)* 2023, *16*.

42. Zsembinszki, G.; Sole, A.; Barreneche, C.; Prieto, C.; Fernández, A.I.; Cabeza, L.F. Review of Reactors with Potential Use in Thermochemical Energy Storage in Concentrated Solar Power Plants. *Energies (Basel)* **2018**, *11*, doi:10.3390/en11092358.

43. Cabeza, L.F.; Martorell, I.; Miró, L.; Fernández, A.I.; Barreneche, C. Introduction to Thermal Energy Storage (TES) Systems. In *Advances in Thermal Energy Storage Systems: Methods and Applications*; 2015.

44. Shkatulov, A.; Aristov, Y. Modification of Magnesium and Calcium Hydroxides with Salts: An Efficient Way to Advanced Materials for Storage of Middle-Temperature Heat. *Energy* **2015**, *85*, 667–676, doi:10.1016/j.energy.2015.04.004.

45. Felderhoff, M.; Urbanczyk, R.; Peil, S. Thermochemical Heat Storage for High Temperature Applications-A Review. *Green* 2013, *3*, 113–123.

46. Cot-Gores, J.; Castell, A.; Cabeza, L.F. Thermochemical Energy Storage and Conversion: A-State-of-the-Art Review of the Experimental Research under Practical Conditions. *Renewable and Sustainable Energy Reviews* 2012, *16*.

47. Carrillo, A.J.; González-Aguilar, J.; Romero, M.; Coronado, J.M. Solar Energy on Demand: A Review on High Temperature Thermochemical Heat Storage Systems and Materials. *Chem Rev* **2019**, *119*, doi:10.1021/acs.chemrev.8b00315.

48. Lin, J.; Zhao, Q.; Huang, H.; Mao, H.; Liu, Y.; Xiao, Y. Applications of Low-Temperature Thermochemical Energy Storage Systems for Salt Hydrates Based on Material Classification: A Review. *Solar Energy* 2021, *214*, 149–178.

49. Clark, R.J.; Mehrabadi, A.; Farid, M. State of the Art on Salt Hydrate Thermochemical Energy Storage Systems for Use in Building Applications. *J Energy Storage* 2020, *27*.

50. Marín, P.E.; Milian, Y.; Ushak, S.; Cabeza, L.F.; Grágeda, M.; Shire, G.S.F. Lithium Compounds for Thermochemical Energy Storage: A State-of-the-Art Review and Future Trends. *Renewable and Sustainable Energy Reviews* 2021, *149*.

51. Molenda, M.; Stengler, J.; Linder, M.; Wörner, A. Reversible Hydration Behavior of CaCl2 at High H2O Partial Pressures for Thermochemical Energy Storage. *Thermochim Acta* **2013**, *560*, 76–81, doi:10.1016/j.tca.2013.03.020.

52. Rammelberg, H.U.; Schmidt, T.; Ruck, W. Hydration and Dehydration of Salt Hydrates and Hydroxides for Thermal Energy Storage - Kinetics and Energy Release. In Proceedings of the Energy Procedia; Elsevier Ltd, 2012; Vol. 30, pp. 362–369.

53. van Essen, V.M.; Cot Gores, J.; Bleijendaal, L.P.J.; Zondag, H.A.; Schuitema, R.; Bakker, M.; van Helden, W.G.J. Characterization of Salt Hydrates for Compact Seasonal Thermochemical Storage. In Proceedings of the Proceedings of the ASME 3rd International Conference on Energy Sustainability 2009, ES2009; 2009; Vol. 2, pp. 825–830.

54. Posern, K.; Kaps, C. Calorimetric Studies of Thermochemical Heat Storage Materials Based on Mixtures of MgSO4 and MgCl2. *Thermochim Acta* **2010**, *502*, 73–76, doi:10.1016/j.tca.2010.02.009.

55. Fopah Lele, A.; N'Tsoukpoe, K.E.; Osterland, T.; Kuznik, F.; Ruck, W.K.L. Thermal Conductivity Measurement of Thermochemical Storage Materials. *Appl Therm Eng* **2015**, *89*, 916–926, doi:10.1016/j.applthermaleng.2015.06.077.

56. Michel, B.; Neveu, P.; Mazet, N. Comparison of Closed and Open Thermochemical Processes, for Long-Term Thermal Energy Storage Applications. *Energy* **2014**, *72*, 702–716, doi:10.1016/j.energy.2014.05.097.

57. N'Tsoukpoe, K.E.; le Pierrès, N.; Luo, L. Numerical Dynamic Simulation and Analysis of a Lithium Bromide/Water Long-Term Solar Heat Storage System. *Energy* **2012**, *37*, doi:10.1016/j.energy.2011.11.020.

58. Donkers, P.A.J.; Beckert, S.; Pel, L.; Stallmach, F.; Steiger, M.; Adan, O.C.G. Water Transport in MgSO4·7H2O during Dehydration in View of Thermal Storage. *Journal of Physical Chemistry C* **2015**, *119*, 28711–28720, doi:10.1021/acs.jpcc.5b08730.

59. N'Tsoukpoe, K.E.; Schmidt, T.; Rammelberg, H.U.; Watts, B.A.; Ruck, W.K.L. A Systematic Multi-Step Screening of Numerous Salt Hydrates for Low Temperature Thermochemical Energy Storage. *Appl Energy* **2014**, *124*, 1–16, doi:10.1016/j.apenergy.2014.02.053.

60. Donkers, P.A.J.; Pel, L.; Adan, O.C.G. Experimental Studies for the Cyclability of Salt Hydrates for Thermochemical Heat Storage. *J Energy Storage* **2016**, *5*, 25–32, doi:10.1016/j.est.2015.11.005.

61. de Jong, A.J.; Trausel, F.; Finck, C.; van Vliet, L.; Cuypers, R. Thermochemical Heat Storage - System Design Issues. In Proceedings of the Energy Procedia; Elsevier Ltd, 2014; Vol. 48, pp. 309–319.

62. Gaeini, M.; Shaik, S.A.; Rindt, C.C.M. Characterization of Potassium Carbonate Salt Hydrate for Thermochemical Energy Storage in Buildings. *Energy Build* **2019**, *196*, 178–193, doi:10.1016/j.enbuild.2019.05.029.

63. Donkers, P.A.J.; Sögütoglu, L.C.; Huinink, H.P.; Fischer, H.R.; Adan, O.C.G. A Review of Salt Hydrates for Seasonal Heat Storage in Domestic Applications. *Appl Energy* 2017, *199*, 45–68.

64. Solé, A.; Martorell, I.; Cabeza, L.F. State of the Art on Gas-Solid Thermochemical Energy Storage Systems and Reactors for Building Applications. *Renewable and Sustainable Energy Reviews* 2015, *47*.

65. Zhao, Y.J.; Wang, R.Z.; Zhang, Y.N.; Yu, N. Development of SrBr2 Composite Sorbents for a Sorption Thermal Energy Storage System to Store Low-Temperature Heat. *Energy* **2016**, *115*, doi:10.1016/j.energy.2016.09.013.

66. Zhao, Q.; Lin, J.; Huang, H.; Wu, Q.; Shen, Y.; Xiao, Y. Optimization of Thermochemical Energy Storage Systems Based on Hydrated Salts: A Review. *Energy Build* 2021, *244*.

67. Ait Ousaleh, H.; Sair, S.; Zaki, A.; Faik, A.; Mirena Igartua, J.; el Bouari, A. Double Hydrates Salt as Sustainable Thermochemical Energy Storage Materials: Evaluation of Dehydration Behavior and Structural Phase Transition Reversibility. *Solar Energy* **2020**, *201*, doi:10.1016/j.solener.2020.03.067.

68. d'Entremont, A.; Corgnale, C.; Hardy, B.; Zidan, R. Simulation of High Temperature Thermal Energy Storage System Based on Coupled Metal Hydrides for Solar Driven Steam Power Plants. *Int J Hydrogen Energy* **2018**, *43*, doi:10.1016/j.ijhydene.2017.11.100.

69. Carrillo, A.J.; Moya, J.; Bayón, A.; Jana, P.; De La Peña O'Shea, V.A.; Romero, M.; Gonzalez-Aguilar, J.; Serrano, D.P.; Pizarro, P.; Coronado, J.M. Thermochemical Energy Storage at High Temperature via Redox Cycles of Mn and Co Oxides: Pure Oxides versus Mixed Ones. *Solar Energy Materials and Solar Cells* **2014**, *123*, 47–57, doi:10.1016/j.solmat.2013.12.018.

70. Harries, D.N.; Paskevicius, M.; Sheppard, D.A.; Price, T.E.C.; Buckley, C.E. Concentrating Solar Thermal Heat Storage Using Metal Hydrides. In Proceedings of the Proceedings of the IEEE; 2012; Vol. 100.

71. Felderhoff, M.; Bogdanović, B. High Temperature Metal Hydrides as Heat Storage Materials for Solar and Related Applications. *Int J Mol Sci* 2009, *10*, 335–344.

72. Sunku Prasad, J.; Muthukumar, P.; Desai, F.; Basu, D.N.; Rahman, M.M. A Critical Review of High-Temperature Reversible Thermochemical Energy Storage Systems. *Appl Energy* 2019, *254*.

73. Zhang, J.; Sun, L.Q.; Zhou, Y.C.; Peng, P. Dehydrogenation Thermodynamics of Magnesium Hydride Doped with Transition Metals: Experimental and Theoretical Studies. *Comput Mater Sci* **2015**, *98*, 211–219, doi:10.1016/j.commatsci.2014.11.016.

74. Zhou, C.; Zhang, J.; Bowman, R.C.; Fang, Z.Z. Roles of Ti-Based Catalysts on Magnesium Hydride and Its Hydrogen Storage Properties. *Inorganics (Basel)* 2021, *9*.

75. Khan, D.; Zou, J.; Zeng, X.; Ding, W. Hydrogen Storage Properties of Nanocrystalline Mg2Ni Prepared from Compressed 2MgH2–Ni Powder. *Int J Hydrogen Energy* **2018**, *43*, doi:10.1016/j.ijhydene.2018.10.055.

76. Banrejee, S.; Kumar, A.; Ruz, P.; Sudarsan, V. Improvement of Hydrogen Storage Characteristics of Catalyst Free Magnesium Nanoparticles Prepared by Wet Milling. *Int J Energy Res* **2021**, *45*, doi:10.1002/er.7046.

77. Chen, X.; Zou, J.; Zeng, X.; Ding, W. Hydrogen Storage Properties of a Mg-La-Fe-H Nano-Composite Prepared through Reactive Ball Milling. *J Alloys Compd* **2017**, *701*, doi:10.1016/j.jallcom.2017.01.056.

78. Silva, R.A.; Leal Neto, R.M.; Leiva, D.R.; Ishikawa, T.T.; Kiminami, C.S.; Jorge, A.M.; Botta, W.J. Room Temperature Hydrogen Absorption by Mg and Mg–TiFe Nanocomposites Processed by High-Energy Ball Milling. *Int J Hydrogen Energy* **2018**, *43*, doi:10.1016/j.ijhydene.2018.04.174.

79. Kim, K.C. A Review on Design Strategies for Metal Hydrides with Enhanced Reaction Thermodynamics for Hydrogen Storage Applications. *Int J Energy Res* 2018, *42*, 1455–1468.

80. Bogdanovi, B.; Reiser, A.; Schlichte, K.; Spliethoff, B.; Tesche, B. Thermodynamics and Dynamics of the Mg-Fe-H System and Its Potential for Thermochemical Thermal Energy Storage. *J Alloys Compd* **2002**, *345*, doi:10.1016/S0925-8388(02)00308-0.

81. Sulaiman, N.N.; Juahir, N.; Mustafa, N.S.; Halim Yap, F.A.; Ismail, M. Improved Hydrogen Storage Properties of MgH2 Catalyzed with K2NiF6. *Journal of Energy Chemistry* **2016**, *25*, doi:10.1016/j.jechem.2016.04.015.

82. Abdul Majid, N.A.; Maeda, N.; Notomi, M. Improved Hydrogen Desorption Properties of Magnesium Hydride with TiFe0.8Mn0.2, Graphite and Iron Addition. *Int J Hydrogen Energy* **2019**, *44*, doi:10.1016/j.ijhydene.2019.02.190.

83. Kumar, E.M.; Rajkamal, A.; Thapa, R. Screening Based Approach and Dehydrogenation Kinetics for MgH2: Guide to Find Suitable Dopant Using First-Principles Approach. *Sci Rep* **2017**, *7*, doi:10.1038/s41598-017-15694-x.

84. Jain, P.; Dixit, V.; Jain, A.; Srivastava, O.N.; Huot, J. Effect of Magnesium Fluoride on Hydrogenation Properties of Magnesium Hydride. *Energies (Basel)* **2015**, *8*, doi:10.3390/en81112330.

85. Zhu, M.; Lu, Y.; Ouyang, L.; Wang, H. Thermodynamic Tuning of Mg-Based Hydrogen Storage Alloys: A Review. *Materials* **2013**, *6*, doi:10.3390/ma6104654.

86. André, L.; Abanades, S.; Flamant, G. Screening of Thermochemical Systems Based on Solid-Gas Reversible Reactions for High Temperature Solar Thermal Energy Storage. *Renewable and Sustainable Energy Reviews* 2016, *64*, 703–715.

87. Schaube, F.; Koch, L.; Wörner, A.; Müller-Steinhagen, H. A Thermodynamic and Kinetic Study of the De- and Rehydration of Ca(OH) 2 at High H 2O Partial Pressures for Thermo-Chemical Heat Storage. *Thermochim Acta* **2012**, *538*, 9–20, doi:10.1016/j.tca.2012.03.003.

88. Schaube, F.; Kohzer, A.; Schütz, J.; Wörner, A.; Müller-Steinhagen, H. De- and Rehydration of Ca(OH)2 in a Reactor with Direct Heat Transfer for Thermo-Chemical Heat Storage. Part A: Experimental Results. *Chemical Engineering Research and Design* **2013**, *91*, doi:10.1016/j.cherd.2012.09.020.

89. Criado, Y.A.; Alonso, M.; Abanades, J.C. Kinetics of the CaO/Ca(OH)2 Hydration/Dehydration Reaction for Thermochemical Energy Storage Applications. *Ind Eng Chem Res* **2014**, *53*, 12594–12601, doi:10.1021/ie404246p.

90. Dai, L.; Long, X.F.; Lou, B.; Wu, J. Thermal Cycling Stability of Thermochemical Energy Storage System Ca(OH)2/CaO. *Appl Therm Eng* **2018**, *133*, 261–268, doi:10.1016/j.applthermaleng.2018.01.059.

91. Huang, C.; Xu, M.; Huai, X. Experimental Investigation on Thermodynamic and Kinetic of Calcium Hydroxide Dehydration with Hexagonal Boron Nitride Doping for Thermochemical Energy Storage. *Chem Eng Sci* **2019**, *206*, doi:10.1016/j.ces.2019.06.002.

92. Shkatulov, A.; Aristov, Y. Calcium Hydroxide Doped by KNO3 as a Promising Candidate for Thermochemical Storage of Solar Heat. *RSC Adv* **2017**, *7*, 42929–42939, doi:10.1039/c7ra06639b.

93. Wang, T.; Zhao, C.Y.; Yan, J. Investigation on the Ca(OH)2/CaO Thermochemical Energy Storage System with Potassium Nitrate Addition. *Solar Energy Materials and Solar Cells* **2020**, *215*, doi:10.1016/j.solmat.2020.110646.

94. Gollsch, M.; Afflerbach, S.; Angadi, B. V.; Linder, M. Investigation of Calcium Hydroxide Powder for Thermochemical Storage Modified with Nanostructured Flow Agents. *Solar Energy* **2020**, *201*, 810–818, doi:10.1016/j.solener.2020.03.033.

95. Cosquillo Mejia, A.; Afflerbach, S.; Linder, M.; Schmidt, M. Experimental Analysis of Encapsulated CaO/Ca(OH)2 Granules as Thermochemical Storage in a Novel Moving Bed Reactor. *Appl Therm Eng* **2020**, *169*, doi:10.1016/j.applthermaleng.2020.114961.

96. Afflerbach, S.; Afflerbach, K.; Trettin, R.; Krumm, W. Improvement of a Semipermeable Shell for Encapsulation of Calcium Hydroxide for Thermochemical Heat Storage Solutions: Material Design and Evaluation in Laboratory and Reactor Scale. *Solar Energy* **2021**, *217*, 208–222, doi:10.1016/j.solener.2021.02.005.

97. Afflerbach, S.; Kappes, M.; Gipperich, A.; Trettin, R.; Krumm, W. Semipermeable Encapsulation of Calcium Hydroxide for Thermochemical Heat Storage Solutions. *Solar Energy* **2017**, *148*, 1–11, doi:10.1016/j.solener.2017.03.074.

98. Yan, J.; Pan, Z.H.; Zhao, C.Y. Experimental Study of MgO/Mg(OH)2 Thermochemical Heat Storage with Direct Heat Transfer Mode. *Appl Energy* **2020**, *275*, doi:10.1016/j.apenergy.2020.115356.

99. Kato, Y.; Yamashita, N.; Yoshizawa, Y. Study of Chemical Heat Pump with Reaction System of Magnesium Oxide/Water. *Japan Science Technology Information Aggregator, Electronic* **1993**, *19*, 1213–1216, doi:10.1252/kakoronbunshu.19.1213.

100. Kato, Y.; Takahashi, F.; Watanabe, A.; Yoshizawa, Y. Thermal Analysis of a Magnesium Oxide/Water Chemical Heat Pump for Cogeneration. *Appl Therm Eng* **2001**, *21*, 1067–1081, doi:10.1016/S1359-4311(00)00103-4.

101. Ryu, J.; Hirao, N.; Takahashi, R.; Kato, Y. Dehydration Behavior of Metal-Salt-Added Magnesium Hydroxide as Chemical Heat Storage Media. *Chem Lett* **2008**, *37*, 1140–1141, doi:10.1246/cl.2008.1140.

102. Shkatulov, A.; Krieger, T.; Zaikovskii, V.; Chesalov, Y.; Aristov, Y. Doping Magnesium Hydroxide with Sodium Nitrate: A New Approach to Tune the Dehydration Reactivity of Heat-Storage Materials. *ACS Appl Mater Interfaces* **2014**, *6*, 19966–19977, doi:10.1021/am505418z.

103. Shkatulov, A.I.; Aristov, Y. Thermochemical Energy Storage Using LiNO3-Doped Mg(OH)2: A Dehydration Study. *Energy Technology* **2018**, *6*, 1844–1851, doi:10.1002/ente.201800050.

104. Sun, L.; Wu, Q.; Zhang, L.; Li, Y.; Li, M.; Gao, T.; Guo, S.; Wang, D. Doping Magnesium Hydroxide with Ce(NO3)3: A Promising Candidate Thermochemical Energy Storage Materials. In Proceedings

of the IOP Conference Series: Earth and Environmental Science; Institute of Physics Publishing, July 26 2019; Vol. 295.

105. Li, S.; Liu, J.; Tan, T.; Nie, J.; Zhang, H. Optimization of LiNO3–Mg(OH)2 Composites as Thermo-Chemical Energy Storage Materials. *J Environ Manage* **2020**, *262*, doi:10.1016/j.jenvman.2020.110258.

106. André, L.; Abanades, S. Investigation of Metal Oxides, Mixed Oxides, Perovskites and Alkaline Earth Carbonates/Hydroxides as Suitable Candidate Materials for High-Temperature Thermochemical Energy Storage Using Reversible Solid-Gas Reactions. *Mater Today Energy* **2018**, *10*, doi:10.1016/j.mtener.2018.08.007.

107. André, L.; Abanades, S. Evaluation and Performances Comparison of Calcium, Strontium and Barium Carbonates during Calcination/Carbonation Reactions for Solar Thermochemical Energy Storage. *J Energy Storage* **2017**, *13*, 193–205, doi:10.1016/j.est.2017.07.014.

108. Lu, S.; Wu, S. Calcination-Carbonation Durability of Nano CaCO3 Doped with Li2SO4. *Chemical Engineering Journal* **2016**, *294*, doi:10.1016/j.cej.2016.02.100.

109. Daud, F.D.M.; Vignesh, K.; Sreekantan, S.; Mohamed, A.R. Improved CO2 Adsorption Capacity and Cyclic Stability of CaO Sorbents Incorporated with MgO. *New Journal of Chemistry* **2016**, *40*, doi:10.1039/c5nj02081f.

110. Wang, K.; Gu, F.; Clough, P.T.; Zhao, P.; Anthony, E.J. Porous MgO-Stabilized CaO-Based Powders/Pellets via a Citric Acid-Based Carbon Template for Thermochemical Energy Storage in Concentrated Solar Power Plants. *Chemical Engineering Journal* **2020**, *390*, doi:10.1016/j.cej.2020.124163.

111. Benitez-Guerrero, M.; Valverde, J.M.; Perejon, A.; Sanchez-Jimenez, P.E.; Perez-Maqueda, L.A. Low-Cost Ca-Based Composites Synthesized by Biotemplate Method for Thermochemical Energy Storage of Concentrated Solar Power. *Appl Energy* **2018**, *210*, 108–116, doi:10.1016/j.apenergy.2017.10.109.

112. Chen, X.; Jin, X.; Liu, Z.; Ling, X.; Wang, Y. Experimental Investigation on the CaO/CaCO3 Thermochemical Energy Storage with SiO2 Doping. *Energy* **2018**, *155*, 128–138, doi:10.1016/j.energy.2018.05.016.

113. Da, Y.; Xuan, Y.; Teng, L.; Zhang, K.; Liu, X.; Ding, Y. Calcium-Based Composites for Direct Solar-Thermal Conversion and Thermochemical Energy Storage. *Chemical Engineering Journal* **2020**, *382*, doi:10.1016/j.cej.2019.122815.

114. Sun, H.; Li, Y.; Yan, X.; Zhao, J.; Wang, Z. Thermochemical Energy Storage Performance of Al2O3/CeO2 Co-Doped CaO-Based Material under High Carbonation Pressure. *Appl Energy* **2020**, *263*, doi:10.1016/j.apenergy.2020.114650.

115. Raganati, F.; Chirone, R.; Ammendola, P. Calcium-Looping for Thermochemical Energy Storage in Concentrating Solar Power Applications: Evaluation of the Effect of Acoustic Perturbation on the Fluidized Bed Carbonation. *Chemical Engineering Journal* **2020**, *392*, doi:10.1016/j.cej.2019.123658.

116. Møller, K.T.; Ibrahim, A.; Buckley, C.E.; Paskevicius, M. Inexpensive Thermochemical Energy Storage Utilising Additive Enhanced Limestone. *J Mater Chem A Mater* **2020**, *8*, 9646–9653, doi:10.1039/d0ta03080e.

117. Block, T.; Schmücker, M. Metal Oxides for Thermochemical Energy Storage: A Comparison of Several Metal Oxide Systems. *Solar Energy* **2016**, *126*, 195–207, doi:10.1016/j.solener.2015.12.032.

118. Silakhori, M.; Jafarian, M.; Arjomandi, M.; Nathan, G.J. Thermogravimetric Analysis of Cu, Mn, Co, and Pb Oxides for Thermochemical Energy Storage. *J Energy Storage* **2019**, *23*, 138–147, doi:10.1016/j.est.2019.03.008.

119. Deutsch, M.; Horvath, F.; Knoll, C.; Lager, D.; Gierl-Mayer, C.; Weinberger, P.; Winter, F. High-Temperature Energy Storage: Kinetic Investigations of the CuO/Cu2O Reaction Cycle. *Energy and Fuels* **2017**, *31*, 2324–2334, doi:10.1021/acs.energyfuels.6b02343.

120. Alonso, E.; Pérez-Rábago, C.; Licurgo, J.; Fuentealba, E.; Estrada, C.A. First Experimental Studies of Solar Redox Reactions of Copper Oxides for Thermochemical Energy Storage. *Solar Energy* **2015**, *115*, 297–305, doi:10.1016/j.solener.2015.03.005.

121. Gigantino, M.; Brunser, S.S.; Steinfeld, A. High-Temperature Thermochemical Heat Storage via the CuO/Cu2O Redox Cycle: From Material Synthesis to Packed-Bed Reactor Engineering and Cyclic Operation. *Energy and Fuels* **2020**, *34*, 16772–16782, doi:10.1021/acs.energyfuels.0c02572.

122. André, L.; Abanades, S.; Cassayre, L. Mixed Co, Cu and Mn-Based Metal Oxides for Thermochemical Energy Storage Application. In Proceedings of the AIP Conference Proceedings; American Institute of Physics Inc., November 8 2018; Vol. 2033.

123. Bielsa, D.; Zaki, A.; Faik, A.; Arias, P.L. Efficiency Improvement of Mn2O3/Mn3O4 Redox Reaction by Means of Different Operation Strategies. In Proceedings of the AIP Conference Proceedings; American Institute of Physics Inc., July 25 2019; Vol. 2126.

124. André, L.; Abanades, S.; Cassayre, L. Experimental and Thermodynamic Study of Co-Fe and Mn-Fe Based Mixed Metal Oxides for Thermochemical Energy Storage Application. In Proceedings of the AIP Conference Proceedings; American Institute of Physics Inc., June 27 2017; Vol. 1850.

125. Neises, M.; Tescari, S.; de Oliveira, L.; Roeb, M.; Sattler, C.; Wong, B. Solar-Heated Rotary Kiln for Thermochemical Energy Storage. *Solar Energy* **2012**, *86*, doi:10.1016/j.solener.2012.07.012.

126. Jahromy, S.S.; Birkelbach, F.; Jordan, C.; Huber, C.; Harasek, M.; Werner, A.; Winter, F. Impact of Partial Pressure, Conversion, and Temperature on the Oxidation Reaction Kinetics of Cu 2 O to CuO in Thermochemical Energy Storage. *Energies (Basel)* **2019**, *12*, doi:10.3390/en12030508.

127. Mette, B.; Kerskes, H.; Drück, H. Experimental and Numerical Investigations of Different Reactor Concepts for Thermochemical Energy Storage. In Proceedings of the Energy Procedia; Elsevier Ltd, 2014; Vol. 57, pp. 2380–2389.

128. Foutch, G.L.; Johannes, A.H. Reactors in Process Engineering. In *Encyclopedia of Physical Science and Technology*; 2003.

129. Schmidt, M.; Szczukowski, C.; Roßkopf, C.; Linder, M.; Wörner, A. Experimental Results of a 10 KW High Temperature Thermochemical Storage Reactor Based on Calcium Hydroxide. *Appl Therm Eng* **2014**, *62*, doi:10.1016/j.applthermaleng.2013.09.020.

130. Ranjha, Q.A.; Vahedi, N.; Oztekin, A. Numerical Study of Thermochemical Storage Using Ca(OH)2/CaO - High Temperature Applications. In Proceedings of the ASME International Mechanical Engineering Congress and Exposition, Proceedings (IMECE); American Society of Mechanical Engineers (ASME), 2016; Vol. 6B-2016.

131. Funayama, S.; Takasu, H.; Zamengo, M.; Kariya, J.; Kim, S.T.; Kato, Y. Performance of Thermochemical Energy Storage of a Packed Bed of Calcium Hydroxide Pellets. *Energy Storage* **2019**, *1*, e40, doi:10.1002/est2.40.

132. Schmidt, M.; Linder, M. A Novel Thermochemical Long Term Storage Concept: Balance of Renewable Electricity and Heat Demand in Buildings. *Front Energy Res* **2020**, *8*, doi:10.3389/fenrg.2020.00137.

133. Schmidt, M.; Gutierrez, A.; Linder, M. Thermochemical Energy Storage with CaO/Ca(OH)2–Experimental Investigation of the Thermal Capability at Low Vapor Pressures in a Lab Scale Reactor. *Appl Energy* **2017**, *188*, 672–681, doi:10.1016/j.apenergy.2016.11.023.

134. Peng, X.; Yao, M.; Root, T.W.; Maravelias, C.T. Design and Analysis of Concentrating Solar Power Plants with Fixed-Bed Reactors for Thermochemical Energy Storage. *Appl Energy* **2020**, *262*, doi:10.1016/j.apenergy.2020.114543.

135. Schaube, F.; Utz, I.; Wörner, A.; Müller-Steinhagen, H. De- and Rehydration of Ca(OH)2 in a Reactor with Direct Heat Transfer for Thermo-Chemical Heat Storage. Part B: Validation of Model. *Chemical Engineering Research and Design* **2013**, *91*, 865–873, doi:10.1016/j.cherd.2013.02.019.

136. Pan, Z.H.; Zhao, C.Y. Gas–Solid Thermochemical Heat Storage Reactors for High-Temperature Applications. *Energy* 2017, *130*, 155–173.

137. Schmidt, M.; Gollsch, M.; Giger, F.; Grün, M.; Linder, M. Development of a Moving Bed Pilot Plant for Thermochemical Energy Storage with CaO/Ca(OH)2. In Proceedings of the AIP Conference Proceedings; American Institute of Physics Inc., May 31 2016; Vol. 1734.

138. Shirzad, M.; Karimi, M.; Silva, J.A.C.; Rodrigues, A.E. Moving Bed Reactors: Challenges and Progress of Experimental and Theoretical Studies in a Century of Research. *Ind Eng Chem Res* 2019, *58*, 9179–9198.

139. Angerer, M.; Becker, M.; Härzschel, S.; Kröper, K.; Gleis, S.; Vandersickel, A.; Spliethoff, H. Design of a MW-Scale Thermo-Chemical Energy Storage Reactor. *Energy Reports* **2018**, *4*, 507–519, doi:10.1016/j.egyr.2018.07.005.

140. Preisner, N.C.; Bürger, I.; Wokon, M.; Linder, M. Numerical Investigations of a Counter-Current Moving Bed Reactor for Thermochemical Energy Storage at High Temperatures. *Energies (Basel)* **2020**, *13*, doi:10.3390/en13030772.

141. Preisner, N.C.; Linder, M. A Moving Bed Reactor for Thermochemical Energy Storage Based on Metal Oxides. *Energies (Basel)* **2020**, *13*, doi:10.3390/en13051232.

142. Huang, W.; Korba, D.; Randhir, K.; Petrasch, J.; Klausner, J.; AuYeung, N.; Li, L. Thermochemical Reduction Modeling in a High-Temperature Moving-Bed Reactor for Energy Storage: 1D Model. *Appl Energy* **2022**, *306*, doi:10.1016/j.apenergy.2021.118009.

143. Di Renzo, A.; Scala, F.; Heinrich, S. Recent Advances in Fluidized Bed Hydrodynamics and Transport Phenomena—Progress and Understanding. *Processes* 2021, *9*.

144. Kant, K.; Pitchumani, R. Advances and Opportunities in Thermochemical Heat Storage Systems for Buildings Applications. *Appl Energy* 2022, *321*.

145. Flegkas, S.; Birkelbach, F.; Winter, F.; Freiberger, N.; Werner, A. Fluidized Bed Reactors for Solid-Gas Thermochemical Energy Storage Concepts - Modelling and Process Limitations. *Energy* **2018**, *143*, 615–623, doi:10.1016/j.energy.2017.11.065.

146. Rougé, S.; Criado, Y.A.; Soriano, O.; Abanades, J.C. Continuous CaO/Ca(OH)2 Fluidized Bed Reactor for Energy Storage: First Experimental Results and Reactor Model Validation. *Ind Eng Chem Res* **2017**, *56*, 844–852, doi:10.1021/acs.iecr.6b04105.

147. Mu, L.; Buist, K.A.; Kuipers, J.A.M.; Deen, N.G. Hydrodynamic and Heat Transfer Study of a Fluidized Bed by Discrete Particle Simulations. *Processes* **2020**, *8*, doi:10.3390/PR8040463.

148. Hawwash, A.A.; Hassan, H.; feky, K. El Impact of Reactor Design on the Thermal Energy Storage of Thermochemical Materials. *Appl Therm Eng* **2020**, *168*, doi:10.1016/j.applthermaleng.2019.114776.

149. Darkwa, K.; Ianakiev, A.; O'Callaghan, P.W. Modelling and Simulation of Adsorption Process in a Fluidised Bed Thermochemical Energy Reactor. *Appl Therm Eng* **2006**, *26*, 838–845, doi:10.1016/j.applthermaleng.2005.10.008.

150. Kim, J.; Han, G.Y. Effect of Agitation on Fluidization Characteristics of Fine Particles in a Fluidized Bed. *Powder Technol* **2006**, *166*, 113–122, doi:10.1016/j.powtec.2006.06.001.

151. Wang, J.J.; Han, Y.; Gu, X.P.; Feng, L.F.; Hu, G.H. Effect of Agitation on the Fluidization Behavior of a Gas-Solid Fluidized Bed with a Frame Impeller. *AIChE Journal* **2013**, *59*, 1066–1074, doi:10.1002/aic.13893.

152. Lv, B.; Deng, X.; Shi, C.; Fang, C. Effect of Agitation on Hydrodynamics and Separation Performance of Gas–Solid Separation Fluidized Bed. *Powder Technol* **2021**, *388*, 129–138, doi:10.1016/j.powtec.2021.04.084.

153. Dong, K.; Zhou, Y.; Huang, Z.; Wang, J.; Yang, Y. Gas Bubble Behaviors in a Gas-Solid Fluidized Bed with an Arch Agitator. *Powder Technol* **2014**, *266*, 38–44, doi:10.1016/j.powtec.2014.06.015.

154. Shi, D.P.; Luo, Z.H.; Guo, A.Y. Numerical Simulation of the Gas-Solid Flow in Fluidized-Bed Polymerization Reactors. *Ind Eng Chem Res* **2010**, *49*, 4070–4079, doi:10.1021/ie901424g.

155. Gbenou, T.R.S.; Fopah-Lele, A.; Wang, K. Macroscopic and Microscopic Investigations of Low-Temperature Thermochemical Heat Storage Reactors: A Review. *Renewable and Sustainable Energy Reviews* 2022, *161*.

156. Maruyama, A.; Kurosawa, R.; Ryu, J. Effect of Lithium Compound Addition on the Dehydration and Hydration of Calcium Hydroxide as a Chemical Heat Storage Material. *ACS Omega* **2020**, doi:10.1021/acsomega.9b04444.

157. Oswald, S.; Thoss, F.; Zier, M.; Hoffmann, M.; Jaumann, T.; Herklotz, M.; Nikolowski, K.; Scheiba, F.; Kohl, M.; Giebeler, L.; et al. Binding Energy Referencing for XPS in Alkali Metal-Based Battery Materials Research (II): Application to Complex Composite Electrodes. *Batteries* **2018**, *4*, doi:10.3390/batteries4030036.

158. Oswald, S. Binding Energy Referencing for XPS in Alkali Metal-Based Battery Materials Research (I): Basic Model Investigations. *Appl Surf Sci* **2015**, *351*, 492–503, doi:10.1016/j.apsusc.2015.05.029.

159. Coetzee, D.; Venkataraman, M.; Militky, J.; Petru, M. Influence of Nanoparticles on Thermal and Electrical Conductivity of Composites. *Polymers (Basel)* 2020, *12*.

160. Gupta, N.; Kumar, A.; Dhasmana, H.; Kumar, V.; Kumar, A.; Shukla, P.; Verma, A.; Nutan, G. V.; Dhawan, S.K.; Jain, V.K. Enhanced Thermophysical Properties of Metal Oxide Nanoparticles Embedded Magnesium Nitrate Hexahydrate Based Nanocomposite for Thermal Energy Storage Applications. *J Energy Storage* **2020**, *32*, doi:10.1016/j.est.2020.101773.

161. Thompson, A.P.; Aktulga, H.M.; Berger, R.; Bolintineanu, D.S.; Brown, W.M.; Crozier, P.S.; in 't Veld, P.J.; Kohlmeyer, A.; Moore, S.G.; Nguyen, T.D.; et al. LAMMPS - a Flexible Simulation Tool for Particle-Based Materials Modeling at the Atomic, Meso, and Continuum Scales. *Comput Phys Commun* **2022**, *271*, doi:10.1016/j.cpc.2021.108171.

162. Steinhauser, M.O.; Hiermaier, S. A Review of Computational Methods in Materials Science: Examples from Shock-Wave and Polymer Physics. *Int J Mol Sci* 2009, *10*.

163. Lindahl, E.; Hess, B.; van der Spoel, D. GROMACS 3.0: A Package for Molecular Simulation and Trajectory Analysis. *J Mol Model* 2001, *7*.

164. Phillips, J.C.; Braun, R.; Wang, W.; Gumbart, J.; Tajkhorshid, E.; Villa, E.; Chipot, C.; Skeel, R.D.; Kalé, L.; Schulten, K. Scalable Molecular Dynamics with NAMD. *J Comput Chem* 2005, *26*.

165. Weiner, P.K.; Kollman, P.A. AMBER: Assisted Model Building with Energy Refinement. A General Program for Modeling Molecules and Their Interactions. *J Comput Chem* **1981**, *2*, doi:10.1002/jcc.540020311.

166. Brooks, B.R.; Brooks, C.L.; Mackerell, A.D.; Nilsson, L.; Petrella, R.J.; Roux, B.; Won, Y.; Archontis, G.; Bartels, C.; Boresch, S.; et al. CHARMM: The Biomolecular Simulation Program. *J Comput Chem* **2009**, *30*, doi:10.1002/jcc.21287.

167. Smith, W.; Forester, T.R. DL-POLY-2.0: A General-Purpose Parallel Molecular Dynamics Simulation Package. *J Mol Graph* **1996**, *14*, doi:10.1016/S0263-7855(96)00043-4.

168. Anderson, J.A.; Lorenz, C.D.; Travesset, A. General Purpose Molecular Dynamics Simulations Fully Implemented on Graphics Processing Units. *J Comput Phys* **2008**, *227*, doi:10.1016/j.jcp.2008.01.047.

169. Plimpton, S. Fast Parallel Algorithms for Short-Range Molecular Dynamics. *J Comput Phys* **1995**, *117*, doi:10.1006/jcph.1995.1039.

170. Srivastava, I.; Kotia, A.; Ghosh, S.K.; Ali, M.K.A. Recent Advances of Molecular Dynamics Simulations in Nanotribology. *J Mol Liq* 2021, *335*.

171. Thompson, A.P.; Plimpton, S.J.; Mattson, W. General Formulation of Pressure and Stress Tensor for Arbitrary Many-Body Interaction Potentials under Periodic Boundary Conditions. *Journal of Chemical Physics* **2009**, *131*, doi:10.1063/1.3245303.

172. National Laboratories, S. LAMMPS Documentation Available online: https://docs.lammps.org/Manual.html (accessed on 23 August 2024).

173. Martinez, L.; Andrade, R.; Birgin, E.G.; Martínez, J.M. PACKMOL: A Package for Building Initial Configurations for Molecular Dynamics Simulations. *J Comput Chem* **2009**, *30*, 2157–2164, doi:10.1002/jcc.21224.

174. Becker, C.A.; Tavazza, F.; Trautt, Z.T.; Buarque De Macedo, R.A. Considerations for Choosing and Using Force Fields and Interatomic Potentials in Materials Science and Engineering. *Curr Opin Solid State Mater Sci* 2013, *17*.

175. Anagnostopoulos, A.; Navarro, H.; Alexiadis, A.; Ding, Y. Wettability of NaNO3 and KNO3 on MgO and Carbon Surfaces-Understanding the Substrate and the Length Scale Effects. *Journal of Physical Chemistry C* **2020**, *124*, 8140–8152, doi:10.1021/acs.jpcc.0c00978.

176. Hu, Y.; He, Y.; Zhang, Z.; Wen, D. Effect of Al2O3 Nanoparticle Dispersion on the Specific Heat Capacity of a Eutectic Binary Nitrate Salt for Solar Power Applications. *Energy Convers Manag* **2017**, *142*, 366–373, doi:10.1016/j.enconman.2017.03.062.

177. Kholmurodov, K.; Abasheva, M.; Yasuoka, K. Molecular Dynamics Simulations of Valinomycin Interactions with Potassium and Sodium Ions in Water Solvent. *Advances in Bioscience and Biotechnology* **2010**, *01*, 216–223, doi:10.4236/abb.2010.13030.

178. Wang, Z.; Wen, G.; Liu, Q.; Huang, S.; Tang, P.; Yu, L. Estimating the Thermal Conductivity of CaO–Al2O3–SiO2 Slags by Equilibrium Molecular Dynamics Simulations. *J Non Cryst Solids* **2020**, *531*, doi:10.1016/j.jnoncrysol.2019.119851.

179. Alexander, J.S.; Maxwell, C.; Pencer, J.; Saoudi, M. Equilibrium Molecular Dynamics Calculations of Thermal Conductivity: A “How-to” for the Beginners. *CNL Nuclear Review* **2020**, *9*, doi:10.12943/cnr.2018.00009.

180. Ni, C. ming; Fan, H. wei; Wang, X. dong; Yao, M. Thermal Conductivity Prediction of MgAl2O4: A Non-Equilibrium Molecular Dynamics Calculation. *Journal of Iron and Steel Research International* **2020**, *27*, doi:10.1007/s42243-020-00364-6.

181. Assael, M.J.; Antoniadis, K.D.; Wakeham, W.A. Historical Evolution of the Transient Hot-Wire Technique. *Int J Thermophys* **2010**, *31*, doi:10.1007/s10765-010-0814-9.

182. Winczewski, S.; Muna, I. Molecular Dynamics Simulations of Thermal Conductivity of Penta-Graphene. *TASK QUARTERLY* **2020**, *24*, 191–220, doi:10.34808/tq2020/24.3/a.

183. Levine, B.G.; Stone, J.E.; Kohlmeyer, A. Fast Analysis of Molecular Dynamics Trajectories with Graphics Processing Units-Radial Distribution Function Histogramming. *J Comput Phys* **2011**, *230*, doi:10.1016/j.jcp.2011.01.048.

184. Wei, X.; Chen, D.; Liu, S.; Wang, W.; Ding, J.; Lu, J. Structure and Thermophysical Properties of Molten Calcium-Containing Multi-Component Chlorides by Using Specific BMH Potential Parameters. *Energies (Basel)* **2022**, *15*, doi:10.3390/en15238878.

185. Schelling, P.K.; Phillpot, S.R.; Keblinski, P. Comparison of Atomic-Level Simulation Methods for Computing Thermal Conductivity. *Phys Rev B Condens Matter Mater Phys* **2002**, *65*, doi:10.1103/PhysRevB.65.144306.

186. NIST Experimental Data for Magnesium Hydroxide Available online: https://cccbdb.nist.gov/exp2x.asp?casno=12141116&charge=0 (accessed on 18 September 2024).

187. Barzegar, A.; Ghaffari, T.; Parizad, A. Effect of Incorporating Aluminum Oxide Nanoparticles on Thermal Conduction and Flexural Strength of Acrylic Resins. *Dent Res J (Isfahan)* **2022**, *19*, 33–39.

188. Bi, H.T.; Li, J. Multiscale Analysis and Modeling of Multiphase Chemical Reactors. In Proceedings of the Advanced Powder Technology; 2004; Vol. 15.

189. Sotudeh-Gharebaagh, R.; Legros, R.; Chaouki, J.; Paris, J. Simulation of Circulating Fluidized Bed Reactors Using ASPEN PLUS. *Fuel* **1998**, *77*, doi:10.1016/S0016-2361(97)00211-1.

190. Al-Malah, K.I.M. *Aspen Plus: Chemical Engineering Applications*; John Wiley & Sons Inc.: Hoboken, New Jersey, 2017; ISBN 9781119293613.

191. Shaul, S.; Rabinovich, E.; Kalman, H. Typical Fluidization Characteristics for Geldart’s Classification Groups. *Particulate Science and Technology* **2014**, *32*, 197–205, doi:10.1080/02726351.2013.842624.

192. Debtera Bejena, B.; Debtera, B.; Ramesh, R.; Neme, I.; Ramesh, K.; Murali, A. *Fluidized Bed Reactor Modelling and Simulation with ASPEN Plus for Alumina (Al2O3) Production Systems*; 2021; Vol. 08;

This page is blank

Appendix A

Appendix A.1a NEMD simulation data for pure MH material.

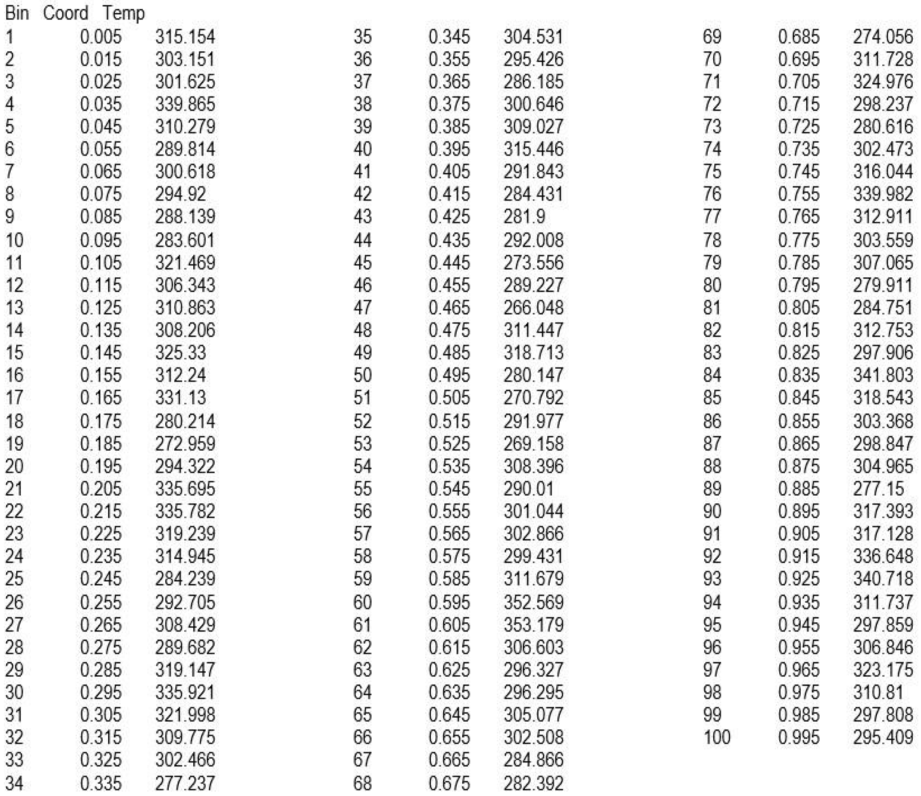

Bin	Coord	Temp
1	0.005	315.154
2	0.015	303.151
3	0.025	301.625
4	0.035	339.865
5	0.045	310.279
6	0.055	289.814
7	0.065	300.618
8	0.075	294.92
9	0.085	288.139
10	0.095	283.601
11	0.105	321.469
12	0.115	306.343
13	0.125	310.863
14	0.135	308.206
15	0.145	325.33
16	0.155	312.24
17	0.165	331.13
18	0.175	280.214
19	0.185	272.959
20	0.195	294.322
21	0.205	335.695
22	0.215	335.782
23	0.225	319.239
24	0.235	314.945
25	0.245	284.239
26	0.255	292.705
27	0.265	308.429
28	0.275	289.682
29	0.285	319.147
30	0.295	335.921
31	0.305	321.998
32	0.315	309.775
33	0.325	302.466
34	0.335	277.237
35	0.345	304.531
36	0.355	295.426
37	0.365	286.185
38	0.375	300.646
39	0.385	309.027
40	0.395	315.446
41	0.405	291.843
42	0.415	284.431
43	0.425	281.9
44	0.435	292.008
45	0.445	273.556
46	0.455	289.227
47	0.465	266.048
48	0.475	311.447
49	0.485	318.713
50	0.495	280.147
51	0.505	270.792
52	0.515	291.977
53	0.525	269.158
54	0.535	308.396
55	0.545	290.01
56	0.555	301.044
57	0.565	302.866
58	0.575	299.431
59	0.585	311.679
60	0.595	352.569
61	0.605	353.179
62	0.615	306.603
63	0.625	296.327
64	0.635	296.295
65	0.645	305.077
66	0.655	302.508
67	0.665	284.866
68	0.675	282.392
69	0.685	274.056
70	0.695	311.728
71	0.705	324.976
72	0.715	298.237
73	0.725	280.616
74	0.735	302.473
75	0.745	316.044
76	0.755	339.982
77	0.765	312.911
78	0.775	303.559
79	0.785	307.065
80	0.795	279.911
81	0.805	284.751
82	0.815	312.753
83	0.825	297.906
84	0.835	341.803
85	0.845	318.543
86	0.855	303.368
87	0.865	298.847
88	0.875	304.965
89	0.885	277.15
90	0.895	317.393
91	0.905	317.128
92	0.915	336.648
93	0.925	340.718
94	0.935	311.737
95	0.945	297.859
96	0.955	306.846
97	0.965	323.175
98	0.975	310.81
99	0.985	297.808
100	0.995	295.409

Appendix A.1b Calculation of standard error.

Step One: Find sample size

$$n = 100$$

Step Two: Find mean of the data points

$\bar{x} = \sqrt{\frac{\sum x_i}{n}}$ = 304.104

Step Three: Find the standard deviation

$$s = \sqrt{\frac{\sum (x_i - \bar{x})^2}{n}} = \sqrt{\frac{35121.435628}{100}} = 18.7407$$

Step Three: Find the standard error

$$SE = \frac{s}{\sqrt{n}} = \frac{18.7407}{\sqrt{100}} = 1.87407$$

Appendix A.2a NEMD simulation data for doped material (MH-PN5).

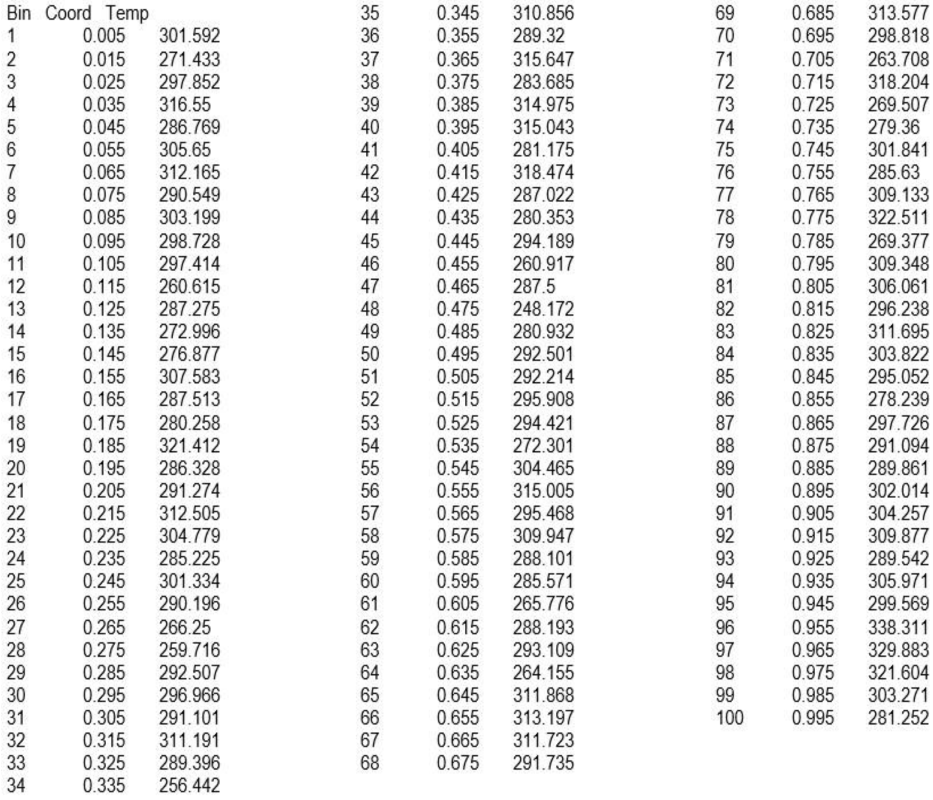

Bin	Coord	Temp
1	0.005	301.592
2	0.015	271.433
3	0.025	297.852
4	0.035	316.55
5	0.045	286.769
6	0.055	305.65
7	0.065	312.165
8	0.075	290.549
9	0.085	303.199
10	0.095	298.728
11	0.105	297.414
12	0.115	260.615
13	0.125	287.275
14	0.135	272.996
15	0.145	276.877
16	0.155	307.583
17	0.165	287.513
18	0.175	280.258
19	0.185	321.412
20	0.195	286.328
21	0.205	291.274
22	0.215	312.505
23	0.225	304.779
24	0.235	285.225
25	0.245	301.334
26	0.255	290.196
27	0.265	266.25
28	0.275	259.716
29	0.285	292.507
30	0.295	296.966
31	0.305	291.101
32	0.315	311.191
33	0.325	289.396
34	0.335	256.442
35	0.345	310.856
36	0.355	289.32
37	0.365	315.647
38	0.375	283.685
39	0.385	314.975
40	0.395	315.043
41	0.405	281.175
42	0.415	318.474
43	0.425	287.022
44	0.435	280.353
45	0.445	294.189
46	0.455	260.917
47	0.465	287.5
48	0.475	248.172
49	0.485	280.932
50	0.495	292.501
51	0.505	292.214
52	0.515	295.908
53	0.525	294.421
54	0.535	272.301
55	0.545	304.465
56	0.555	315.005
57	0.565	295.468
58	0.575	309.947
59	0.585	288.101
60	0.595	285.571
61	0.605	265.776
62	0.615	288.193
63	0.625	293.109
64	0.635	264.155
65	0.645	311.868
66	0.655	313.197
67	0.665	311.723
68	0.675	291.735
69	0.685	313.577
70	0.695	298.818
71	0.705	263.708
72	0.715	318.204
73	0.725	269.507
74	0.735	279.36
75	0.745	301.841
76	0.755	285.63
77	0.765	309.133
78	0.775	322.511
79	0.785	269.377
80	0.795	309.348
81	0.805	306.061
82	0.815	296.238
83	0.825	311.695
84	0.835	303.822
85	0.845	295.052
86	0.855	278.239
87	0.865	297.726
88	0.875	291.094
89	0.885	289.861
90	0.895	302.014
91	0.905	304.257
92	0.915	309.877
93	0.925	289.542
94	0.935	305.971
95	0.945	299.569
96	0.955	338.311
97	0.965	329.883
98	0.975	321.604
99	0.985	303.271
100	0.995	281.252

Appendix A.2b Calculation of standard error.

Step One: Find sample size

$$n = 100$$

Step Two: Find mean of the data points

$\bar{x} = \sqrt{\frac{\sum x_i}{n}}$ = 294.619

Step Three: Find the standard deviation

$$s = \sqrt{\frac{\sum(x_i - \bar{x})^2}{n}} = \sqrt{\frac{29881.382264}{100}} = 17.2862$$

Step Three: Find the standard error

$$SE = \frac{s}{\sqrt{n}} = \frac{17.2862}{\sqrt{100}} = 1.72862$$

Appendix A.3a NEMD simulation data for enhanced material (MH-PN5AO15).

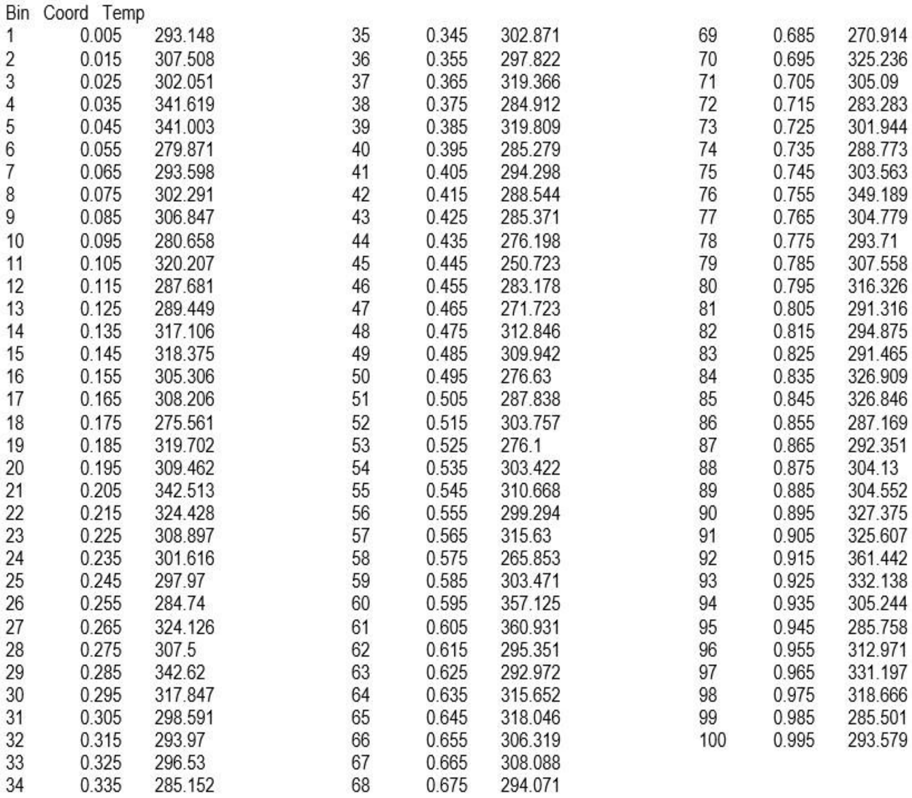

Bin	Coord	Temp
1	0.005	293.148
2	0.015	307.508
3	0.025	302.051
4	0.035	341.619
5	0.045	341.003
6	0.055	279.871
7	0.065	293.598
8	0.075	302.291
9	0.085	306.847
10	0.095	280.658
11	0.105	320.207
12	0.115	287.681
13	0.125	289.449
14	0.135	317.106
15	0.145	318.375
16	0.155	305.306
17	0.165	308.206
18	0.175	275.561
19	0.185	319.702
20	0.195	309.462
21	0.205	342.513
22	0.215	324.428
23	0.225	308.897
24	0.235	301.616
25	0.245	297.97
26	0.255	284.74
27	0.265	324.126
28	0.275	307.5
29	0.285	342.62
30	0.295	317.847
31	0.305	298.591
32	0.315	293.97
33	0.325	296.53
34	0.335	285.152
35	0.345	302.871
36	0.355	297.822
37	0.365	319.366
38	0.375	284.912
39	0.385	319.809
40	0.395	285.279
41	0.405	294.298
42	0.415	288.544
43	0.425	285.371
44	0.435	276.198
45	0.445	250.723
46	0.455	283.178
47	0.465	271.723
48	0.475	312.846
49	0.485	309.942
50	0.495	276.63
51	0.505	287.838
52	0.515	303.757
53	0.525	276.1
54	0.535	303.422
55	0.545	310.668
56	0.555	299.294
57	0.565	315.63
58	0.575	265.853
59	0.585	303.471
60	0.595	357.125
61	0.605	360.931
62	0.615	295.351
63	0.625	292.972
64	0.635	315.652
65	0.645	318.046
66	0.655	306.319
67	0.665	308.088
68	0.675	294.071
69	0.685	270.914
70	0.695	325.236
71	0.705	305.09
72	0.715	283.283
73	0.725	301.944
74	0.735	288.773
75	0.745	303.563
76	0.755	349.189
77	0.765	304.779
78	0.775	293.71
79	0.785	307.558
80	0.795	316.326
81	0.805	291.316
82	0.815	294.875
83	0.825	291.465
84	0.835	326.909
85	0.845	326.846
86	0.855	287.169
87	0.865	292.351
88	0.875	304.13
89	0.885	304.552
90	0.895	327.375
91	0.905	325.607
92	0.915	361.442
93	0.925	332.138
94	0.935	305.244
95	0.945	285.758
96	0.955	312.971
97	0.965	331.197
98	0.975	318.666
99	0.985	285.501
100	0.995	293.579

Appendix A.3b Calculation of standard error.

Step One: Find sample size

$$n = 100$$

Step Two: Find mean of the data points

$\bar{x} = \sqrt{\frac{\sum x_i}{n}}$ = 304.497

Step Three: Find the standard deviation

$$s = \sqrt{\frac{\sum (x_i - \bar{x})^2}{n}} = \sqrt{\frac{41940.961963}{100}} = 20.4795$$

Step Three: Find the standard error

$$SE = \frac{s}{\sqrt{n}} = \frac{20.4795}{\sqrt{100}} = 2.04795$$

Appendix B

Appendix B.1a Experimental data for pure material

0.06487

0.06510

0.06534

0.06499

0.06502

0.06511

0.06693

0.06696

0.06691

0.06499

Appendix B.1b Calculation of accuracy range (AR).

Step One: Find sample size

$$n = 10$$

Step Two: Find mean of the data points

$\bar{x} = \sqrt{\frac{\sum x_i}{n}}$ = 0.065622

Step Three: Find the standard deviation

$$s = \sqrt{\frac{\sum (x_i - \bar{x})^2}{n}} = \sqrt{\frac{7.50096E - 6}{10}} = 0.00086608082763677$$

Step Three: Find the standard error

$$SE = \frac{s}{\sqrt{n}} = \frac{0.00086608082763677}{\sqrt{10}} = 0.00027387880531359$$

Step Four: Find the confidence level

$$\mathrm{CL} = (\mathrm{SE}).(\mathrm{t_{value}}) = (0.00027387880531359)(1.960) = 0.000537$$

Step Five: Find the confidence interval and accuracy range

$$\mathrm{CI} = \pm(\mathrm{CL}) = \pm 0.000537$$

$$AR = \bar{x} \pm (\mathrm{CL}) = 0.065622 \pm 0.000537 = 0.065083 \text{ to } 0.066157$$

Appendix B.2a Experimental data for doped material

0.04926

0.04942

0.04939

0.04938

0.04934

0.04943

0.04937

0.04936

0.04926

0.04935

Appendix B.2b Calculation of accuracy range (AR).

Step One: Find sample size

$$n = 10$$

Step Two: Find mean of the data points

$\bar{x} = \sqrt{\frac{\sum x_i}{n}}$ = 0.049356

Step Three: Find the standard deviation

$$s = \sqrt{\frac{\sum(x_i - \bar{x})^2}{n}} = \sqrt{\frac{3.02400000000001E - 8}{10}} = 5.4990908339471\text{E} - 5$$

Step Three: Find the standard error

$$SE = \frac{s}{\sqrt{n}} = \frac{5.4990908339471\text{E} - 5}{\sqrt{10}} = 1.7389652095428E - 5$$

Step Four: Find the confidence level

$$\text{CL} = (\text{SE}).(\text{t}_{\text{value}}) = (1.7389652095428\text{E} - 5)(1.960) = 0.00003408$$

Step Five: Find the confidence interval and accuracy range

$$\text{CI} = \pm(\text{CL}) = \pm\, 0.00003408$$

$$AR = \bar{x} \pm (\text{CL}) = 0.049356 \pm 0.00003408 = 0.049322 \text{ to } 0.049390$$

Appendix B.3a Experimental data for enhanced material

0.66517

0.66144

0.65678

0.65238

0.64925

0.64527

0.64285

0.63953

0.63702

0.63443

Appendix B.3b Calculation of accuracy range (AR).

Step One: Find sample size

$$n = 10$$

Step Two: Find mean of the data points

$\bar{x} = \sqrt{\frac{\sum x_i}{n}}$ = 0.648412

Step Three: Find the standard deviation

$$s = \sqrt{\frac{\sum(x_i - \bar{x})^2}{n}} = \sqrt{\frac{0.00098200196}{10}} = 0.0099096012028739$$

Step Three: Find the standard error

$$SE = \frac{s}{\sqrt{n}} = \frac{0.0099096012028739}{\sqrt{10}} = 0.0031336910505026$$

Step Four: Find the confidence level

$$\mathrm{CL} = (\mathrm{SE}).(\mathrm{t_{value}}) = (0.0031336910505026)(1.960) = 0.006142$$

Step Five: Find the confidence interval and accuracy range

$$\mathrm{CI} = \pm(\mathrm{CL}) = \pm\, 0.006142$$

$$AR = \bar{x} \pm (\mathrm{CL}) = 0.648412 \pm 0.006142 = 0.64227 \text{ to } 0.654554$$